Nature-Inspired Carbon Materials for Emerging Sodium-Based Energy Storage Technologies

Zhen Xu

Department of Chemical Engineering

Imperial College London

2022

Supervised by Professor Maria-Magdalena Titirici

Submitted in partial fulfilment of the requirements for the degree of

Doctor of Philosophy

Imperial College London

Originality declaration

I, Zhen Xu, hereby declare that this thesis is my own work, except where references and data sources are appropriately listed. My own published materials related to this thesis are also acknowledged below. This thesis has not been previously submitted for the reward of a degree course at this or any other institute.

Zhen Xu (徐朕)

London, United Kingdom

January 2022

Copyright declaration

The copyright of this thesis rests with the author and is made available under a Creative Commons Attribution-NonCommercial 4.0 International Licence (CC BY-NC). Under this licence, you may copy and redistribute the material in any medium or format. You may also create and distribute modified versions of the work. This is on the condition that: you credit the author and do not use it, or any derivative works, for a commercial purpose. When reusing or sharing this work, ensure you make the licence terms clear to others by naming the licence and linking to the licence text. Where a work has been adapted, you should indicate that the work has been changed and describe those changes. Please seek permission from the copyright holder for uses of this work that are not included in this licence or permitted under UK Copyright Law.

Contents

Acknowledgement **5**

Abstract **7**

List of publications related to this thesis **8**

List of figures **9**

List of tables **23**

Acronyms **25**

Chapter 1. Introduction **29**

1.1 The necessity of novel energy conversion and storage technologies 29

1.2 Electrochemical energy storage technologies – batteries and capacitors 29

1.3 Objectives and outlines of this thesis 32

Chapter 2. Literature overview **36**

2.1 Sodium-based energy storage technologies 36

2.1.1 Definitions, principles and metrics 37

2.1.2 Sodium batteries 48

2.1.2.1 Anodes 49

2.1.2.2 Cathodes 66

2.1.2.3 Electrolytes 71

2.1.2.4 Electrode architecture and cell assembly 74

2.1.3 Sodium capacitors 76

2.1.3.1 Electrodes 78

2.1.3.2 Electrolytes 80

2.2 Summary and perspective 81

Chapter 3. Materials and methodologies **83**

3.1 Materials 83

3.2 Methodologies 85

3.2.1 Synthesis 85

3.2.2 Characterisation 94

3.2.3. Theoretical modelling and simulations. 102

Chapter 4. From glucose to sodium-ion batteries 106

4.1 Synthesis and structural characterisation of bio-derived hard carbons .. 108

4.2 Electrochemical testing in the half cell configuration 113

4.3 Electrochemical kinetic calculation and analysis 115

4.4 Fundamental mechanistic insights into sodium-ion insertion behaviours and interfacial phenomena 118

4.5 Life cycle assessment of hard carbon anodes for sodium-ion storage 127

4.6 Practical applications of sodium-ion full cells 129

4.5 Conclusions 131

Chapter 5. From cellulose to sodium-ion capacitors 133

5.1 Carbon anodes from cellulose nanocrystals 135

5.2 Carbon cathodes from cellulose microfibrils 142

5.3 Full cells with liquid electrolytes 148

5.4 Full cells with cellulose-based gel electrolytes 152

5.5 Conclusions 154

Chapter 6. From lignin to sodium-metal batteries 155

6.1 Synthesis and structural characterisation of carbon skeletons 156

6.2 Electrochemical performance in half cell configurations 161

6.3 Fundamental mechanism insights into interfacial phenomena and deposition behaviours 168

6.4 Practical applications of sodium metal batteries 178

6.5 Conclusions 184

Chapter 7. Summary and outlook 186

Appendix 189

A1. Supplementary figures and tables for Chapter 4 189

A2. Supplementary figures and tables for Chapter 5 199

A3. Supplementary figures and tables for Chapter 6 212

A4. Premissions 223

Bibliography 230

Acknowledgement

It is a great honour for me to have a chance to pursue a PhD degree. The past four years provide me with a lot of valuable memories.

First of all, I would like to thank my supervisor, Prof. Magda Titirici, for providing me with continuous support, guidance and encouragement during the past four years. She opened the door of science for me and brought me into the research field of sustainable carbon materials and battery science when I was a newcomer to this field. At the same time, she gave me enough freedom to explore different research directions and funding support to complete those experimental studies. I am very grateful to have her as my PhD supervisor. We also travelled together around the world such as Cambridge, Oxford, Berlin and Beijing to attend a lot of conferences and activities together. She is not only my supervisor but also my friend. After that, I also want to thank my colleague, Dr. Fei Xie. When I entered the group, he was the senior PhD student who provided detailed guidance to my research works. We worked and studied together to solve numerous problems and overcome numerous difficulties. Without his help and guidance, it is impossible for me to conduct my experiments smoothly at the beginning of my PhD study. Furthermore, I greatly appreciate Mr. Zhenyu Guo, Dr. Hande Alptekin, Dr. Heather Au, Ms. Anastasia Teck, Dr. Maria Crespo and Dr. Anders Jensen who worked together with me in the battery sub-group. We collaborated on the projects of battery technologies to obtain a lot of wonderful scientific results. Of course, I would like to thank all my colleagues, especially Dr. Hui Luo, Dr. Jingyu Feng, Ms. Qian Guo, Dr. Yan Yang, Mr. Gengyu Tian, Mr. Ruixuan Chen, Mr. Jinglin Jiang, Ms. Mengnan Wang, Dr. Rajesh Madhu, Dr. Servann Herou, Dr. Philipp Schlee, Dr. Pierpaolo Modugno, Dr. Sabina Nicolae, Dr. Mo Qian and Dr. Alain Li, for accompanying me and studying together during the past four years, which brings me a lot of meaningful memories. My PhD life in the UK became more and more amazing after I met with them. It is because of all of them that I have spent meaningful four years here.

Moreover, I would like to thank my collaborators including Prof. Yong-Sheng Hu, Prof. Stephen Eichhorn, Prof. Silvia Vignolini, Dr. Mike Tebyetekerwa, Prof. Shengyuan Yang for sharing valuable knowledge and techniques with me. This thesis cannot be finished without

their professional assistance and advice. Meanwhile, the technicians at Imperial College London and Queen Mary University of London are also much appreciated for aiding me to conduct relative measurement and characterisation.

For my family including my father Mr. Xin Xu, my mother Ms. Hui Bao and my girlfriend Ms. Jing Wang, I would like to send my great appreciation to them as well. Their love makes me overcome every problem, challenge as well as desperate situation. They are the big heroes for me, and I love them so much.

Finally, the joint PhD scholarship from China Scholarship Council and Imperial College London is much appreciated. The completion of this paper includes my gratitude to many people and also proves that I have been fighting hard and working hard in this complex world.

Abstract

Although the commercialisation of lithium-ion batteries is indisputably successful, their financial and environmental issues have raised wide concerns because the resources of elements on which the current lithium-ion batteries highly depend (*e.g.,* lithium, cobalt, copper, nickel, *etc.*) are critically restricted and unevenly distributed. Therefore, the development of next-generation energy storage devices is of great necessity. In comparison to lithium, sodium-based energy storage technologies belong to one of the promising alternative technologies for next-generation energy storage devices due to the abundance and wide distribution of sodium resources and many other advantages.

This thesis presents a series of works on the rational design of sustainable carbon materials inspired by the hierarchical building blocks of natural biomass (*i.e.,* glucose, cellulose and lignin) for the applications of the emerging sodium-based energy storage technologies (*i.e.,* sodium-ion batteries, sodium-ion capacitors and sodium-metal batteries). 1) The first project focused on developing glucose-derived hard carbon anodes with a reversible capacity of 347.4 mAh g^{-1} (30 mA g^{-1}) for sodium-ion storage through hydrothermal pre-treatment and high-temperature carbonisation. 2) The second project focused on developing cellulose-derived carbon materials as electrodes for sodium-ion hybrid capacitors with the energy density of 181 Wh kg^{-1} at 250 W kg^{-1}. 3) The third project focused on developing lignin-derived carbon skeletons with abundant defects as functional hosts to stabilise the metallic sodium anode, which can retain a high Coulombic efficiency (~99.9%) after long cycling (>1200 hours).

By correlating their structural features and electrochemical performance, the structures of sustainable carbon materials for sodium-based energy storage were optimised to obtain enhanced performance and improved sustainability. Meanwhile, kinetic analysis, advanced characterisation methods and multi-scale modelling were also employed to elucidate the detailed energy storage mechanisms of different applications, which can also benefit the fundamental understanding of the structure-performance relationship of sustainable carbon materials. After the systematic research in this thesis, the promise of emerging sodium-based energy storage technologies can be further consolidated based on sustainable carbon materials inspired by nature with advanced architectures.

List of publications related to this thesis

I really appreciate the publisher grants me the permission to reuse my related publications including main texts, images and tables in my thesis. Copies of all permission documents are attached in the Appendix.

Publications related to this thesis:

[1] **Z. Xu** *et al.* Toward Emerging Sodium-Based Energy Storage Technologies: From Performance to Sustainability. *Advanced Energy Materials*, **2022**, 12, 2201692. (Chapter 1, 2 and 3)

[2] **Z. Xu*** *et al*. The rational design of biomass-derived carbon materials towards next-generation energy storage: A review. *Renewable & Sustainable Energy Reviews*, **2020**, 134, 110308. (Chapter 1, 2 and 3)

[3] **Z. Xu** *et al.* The role of hydrothermal carbonisation in sustainable sodium-ion battery anodes. *Advanced Energy Materials*, **2022**, 12, 2200208. (Chapter 4)

[4] **Z. Xu** *et al.* All-cellulose-based quasi-solid-state sodium-ion hybrid capacitors enabled by structural hierarchy. *Advanced Functional Materials*, **2019**, 1903895. (Chapter 5)

[5] **Z. Xu** *et al.* Homogenous metallic deposition regulated by defect-rich skeletons for sodium metal batteries. *Energy & Environmental Science*, **2021**, 14, 6381-6393. (Featured as Back Cover) (Chapter 6)

List of figures

Figure 1.1. a) The average CO_2 amount within the atmosphere during the past thousands of years (Reproduced with permission from [1], Copyright 2021, NASA); b) The global energy consumption by fossil fuel including coal, oil and gas during the past hundreds of years (Reproduced with permission from [2], Copyright 2021, Our World in Data). 29

Figure 1.2. The distribution of lithium resources around the world (Reproduced with permission from [8], Copyright 2021, Springer Nature). 30

Figure 1.3. The Ragone plot of different types of energy storage devices, where the red lines indicate the energy density of 100 Wh kg^{-1} and the power density of 10 kW kg^{-1} (Reproduced with permission from [17], Copyright 2016, Springer Nature).....31

Figure 1.4. Hierarchical building units of natural woods (Reproduced with permission from [22], Copyright 2011, Royal Society of Chemistry). 33

Figure 2.1. a) Estimated energy storage demand until 2050, where the number of devices with different battery sizes and energy storage demand (GWh) on small and large batteries are presented (Reproduced with permission from [26], Copyright 2018, Springer Nature); b) Numbers of publications containing sodium batteries and capacitors since 2001 indexed by Web of Science with the inset of top 10 related areas. 37

Figure 2.2. The schematic illustrations of working principles of a) sodium batteries, and b) sodium capacitors; c) The brief categories of sodium-based energy storage technologies....39

Figure 2.3. The simplified typical GCD curves of cathode, anode and full cell and their corresponding CV curves in a) battery, b) supercapacitor and c) hybrid capacitor.....40

Figure 2.4. a) Dynamics of polarisations in typical energy storage devices; b) The schematic diagram of the energy levels and potentials of electrodes and electrolytes with the formation of SEI and CEI (*i.e.,* the SEI at the cathode side). 43

Figure 2.5. a) The typical discharge-charge curves of graphite anodes to store cations in the half cell configuration with the inserted photography of graphite and graphite intercalation compounds including LiC_6 and KC_8 (Reproduced with permission from [45], Copyright 2018, Wiley); b) The redox potentials of electrode materials vs. Li^+/Li or Na^+/Na; c) The schematic illustrations of intercalation behaviours of lithium and potassium ions into graphite in ester electrolytes. 46

Figure 2.6. The visualised statistics of keywords in publications related to sodium batteries, where the colour represents the average publication year, the size indicates the reported frequency in the literature. 49

Figure 2.7. a) Schematic illustrations of inner structures of hard carbon, soft carbon and graphite; b) Scanning electron microscopy (SEM) images of cellulose-rich cotton before and after the carbonisation with the inserted photography of cotton (Reproduced with permission from [57], Copyright 2016, Wiley); c) The transmission electron microscopy image of typical hard carbons with the illustrated active sites including closed nanovoids and defect sites;[57] The sodium-ion storage mechanism models of hard carbons including d) "insertion/intercalation-adsorption", e) "adsorption-insertion/intercalation" and f) "adsorption-filling" models (Reproduced with permission from [56], Copyright 2018, American Chemical Society). 51

Figure 2.8. The modification of a) morphologies, b) pore and c) defect structures of bio-derived hard carbons to enhance their electrochemical performance; d) The typical GCD curves of hard carbons dominated by the adsorption of sodium ions at defect sites; e) The typical GCD curves of hard carbons dominated by the filling of sodium ions within closed nanovoids. 52

Figure 2.9. a) Crystal structures of titanate-based anode materials; b) Typical GCD curves of TiO_2 electrodes in the half-cell configuration with the phase transformation between TiO_2 and $NaTiO_2$ during the sodiation and de-sodiation process; c) Summaries and comparisons of redox potentials and capacities of different titanate-based anode materials. 54

Figure 2.10. a) Schematically illustrating redox activities of organic moieties to interact with sodium ions; b) Molecular structures of redox-active organics for sodium-ion battery anodes; c) Typical GCD curves of Na_2TP in the half cell during the sodiation and de-sodiation process; d) Redox potentials of redox-active organics from Figure 2.10b with different redox states. 55

Figure 2.11. a) The crystal structures of tin, antimony and their alloys of SnSb; b) The typical GCD curves of tin anode materials for sodium-ion storage with the corresponding phase transformation stages at specific potentials; c) The molecular structures of three allotropes of phosphorus; d) The typical GCD curves of phosphorus-based electrode for sodium-ion storage with the corresponding phase transformation stages at specific potentials; e) *In-situ* TEM images of black phosphorus illustrating its layer-by-layer structure and the volume expansion during the sodiation process from pristine to different sodiated states at 0, 80 and 170 s. (Reproduced with permission from [73], Copyright 2015, Springer Nature). 57

Figure 2.12. a) The crystal structures of typical conversion-type anode materials; b) The typical GCD curves of Fe_2O_3 anodes for sodium-ion storage with the schematic illustrations of the two-stage phase transformation based on the redox pairs of Fe^{3+}/Fe^{2+} and Fe^{2+}/Fe^{0} during the sodiation process; c) The summaries of reaction potentials and specific capacities of different conversion-type anodes. 60

Figure 2.13. a) Schematic illustrations of the sodium plating and stripping processes upon cycling; b) Optical microscopy images of the sodium dendrite formation during the metallic sodium deposition in carbonate-based electrolytes (Reproduced with permission from [98], Copyright 2017, Wiley); c) Schematic illustrations of strategies to suppress the dendrite

formation and stabilise the sodium metal anodes. 63

Figure 2.14. Typical crystal structures of a) layered oxides, b) polyanionic compounds and c) Prussian blue analogues; d) Typical discharge curves of layered oxides, polyanionic compounds and Prussian blue analogues with the schematic illustrations of single- and two-phase reactions; e) Comparison of average working potentials and capacities of different sodium cathode materials. 66

Figure 2.15. a) Structural illustration of sulphur; b) Typical discharge-charge curve of sulphur cathodes for sodium-ion storage; c) Schematic illustration of functional carbon hosts for the protection of sulphur cathodes; d) Crystal structures of NaO_2 and Na_2O_2; e) Typical discharge-charge curve of oxygen cathode for sodium-ion storage; f) Schematic illustration of functional carbon hosts for oxygen reduction and evolution reactions. 70

Figure 2.16. a) Molecular structures of solvents for liquid electrolytes; b) Crystal structures of inorganic ceramics for solid electrolytes. 72

Figure 2.17. a) The comparison between traditional electrode architectures and novel three-dimensional electrode architectures with optimised structures; b) The cost comparison between the commercial lithium-ion battery cell and the future sodium-ion battery cell; c) Schematic illustrations of cylindrical, prismatic and pouch cells (Reproduced with permission from [159], Copyright 2016, Springer Nature). 75

Figure 2.18. The visualised statistics of keywords in publications related to sodium capacitors, where the colour represents the average publication year, the size indicates the reported frequency in the literature. 77

Figure 2.19. a) Schematic diagrams of active materials for cathodes of sodium capacitors; b) Schematic illustration of porous carbon materials as the cathode to store anions through different mechanisms at various active sites; c) Material synthesis process employed for each electrode in sodium capacitors (Reproduced with permission from [166], Copyright 2015, Royal Society of Chemistry); d) Comparison of the relevant cathode/anode charge storage mechanisms in sodium capacitors. 78

Figure 2.20. a) Photographs of sodium-based energy storage devices in the coin cells; b) Summary of fabrication processes and advantages of nature-inspired carbon materials. 81

Figure 3.1. a) Schematic diagram of biomass with the photosynthesis process; b) Schematic diagram of the structure of hard carbons; Chemical structure depictions of c) glucose, d) cellulose and e) lignin. 83

Figure 3.2. Schematic summary of various synthesis methods of sustainable carbon materials. 85

Figure 3.3. The photograph of a) biochar from the hydrothermal process of biomass, b)

HG1300, and c) DG1300. 87

Figure 3.4. a) Photograph and b) TEM image of cellulose nanocrystal (NC) suspensions; c) Photograph and d) SEM images of obtained iridescent NC films with the self-assembled chiral nematic structures; e) Schematic of the chiral nematic ordering present in NC, along with an illustration of the half-helical pitch P/2, and (f) Illustration of the light reflected by a chiral nematic structure. 88

Figure 3.5. a) The photograph of a piece of electrospun lignin mat and b) a non-woven fabric piece of carbonised skeletons. c) Demonstration of the flexibility of lignin-derived carbon mats by bending and releasing. 91

Figure 3.6. The photograph of $NaCF_3SO_3$ in EC-DMC, EC-PC or diglyme. 99

Figure 4.1. Material characterisation. a) The schematic illustration of the two synthesis routes of glucose-derived hard carbons. One is the direct carbonisation of glucose (DG), and the other is the hydrothermal pre-treatment of glucose at 200 ºC (HG) followed by the high-temperature carbonisation; SEM images with inserted TEM images of b) HG1300 and c) DG1300; HRTEM images with SAED patterns of d) HG1300 and e) DG1300; f) N_2 adsorption and desorption isotherms with the corresponding pore distributions, g) Raman spectra, h) XRD patterns, and i) XPS surveys, of HG1300 and DG1300; Fitted C 1s and O 1s core-level XPS spectra of j) HG1300 and k) DG1300. 108

Figure 4.2. Electrochemical testing. a) The first cycle of GCD curves of different samples including HG1000, HG1300, HG1500, DG1000, DG1300 and DG1500 at 0.1 C (1 C = 300 mA g^{-1}) within the potential range of 0.001-2.5 V vs Na^+/Na using 1 M $NaClO_4$ in EC-DMC; b) The contributions of sloping and plateau capacities in each sample; c) Specific capacities of HG1300 and DG1300 in comparison to reported carbon anodes for sodium-ion batteries; d) Rate performance at different current densities including 0.1, 0.2, 0.5, 1.0 and 2.0 C, and e) Cycling performance at 0.5 C, of HG1300 and DG1300. 113

Figure 4.3. Kinetic analysis. a) CV curves of HG1300 and DG1300 at different scan rates of 0.1, 0.2, 0.5, 1.0, 2.0 and 5.0 mV s^{-1} (the second cycle at each scan rate), inserted with the very first three cycles of CV curves of HG1300 and DG1300 at 0.1 mV s^{-1}; b) The surface-controlled current separated from the diffusion-controlled one at each potential in CV curves of HG1300 and DG1300 at 0.5 mV s^{-1}; c) Calculated contributions of the surface- and diffusion-controlled proportions varying from 0.1 to 5.0 mV s^{-1} in HG1300 and DG1300; d) Linear relationship between log (peak current) and log (scan rate) of HG1300 and DG1300 for calculating the exponent (b values) in half cells; e) and f) GITT profiles of HG1300 and DG1300 (left) by discharging the half cells with a pulse current at 0.1 C for 30 min followed by an interval for 3 h, and calculated D_{Na+} (right) at different potentials. 115

Figure 4.4. *Operando* and *ex-situ* characterisations. a) *Operando* Raman spectra of HG1300 and the corresponding 3D mapping image during the second discharge-charge process using

the illustrated *operando* Raman cell; b) Schematic illustrations of the sodium-ion storage behaviours in HG1300 and DG1300 with different structural features; c) Fitted EIS of cycled HG1300 and DG1300 at the same de-sodiated state based on the modified equivalent circuits with two charge-transfer resistances in two interphases (S1 and S2); d) Fitted C 1s (left) and O 1s (right) core level XPS spectra of HG1300 and DG1300 after the first discharge-charge process; e) Corresponding composition contributions of the interphase upon de-sodiated HG1300 and DG1300; f) Schematic diagrams of the interface conditions of cycled carbons (left) with detailed illustrations of possible SEI compositions upon cycled HG1300 and DG1300 (right). 118

Figure 4.5. a) Full-range *operando* Raman spectra with detailed spectrum at the specific discharge-charge state or at the specific Raman shift of HG1300 in the *operando* cell during the discharge-charge process; b) Schematic illustrations of the pristine E_{2g} in-plane bond-stretching motion of pairs of sp^2 atoms and suppressed G stretching mode by the filling of sodium ions in closed nanovoids enclosed by curved graphene layers; c) Schematic illustrations of the pristine A_{1g} breathing mode of sp^2 atoms of the benzene rings and restricted D breathing mode by the absorption of sodium ions at defect sites. 120

Figure 4.6. Fitted C 1s, O 1s, Na 1s and Cl 2p core-level XPS spectra of a) HG1300 and b) DG1300 after the first discharge-charge process. 124

Figure 4.7. Modelling and assessment. a) Electrostatic potential mapping of EC and DMC with the dipole-dipole interaction between EC and oxygen functional groups of carbons; b) The schematic illustration of the uniform sodium-ion flux from the electrolyte to carbon spheres; c) 2D electric field distribution vector profiles of the sodium-ion flux from the electrolyte to spherical HG1300 and lumpy DG1300 under a constant electric field of 0.1 V; d) The 3D electric field distribution vector profile and voltage change profile of the sodium-ion flux from the electrolyte to spherical HG1300 under a constant electric field of 0.1 V. e) The life cycle diagram of the preparation of hard carbons from the same precursor *via* two different routes for sodium-ion batteries, compared with graphite for lithium-ion batteries; f) The measured carbon yields at different stages of routes for HG1300 and DG1300; g) The calculated environmental impacts of hard carbons including HG1300 and DG1300 from two different routes for sodium-ion batteries, compared with those of graphite for lithium-ion batteries. 126

Figure 4.8. Full cells. a) The schematic illustration of the full configuration, where the hard carbon anode is coupled with the $Na_3V_2(PO_4)_3$ cathode during the charge process; b) The first charge-discharge cycles of the hard carbon anode and the $Na_3V_2(PO_4)_3$ cathode in their half-cell configurations at the same current density; c) GCD curves of the full-cell using the HG1300 anode and the $Na_3V_2(PO_4)_3$ cathode (HG1300//NVP) at the current densities of 30, 60, 150, 300, 600 mA g^{-1}, whose capacities are normalized by the active mass of the anode; Comparison of d) the rate performance at the current densities of 30, 60, 150, 300, 600 mA g^{-1}, and e) the cycling performance at 150 mA g^{-1}, between HG1300//NVP and DG1300//NVP whose capacities are normalized by the active mass of the anode, with an inserted image of a LED light powered by the full cell of HG1300//NVP; f) The Ragone plot to compare the

energy and power densities of the full cells with other types of energy storage devices, where the energy and power densities are normalised by the overall active mass of both the anode and cathode. 129

Figure 5.1. Schematic diagram illustrating the 'one-for-all' synthesis processes of electrodes and electrolytes as well as the asymmetric configuration of NICs. 134

Figure 5.2. Material characterisation of carbon anodes. a) Photograph, b) SEM image and c) TEM image of CNC1000; d) Photograph, e) SEM image and f) TEM image of CMF1000 g) Raman spectra, h) XRD patterns, and i) N_2 adsorption/desorption isotherms (77 K) of CNC1000 and CMF1000. 135

Figure 5.3. Electrochemical testing of carbon anodes in half cells. Comparison of a) Specific capacities and b) Rate performance of charge capacities of CNC1000 and CMF1000; c) Specific capacities of CNC1000 in comparison to reported anodes in NICs; d) GCD curves of CNC1000 at 0.1 to 2.0 A g^{-1} (the second cycle of each rate current); e) CV curves of CNC1000 at 0.1 to 10.0 mV s^{-1} (the second cycle of each sweep rate); f) Linear relationship between log i and log ν of CNC1000 at different potentials; g) Calculated contribution proportions of the surface- and diffusion-controlled processes at 0.1 to 5.0 mV s^{-1} in CNC1000; and h) GITT profiles of CNC1000 (left) and calculated D_{Na+} (right). 138

Figure 5.4. Material characterisation of carbon cathodes. a-b) SEM images of CHKM800 with an inserted picture of coral and CHK800; c) Left: N_2 adsorption/desorption isotherms at 77 K, Right: Pore size distributions obtained from the adsorption isotherms based on non-local density functional theory (NLDFT) method, of CHKM800 and CHK800; d) Schematic illustration of the hierarchical pores of CHKM800; e) Raman spectra and f) XPS survey spectra with the atomic percentage of different elements, of CHKM800 and CHK800; g) Fitted N 1s (left) and O 1s (right) core level XPS spectra of CHKM800; h) Fitted O 1s spectrum of CHK800; and i) Fitted C 1s spectra of CHK800 and CHKM800. 142

Figure 5.5. Electrochemical testing of carbon cathodes in half cells. a) Comparison of specific capacitances of CHKM800 and CHK800; b) Specific capacitances of CHKM800 with the comparison to published cathodes in NICs; c) GCD curves of CHKM800 at 0.1 to 2.0 A g^{-1} (the second cycle of each rate current); d) CV curves of CHKM800 under 0.5 to 10.0 mV s^{-1} (the second cycle of each sweep rate); e) The b-values of CHKM800 at different measured potentials; and f) Calculated contribution proportions of the surface- and diffusion-controlled processes at 0.5 to 10.0 mV s^{-1} in CHKM800. 145

Figure 5.6. Electrochemical testing of NICs with different configurations. a) Illustration of the corresponding charge-discharge processes in cathodes and anodes during NICs operation; b) Ragone plot comparing a device based on different combinations of CHKM800//CNC1000, CHKM800//CNC1300, CHKM800//CNC800, CHKM800//CMF1000 and CHK800//CMF1000; c) Energy–power density performance comparison of NICs *versus* reported carbon-based hybrid capacitor systems; d) GCD curves at 0.1 to 2.0 A g^{-1} (the second

cycle of each rate current), e) CV curves under 0.5 to 10.0 mV s^{-1} (the second cycle of each sweep rate), of CHKM800//CNC1000; f) The related b-values at different measured voltages; and g) Calculated contribution proportions of the surface- and diffusion-controlled processes at 0.5 to 10.0 mV s^{-1} in CHKM800//CNC1000. (All the parameters in the full cell configuration are normalised by the total active mass of both anode and cathode.).....148

Figure 5.7. Gel polymer electrolytes and QSD NICs: schematics, performance and mechanisms. a) Photographs of HEC-PEO composite membrane with an insert photo illustrating its flexibility; b) SEM image of HEC-PEO composite membrane; c) Voltage profiles at room temperature for sodium stripping/plating in a symmetric Na/HEC-PEO/Na cell at 1 mA cm^{-2}; d) TGA curves of HEC-PEO membrane and glass fibre membrane absorbing the same amount of electrolyte (150 ^{o}C, 5 ^{o}C min^{-1}, N_2 flow) with an inserted photograph of QSD gel electrolyte; e) Schematic of the transport of anions and cations inside the polymer network of HEC-PEO formed by the hydrogen binding effect (left), and schematic illustration of the interactions of hydroxyl groups in HEC with PEO and EC/DMC organic electrolytes (right); f) Schematic of all-cellulose-based QSD NICs; g) GCD curves (the second cycle of each rate current) and rate performance at 0.2 to 2.0 A g^{-1}, of the QSD device (CHKM800/HEC-PEO/CNC1000) with an inserted photograph of the LED powered by the NIC. 152

Figure 6.1. Material Characterisation. a) Photograph of L700 with an inserted illustration of its flexibility. b) SEM image and c) TEM image of L700. d) Schematic diagram illustrating the electrospinning process of lignin nanofibres. e) N_2 adsorption and desorption isotherms (77 K) with inserted SAXS patterns. f) Raman spectra, g) Rada curve of structural properties, h) XRD patterns, and i) XPS survey, of L700, L1100 and L1500. 156

Figure 6. 2. Fitted C 1s, N 1s and O 1s core-level XPS spectra of a) L700, b) L1100 and c) L1500 159

Figure 6.3. Electrochemical Characterisation. a) The potential-capacity profiles (the 1st cycles) showing the initial nucleation overpotentials of sodium deposition on L700, L1100 and L1500 at 1.0 mA cm^{-2} using 1 M $NaCF_3SO_3$ in diglyme. b) The overview of nucleation overpotentials of sodium deposition on different substrates (Al, Sn, Ni, Cu, L700, L1100 and L1500) in different electrolytes (1 M $NaCF_3SO_3$ in EC-PC, EC-DMC or diglyme) at 1.0 mA cm^{-2}. c) The electrostatic potential maps of EC and diglyme, where the red regions represent the negative charge, and the white regions represent the positive charge. d) The schematic illustration of the dipole-dipole interaction between EC and oxygen functional groups of L700. e) Left: the schematic illustration of the interaction between the nitrogen-doped graphene layer with sodium atoms, and Right: the calculated binding energy (E_b) of sodium atoms with the nitrogen-doped graphene layers. f) The Coulombic efficiencies of sodium plating and stripping on L700, L1100 and L1500 in different electrolytes (1 M $NaCF_3SO_3$ in EC-PC, EC-DMC or diglyme) at 1.0 mA cm^{-2} with a specific charge and discharge capacity of 2.0 mAh cm^{-2}. g) The specific GCD curves (the 2nd cycle) of metallic sodium plating and stripping on

L700, L1100 and L1500 at 1mA cm^{-2} using 1 M $NaCF_3SO_3$ in diglyme. 161

Figure 6.4. The GCD of the plating/stripping of metallic sodium onto/from L700, L1100 and L1500 using 1 M $NaCF_3SO_3$ in a) EC-DMC, b) EC-PC or c) diglyme, respectively.....165

Figure 6.5. a) Raman spectrum of carbon mats from Toray with the inserted photography of the sample; b) The charge-discharge curves of carbon mats from Toray in the half cell configuration for sodium plating and stripping using 1 M $NaCF_3SO_3$ in diglyme; c) Raman spectrum of commercial graphite substrate from Sigma-Aldrich with the inserted photography of the sample; b) The charge-discharge curves of commercial graphite substrate from Sigma-Aldrich in the half cell configuration for sodium plating and stripping using 1 M $NaCF_3SO_3$ in diglyme.....167

Figure 6.6. Interface analysis. Schematic diagrams of sodium deposition onto a) bare metallic sodium with obvious nuclei, leading to non-uniform ion flux, and b) carbon matrix with homogenous ion flux. Two-dimensional electric field distribution vector profiles of the metallic electrodeposition onto the metallic sodium with the same surface situation in c) the ester-based electrolyte, and d) the ether-based electrolyte under a constant electric field of 0.1 V. Two-dimensional electric field distribution vector profiles of the metallic electrodeposition onto the metallic sodium with e) bulging nuclei, and f) concave nuclei, in the ether-based electrolyte under a constant electric field of 0.1 V. g) Three-dimensional electric field distribution, and h) its differential vector profile of the metallic electrodeposition onto the carbon matrix in the ether-based electrolyte under a constant electric field of 0.1 V. i) Fitted C 1s (left) and O 1s (right) core level XPS spectra of plated L700 using (1) 1 M $NaCF_3SO_3$ in diglyme, (2) 1 M $NaCF_3SO_3$ in EC-PC, and (3) 1 M $NaCF_3SO_3$ in EC-DMC after the first cycle of metallic deposition at 1.0 mA cm^{-2} with a specific discharge capacity of 2.0 mAh cm^{-2}. j) The corresponding composition calculations of the interface upon the metal/carbon composite anode using (1) 1 M $NaCF_3SO_3$ in diglyme, (2) 1 M $NaCF_3SO_3$ in EC-PC, and (3) 1 M $NaCF_3SO_3$ in EC-DMC. Schematic illustration of possible SEI situation upon the metal/carbon composite anode in k) the ether-based electrolyte, and l) the ester-based electrolyte. 168

Figure 6.7. a) The electrostatic potential maps of DMC, EC, PC and diglyme (Red colour means the negative charge, and white colour means the positive charge); b) Schematic illustration of energy states of electrodes, ester-based electrolytes and ether-based electrolytes, where the lowest unoccupied molecular orbital (LUMO), the highest occupied molecular orbital (HOMO) levels and their corresponding electron cloud distribution of free electrolyte solvent molecules (*i.e.,* DMC, EC, PC and diglyme) are presented as well. 170

Figure 6.8. Deposition behaviour study. *Ex-situ* SEM morphology evolution of the surface conditions of a) plated L700 in 1 M $NaCF_3SO_3$ in EC-PC, b) plated L700 in 1 M $NaCF_3SO_3$ in EC-DMC, c) plated L700 in 1 M $NaCF_3SO_3$ in diglyme, d) plated L1100 in 1 M $NaCF_3SO_3$ in diglyme, and e) plated L1500 in 1 M $NaCF_3SO_3$ in diglyme, after 10 cycles at 1.0 mA cm^{-2} with a specific discharge capacity of 2.0 mAh cm^{-2}, with inserted photography of the cycled coin cells. f) *Operando* Raman spectra of L700 during the first plating process in 1 M

$NaCF_3SO_3$ in diglyme, with the corresponding plating electrochemical curve (left), the mapping of the intensity of Raman spectra (middle), and the specific Raman spectra at different plating stages (right). g) EIS of L700 at OCV, plated stage and stripped stage of the first cycle, with fitted EIS and corresponding equivalent circuits. h) The schematic diagrams of the interface conditions of carbon fibre at OCV, plated stage and stripped stage.....172

Figure 6.9. GITT profiles of a) L700, b) L1100 and c) L1500 using 1 M $NaCF_3SO_3$ in diglyme (left) and their calculated diffusion coefficient of Na^+ ions (right).....174

Figure 6.10. Practical applications. a) Rate performance of the Na/C composites in the symmetrical cell at current densities of 0.1, 0.2, 0.5, 1.0 and 2.0 mA cm^{-2} for 0.5 h per (dis-)charge process using 1 M $NaCF_3SO_3$ in diglyme. b) Cycling stability of Na/C composite anodes in the symmetrical cell at current densities of 1 mA cm^{-2} with a specific capacity of 0.5 mAh cm^{-2} using 1 M $NaCF_3SO_3$ in diglyme. c) Illustration images of L700 with defect structures and L1500 with pore structures before and after cycling. d) SEM image, element mapping, photography and schematic illustration of the obtained Na/L700 composite anodes with a certain amount of plated metallic sodium (8 mAh cm^{-2}). e) GCD curves of the Na/L700 composite anode in a full cell at current densities of 30, 150, 300 and 600 mA cm^{-2}, based on the active mass of the coupled Prussian blue cathode. f) Ragone plot of the full cell with the Na/L700 composite anode and Prussian blue cathode, the full cell with the Na/L700 composite anode and sulphur/L1500 cathode, and their comparison with other kinds of energy devices (the energy density and power density of the full cell are normalised by the total mass of active materials in both electrodes). g) Schematic illustration of the design idea of the current "anode-less" sodium metal batteries and future "anode-free" sodium metal batteries, in comparison to the traditional sodium-ion batteries.....178

Figure 6.11. The potential hysteresis of the plating and stripping of bare metallic sodium symmetric cells using 1 M $NaCF_3SO_3$ in EC-DMC, 1 M $NaCF_3SO_3$ in EC-PC and 1 M $NaCF_3SO_3$ in diglyme during cycling at 1.0 mA cm^{-2} with a specific capacity of 0.5 mAh cm^{-2}.....180

Figure 6.12. a) and b) SEM images of synthesized Prussian blue; c) Rate performance and d) cycling performance of sodium metal batteries with the Prussian blue cathode; e) Schematic illustration of the Na^+ ion storage mechanism of Prussian blue $Fe^{III}Fe^{III}(CN)_6$.....181

Figure 6.13. a) Fitted C 1s and S 2p core-level XPS spectra of the bare sulphur cathode (S/CB) and sulphur/L1500 cathode (S/L1500), and b) their corresponding atomic percentage; c) GCD curves of the full cells of Na/L700-S/L1500 and bare Na-S before and after cycling at 167.5 mA g^{-1}; d) Schematic illustration of sodium-sulphur batteries with the configuration of Na/L700 anode and sulphur/L1500 cathode (Na/L700-S/L1500). 182

Figure A1.1. a) and b) SEM images of HG1300 at different magnifications; c) and d) SEM images of DG1300 at different magnifications. More SEM images of coated electrodes of hydrothermal carbons can be referred to our previous study.[281] (Scale bar: (a) 5 μm, (b) 1 μm,

(c) 100 μm, (d) 10 μm) 189

Figure A1.2. a) and b) TEM images of HG1300 at different magnifications; c) and d) TEM images of DG1300 at different magnifications. 189

Figure A1.3. a) N_2 adsorption and desorption isotherms, b) the corresponding pore size distributions, of HG1000, DG1000, HG1300, DG1300, HG1500 and DG1500; c) Schematic illustration of the closure of micropores to form closed nanovoids when the carbonisation temperature increases. 190

Figure A1.4. a) Raman spectra of HG1000, DG1000, HG1300, DG1300, HG1500 and DG1500; b) Fitted Raman spectra of HG1000, DG1000, HG1300, DG1300, HG1500 and DG1500. 191

Figure A1.5. XRD patterns of HG1000, DG1000, HG1300, DG1300, HG1500 and DG1500. 191

Figure A1.6. a) XPS surveys, and b) Fitted C 1s and O 1s core-level XPS spectra, of HG1000, DG1000, HG1300, DG1300, HG1500 and DG1500. 192

Figure A1.7. Ultra-long cycling performance of HG1300 in the half cell configuration at 0.5C. 193

Figure A1.8. GCD curves, rate and cycling performance of a) HG1000, b) DG1000, c) HG1300, d) DG1300, e) HG1500 and f) DG1500 194

Figure A1.9. CV curves at different scan rates of 0.1, 0.2, 0.5, 1.0, 2.0 and 5.0 mV s^{-1} (the second cycle of each scan rate), inserted with the very first three cycles of CV curves at 0.1 mV s^{-1}, of a) HG1000, b) DG1000, c) HG1300, d) DG1300, e) HG1500 and f) DG1500. . 195

Figure A1.10. GITT profiles by discharging and charging the half cells with a pulse current at 0.1 C for 30 min followed by an interval for 3 h, of HG1000, DG1000, HG1300, DG1300, HG1500 and DG1500. The discharge time decides how many steps and points of diffusion coefficients that can be obtained, while the interval time should be 5 to 10-fold of the discharge time to make sure that sodium ions have enough time to relax and diffuse automatically. . 195

Figure A1.11. EIS of HG1000, DG1000, HG1300, DG1300, HG1500 and DG1500 at the same de-sodiated state. 196

Figure A1.12. GCD curves, rate and cycling performance of a) HG1300//NVP and b) DG1300//NVP (capacities are normalized by the active mass of the anode)..... 196

Figure A2.1. SEM images of a) Carbon films (CNC800) with structural hierarchy by direct carbonisation of cellulose nanocrystals at 800°C, and b) CNC1300. 199

Figure A2.2. a) Raman spectra, b) XRD patterns, c) N_2 adsorption/desorption isotherms (77

K), and d) Pore size distributions obtained from the adsorption isotherms based on non-local density functional theory (NLDFT) method, of different samples (CMF1000, CNC800, CNC1000 and CNC1300). Using the non-local density functional theory (NLDFT) model from the adsorption part of the isotherm, the average pore sizes of CNC1000 and CMF1000 can be obtained. The average pore sizes of CNC1000 and CMF1000 are 4.7 nm and 1.2 nm; therefore, in comparison to CMF1000 with many micropores responsible for the extensive formation of the solid electrolyte interface (SEI), CNC1000 only possesses a few mesopores which could contribute to the ion diffusion without much consumption of Na^+ ions.....199

Figure A2.3. a-d) Fitted Raman spectra of CMF1000, CNC800, CNC1000 and CNC1300; e-g) Fitted Raman spectra of CHK800, CHKM700 and CHKM800, respectively (Peak Fitted by Lorentz models).....200

Figure A2.4. Electrochemical performance (GCD curves, rate and cycling performance) of a-c) CMF1000, d-f) CNC800, g-i) CNC1000, and j-l) CNC1300. For carbon anodes, different carbonisation temperatures of cellulose nanocrystals do not result in significant changes in surface areas of carbon samples (CNC800, CNC1000 and CNC1300), all being below 35 $m^2 g^{-1}$.....202

Figure A2.5. a) The first three cycles of CV curves of CNC1000 at 0.1 mV s^{-1}; b) Linear fitting plots of scan rates vs. peak currents for calculating constants b of CNC1000 in half cells; c) Linear fitting plots of $\nu^{1/2}$ vs. $i/\nu^{1/2}$ used for calculating constants k_1 and k_2 of CNC1000 in half cells at different potentials; d) Separation of the capacitive and diffusion currents in CNC1000 anodes; e) GITT profiles of CNC1000 (upper) and calculated Na-ion diffusion coefficients (bottom); f) Linear relationship between lg i and lg ν of CHKM800 in half cells at different measured potentials; g) Linear fitting plots of $\nu^{1/2}$ vs. $i/\nu^{1/2}$ used for calculating constants k_1 and k_2 of CHKM800 in half cells at different potentials; h) Separation of the capacitive and diffusion currents in CHKM800 cathodes; i) Linear relationship between lg i and lg ν of CHKM800//CNC1000 in full cells at different measured potentials; j) Linear fitting plots of $\nu^{1/2}$ vs. $i/\nu^{1/2}$ used for calculating constants k_1 and k_2 of CHKM800//CNC1000 in full cells at different potentials; and k) Separation of the capacitive and diffusion currents in full cells of CHKM800//CNC1000.....203

Figure A2.6. a) and b) SEM images of carbon microtubes derived from cellulose microfibrils *via* hydrothermal treatment; c) and d) SEM images of coral-shape nitrogen-doped carbon materials (CHKM700) with a hierarchically porous architecture prepared by $KHCO_3$ and Melamine co-activation at 700°C. Cellulose microfibrils as the carbon precursor can maintain the cross-linked networks of hierarchically porous carbons after thermal treatment and chemical co-activation.....204

Figure A2.7. a) Raman spectra, and b) XRD patterns of carbon cathodes (CHKM800, CHKM700 and CHK800); c) N2 adsorption/desorption isotherms at 77 K, and d) Pore size distributions calculated from the adsorption isotherms using NLDFT method, of CHKM700; e) XPS survey spectra of CHK700 with the atomic percentage of different elements; f) C 1s, g) N 1s and h) C 1s core level XPS spectra of CHKM700. 205

Figure A2.8. Electrochemical performance (GCD curves, rate and cycling performance) of a-c) CHKM800, d-f) CHKM700 and g-i) CHK800. 206

Figure A2.9. Electrochemical performance (GCD curves, rate and cycling performance) of a-c) CHKM800//CNC1300, d-f) CHKM800//CNC1000, g-i) CHKM800//CNC800, j-l) CHKM800//CMF1000, and m-o) CHK800//CMF1000. (All the parameters in the full cell configuration are normalized by the total active mass of both anode and cathode.) 209

Figure A2.10. a) TGA curve of HEC-PEO composite membrane (800 °C, 10 °C min^{-1}, N_2 flow); b) FTIR spectra of HEC-PEO composite membrane. 210

Figure A2.11. a) Impedance curves of CHKM800, CNC1000 in half cells and CHKM800//CNC1000, CHKM800/HEC-PEO/CNC1000 in full cells; and b) Equivalent series resistance (ESR) of the half cells and full cells consisting of the internal resistance (R_s) and the charge-transfer resistance (R_{ct}); and c) Cycling performance of CHKM800/HEC-PEO/CNC1000 in full cells tested at 0.1 A g^{-1} after 30 cycles (All the parameters in the full cell configuration are normalized by the total active mass of both anode and cathode)..... 210

Figure A2.12. Voltage profiles at room temperature for sodium stripping/plating in a symmetric Na//Na cell with glass fibre membrane in liquid electrolyte at 1 mA cm^{-2}. 211

Figure A3.1. a) The pore size distribution based on the non-local density functional theory (NLDFT) method L700, L1100 and L1500; b) The photograph of sample grid for SAXS measurement with an inserted photograph of a washer used to fix the samples. c) The small-angle X-ray scattering (SAXS) patterns of L700, L1100 and L1500; d) Fitted SAXS patterns of L700 based on Equation S5 for the value of C; Fitted SAXS patterns of e) L1100 and f) L1500 based on Equation S3 for the value of B_1; Fitted SAXS patterns of g) L1100 and h) L1500 based on Equation S4 for the value of B_2; (The SAXS results have already removed the background)..... 212

Figure A3.2. Fitted Raman spectra of a) L700, b) L1100 and c) L1500 using the Lorentzian methods; d) Raman spectra of an area of L700 through the multi-point scanning model, which is conducted to further prove the uniformity of defect sites of L700. With the uniformly distributed defect sites, L700 can prevent the dendrite growth as a protection skeleton for sodium metal anodes. 213

Figure A3.3. a) The potential-capacity profiles (the 1st cycle) showing initial nucleation overpotentials of sodium deposition on Al, Cu, Ni and Sn at 1 mA cm^{-2} using 1 M $NaCF_3SO_3$ in EC-PC (left), EC-DMC (middle) or diglyme (right); b) The specific GCD curves (the 2nd cycle) of sodium plating/stripping on Al, Cu, Ni and Sn at 1mA cm^{-2} using 1 M $NaCF_3SO_3$ in EC-PC (left), EC-DMC (middle) or diglyme (right)..... 214

Figure A3.4. The wettability testing of L700 with diglyme, where the 100μL diglyme can be fully absorbed in a piece of L700 since no diglyme can penetrate the L700. 214

Figure A3.5. a) The potential-capacity profiles (the 1st cycle) at 1 mA cm^{-2} showing initial nucleation overpotentials of sodium deposition on L700, L1100 and L1500 using 1 M $NaCF_3SO_3$ in EC-PC, 1 M $NaCF_3SO_3$ in EC-DMC or 1 M $NaCF_3SO_3$ in diglyme, respectively; b) Schematic illustration of ion flux distribution and metallic deposition on the carbon with pore structures or defect structures; c) GCD curves (the 2nd cycle) of metallic sodium plating/stripping at 1mA cm^{-2} on L700, L1100 and L1500 using 1 M $NaCF_3SO_3$ in EC-PC, 1 M $NaCF_3SO_3$ in EC-DMC or 1 M $NaCF_3SO_3$ in diglyme, respectively. 215

Figure A3.6. a) Left: Spin densities between sodium atoms and L1500 with intact graphene layers, Right: Spin densities between sodium atoms and L700 with quaternary nitrogen-doped graphene layers; b) Left: Local charge densities between sodium atoms and L1500 with intact graphene layers, Right: the local charge densities between sodium atoms and L700 with quaternary nitrogen-doped graphene layers. 216

Figure A3.7. a) EIS plots of L700, L1100 and L1500 using 1 M $NaCF_3SO_3$ in diglyme before and after cycling; b) EIS plots of L700 using 1 M $NaCF_3SO_3$ in diglyme, 1 M $NaCF_3SO_3$ in EC-PC or 1 M $NaCF_3SO_3$ in EC-DMC before and after cycling.....216

Figure A3.8. a) Schematic illustration of the sodium stripping and plating process in EC-PC or EC-DMC. Stage 1: The SEI forms and Na^+ ions insert into the carbon skeleton above 0 V vs Na^+/Na, while the metallic sodium keeps plating onto the carbon skeleton below 0 V vs Na^+/Na; Stage 2: The volume change caused by sodium plating and striping makes the SEI crack, followed by the reformation of the SEI. Afterwards, the uneven plating results in Na dendrites; Step N: sodium stripping isolates sodium dendrites into electrolytes. b-c) Finite element modelling of the electric fields in different stages of sodium plating and striping, which proves the rough surface can induce uneven current flows. e) Schematic illustration of the sodium stripping and plating process in diglyme, which is more uniform. 217

Figure A3.9. a) Fitted C 1s, O 1s, N 1s and Na 1s core-level XPS spectra of pristine L700, plated L700 using 1 M $NaCF_3SO_3$ in diglyme, plated L700 using 1 M $NaCF_3SO_3$ in EC-PC, and plated L700 using 1 M $NaCF_3SO_3$ in EC-DMC after the first cycle of metallic deposition at 1.0 mA cm^{-2} with a specific discharge capacity of 2.0 mAh cm^{-2}; b) Fitted C 1s, O 1s, N 1s and Na 1s core-level XPS spectra of pristine L1100, plated L1100 using 1 M $NaCF_3SO_3$ in diglyme after the same deposition process; c) Fitted C 1s, O 1s and Na 1s core-level XPS spectra of pristine L1500, plated L1500 using 1 M $NaCF_3SO_3$ in diglyme after the same deposition process. 219

Figure A3.10. a) The photograph of *operando* Raman measurement; b) The configuration of the *operando* Raman cell; c) Raman spectra of L700 during the first stripping process in 1 M $NaCF_3SO_3$ in diglyme (right), with the corresponding plating electrochemical curve (left) at 0.5 mA cm^{-2}. 220

Figure A3.11. Cycling stability of Na/L700 composite anodes in the symmetrical cell at current densities of 2.0 and 3.0 mA cm^{-2} with a specific capacity of 1.0 and 1.5 mAh cm^{-2}, respectively, using 1 M $NaCF_3SO_3$ in diglyme. 221

List of tables

Table 2.1. Comparison of sodium and lithium's properties.[8, 9] 48

Table 4.1. Physical parameters of carbon materials. 112

Table 4.2. Fitted elements of EIS of HG1300 and DG1000 at the same de-sodiated state..123

Table 4.3. Comparison of energy densities of sodium-ion batteries. 131

Table 5.1. Physical parameters of the carbon materials for anodes. 137

Table 5.2. Specific electrochemical performance of the half cells of anodes. 140

Table 5.3. Physical parameters of the carbon materials for cathodes.....144

Table 5.4. Specific electrochemical performance of the half cells of cathodes. 146

Table 5.5. Specific electrochemical performance of full cells. 150

Table 6.1. Physical parameters of L700, L1100 and L1500.....157

Table 6.2. The atomic percentage of different elements (C, N, O) in L700, L1100 and L1500. 160

Table 6.3. Fitted elements of EIS of L700 at OCV, plated state and stripped state. 177

Table 6.4. Comparison of energy densities of sodium batteries.....184

Table A1.1. Inventory data of LCA of HG1300 and DG1300. 197

Table A1.2. Environmental impact results of System A and System B for sodium-ion batteries. 198

Table A2.1. The vibration modes of each peak in FTIR spectra of HEC-PEO.....211

Table A3.1. Fitted terms including A, a_1, a_2, B_1 and B_2 from SAXS. 221

Table A3.2. a) The calculated binding energy between sodium atoms (at different positions including centre and edges) and the graphene layers with(out) nitrogen doping; 221

Acronyms

NIB	Sodium-ion battery
NIC	Sodium-ion capacitor
NMB	Sodium-metal battery
LIB	Lithium-ion battery
SHE	Standard hydrogen electrode
GCD	Galvanostatic charge-discharge
CV	Cyclic voltammetry
SEI	Solid electrolyte interphase
ICE	Initial Coulombic efficiency
LUMO	Lowest unoccupied molecular orbital
HOMO	Highest occupied molecular orbital
NBO	Natural bond orbital
GICs	Graphite intercalation compounds
DFT	Density functional theory
PB	Prussian blue
Na-S	Sodium-sulphur
Na-O_2	Sodium-oxygen
ORR	Oxygen reduction reactions

OER	Oxygen evolution reactions
EDLC	Electrochemical double-layer capacitance
HTC	Hydrothermal carbonisation
ALD	Atomic-layer deposition
SEM	Scanning electron microscopy
TEM	Transmission electron microscopy
HRTEM	High-resolution transmission electron microscopy
NMR	Nuclear magnetic resonance
I_D/I_G	Intensity ratio of D- to G-peaks
d_{002}	Interlayer spacing of (002) planes
$FWHM_{002}$	Full width at half maximum of (002) planes
D_{Na+}	Diffusion coefficient of sodium ions
BET	Brunauer–Emmett–Teller
S_{BET}	Brunauer–Emmett–Teller specific surface area
V_t	Total pore volume
E_b	Binding energy
D_A	Average pore diameter
NLDFT	Non-Local Density Functional Theory
SAXS	Small-angle X-ray scattering

L_a	In-plane distances
XPS	X-ray photoelectron spectroscopy
XRD	X-ray diffraction
GITT	Galvanostatic intermittent titration technique
FTIR	Fourier transform infrared spectroscopy
TGA	Thermogravimetric analysis
GGA	Generalised gradient approximation
EIS	Electrochemical impedance spectroscopy
DI	Deionized
NMP	1-Methyl-2-pyrrolidinone or N-methyl-2-pyrrolidone
NC	Nanocrystal
EISA	Evaporation induced self-assembly
DMF	N, N-dimethyl formamide
NVP	$Na_3V_2(PO_4)_3$
LCA	Life cycle assessment
LCIA	Life cycle impact assessment
GWP	Global warming potential
HTP	Human toxicity potential
POCP	Photochemical oxidants creation potential

AP	Acidification potential
EP	Eutrophication potential
PEF	Product Environmental Footprints
Na_2TP	Disodium terephthalate
4G	Fourth-generation
3D	Three-dimensional
HEC	Hydroxyethyl cellulose
QSD	Quasi-solid-state
ESR	Equivalent series resistance
OCV	Open-circuit voltage

Chapter 1. Introduction

1.1 The necessity of novel energy conversion and storage technologies

The global average temperatures have reached the highest point during the past 2000 years (**Figure 1.1a**), as activities of human beings have profoundly raised the average level of carbon dioxide (CO_2) in the atmosphere of the Earth since the Industrial Revolution (**Figure 1.1**b).[1] The global warming induced by the "greenhouse" effect has made the ice sheets melt and the sea level increase, which will endanger the survival of human beings in the future.[2] Therefore, the development of novel energy conversion and storage technologies based on renewable energy resources is of great necessity.

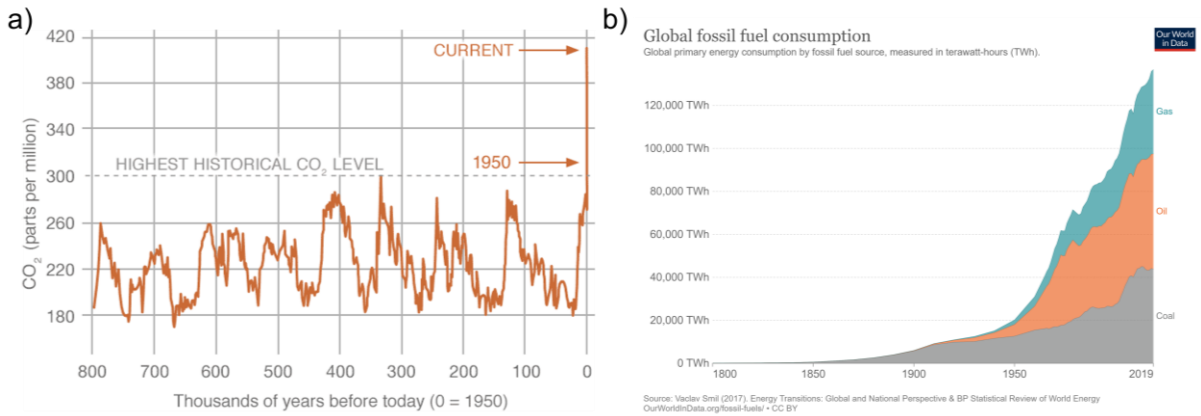


Figure 1.1. a) The average CO_2 amount within the atmosphere during the past thousands of years (Reproduced with permission from [1], Copyright 2021, NASA); b) The global energy consumption by fossil fuel including coal, oil and gas during the past hundreds of years (Reproduced with permission from [2], Copyright 2021, Our World in Data).

1.2 Electrochemical energy storage technologies – batteries and capacitors

The lithium-ion battery technologies awarded by the Nobel Prize in Chemistry in 2019 have created a rechargeable world with greatly enhanced energy storage efficiency, thus facilitating various applications including portable electronics, electric vehicles and grid energy storage.[3] Unfortunately, lithium-based energy storage technologies suffer from the limited resources (only 0.0017 wt% of lithium on Earth crust) with a confined geographical availability (**Figure 1.2**), which is predicted to be insufficient for the global market in the near future.[4] Many strategies, hence, have been studied to relieve this emergency, including designing higher-energy anode-free cells,[5] upcycling end-of-life devices,[6] and developing alternative

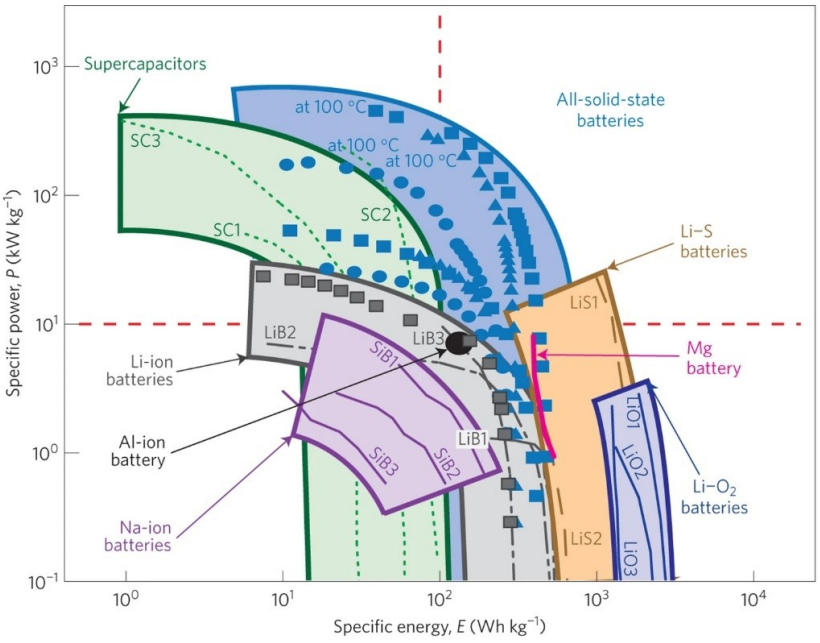
technologies.[7] Among these solutions, the sodium-based energy storage technologies gradually become a promising successor to the current lithium-based technologies in the field of grid energy storage and electric vehicles due to the abundant resources of sodium (2.3 wt% of sodium on Earth crust) and its similar properties to lithium. Therefore, the sodium-based energy storage technology which has been listed as the key technology towards carbon neutrality in many countries.[8]



Figure 1.2. The distribution of lithium resources around the world (Reproduced with permission from [8], Copyright 2021, Springer Nature).

Based on varied working principles, sodium-based energy storage technologies can be further categorised into sodium batteries and capacitors to fulfil different energy and power requirements of the market. First, sodium-ion batteries represent the most typical device operating based on the classic "rocking-chair" principle where sodium ions move from the cathode side to the anode side during the charging process.[9] The state-of-the-art sodium-ion batteries possess an energy density of around 200 Wh kg^{-1} close to the commercial lithium-ion batteries based on the $LiFe(PO)_4$ cathode which is around 210 Wh kg^{-1} (**Figure 1.3**).[10] Aiming to obtain higher power, sodium-ion capacitors are fabricated through the dual-ion mechanism where the sodium ions insert into the anode, whilst the counter ions are adsorbed on the cathode during the charging process.[11] With the combination of the capacitor-type cathode and the battery-type anode, sodium-ion capacitors can realize an energy density between 10 and 200

Wh kg^{-1} with a power density from 10000 to 100 W kg^{-1} (**Figure 1.3**).[12] Furthermore, sodium metal batteries are established to pursue higher energy with the metallic sodium anode whose theoretical capacity is 1166 mAh g^{-1}.[13] Differing from the typical anodes in sodium-ion batteries, the metallic sodium anode stores cations based on the redox pairs of Na^+/Na instead of the insertion or conversion mechanism.[14] By coupling with high-energy cathodes such as sulphur cathode or oxygen cathode, the energy density is estimated to reach over 350 Wh g^{-1} or even close to 500 Wh g^{-1} (**Figure 1.3**).[15] In general, the development of sodium-ion batteries has the potential to enter the industrial production stage,[16] while the demonstration of sodium-ion capacitors and sodium metal batteries remains at the lab-scale level,[12, 14] which both need more efforts from scientists and engineers to overcome their corresponding significant challenges such as the lack of low-cost and high-performance electrode materials as well as cost-effective electrolyte systems for the final commercialisation of these technologies. Hence, the engineering optimisation of sodium-ion batteries and the scientific innovation of sodium-ion capacitors and sodium metal batteries are becoming the most important research directions in the community of energy storage currently.



■ $Li_4Ti_5O_{12}$/$LiNbO_3$-coated $LiCoO_2$
● $Li_4Ti_5O_{12}$ + LGPS/LGPS/$LiNbO_3$-coated $LiCoO_2$ + LGPS
▲ $Li_4Ti_5O_{12}$ + LSiPSCl/LSiPSCl/$LiNbO_3$-coated $LiCoO_2$ + LSiPSCl
■ Graphite + LPS/LPS | LGPS/$LiNbO_3$-coated $LiCoO_2$ + LGPS

SC1: activated carbon/activated carbon
SC2: reduced graphene oxide RuO_2/RuO_2-polyaniline
SC3: activated carbon/activated carbon

LiB1: graphite/$LiCoO_2$
LiB2: Li/$LiFePO_4$
LiB3: $Li_4Ti_5O_{12}$/$LiNi_{0.5}Mn_{1.5}O_4$

SiB1: $Na_3V_2(PO_4)_3$ (NVP) + graphene/NVP + graphene
SiB2: NVP + CNT/NVP + CNT
SiB3: NVP + activated carbon (AC)/NVP + AC
Al-ion battery: Al/graphite
Mg battery: Mg/V_2O_5

LiS1: Li/S (graphene + single-walled CNT)
LiS2: Li/S

LiO1: Li/O_2 (graphene)
LiO2: Li/O_2 (carbon nanofibres)
LiO3: Li/O_2 (carbon nanotubes (CNT))

Figure 1.3. The Ragone plot of different types of energy storage devices, where the red lines

indicate the energy density of 100 Wh kg^{-1} and the power density of 10 kW kg^{-1} (Reproduced with permission from [17], Copyright 2016, Springer Nature).

1.3 Objectives and outlines of this thesis

During the development of sodium-based energy storage technologies, hard carbons consisting of short-range graphitic domains and long-range amorphous features have been widely applied as not only conductive agents and active materials but also functional hosts on account of their low cost, high electrical conductivity and stable physicochemical properties.[18] However, there are two main challenges of hard carbon materials.

(1) Most hard carbons are derived from non-renewable fossil fuels, thus hindering the overall sustainability of sodium-based energy storage technologies.[19]

(2) The structural features of hard carbons containing morphologies, surface chemistries, defects and pores are complicated to be accurately tuned by conventional carbonisation methods.[18]

Therefore, the main objectives of this thesis are the development and demonstration of nature-inspired strategies to address those issues of hard carbons, thus enhancing the performance and sustainability of hard carbons in the application of sodium-based energy storage technologies. Inspired by multi-scale structures of bio-resources, sustainable hard carbons can be synthesised from the hierarchical building units of renewable biomass and rationally designed by various novel preparation methods such as hydrothermal process, self-assembly, chemical activation and electrospinning.[20] Being one of the fourth-generation clean energy technologies,[21] natural woods with hierarchical structures optimised over millions of years by nature are utilised as the main precursor of sustainable hard carbons for sodium-based energy storage here. From the cellulose chains based on the repeat units of D-glucose to microfibrils composed of elementary nanofibrils embedded in the matrix of lignin and hemicellulose molecules (**Figure 1.4**),[22] each level of components with different physicochemical properties is individually extracted for specific synthesis and applications in this PhD project. At the same time, the correlations between structural features of hard carbons and corresponding electrochemical performance are explored based on advanced characterisation and simulation to obtain the fundamental understanding of energy storage mechanisms in each device, which is beneficial to the rational design of nature-inspired carbons

for emerging sodium-based energy storage technologies.

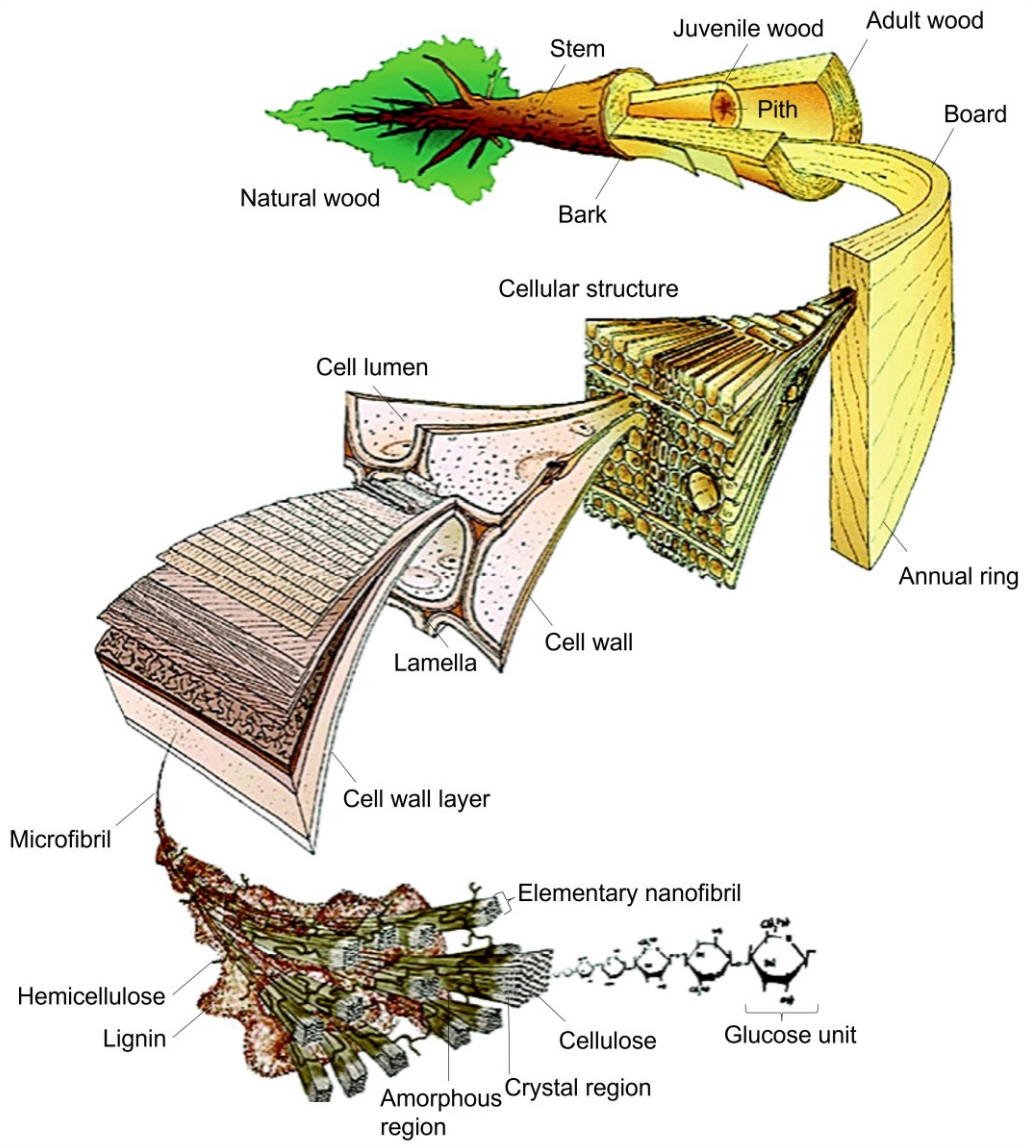


Figure 1.4. Hierarchical building units of natural woods (Reproduced with permission from [22], Copyright 2011, Royal Society of Chemistry).

This PhD thesis is composed of 7 chapters which are introduced as follows:

In Chapter 1, the research background of sodium-based energy storage technologies is briefly introduced. The challenges of state-of-the-art sodium-based energy storage technologies using hard carbons and the topic of this PhD project are proposed in this section.

In Chapter 2, the relative working principles of sodium-based energy storage are summarised, along with the comparison to lithium-based technologies. Afterwards, the recent research progress of specific sodium-based energy storage technologies is reviewed, and the corresponding challenges remaining to be addressed are critically analysed. Meanwhile, a

perspective to the necessity and promises of sustainable hard carbons for addressing the existing issues of sodium-based energy storage technologies is also discussed, based on the current situations of utilising carbon materials in those technologies.

In Chapter 3, the information of materials and general methodologies including material synthesis and characterisation is delivered.

In Chapter 4, the project entitled: "The role of hydrothermal carbonisation in sustainable sodium-ion battery anodes" is presented. To enhance the performance and sustainability of hard carbon anodes for sodium-ion storage, the hydrothermal carbonisation process is employed as a versatile pre-treatment method of renewable precursors, followed by high-temperature carbonisation, for producing advanced hard carbon anodes. A well-performing hard carbon anode is developed from D-glucose with a specific capacity of 347.4 mAh g^{-1} (30 mA g^{-1}) *via* hydrothermal process and subsequent carbonisation. The critical role of hydrothermal pre-treatment in regulating the structure for an optimised performance of hard carbon anodes is elucidated, while the sodium-ion storage mechanism is revealed using electrochemical kinetic calculations, advanced characterisation and multi-scale modelling. Furthermore, the environmental impacts of hydrothermal pre-treatment and subsequent carbonisation are evaluated using life cycle assessment compared to direct carbonisation. By comparing hard carbon anodes with and without the hydrothermal pre-treatment, it can be verified that the additional hydrothermal process is responsible for enhanced electrochemical performance, increased carbon yields and reduced carbon emissions. This work provides a systematic understanding of functions and energy consumptions of hydrothermal systems to achieve next-generation sustainable sodium-ion battery anodes.

In Chapter 5, the project entitled: "All-cellulose-based quasi-solid-state sodium-ion hybrid capacitors enabled by structural hierarchy" is presented. In this chapter, hierarchically structured carbon materials inspired by multiscale building units of cellulose from nature are assembled with cellulose-based gel electrolytes into sodium-ion capacitors. Nonporous hard carbon anodes are obtained through the direct thermal pyrolysis of cellulose nanocrystals. Nitrogen-doped carbon cathodes with a coral-like hierarchically porous architecture are prepared *via* hydrothermal carbonisation and activation of cellulose microfibrils. The reversible charge capacity of the anode is 256.9 mAh g^{-1} when operating at 0.1 A g^{-1} from 0 to 1.5 V

versus Na^+/Na, and the discharge capacitance of cathodes tested within 1.5 to 4.2 V versus Na^+/Na is 212.4 F g^{-1} at 0.1 A g^{-1}. Utilizing Na^+ and ClO_4^- as charge carriers, the energy density of the full sodium-ion capacitor with two asymmetric carbon electrodes can reach 181 Wh kg^{-1} at 250 W kg^{-1}, which is one of the highest energy devices reported until now. Combined with modified cellulose-based gel electrolytes, all-cellulose-based quasi-solid-state devices are demonstrated possessing additional advantages in terms of overall sustainability.

In Chapter 6, the project entitled: "Homogenous metallic deposition regulated by defect-rich skeletons for sodium metal batteries" is presented. In this chapter, the structural features of sustainable carbon skeletons are rationally designed from lignin to unveil the roles of defects and pores for metallic deposition. The obtained carbon skeleton with rich defects and negligible pores exhibits the best performance when applied to protect metal anodes. After long cycling (>1200 hours), the retained high Coulombic efficiency (~99.9%) of the plating and stripping processes indicates the importance of defects for inducing uniform metallic deposition. Combined with different types of cathodes (*e.g.,* Prussian blue and sulphur), "anode-less" sodium metal batteries with enhanced electrochemical performance are also demonstrated in terms of sustainability.

In Chapter 7, a summary of this PhD thesis is provided, together with the discussion and outlook of these research projects.

Chapter 2. Literature overview

2.1 Sodium-based energy storage technologies

Harvested clean electrical energy needs a suitable place to be stored, and sodium-based energy storage technologies including sodium batteries and capacitors are becoming the most promising choices because of their low cost, enhanced sustainability and appropriate capacity.[8] However, when we look into the history of sodium-based energy storage technologies, the development of sodium batteries and capacitors was not plain sailing although it happened side-by-side with the lithium batteries since the 1970s.[23] At the very beginning, metallic anodes were employed in the prototype cells, but the high risk of short circuits due to the metallic dendrite formation questioned the commercialisation of lithium and sodium batteries.[24] When scientists discovered that readily available graphite can be a perfect host material for lithium ions rather than sodium ions, the promise of commercialising lithium-ion batteries finally exceeded that of sodium batteries in the 1990s,[25] thus underestimating the value of sodium-based energy storage technologies for a long time. Nevertheless, with the successful commercialisation and growing demands of lithium-ion batteries in the worldwide market (**Figure 2.1**a), the shortage and uneven distribution of lithium recourse gradually attract global attention.[26] Driven by this situation, sodium-based energy storage technologies witnessed a revival in interests in the 2010s, as the numbers of publications containing sodium batteries and capacitors rapidly increased from 2010 (**Figure 2.1**b).

In this chapter, the basic knowledge and fundamental understanding of sodium batteries and capacitors are introduced and compared with lithium-based energy storage. Meanwhile, the recent progress of sodium batteries and capacitors is also summarised to critically analyse the state-of-the-art challenges and research directions in these fields, thus clearly stating the research background and significance of this thesis.

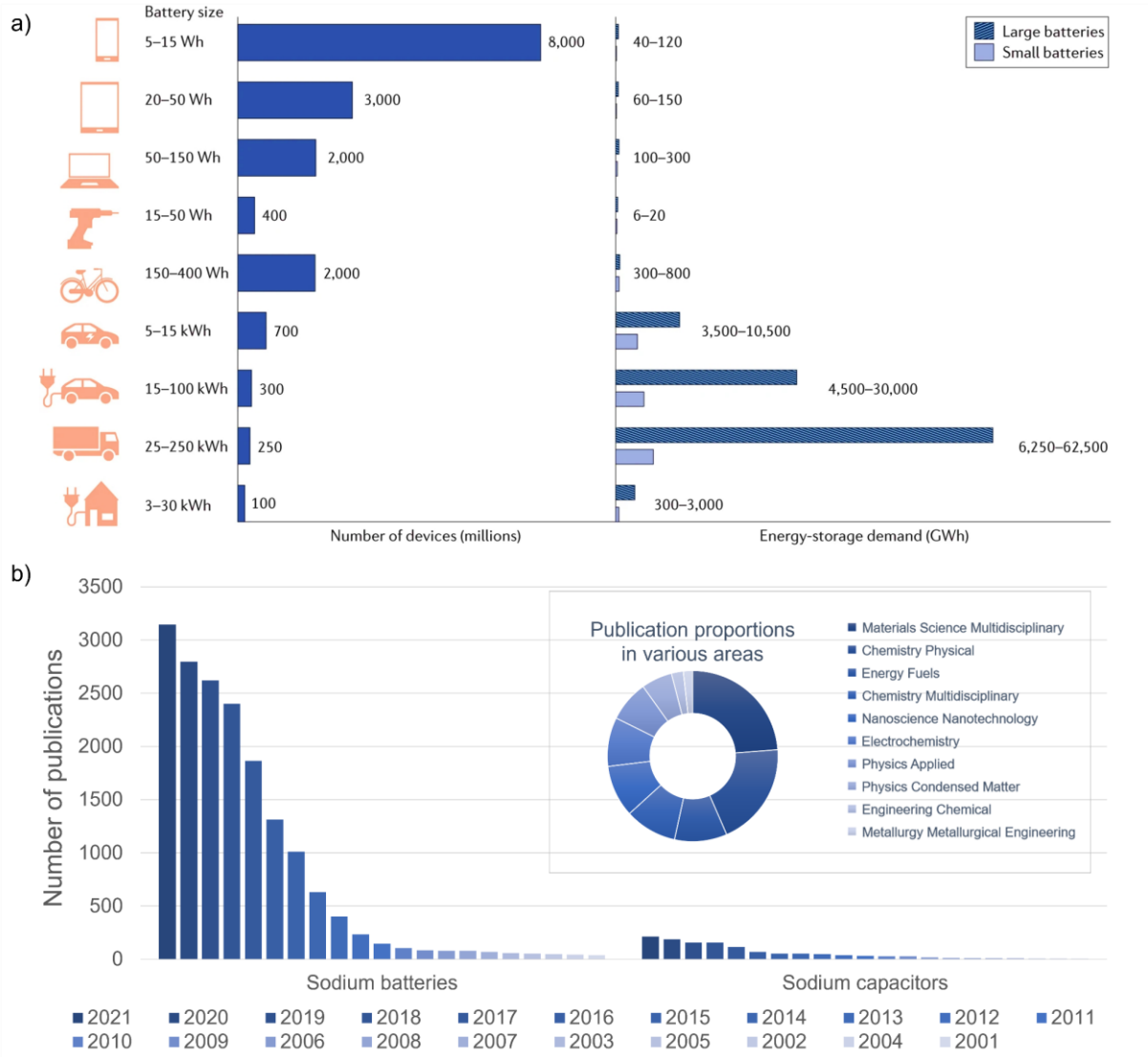


Figure 2.1. a) Estimated energy storage demand until 2050, where the number of devices with different battery sizes and energy storage demand (GWh) on small and large batteries are presented (Reproduced with permission from [26], Copyright 2018, Springer Nature); b) Numbers of publications containing sodium batteries and capacitors since 2001 indexed by Web of Science with the inset of top 10 related areas.

2.1.1 Definitions, principles and metrics

Definitions and principles. For sodium batteries and capacitors, the working principles highly depend on the type of electrode materials.

(1) Sodium-ion batteries are the most typical type of sodium batteries based on the "rocking-chair" mechanism, in which host materials of sodium ions are used as the electrodes (**Figure 2.2**a).[9] During the charging process, sodium ions move from the cathode to the anode through the electrolyte, while electrons move along the external circuit in the same direction.

Meanwhile, the cathode materials are oxidised mostly through the de-intercalation mechanism, while the anode materials are reduced according to three main mechanisms including insertion, conversion or alloying.[10] Since the whole process is reversible, sodium-ion batteries are considered as the rechargeable secondary batteries.

(2) Sodium metal batteries and their derivatives can be fabricated when using metallic sodium as the anode material. Based on the redox pairs of Na^+/Na, sodium metal anode can provide a low potential of -2.714 V vs. standard hydrogen electrode (SHE) and an outstanding theoretical specific capacity of 1166 mAh g^{-1}.[14] When coupling with cathode materials such as sulphur or oxygen according to different reaction mechanisms, the so-called sodium-sulphur or sodium-oxygen batteries can be achieved.[14] All these technologies using sodium metal anodes can be collectively referred to as sodium metal batteries. In short, sodium batteries are mainly composed of sodium-ion batteries and sodium metal batteries at the time of writing.

(3) Sodium capacitors apply the dual-ion mechanism where sodium ions cross the electric double layer and enter the bulk phase of the anode materials, while counter ions are mainly adsorbed on the surface of the cathode materials during the charging process (**Figure 2.2**b).[12] Namely, the Faradic redox reactions happen inside the anode, and the non-Faradic physical accumulation of ions dominates at the cathode side.[27] Combined with the battery-type anode and the capacitor-type cathode, sodium capacitors have the potential to bridge the gap between sodium batteries and supercapacitors, possessing excellent power and energy simultaneously.[11] However, the kinetic imbalance between the battery-type anode and the capacitor-type cathode would be a main challenge for this technology.

The brief categories of sodium-based energy storage technologies are shown in **Figure 2.2**c.

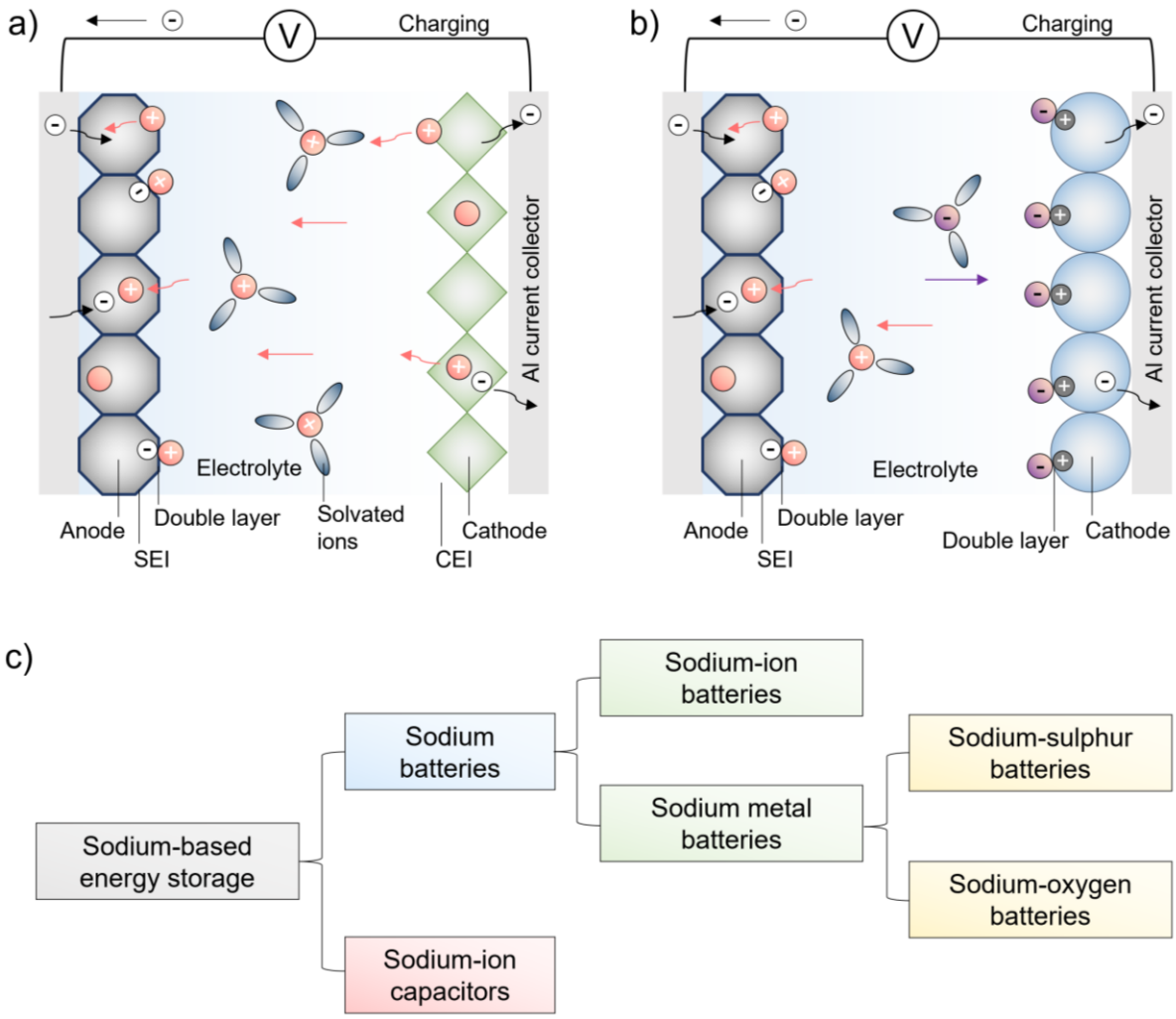


Figure 2.2. The schematic illustrations of working principles of a) sodium batteries, and b) sodium capacitors; c) The brief categories of sodium-based energy storage technologies.

Metrics. The electrochemical performance metrics of sodium batteries and capacitors are similar, containing specific capacity, energy and power densities, rate and cycling performance, Coulombic efficiency. Sodium capacitors can also be evaluated based on the specific capacitance.

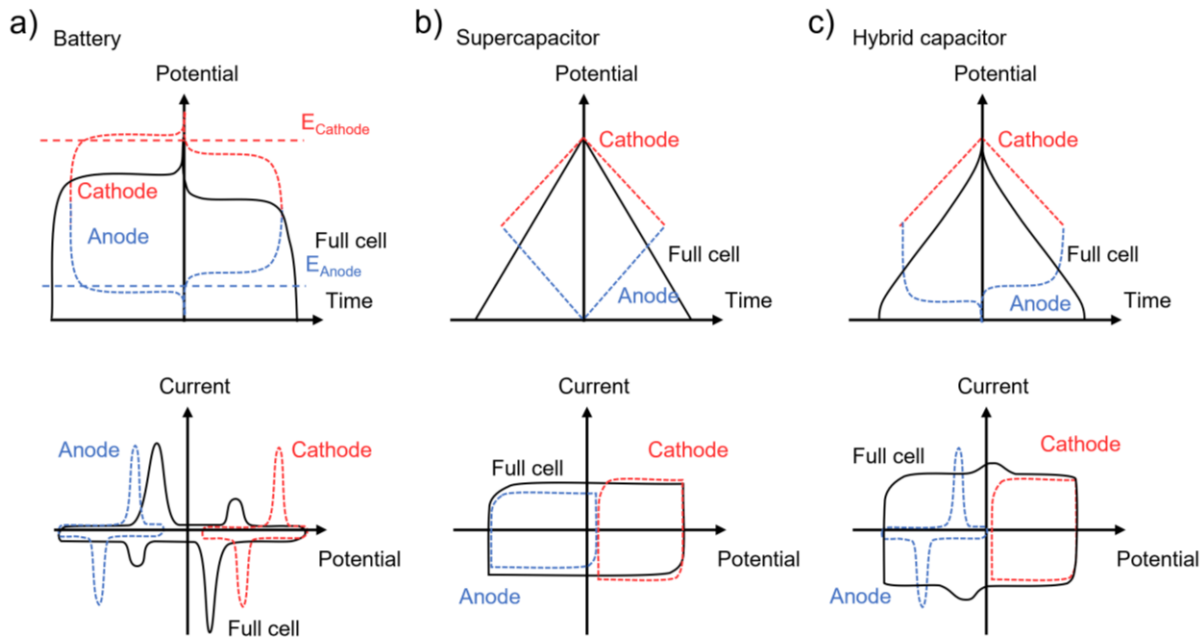


Figure 2.3. The simplified typical GCD curves of cathode, anode and full cell and their corresponding CV curves in a) battery, b) supercapacitor and c) hybrid capacitor.

For experimental results, the charge or discharge specific capacitance and capacity of the working electrodes in half cell configurations can be calculated from galvanostatic charge-discharge (GCD) curves (**Figure 2.3**) according to Equations 2.1 and 2.2, respectively:[18]

$$C_{electrode} = \frac{I\Delta t}{m\Delta U} \qquad \text{Equation 2.1}$$

$$Q_{electrode} = \frac{I\Delta t}{3.6m} \qquad \text{Equation 2.2}$$

where $C_{electrode}$ (F g^{-1}) refers to the discharge or charge specific capacitance of the working electrodes, while $Q_{electrode}$ (mAh g^{-1}) is the discharge or charge specific capacity. I (A) is the constant discharge or charge current. ΔU (=U_{max}-IR_{drop}-U_{min}, V) is the working voltage window, and m (g) is the mass of active material loaded on the working electrodes. Δt (s) is the discharge or charge time. Notably, Equation 2.1 is only suitable for For batteries, the plateau regions of GCD curves correspond to the redox peaks in cyclic voltammetry (CV) curves (**Figure 2.3**a). For hybrid capacitors, the GCD curves of typical full cells is a combination of the GCD curves of their anode and cathode, so are their CV curves (**Figure 2.3**c). The nearly linear GCD curves and rectangular CV curves are based on capacitor-type reactions (**Figure 2.3**b). The energy and power densities of the full cells can be calculated using Equations 2.3 and 2.4, respectively:[18]

$$E_{device} = \frac{I}{3.6M}\int_{t_1}^{t_2} U(t)dt \quad \text{Equation 2.3}$$

$$P_{device} = \frac{3600E_{device}}{\Delta t} \quad \text{Equation 2.4}$$

where E_{device} (Wh kg^{-1}) and P_{device} (W kg^{-1}) are the energy and power densities of devices, respectively. I (A), M (g) and Δt (s) are the constant discharge or charge current, the total mass of active materials in both anodes and cathodes, and the discharge or charge time, respectively. In addition, $U(t)$ is the voltage that changes with time under galvanostatic discharging or charging, t_1 is the start time of charge/discharge processes, and t_2 is the end time. Importantly, the other inactive components of devices including the encapsulation materials, current collectors, electrolytes and binders should be stable under such a working voltage window. When it comes to the industry level, the M for calculating the energy density will include not only the mass of active materials but also the total weight of the whole device containing those inactive components.

In theoretical situations, ΔG is the change of Gibbs free energy for a system. ΔG can be determined according to Equation 2.5:[28]

$$\Delta_r G = \Delta_f G_p - \Delta_f G_r \quad \text{Equation 2.5}$$

where $\Delta_r G$, $\Delta_f G_p$ and $\Delta_f G_r$ are the Gibbs free energy change of a system, the formation energy of the reactants and the formation energy of the products, respectively. ΔG^0 is the Gibbs energy change for a system under standard conditions (1 atm, 298 K, 1 M, etc.). The relationship between ΔG and ΔG^0 can be demonstrated based on Equation 2.6:[28]

$$\Delta G = \Delta G^0 + RT\ln Q \quad \text{Equation 2.6}$$

where R is the universal gas constant (8.314 J/(mol K)), T (K) is the temperature, and Q is the reaction quotient of the rection.

In a half reaction, an oxidant can be converted into the reductant by accepting a number of electrons ($Ox + n\ e^- \rightarrow Red$). The reaction quotient (Q) corresponds to the ratio of the chemical activities of the reductant (a_{Red}) to the chemical activities of the oxidant (a_{Ox}):[28]

$$Q = \frac{a_{Red}}{a_{Ox}} \quad \text{Equation 2.7}$$

where the chemical activity (a) of one specific dissolved species is related to its true thermodynamic concentration which is affected by the electrical interactions between all ions

in the solution at elevated concentrations. For one specific dissolved species, its chemical activity (a) is equal to its activity coefficient (γ) multiplied by its concentration (C):[28]

$$a = \gamma C \qquad \text{Equation 2.8}$$

If the concentration (C, also denoted with square brackets [ ]) of all the dissolved species are sufficiently low, their activity coefficients would be close to unity. Therefore, their chemical activities can be approximated by their concentrations. After that, the calculation of the reaction quotient (Q) can be simplified into:[28]

$$Q = \frac{[Red]}{[Ox]} \qquad \text{Equation 2.9}$$

Afterwards, the standard thermodynamic equilibrium cell potential (E^0) associated with the electrochemical reaction is defined as the decrease in standard Gibbs free energy per coulomb of charge transferred, as shown in Equation 2.10:[28, 29]

$$\Delta G^0 = -nFE^0 \qquad \text{Equation 2.10}$$

where n is the number of mol of transferred electrons per one-mole reactant in the reaction, F is the Faraday constant (96485 C mol^{-1}). For a spontaneous reaction, ΔG^0 is negative, so E^0 is positive. In contrast, E is the non-standard cell potential under the non-standard states. With Equation 2.10, Equation 2.6can be converted into Equation 2.11 and thus Equation 2.12:[28]

$$-nFE = -nFE^0 + RT\ln Q \qquad \text{Equation 2.11}$$

$$E = E^0 - \frac{RT}{nF}\ln Q \qquad \text{Equation 2.12}$$

Here, Equation 2.12 revealing the relationship between E^0 and E is the Nernst Equation. With the reaction happening, the concentration of reactants decreases, while the concentration of products increases. Hence, the cell potential gradually decreases until the reaction is at the chemical equilibrium, where ΔG and E are equal to 0. At the chemical equilibrium, the reaction quotient is equal to the equilibrium constant (K_{eq}) of the reaction:[28]

$$K_{eq} = Q = \frac{a_{Red}}{a_{Ox}} \qquad \text{Equation 2.13}$$

Therefore, the Nernst Equation can be changed into Equation 2.14:[28]

$$E^0 = \frac{RT}{nF}\ln K_{eq} \qquad \text{Equation 2.14}$$

In a full reaction, the standard full-cell voltage (E^0_{cell}) is the electromotive force between two half cells, which can be calculated based on Equation 2.15 or 2.16:[28]

$$E^0_{cell} = E^0_{reduction} - E^0_{oxidation} \quad \text{Equation 2.15}$$

or

$$E^0_{cell} = E^0_{cathode} - E^0_{anode} \quad \text{Equation 2.16}$$

where $E^0_{reduction}$ or $E^0_{cathode}$ is the standard half-cell potential of the reduction reaction at the cathode side, and $E^0_{oxidation}$ or E^0_{anode} is the standard half-cell potential of the oxidation reaction at the anode side. When E^0_{cell} is larger, the driving force of electrons through the system is stronger. For a complete electrochemical reaction (full cell), the Nernst Equation can be written as:[28]

$$E_{cell} = E^0_{cell} - \frac{RT}{nF} \ln Q \quad \text{Equation 2.17}$$

Moreover, the specific capacity of materials as an electrode can be calculated based on the converted Faraday's law of Equation 2.20:[28]

$$Q_t = \frac{nF}{3.6m} \quad \text{Equation 2.18}$$

where Q_t (mAh g^{-1}), n, F and m (g mol^{-1}) are the theoretical capacity, the number of transferred electrons, the Faraday constant (96485 C mol^{-1}), and the molecular mass of the active material.

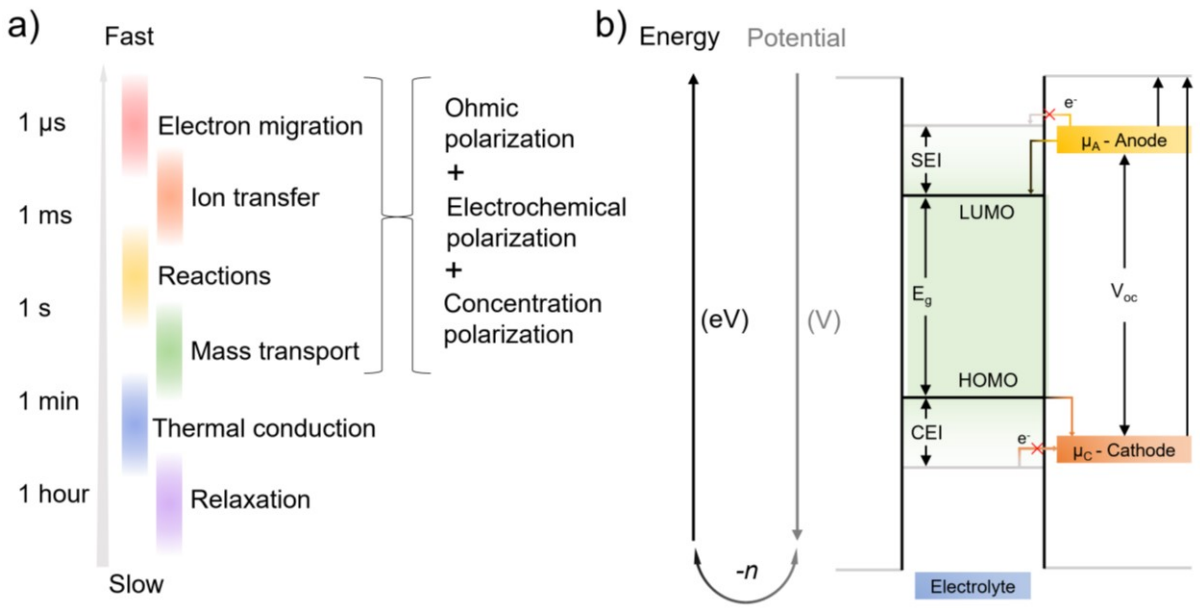


Figure 2.4. a) Dynamics of polarisations in typical energy storage devices; b) The schematic diagram of the energy levels and potentials of electrodes and electrolytes with the formation of SEI and CEI (*i.e.,* the SEI at the cathode side).

Rate and cycling performance are another two key parameters to evaluate the electrochemical performance of devices, which represents their fast charge-discharge capabilities and lifetime.[30] These two metrics can be tested using the galvanostatic charge-discharge process under different current densities with different cycle numbers. For the rate performance, the polarisation phenomena of the cell, including the concentration polarisation, electrochemical polarisation and ohmic polarisation, can induce unfavourable decreases in the cell voltage and specific capacities at a higher current density (**Figure 2.4**a).[31] First of all, the concentration polarisation means the existence of ionic concentration gradients in the electrolyte, which is related to the ion diffusion kinetics in the electrolyte.[32] For example, with a fast depletion of ions at the electrode boundary, the slower ion diffusion kinetic in the electrolyte can cause the larger concentration polarisation. In addition, the electrochemical polarisation is related to the kinetics of ion transfer at the electrode-electrolyte interface and inside the electrode.[31] For instance, when the applied electronic currents in the external circuit increase, the faster kinetics of ion transfer at the electrode-electrolyte interface and inside the electrode, along with a faster electrochemical reaction, can lead to less electrochemical polarisation. Meanwhile, the lower intrinsic electrical resistance or the higher ionic conductivity of the cell components can result in the weaker ohmic polarization during the fast charge-discharge process.[32] The corresponding response time of ion transfer in the liquid electrolyte should be quicker than the ion transfer at the electrode-electrolyte interface and inside the electrode.[33] Besides, the reaction-driven response time should be the slower, while the electron migration is the fastest. For the cycling performance, the stability of the electrode, electrolyte and their interface as well as the reversibility of electrochemical reactions are all highly involved in the lifetime of devices. In brief, the physicochemical properties of each component in the device affect the rate and cycling performance.

The Coulombic efficiency in each cycle also matters because the Coulombic efficiency describes the reversibility and stability of electrochemical reactions, which is highly linked with the cycling performance.[34] The Coulombic efficiency is equal to the ratio of the discharge capacity to the charge capacity in full cells. The irreversible capacity in each cycle results from the so-called “dead” sodium, including sodium for the solid electrolyte interphase (SEI) formation, sodium trapped in electrode structures and isolated sodium after cycling.[35] First,

since SEI mainly forms in the first cycle, the initial Coulombic efficiency (ICE) can be defined to evaluate the SEI formation. In principle, if the lowest unoccupied molecular orbital (LUMO) of the electrolyte is lower than the Fermi level (μ_A) of anodes, the electrons will transfer from μ_A of the anode to LUMO of the electrolyte, indicating the reduction of electrolytes in the first cycle (**Figure 2.4**b).[36] Also, if the highest occupied molecular orbital (HOMO) of the electrolyte is higher than the Fermi level (μ_C) of cathodes, the electrons will transfer from HOMO of electrolytes to μ_C of cathodes, which means the oxidation of electrolytes.[36] Afterwards, a passivation SEI layer will be formed from the decomposition of electrolytes to fully cover electrodes as a barrier to prevent the direct electron transfer with electrolytes.[37] A higher ICE means fewer sodium ions needed for producing excessive SEI, which can save active materials. If the interface is unstable, SEI layers will break and reform over and over again during cycling with a low Coulombic efficiency in each cycle.[38] Therefore, stabilising SEI at the interface is of great importance for cycling performance. Except for SEI formation, sodium trapped in the electrode structures can also decrease the Coulombic efficiency, which is related to the inherent reversibility of sodium storage reactions and the accessibility of ion pathways within the electrode structure.[39] Last but not least, the isolated sodium during cycling can reduce the Coulombic efficiency as well.[40] Generally, the optimisation of electrolytes and electrodes can contribute to the improvement of the Coulombic efficiency in each cycle. An ICE of over 80 % and the Coulombic efficiency close to 100 % after the first cycle are desirable for devices with an ideal reversibility and cycling performance.[41]

Comparisons to lithium. Both \ alkali metals, sodium and lithium are located in the first group of the periodic table. The ionic radius and molar mass of sodium are inherently larger than those of lithium.[42] Compared to lithium, the natural properties of sodium lead to discrepancies in its electrochemical behaviour, and thus mainly obstruct the previous development of sodium-based energy storage technologies. On one hand, sodium ions cannot intercalate into graphite which is a cost-effective anode material to store lithium ions (**Figure 2.5**a).[43] On the other hand, since the redox potential of sodium is higher than that of lithium, the energy of sodium-based full cells with the narrower working voltage window based on the $NaCoO_2$ or $NaFePO_4$ cathode and the sodium anode is theocratically lower than that of lithium-based one based on the

$LiCoO_2$ or $NaFePO_4$ cathode and the lithium anode (**Figure 2.5**b).[44]

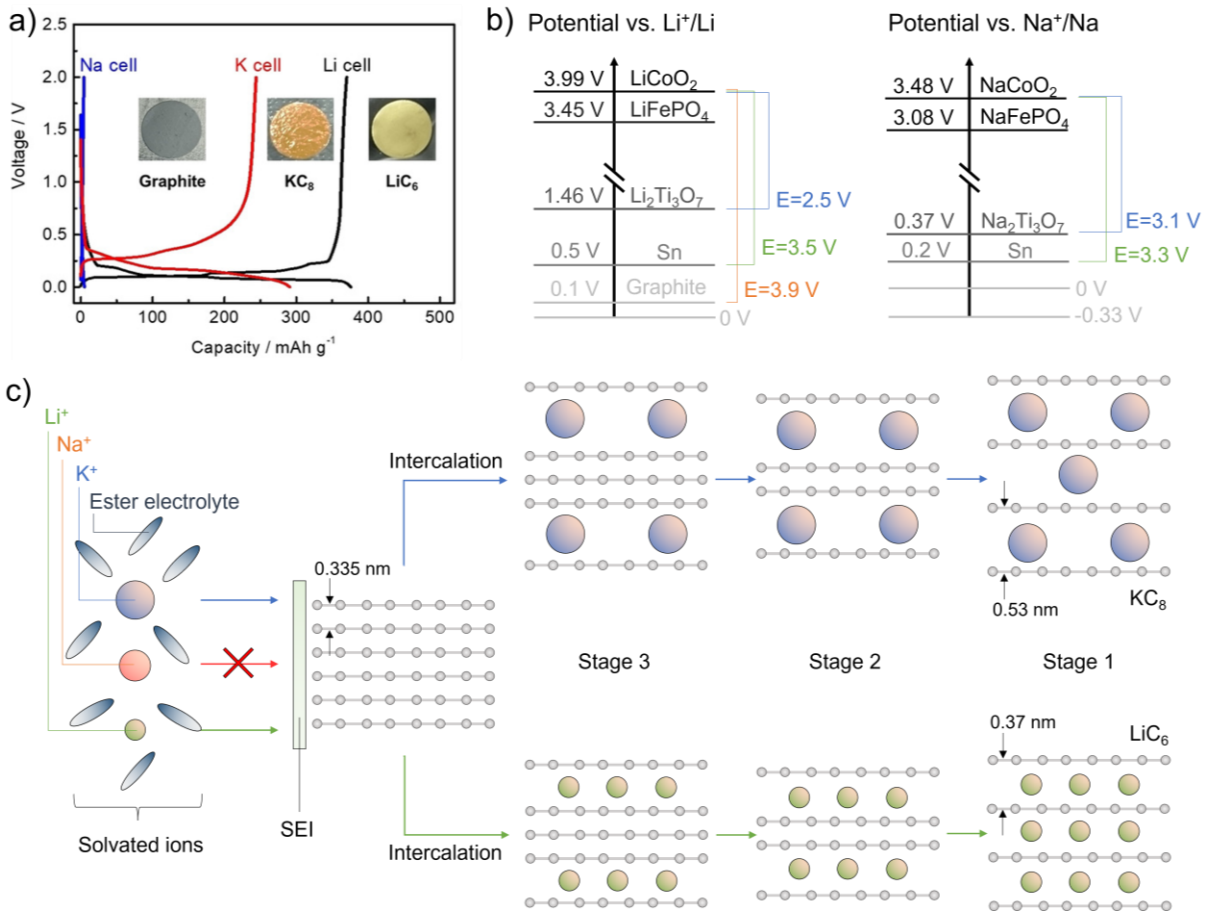


Figure 2.5. a) The typical discharge-charge curves of graphite anodes to store cations in the half cell configuration with the inserted photography of graphite and graphite intercalation compounds including LiC_6 and KC_8 (Reproduced with permission from [45], Copyright 2018, Wiley); b) The redox potentials of electrode materials vs. Li^+/Li or Na^+/Na; c) The schematic illustrations of intercalation behaviours of lithium and potassium ions into graphite in ester electrolytes.

As mentioned above, the successful application of graphite anodes has greatly contributed to the industrialisation of lithium-ion batteries. Until now, graphite still dominates the choice of anode materials, although the lithium cathode materials have achieved tremendous progress from $LiCoO_2$ to $LiFePO_4$ and $LiNi_{0.8}Mn_{0.1}Co_{0.1}O_2$.[46] At the very beginning, scientists assume that the too large size of sodium ions fails their intercalation into graphite. However, this explanation is actually oversimplified because potassium ions with an even larger ionic radius (1.38 Å) than sodium ions can still intercalate into graphite (**Figure 2.5**a).[47] The graphite intercalation compounds (GICs) formed by lithium and potassium ions are LiC_6 and KC_8, respectively, and thus the theoretical capacities of graphite to store lithium and potassium ions

are 372 and 279 mAh g^{-1}, correspondingly (**Figure 2.5**c).[48] In contrast, the GIC formation of NaC_{64} is predicted with a low theoretical capacity of 35 mAh g^{-1}, which implies sodium ions can hardly intercalate into the graphite lattices.[49] Therefore, the restricted intercalation of sodium ions into graphite does not result from the large size of sodium ions. According to van der Waals density functional theory (DFT) calculations in literature reported by Li *et al*.,[49] the formation enthalpies of NaC_6 or NaC_8 are positive, so the formation of sodium-rich GICs needs a redox potential below 0 V vs. Na^+/Na, where the precipitation of sodium metal will take place first. When the redox potential is positive, the interaction between sodium ions and in-plane graphene layers are too weak to stabilise the formed GICs.[50] Moreover, the stokes radius and desolvation energy of sodium ions in traditional ester electrolytes are even smaller than those of lithium ions (**Table 2.1**). Hence, the intercalation of lithium ions into graphite is, in fact, the abnormal existence with a negative formation enthalpy of LiC_6.[50] To overcome these intrinsic shortcomings of sodium ions, great efforts have been made by scientists to develop efficient and durable sodium-ion storage materials.

However, sodium still has advantages such as low cost and better possible electrochemical performance under higher operation currents or lower running temperatures because of its abundant resources as well as smaller stokes radius and desolvation energy of sodium ions, respectively (**Table 2.1**).[51] In addition, there is one more advantage of sodium-based energy storage for its energy density compared to lithium-based one, which is the possible usage of lighter and cheaper aluminium (Al) current collectors on both sides.[51] In commercial lithium-ion batteries, the anode can only employ copper (Cu) foils as the current collector because lithium alloys with aluminium. The usage of Al current collectors can contribute to the increase in the energy density and the decrease in the fabrication cost. Detailed examples will be provided in the following case study parts.

Table 2.1. Comparison of sodium and lithium's properties.[8, 9]

Element	Ionic radius (Å)	Molar mass (g mol^{-1})	Redox potential (V vs. SHE)	Stokes radius in PC (Å)	Desolvation energy in PC (kJ mol^{-1})
Sodium	1.02	23.0	-2.71	4.6	157.3
Lithium	0.76	6.9	-3.04	4.8	218.0

2.1.2 Sodium batteries

According to the visualised statistics of keywords in publications related to sodium batteries (**Figure 2.6**), it is the performance of sodium batteries that attracts the greatest attention from scientists. Compared to cathodes and electrolytes, anodes are mentioned more regularly in recent literature, which indicates the importance of anodes for the current stage of sodium batteries. Meanwhile, anode materials like graphene, reduced graphene oxide, carbon nanotube, carbon nanofibre, hard carbon, MoS_2 and anatase TiO_2 are frequently reported. Therefore, carbon materials for sodium-ion batteries become the most popular research direction, along with the latest average publication per year and the strong links with other keywords. In addition, P2-type layered metal oxide, $Na_3V_2(PO_4)_3$ and Prussian blue dominate the choices of cathode materials.

As discussed above, the physicochemical properties of electrodes and electrolytes occupy a significant position in determining the electrochemical performance of sodium batteries, hereby the detailed case studies and corresponding critical analysis are provided to deepen the understanding of the specific correlations.

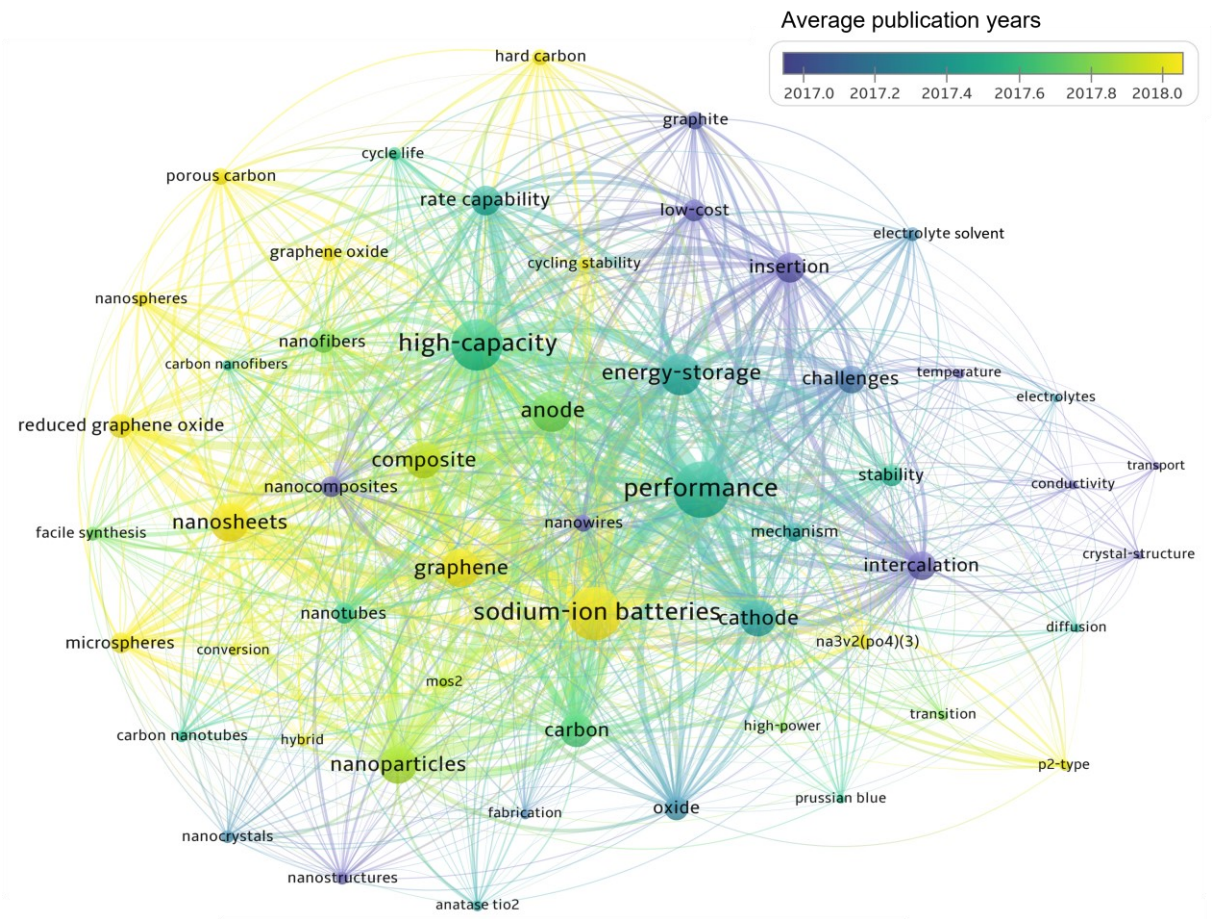


Figure 2.6. The visualised statistics of keywords in publications related to sodium batteries, where the colour represents the average publication year, the size indicates the reported frequency in the literature.

2.1.2.1 Anodes

The anode materials for sodium batteries can be categorised according to their different kinds of mechanisms, namely insertion, alloying and conversion.[52] In addition, metallic sodium can be employed as the anode directly to achieve a high energy density based on the redox couple of Na^+/Na.[53]

Insertion-type. This type of anode material as the host material for sodium ions usually possesses high electrochemical stability and reversibility. Graphite has been the benchmark anode material to store lithium ions in the industry since the 1990s, but unfortunately, the intercalation of sodium ions into graphite cannot happen without solvent.[44] Sodium ions can only enter the graphite through the co-intercalation together with ether-based electrolyte

molecules, which can achieve a capacity of around 90 mAh g^{-1}.[44] Unlike graphite, long-range amorphous carbons such as hard or soft carbons were discovered to be the suitable insertion-type candidate to store sodium ions with a reversible capacity of 250 to 300 mAh g^{-1}.[50] However, the detailed sodium-ion storage mechanism of amorphous carbons is still under debate, thus obstructing the rational design of high-performance carbon anodes.[50] Typically, amorphous carbons are composed of curved graphene layers which are turbostratically stacked (**Figure 2.7**a). As the main differences between soft and hard carbons, soft carbons can still be graphitised at a high temperature like 2000 °C, but hard carbons cannot, which means hard carbons are generally more disordered than soft carbons in similar preparation circumstances (**Figure 2.7**a).[54] While various carbonaceous precursors including crosslinked polymers, coal and pitch can be utilised to synthesise amorphous carbons, the fossil fuel-based resources hinder the overall sustainability of sodium-ion batteries.[54] Hence, the bio-inspired hard carbons with various microstructures represent a more sustainable choice of anode materials. For example, the cotton-derived carbon materials can maintain the hollow microstructures after carbonisation (**Figure 2.7**b). Until now, hard carbon anodes with capacities as high as 350-400 mAh g^{-1} have been reported with optimised pore and defect structures (**Figure 2.7**c).[55] Meanwhile, three derivative models have been established to explain the insertion mechanism of sodium ions in the sloping region and the plateau region of GCD curves, including "insertion/intercalation-adsorption", "adsorption-insertion/intercalation" and "adsorption-filling" model (**Figure 2.7**d-f).[56] In these models, "insertion/intercalation" obviously represents the insertion/intercalation of sodium ions into graphene layers of hard carbons, while "adsorption" and "filling" mean the adsorption of sodium ions onto defect sites of graphene layers and the sodium-ion filling into nanovoids, respectively.[56]

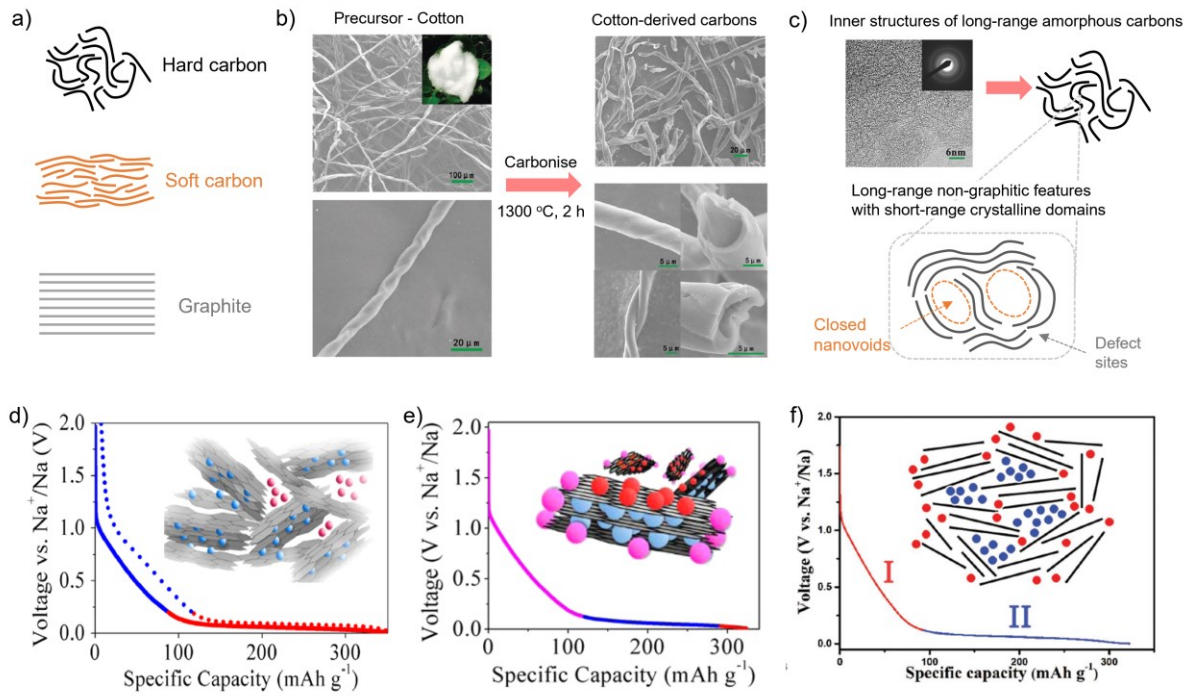


Figure 2.7. a) Schematic illustrations of inner structures of hard carbon, soft carbon and graphite; b) Scanning electron microscopy (SEM) images of cellulose-rich cotton before and after the carbonisation with the inserted photography of cotton (Reproduced with permission from [57], Copyright 2016, Wiley); c) The transmission electron microscopy image of typical hard carbons with the illustrated active sites including closed nanovoids and defect sites;[57] The sodium-ion storage mechanism models of hard carbons including d) "insertion/intercalation-adsorption", e) "adsorption-insertion/intercalation" and f) "adsorption-filling" models (Reproduced with permission from [56], Copyright 2018, American Chemical Society).

For example, Tang *et al.*[58] studied the structural effects on the electrochemical performance of glucose-derived hard carbons at 1000 °C. The reversible charge capacity of their hard anodes reached 168 mAh g^{-1} at 0.2 A g^{-1}. The charge capacity still reached 75 mAh g^{-1} at 5 A g^{-1} since the obtained hollow carbon spheres with high porosity can shorten the ion diffusion pathway to active sites (**Figure 2.8**a). However, excessive opening pores also possess disadvantages. Li *et al.*[57] prepared a kind of cellulose-derived hard carbon anodes to store sodium ions. Through controlling the carbonisation temperatures between 1000 and 1600 °C, the pore and defect structures of hard carbons can be tuned to achieve the optimised electrochemical performance. With the increase in temperatures, the decrease in accessible surface areas of hard carbons can be attributed to the closure of opening pores (**Figure 2.8**b). Under the carbonisation temperature of 1300 °C, the highest reversible capacity of 315 mAh g^{-1} at 0.03 A g^{-1} was achieved in the half cell configuration of hard carbon electrodes with a low surface area of 38

m^2 g^{-1} and a suitable ICE of over 80 %. In contrast, the hard carbon anodes prepared at 1000 °C only delivered the reversible capacity of around 100 mAh g^{-1} with a low ICE of 26%. The irreversible capacity mainly resulted from the excessive SEI formed on their large accessible surface area (538 m^2 g^{-1}), so the modification of pore structures is essential to suppress unnecessary SEI formation. Except for pores, defects are also notable. Xu *et al.*[59] synthesised cellulose-derived hard carbon anodes with nitrogen and sulphur co-doping for sodium-ion batteries. The obtained hard carbon showed a reversible charge capacity of 280 mAh g^{-1} at 0.03 A g^{-1} and an excellent rate retention of 46% at 10 A g^{-1}. In conjunction with theoretical calculations, they implied that the heteroatom-doping can produce more defects into hard carbons with enlarged interlayer spaces to reduce the diffusion barriers and provide more favourable sodium-ion interactions with defect sites (**Figure 2.8**c). To sum up, tuning the morphologies, pore and defect structures of bio-derived hard carbons can contribute to the enhanced electrochemical performance of sodium-ion storage.

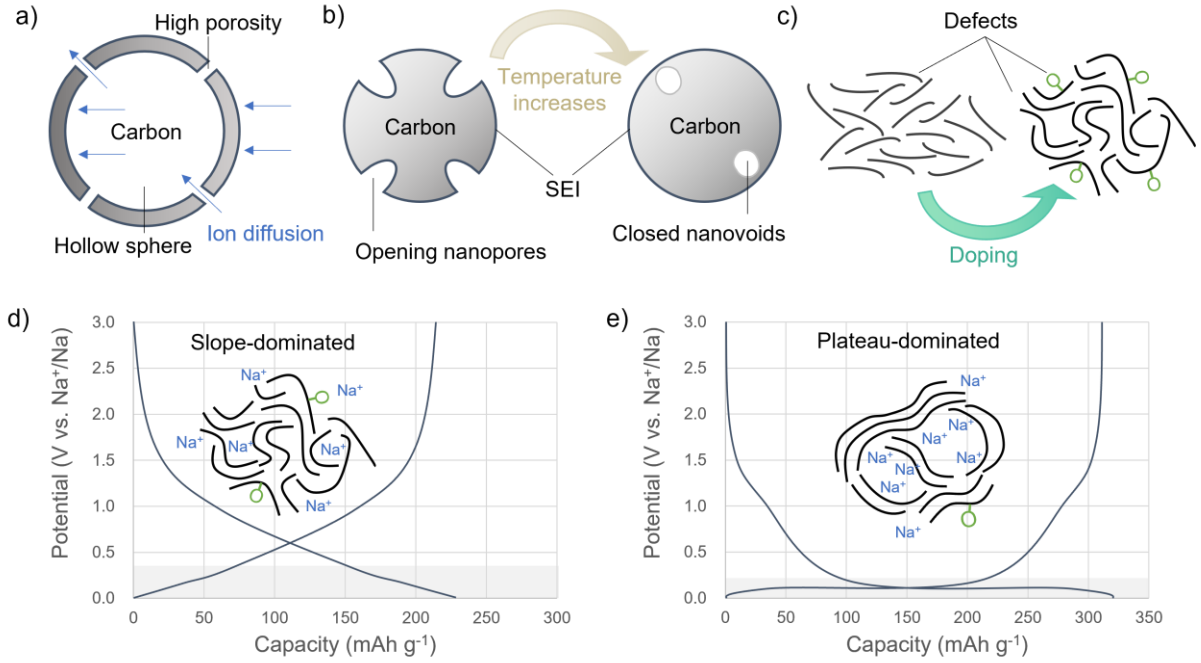


Figure 2.8. The modification of a) morphologies, b) pore and c) defect structures of bio-derived hard carbons to enhance their electrochemical performance; d) The typical GCD curves of hard carbons dominated by the adsorption of sodium ions at defect sites; e) The typical GCD curves of hard carbons dominated by the filling of sodium ions within closed nanovoids.

Furthermore, according to the correlations between hard carbon structures and electrochemical performance, Au *et al.*[60] from our group claimed sodium ions were adsorbed

on the defect sites in the sloping region, while the filling of sodium ions into closed nanovoids happened in the plateau region. This "adsorption-filling" mechanism model has also been confirmed by Stratford *et al.*[61] using advanced characterisation methods like the pair distribution function analysis and *operando* solid-state ^{23}Na NMR. Interestingly, we can see from many reported studies that the shapes of GCD curves mostly depend on the interaction behaviours of sodium ions with active sites. For instance, the slope-dominated GCD curves represent the high-power features of hard carbons, which is related to the rapid kinetics of adsorbing sodium ions at defect sites (**Figure 2.8**d).[62] That is to say that the adsorption of sodium ions at defect sites with rapid kinetics can be considered as a kind of surface-controlled reaction. In contrast, the plateau-dominated GCD curves represent the high-energy features of hard carbons, linked with the sluggish kinetics of sodium-ion filling within closed nanopores (**Figure 2.8**e).[63] Namely, the kinetically slow filling of sodium ions within closed nanovoids can be considered as a kind of diffusion-controlled reaction. Since sodium ions will penetrate the solid electrolyte interphase and cross the interface to combine with electrons, the sodium-ion storage behaviours demonstrated above both belong to the Faradic process.[64] Until now, the specific sodium-ion mechanisms in hard carbon are still uncertain, such as what the state of sodium stored inside the closed nanovoids is, and how sodium ions interact with different kinds of defect sites. Therefore, solid evidence is needed to prove these unknown details in hard carbons, thus paving the way for rationally preparing high-performance hard carbons from biomass in the future.

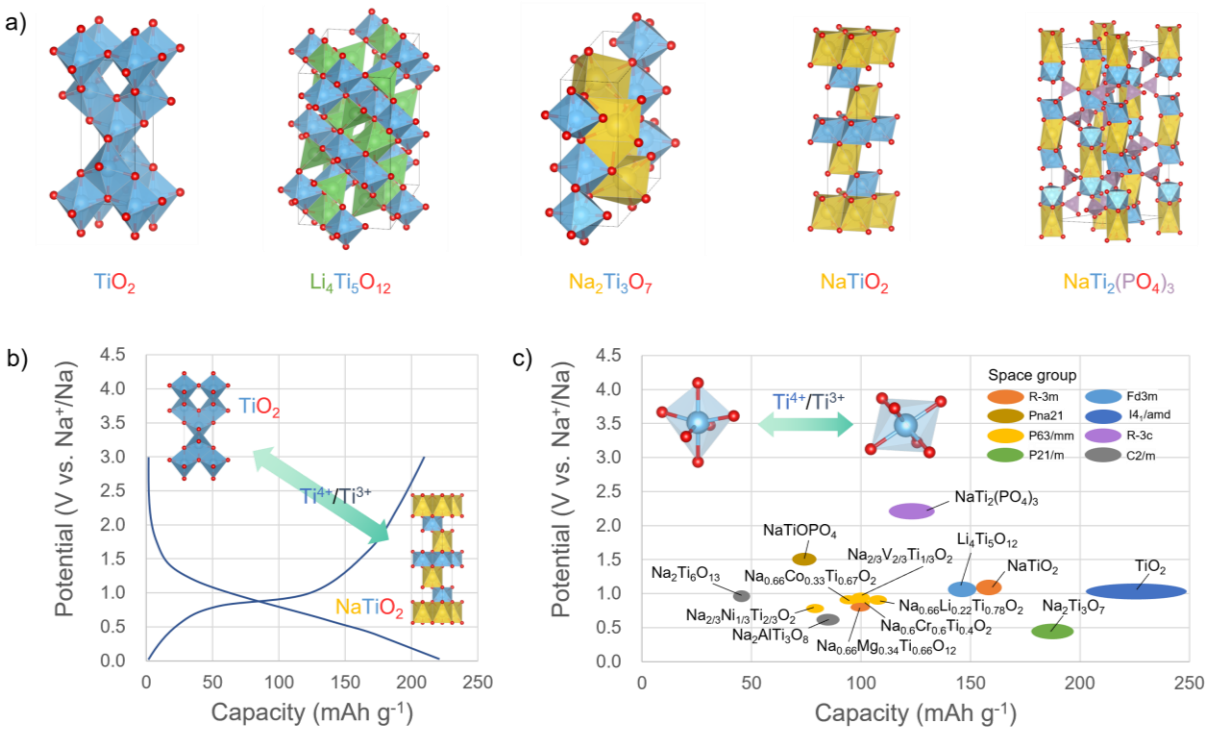


Figure 2.9. a) Crystal structures of titanate-based anode materials; b) Typical GCD curves of TiO_2 electrodes in the half-cell configuration with the phase transformation between TiO_2 and $NaTiO_2$ during the sodiation and de-sodiation process; c) Summaries and comparisons of redox potentials and capacities of different titanate-based anode materials.

As alternatives to hard carbons, some titanate, organic and phosphorus-based electrodes also provide reasonable capacities. For titanates such as TiO_2, $Li_4Ti_5O_{12}$, $Na_2Ti_3O_7$, $NaTiO_2$ and $NaTi_2(PO_4)_3$ based on different space groups (**Figure 2.9**a), they usually accommodate sodium ions through the reduction of Ti^{4+} into Ti^{3+} during the sodiation process (**Figure 2.9**b).[8] Their corresponding capacities can reach around 110 to 180 mAh g^{-1} as the critical elements contained in titanates are heavier than carbon.[65] Meanwhile, their redox potentials of around 1.0 vs. Na^+/Na are higher than the plateau region of hard carbons (0.1 V vs. Na^+/Na), which can prevent the dendrite formation but also decrease the energy density of the full cell.[65] The summaries and comparisons of redox potentials and capacities of different titanate-based anode materials are shown in **Figure 2.9**c.[66] In addition, the specific channel structures inside titanates can provide an outstanding rate and cycling performance with short ion diffusion pathways and small volume changes during the charge-discharge process.[67] In comparison to hard carbon anodes, the low electrical conductivity, high costs and high redox potentials of titanates may challenge their future applications.[68]

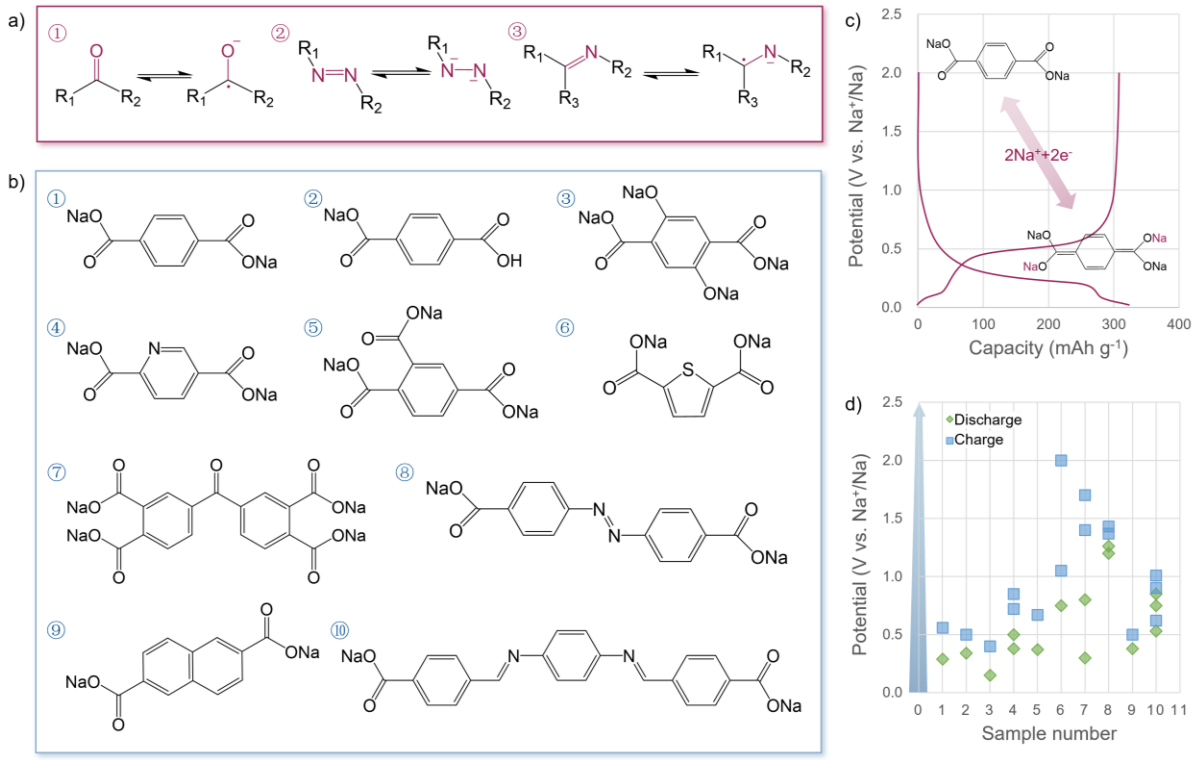


Figure 2.10. a) Schematically illustrating redox activities of organic moieties to interact with sodium ions; b) Molecular structures of redox-active organics for sodium-ion battery anodes; c) Typical GCD curves of Na_2TP in the half cell during the sodiation and de-sodiation process; d) Redox potentials of redox-active organics from Figure 2.10b with different redox states.

Given the low redox potentials and existence of active sites, some organics can be also used as solid-state anode materials to store sodium ions. In principle, functional groups like carboxylate, imine and azo have redox activity at the low redox potentials.[69] For example, electrons of π bonds between oxygen and carbon atoms in carboxylate can be delocalised to oxygen and carbon atoms, and the polarised state of moieties can interact with sodium ions (**Figure 2.10**a).[69] During the sodiation process, the oxygen atom gains one more electron from the initial state to bond with sodium atoms. The more redox-active sites in organic molecules can increase the storage ability of sodium ions, so the molecular engineering of organics to enhance the active-site concentration is essential. The structures of some reported organic anode materials with their redox potentials are listed in **Figure 2.10**b and d.[69] Among them, disodium terephthalate (Na_2TP) and its derivates are the most classical organic anode materials because of the active functional groups existing.[70] In addition, they can be easily synthesised using the recrystallization method. As the bipolar system, Na_2TP can access both positive and negative states from the neutral state. When used as the anode, each molecular unit can store

two sodium ions at the sodiation potential of around 0.3 V vs. Na^+/Na, thus achieving a capacity of around 250-300 mAh g^{-1} (**Figure 2.10**c).[70] Except for these small organic molecules, the organic building blocks with active functional groups can be polymerised to form polymers, metal-organic frameworks and covalent organic frameworks for sodium-ion storage.[71] However, organic anodes suffer from the low electrical conductivity, short lifetime and low volumetric energy density, which still needs the contribution of conductive agents like carbon black or carbon nanotubes.[69]

In short, at the current stage of commercialising sodium-ion batteries, hard carbons from biomass are the most cost-effective choice of anode materials because of their low-cost and suitable electrochemical performance compared with other insertion-type anode materials. For other insertion-type anodes, the utilisation of hard carbons from biomass is also of vital importance to improve their inadequate electrical conductivities.

Alloying-type. While insertion-type anodes, especially hard carbons, have shown satisfactory capacities for sodium-ion storage at the current stage, developing higher-energy anode materials beyond insertion for next-generation sodium-ion batteries is also very important in order to compete with lithium-ion batteries. Alloying anodes typically can provide high capacities because one redox centre is responsible for multiple electron transfer ($xNa^+ + M + xe^- \leftrightarrow Na_xM$, M = alloying elements).[72]

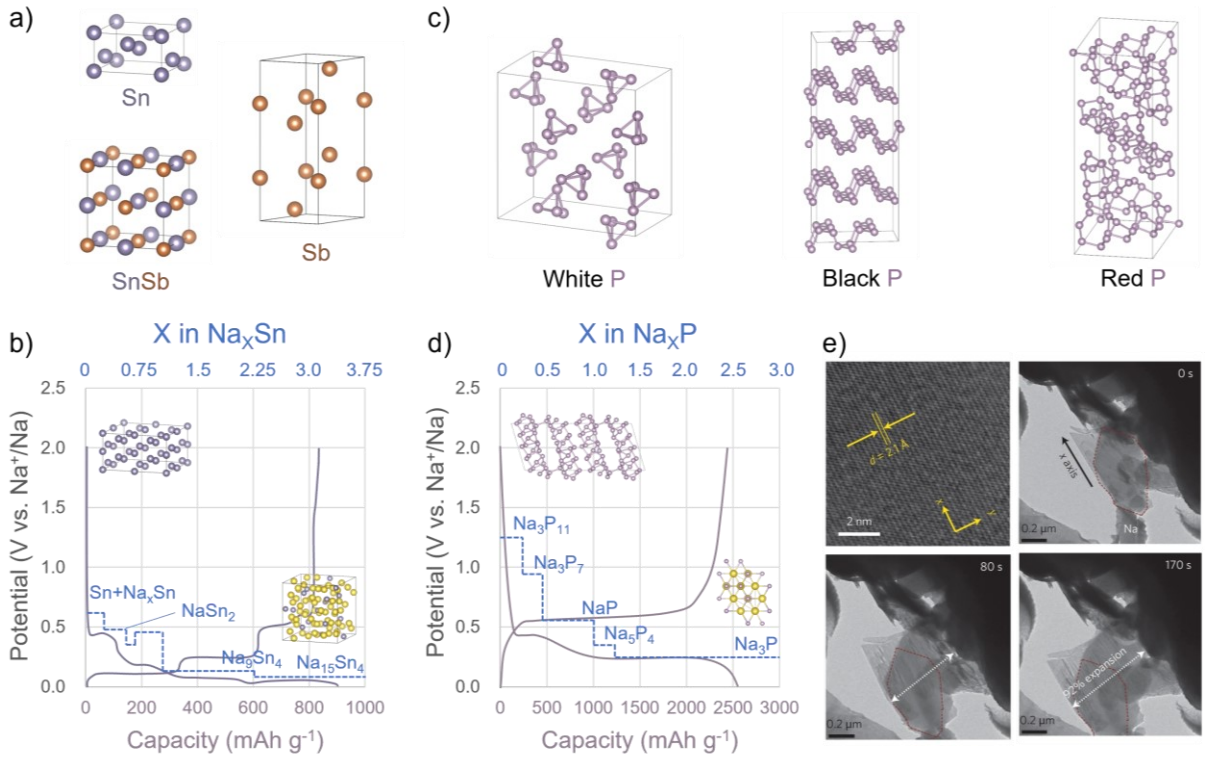


Figure 2.11. a) The crystal structures of tin, antimony and their alloys of SnSb; b) The typical GCD curves of tin anode materials for sodium-ion storage with the corresponding phase transformation stages at specific potentials; c) The molecular structures of three allotropes of phosphorus; d) The typical GCD curves of phosphorus-based electrode for sodium-ion storage with the corresponding phase transformation stages at specific potentials; e) *In-situ* TEM images of black phosphorus illustrating its layer-by-layer structure and the volume expansion during the sodiation process from pristine to different sodiated states at 0, 80 and 170 s. (Reproduced with permission from [73], Copyright 2015, Springer Nature).

Metallic tin (Sn) and antimony (Sb) are the most investigated alloying anodes for sodium-ion storage (**Figure 2.11**a). Since each tin atom can combine with 3.75 sodium atoms, the high theoretical capacity of 847 mA h g^{-1} can be estimated with the resulting alloy of $Na_{15}Sn_4$ (**Figure 2.11**b).[74] The alloying of $Na_{15}Sn_4$ slowly happens at the potential of 0.21 V vs. Na^+/Na.[75] However, pristine tin anodes usually go through a 4.2-fold volume expansion during the sodiation process, which leads to the continuous reconstruction of the SEI layer and the pulverisation of the electrode.[74] Therefore, the Coulombic efficiency and lifetime of tin anodes are impractical. Furthermore, antimony anodes have a similar situation. Each antimony atom can alloy with 3 sodium atoms to form the hexagonal Na_3Sb phase with a calculated theoretical capacity of 660 mAh g^{-1}.[76] Nevertheless, antimony anodes also suffer from a volume expansion of 390 % and sluggish reaction kinetics.[76] Meanwhile, the alloying potential of antimony is

above 0.5 V vs. Na^+/Na, which further decrease their energy densities.[76] Interestingly, the binary alloy of SnSb with decreased particle sizes can show enhanced structural stability based on reduced strain during the cycling testing, implying that the inherent properties including the particle size of alloys all affect the electrochemical performance.[77] Inspired by this phenomenon, other metals can also be introduced into tin or antimony to form stable intermetallic compounds with suitable nanostructures and thus overcome the drawbacks of bare alloying-type anodes.[78] Besides, carbon nanomaterials like carbon nanotubes, carbon nanofibres, graphene and carbon nanospheres have widely been employed as the matrix to allocate the volume expansion, avoid the agglomeration and shorten ion diffusion pathway, thus engineering the nanostructured alloying-type anodes with improved electrochemical performance.[79] Combined with additives of electrolytes such as fluoroethylene carbonate (FEC), the obtained fluorine-rich SEI layer can exhibit the great stability to cover the varied volumes of anode materials upon cycling.[80]

As an abundant resource with environmental benignity, phosphorus can also offer an impressive theoretical capacity of 2596 mAh g^{-1} for sodium-ion storage because one phosphorus atom can ideally combine with three sodium atoms to form Na_3P during the sodiation process (**Figure 2.11**d).[81] Meanwhile, the sodiation potential of phosphorus is around ~0.3 V vs. Na^+/Na, which can promise a broad working voltage in full cells.[81] In nature, there are three allotropes of phosphorus: white phosphorus, red phosphorus and black phosphorus with different structural features (**Figure 2.11**c).[82] First, toxic white phosphorus exists in the molecular form of tetrahedral P_4, but it ignites in air at only around 50 °C, so it is not the best choice of anode materials.[82] Second, being prepared by the mild heating of white phosphorus, red phosphorus with a chain-like structure is more stable than white phosphorus.[42] Although commercial red phosphorus is very cheap, its low electrical conductivity significantly restricts its further application in batteries.[83] The last allotrope is black phosphorus, which can be made through the high-pressure heating of white phosphorus.[84] In the form of multiple stacked two-dimensional layers, it is the most stable one from the point of view of thermodynamic.[84] Differing from the other two allotropes, black phosphorus is the semiconductor with a narrow band gap of around 0.3 eV, thus offering a potential in the field of energy storage.[84] However, black phosphorus still suffers from the large volume changes if fully sodiated during the

charge-discharge process with a resulting unstable SEI layer and the electrode pulverization (**Figure 2.11**e).[73] By sandwiching the black phosphorus layer between graphene layers, the obtained hybrid electrode materials can exhibit a high conductivity and stability with a reversible capacity close to 2500 mAh g^{-1}, but such kinds of nano-construction technologies still have a huge gap from large-scale applications at present.[73] Hence, efficiently combining sustainable carbons inspired by nature with alloying-type anode materials represents the more promising modification methods to enhance the electrochemical behaviours of alloying reactions in the near future.[24]

Conversion-type. Similar to the alloying-type anodes, conversion-type anode materials also store sodium ions based on the multi-electron reactions. Most conversion-type anode materials are transition metal-based compounds of MN_x (M = transition metal elements, N = non-metal elements like oxygen, sulphur, nitrogen, phosphorus, fluorine, *etc.*) (**Figure 2.12**a).[72] Based on the multiple electrons transferring with each transition metal ($MN_x + yNa^+ + ye^- \leftrightarrow M + xNa_{y/x}N$), the reduction of conversion-type materials happens to form the two-phase materials where converted transition metal nanoparticles embedded in a $Na_{y/x}N$ matrix.[72]

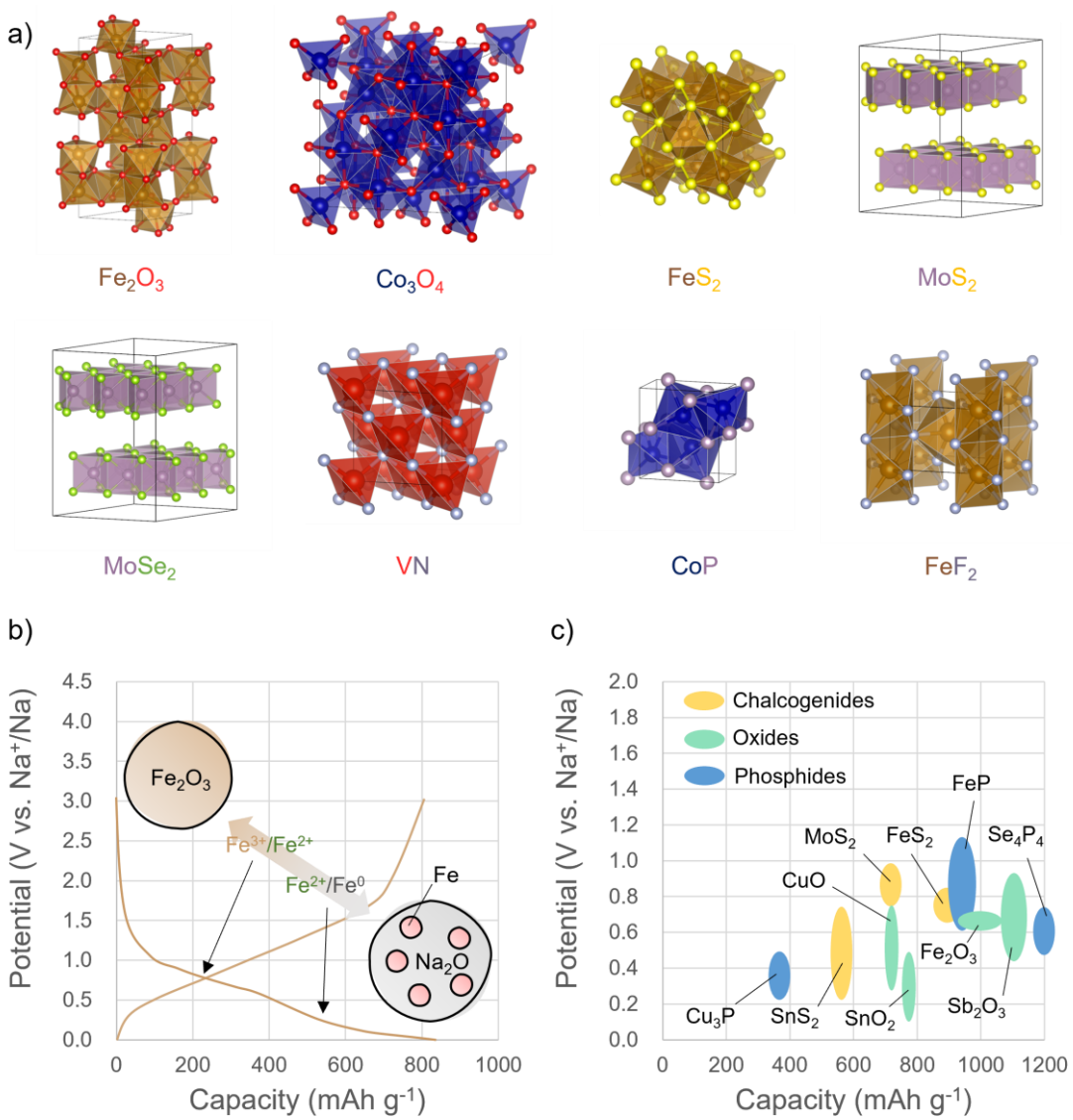


Figure 2.12. a) The crystal structures of typical conversion-type anode materials; b) The typical GCD curves of Fe_2O_3 anodes for sodium-ion storage with the schematic illustrations of the two-stage phase transformation based on the redox pairs of Fe^{3+}/Fe^{2+} and Fe^{2+}/Fe^{0} during the sodiation process; c) The summaries of reaction potentials and specific capacities of different conversion-type anodes.

Transition metal oxides represent the most classic conversion-type anode materials. Among various transition metals, earth-abundant iron is a promising active redox centre because of iron's variable valences. Therefore, the theoretical capacity of Fe_2O_3 anode materials is approaching 1000 mAh g^{-1} based on the redox pairs of Fe^{3+}/Fe^{0}.[85] According to the reported mechanism study, the sodiation of Fe_2O_3 anodes is a two-stage process with reduction of Fe^{3+} into Fe^{2+} to form $Na_xFe_2O_3$ intermediate phases at the potential of around 0.8 V vs. Na^+/Na, and then into Fe^0 to form Fe nanoparticles embedded in Na_2O matrix at the potential

of around 0.4 V vs. Na^+/Na (**Figure 2.12**b).[85] However, in practical applications, the reversibility of Fe_2O_3 anodes is limited by the low electrical conductivity, detrimental particle size and sluggish sodiation kinetics.[86] In addition to Fe_2O_3, other transition metal oxides like Fe_3O_4, Co_3O_4 and CuO suffer from similar challenges.[87] For example, even coupling with carbon nanomaterials, nanostructured electrode design or FEC additives, the reversible capacity of Co_3O_4 is still much lower than its theoretical capacity of 890 mAh g^{-1}.[88] With a large ionic radius of sodium ions, extracting sodium ions from the insulating Na_2O matrix is kinetically unfavourable and thus decrease the Coulombic efficiency of each sodiation and de-sodiation process of these transitional metal oxide anodes.[87] Therefore, transitional metal chalcogenides, especially sulphides, are considered to be the more promising anode materials than oxides on account of the higher conductivity of formed Na_2S and the weaker chemical bonding between transitional metal and sulphur.[89] Except for traditional transition metal chalcogenides such as cubic FeS_2, there are other types of transition metal chalcogenides with layered structures, including MoS_2, $MoSe_2$, WS_2 and VS_2.[90] The layers within this kind of chalcogenides interact with each other through the weak van der Waals force, enabling the better ion diffusion between layers.[90] Meanwhile, the sodium-ion storage mechanism of layered chalcogenides differs from FeS_2. Taking MoS_2 as an example, the Na_xMoS_2 phase ($x<2$) will be firstly formed by the intercalation of sodium ions into the layered structures at the potential above 0.4 V vs. Na^+/Na.[91] With the sodiation process continuing at the potential below 0.4 V vs. Na^+/Na, the Na_xMoS_2 phase is transformed into metallic Mo embedded in Na_2S.[91] When incorporated with conductive carbons, the nanostructured MoS_2 reported in the literature can deliver a specific capacity of 854 mAh g^{-1} (0.1 A g^{-1}).[92] Nevertheless, the formed intermediate products such as polysulphides are soluble in nonaqueous electrolytes, which means during the cycling, the reversibility and lifetime of anodes still encounter challenges.[92] Furthermore, transition metal nitrides, phosphides and fluorides such as VN, CoP and FeF_2 have also been explored as conversion-type anode materials.[87] Indeed, conversion-type anode materials can exhibit electrochemical activity to store sodium ions, but the fundamental understanding of the complexly formed intermediate phases during the discharge-charge process is still needed to guide the rational design of nanostructured electrodes with enhanced electrochemical performance. Additionally, from the reported cases, the importance of carbon materials can be

observed for conversion-type anodes to improve the electrical conductivity and stabilise the structural changes.[93]

If the transition metal elements in conversion-type oxides or sulphides are located in Groups IV and V that can further alloy with sodium ions, the conversion-alloying anode materials can be achieved including SnO_2, SnS_2, Sb_2O_3 and Sb_2S_3.[94] Due to the higher redox potentials, conversion reactions happen first during the sodiation process to obtain the transition metal nanoparticles.[95] At the lower potentials, sodium ions alloy with the reduced transition metals to deliver a higher sodium-ion capacity.[95] The formed Na_2O or Na_2S matrix can allocate the volume change derived from the alloying reaction as well as alleviate the agglomeration of anode materials upon cycling to some extent.[95] However, as a combination of previously mentioned alloying- and conversion-type anodes, the sluggish kinetics of these two reactions based on sodium ions still result in the limited rate performance of these conversion-alloying anode materials.[96] Carbon materials with good conductivity (10^6 -10^7 S m^{-1}) and mechanical properties (tensile strength:10 GPa) are suitable additives to accelerate and stabilise the electrochemical behaviour of both alloying and conversion reactions.[96] The summaries of reaction potentials and specific capacities of different conversion-type anodes are shown in **Figure 2.12**c.[97]

Metallic sodium. Compared to the above-mentioned anode materials, metallic sodium is actually the original and ultimate anode material for sodium-ion storage because of its high theoretical capacity of 1166 mAh g^{-1} and the lowest redox potential based on the redox pair of Na^+/Na.[53] At the very beginning of sodium battery development, metallic sodium was the initial choice of anodes, but the major problem of sodium metal anodes is the dendrite formation derived from the random nucleation and deposition processes of metallic sodium (**Figure 2.13**a).[13] The formation of sodium dendrites can lead to excessive inactive sodium upon cycling because of the continuous crack and reconstruction of the SEI layer under the large volume variation of metallic sodium, which decreases the reversibility of the sodiation and de-sodiation process (**Figure 2.13**b).[14] Furthermore, the lifetime of battery cells is restricted by the short-circuiting after the sodium dendrites penetrate the separator.[14] To avoid such challenging issues in efficiency and safety of metallic sodium, scientists abandoned metallic sodium and turned

to develop host materials to store sodium ions more stably based on the "rocking-chair" mechanism. However, with the development of battery technologies using the electrolyte engineering, interface engineering, solid-state electrolytes or versatile functional hosts, the aim to revive the metallic sodium anode for high-energy sodium batteries is attracting wide attention from the battery community again (**Figure 2.13**c).[13]

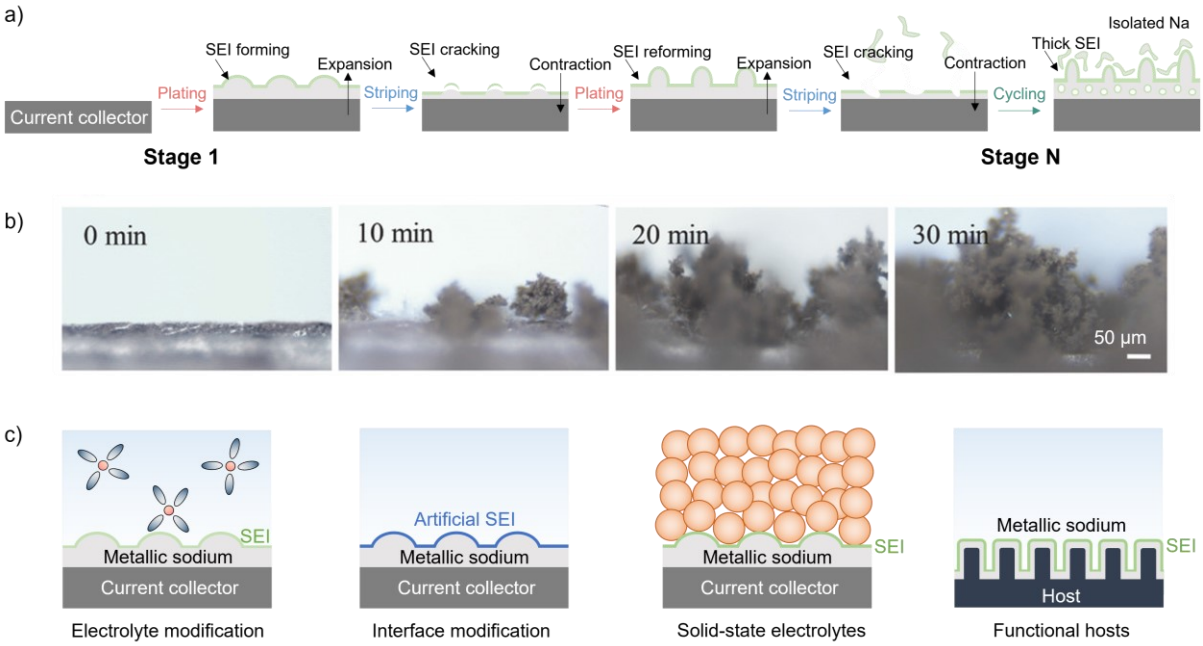


Figure 2.13. a) Schematic illustrations of the sodium plating and stripping processes upon cycling; b) Optical microscopy images of the sodium dendrite formation during the metallic sodium deposition in carbonate-based electrolytes (Reproduced with permission from [98], Copyright 2017, Wiley); c) Schematic illustrations of strategies to suppress the dendrite formation and stabilise the sodium metal anodes.

First of all, electrolyte modification has been widely used to improve the stability of metallic sodium anodes. Traditional carbonate-based electrolytes like 1 M $NaPF_6$ in the mixed solvent of ethylene carbonate (EC) and dimethyl carbonate (DMC) (1:1 in volume) during the reduction and decomposition will form the SEI layer composed of the mixture of organics such as sodium alkyl carbonates and inorganics including Na_2CO_3 and Na_2O.[99] This kind of SEI layer is brittle, fragile and inhomogeneous, which can cause the inhomogeneous ion flux and thus form the uncontrollable sodium dendrites during the continuous plating and stripping process.[99] Therefore, additives like fluorinated compounds have been used to increase the amount of sodium fluoride in the SEI layer and thus densify the SEI layer.[99] However, the most fluorinated additives such as hydrofluoric acid (HF) are toxic and harmful to human beings and

environments. Except for carbonate-based electrolytes, ether-based electrolytes are also the choice to stabilise sodium metal anodes, which is attributed to the formation of flexible organic-dominated SEI layers.[38] The limitations of ether-based electrolytes are still obvious because they are easier to be decomposed under the low anodic potentials (~4 V vs. Na^+/Na), thus decreasing the working voltage windows and safety of the full cells.[38] Another choice to suppress sodium dendrites is the utilisation of high-concentration electrolytes.[100] When the concentration of electrolytes is high enough to have limited free solvent molecules, sodium ions cannot be fully solvated by solvent molecules and thus become favourable for fast ion transfer,[101] which can increase the critical current needed for non-uniform metallic deposition. Nevertheless, the high cost of high-concentration electrolytes is not ideal for the commercialisation of sodium metal batteries.[102]

The interface modification like the artificial SEI layer can also be used to stabilise sodium metal anodes. The most classic protective and ionic conducting layer is the Al_2O_3 nanolayer coated by atomic-layer deposition (ALD), which not only mechanically alleviates the sodium dendrite formation but also delay the corrosion of sodium metal anodes both in air and in electrolytes.[103] The main disadvantage of advanced coating methods of thin films is their high expense at the industry level.[103]

Since solid-state electrolytes can physically suppress the sodium dendrite growth,[104] the development of solid-state electrolytes is also of great importance to obtain sufficient mechanical and electrochemical properties for sodium metal batteries. In addition, the interface between electrodes and electrolytes needs to be improved to decrease the polarisation within solid phases.[104] Solid-state electrolytes can be categorised into three main kinds including inorganic ceramics, organic polymers and inorganic-polymer composites.[105] In general, inorganic ceramics such as sodium-containing oxides, sulphides, nitrides and phosphates show suitable ionic conductivity (0.1 to 10 mS cm^{-1}) at room temperature and appropriate mechanical properties (Young's modulus: 10 to 200 GPa).[40] However, their poor adhesion with sodium metal anodes can increase the interface resistance and thus limit the fast-charge performance of sodium metal batteries.[40] In addition, oxides are usually obtained by high-temperature sintering based on energy consumptions, while the limited electrochemical stability window of sulphides usually induces the side reactions within sodium metal batteries.[40] In contrast, the

interface between solid polymer electrolytes and sodium metal anodes are more adhesive and compact, but their ionic conductivity (0.001-0.1 mS cm^{-2} at 25 ºC) and mechanical properties (Young's modulus: ~ 0.1 GPa) seem to be unsatisfactory.[106] Hence, the inorganic-organic composite electrolytes are an essential option for stable sodium metal anodes. For instance, a polymer/ceramic/polymer sandwich structure can be employed to solve the dilemma between mechanical/electrochemical properties and interface contact.[107] More efforts are still needed to further enhance the performance of solid-state electrolytes, thus achieving the high-energy solid-state sodium batteries with sodium metal anodes.

Last but not least, functional hosts for accommodating sodium metal anodes is one of the most promising methods for stable sodium metal batteries. An efficient host can induce the uniform metallic sodium deposition by regulating the homogeneous heat transferring and ion flux.[108] In addition, the volume changes can be accommodated in functional hosts by dividing dense sodium metal anodes into smaller sodium clusters.[109] Therefore, the sodium dendrites can be alleviated when the even metallic deposition process is controlled. Excellent sodiophilicity of the host materials with uniformly disturbed nucleation sites on the surface is essential.[110] Numerous substrates with three-dimensional structures have been employed to act as the function host for sodium metal anodes.[111] However, most commercial substrate materials like copper and aluminium lack good wettability with metallic sodium.[112] Therefore, surface functionalisation methods are usually used to modify those functional hosts, including the growth of ZnO nanorods on their surfaces which can increase the sodiophilicity and act as the nucleation sites of metallic sodium.[112] In this situation, versatile carbon materials with better sodiophilicity and natural nucleation sites like oxygen functional groups can be another good choice for functional hosts.[113] For example, the reduced graphene oxide can be used as the matrix to stabilise sodium metal anodes.[114] The obtained reduced graphene oxide/metallic sodium composite anodes can exhibit an improved lifetime and less polarisation.[114] The next step is to develop high-performance, low-cost and sustainable carbon hosts for sodium metal anodes, which is promising for the application of next-generation sodium metal batteries.[115]

To sum up, according to the critical insight into the fundamentals, status, promise of all types of anode materials, the utilisation of sustainable carbons inspired by nature is probed to be

indispensable to anode materials as not only the active material directly to store sodium ions but also the functional host or additive to stabilise other anode materials, which deserves more efforts from scientists in the near future.

2.1.2.2 Cathodes

In accordance with the literature analysis, the most promising cathode materials for sodium batteries can be respectively grouped into three main families which are layered oxides, polyanionic compounds and Prussian blue analogues.[116] Except for the three main families based on the intercalation/insertion mechanism, advanced sulphur or oxygen cathodes based on redox reactions of polysulfides or oxygen gas can be coupled with sodium metal anodes to achieve higher energy densities.[117, 118]

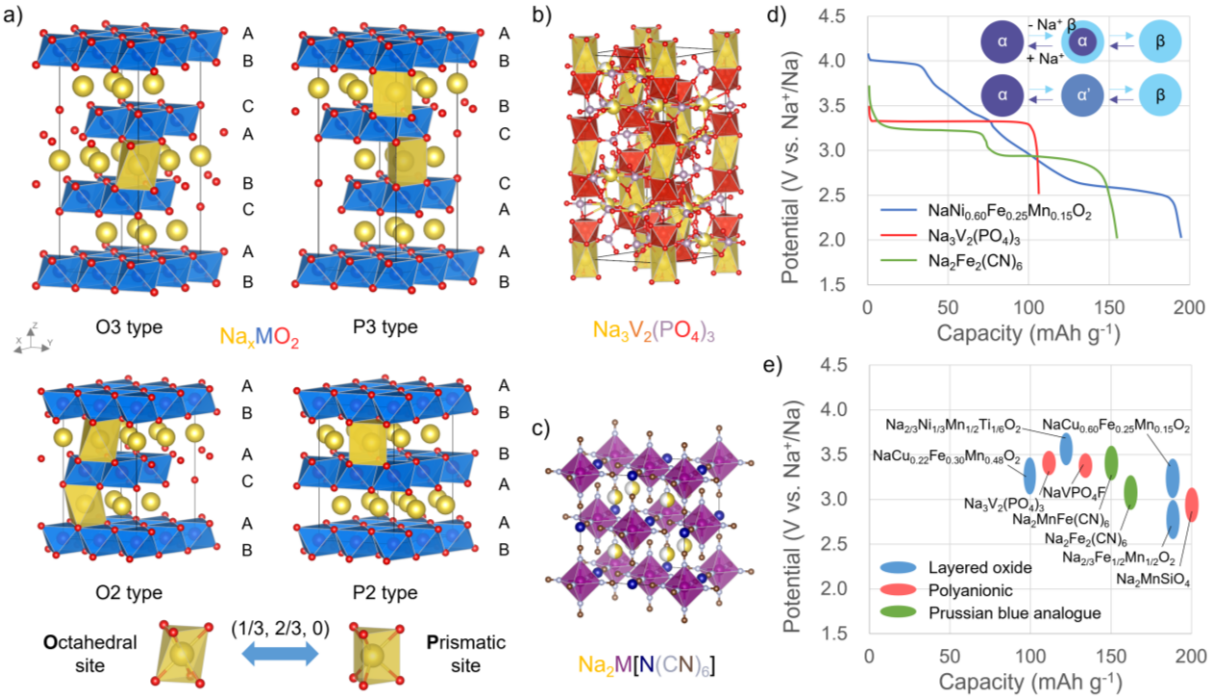


Figure 2.14. Typical crystal structures of a) layered oxides, b) polyanionic compounds and c) Prussian blue analogues; d) Typical discharge curves of layered oxides, polyanionic compounds and Prussian blue analogues with the schematic illustrations of single- and two-phase reactions; e) Comparison of average working potentials and capacities of different sodium cathode materials.

Layered oxides. The sodium-based layered oxides (Na_xMO_2) usually consist of one or more kinds of (transition) metals noted as M (*e.g.,* Fe, Mn, Ni, Ti, Co, Al, Cu, *etc.*).[119] According to the different coordinate types of sodium atoms, the layered oxides can be divided into

octahedral or prismatic types.[119] In addition, depending on how the stacking arrangement of layers repeats, the octahedral- or prismatic-type layered oxides can be further sorted into O2 (P2) or O3 (P3) types (**Figure 2.14**a).[119] The sodium atoms are stored between the metal oxide layers based on the redox pairs of metals. In a normal situation, layer oxides can have a specific capacity ranging from 100 to 200 mAh g^{-1}, with an average working potential between 2.5 and 3.5 V vs Na^+/Na (**Figure 2.14**d and e).[120] One of the challenges of layered oxides is the structural degradation during cycling, which can cause the loss of reversible capacity.[120] Hence, the introduction of other transition metals to reconstruct the crystal structure is meaningful. For instance, titanium (Ti) and nickel (Ni) were introduced into $Na_{0.9}Cu_{0.22}Fe_{0.30}Mn_{0.48}O_2$ to form $Na_{0.9}Cu_{0.12}Ni_{0.10}Fe_{0.30}Mn_{0.43}Ti_{0.05}O_2$,[121] thus manipulating the originally unfavourable phase transformation. On the other hand, although the existence of titanium (Ti) and nickel (Ni) components within the structure can increase the reversible capacity and working potential, titanium (Ti) and nickel (Ni) as critical elements in the battery industry usually challenges the overall cost and sustainability of cathodes materials for sodium batteries.[120] Therefore, the employment of earth-abundant elements like iron (Fe) and manganese (Mn) to fabricate the high-performance and low-cost cathode materials is also important for sodium batteries. For example, Yabuuchi *et al.*[122] prepared a P2-type $Na_{2/3}Fe_{1/2}Mn_{1/2}O_2$ without cobalt (Co) or nickel (Ni), thus achieving a specific capacity of 190 mAh g^{-1} and an average working potential of 2.75 V vs Na^+/Na. Moreover, the MO_6 octahedra composed of M-O bonds with covalent character exists in the layered oxides, where the changes of the valence of oxygen element (O) can happen based on the redox pairs of O^{2-}/O.[123] Such a kind of anionic redox behaviour in layered oxides at high potentials can enhance the sodium-ion storage capability and energy density.[124] Nevertheless, the oxidation of oxide ions, along with the release of O_2 on the surface, usually triggers the permanent structural reconstruction of layered oxides, inducing the irreversible loss of high-potential capacity.[125] Strategies to cage O_2 within the bulk phase of layered oxides for reversible redox reactions can avoid the structural instability.[125] House *et al.*[126] found that the ribbon-ordered superstructure in $Na_{0.6}[Li_{0.2}Mn_{0.8}]O_2$ can overcome the migration of transition metals and promote stable electron holes on O^{2-} to reduce the hysteresis during the first cycle. Besides, the electron and ion diffusivities are limited in layered oxides, so combined with carbon materials, the electrode architecture strategies like nanocarbon

material coating are often used to enhance the electrical and ionic conductivity, which can provide potential routes for high-energy cathodes.

Polyanionic compounds. Similar to layered metal oxides, polyanionic compounds are composed of the transition metal (*e.g.,* V, Mn, Fe, Co, *etc.*) with the anion (*e.g.,* PO_4^{3-}, $P_2O_7^{4-}$, SO_4^{2-}, SiO_4^{4-}, F^-, *etc.*) to store sodium ions through the redox reaction of the transition metal (**Figure 2.14**b).[127] Compared to layered metal oxides described above, polyanionic compounds usually possess higher redox potentials ranging from 3.0 to 4.0 V vs. Na^+/Na (**Figure 2.14**d), because the existence of anionic centres with increased electronegativities can de-localise the electron from the bonds between transition metal atoms and oxygen atoms to decrease the reactivity of transitional metals.[127] Such a kind of inductive effect of polyanionic compounds affects the redox potentials of transitional metals, which is beneficial to the increase in working voltages of full cells using polyanionic compound cathodes.[128] However, the molar mass of polyanions is usually higher than that of oxide ions when coupled with the similar number of transitional metal atoms, thus resulting in the decrease in the specific capacity of polyanionic compounds to around 100 mAh g^{-1} (**Figure 2.14**e).[128] Furthermore, unlike the layered oxides with the ordered layer structures which can facilitate the chemical diffusivity, the ion and electron diffusions within polyanionic compounds are further restricted by their intrinsic crystal structures to some extent.[127] Hence, there are two common strategies to enhance the chemical diffusivity of polyanionic compounds: one is the carbon coating of the particles, and the other is decreasing the particles of compounds to the sub-micrometre level.[129] Until now, NASICON-type $Na_3V_2(PO_4)_3$ has been considered to be the most classical polyanionic compound cathode for sodium batteries due to its satisfactory reaction kinetics, the acceptable capacity of around 110 mAh g^{-1} and the average working potential of around 3.4 V vs. Na^+/Na (**Figure 2.14**e).[130] Similar to the commercial $LiFePO_4$ cathode for lithium batteries, the desodiation and sodiation of $Na_3V_2(PO_4)_3$ cathode belong to the two-phase reaction with a plateau redox potential.[130] More efforts are still needed to further increase the capacity and rate performance of polyanionic compounds, such as developing the high-performance Na_2MnSiO_4 cathode with a specific capacity of around 200 mAh g^{-1}.[131]

Prussian blue analogues. Prussian blue (PB) and its analogues are a family of perovskite-type compounds mainly in the form of $Na_xM[N(CN)_6]\cdot nH_2O$, where M and M' are both transitional metals (*e.g.,* Fe, Co, Ni, Mn, Cu, Zn, *etc.*) (**Figure 2.14**c).[132] Through the two-electron redox reactions of transitional metals, Prussian blue analogues can achieve a high capacity of sodium-ion storage usually ranging from 150 to 200 mAh g^{-1} as per molecular unit can store two sodium ions during the potential range between 3.0 and 3.5 V vs. Na^+/Na (**Figure 2.14**d and e).[132] Meanwhile, their open-framework, cubic crystal structures can allow the more rapid sodium-ion insertion and extraction with the minimal structural change than conventional insertion-type layered metal oxides, thus ensuring their excellent rate and cycling performance.[133] Differing from the complex synthesis methods of layered metal oxides and polyanionic compounds involving the ball milling and high-temperature sintering, Prussian blue analogues can be synthesised and tuned using a convenient coprecipitation reaction of variable precursors in the aqueous system.[133] However, the coordinated water in the lattice of Prussian blue analogues highly retained from this facile synthesis method can decrease their electrochemical stability under high potentials and reduce their specific capacity, as the coordinated water not only diffuses to the organic electrolyte but also occupies the interstitial spaces of Prussian blue analogues.[134] Therefore, decreasing the coordinated or interstitial water content and increasing the crystal quality of Prussian blue analogues are very important but challenging for achieving outstanding electrochemical performance. The vacuum drying of as-prepared samples such as $Na_2MnFe(CN)_6$ at 100 °C for 30 h can eliminate the interstitial H_2O to some extent, which was found by Song *et al.*[135] Furthermore, making use of this feature of Prussian blue analogues, Jiang *et al.*[136] also employed them as the cathode materials for some aqueous batteries, which can avoid the drawbacks of coordinated water. Last but not least, Prussian blue analogues have the potential toxicities because of the possible cyanide releasing at high temperatures (> 200 °C) or under ultra-acidic conditions (pH < 1), which needs more assessments on this issue,[132] and yet sodium-ion battery companies such as CALT, Natron Energy and ALTRIS are working on this chemistry.

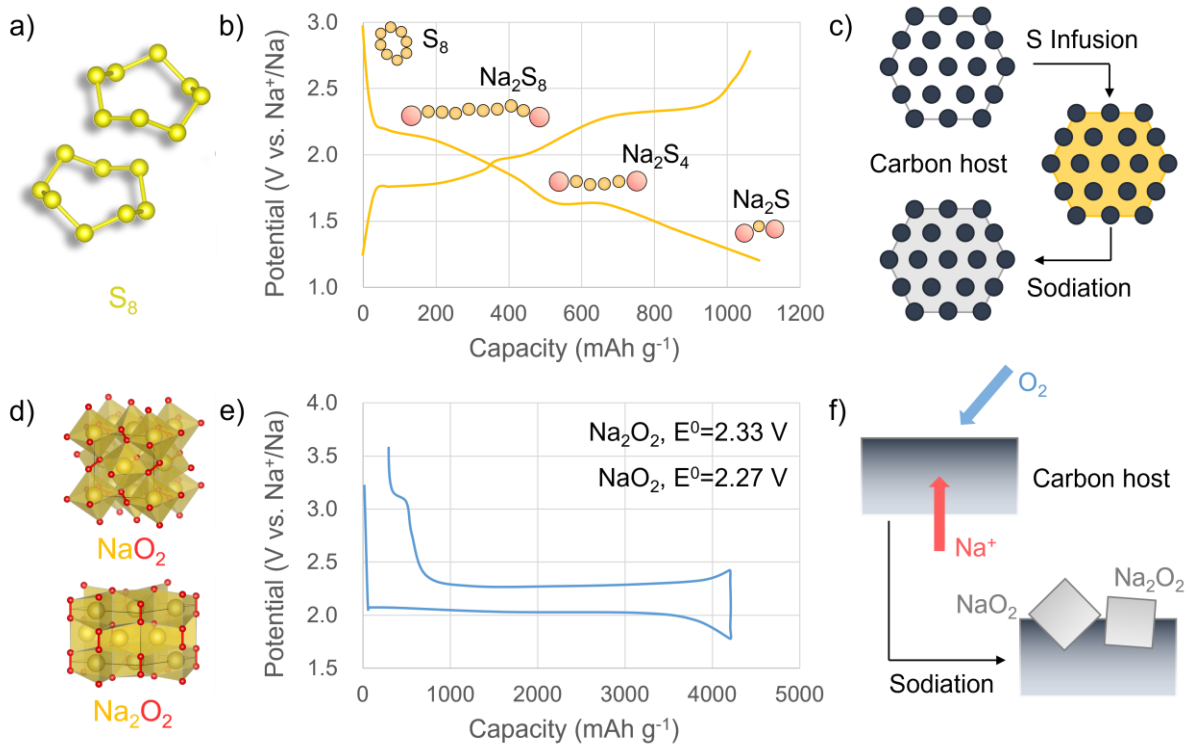


Figure 2.15. a) Structural illustration of sulphur; b) Typical discharge-charge curve of sulphur cathodes for sodium-ion storage; c) Schematic illustration of functional carbon hosts for the protection of sulphur cathodes; d) Crystal structures of NaO_2 and Na_2O_2; e) Typical discharge-charge curve of oxygen cathode for sodium-ion storage; f) Schematic illustration of functional carbon hosts for oxygen reduction and evolution reactions.

Sulphur and oxygen cathodes. As metallic sodium is considered to be the ultimate choice of the anode for sodium batteries, scientists are keen to develop suitable cathode materials that can couple with metallic sodium. In this situation, sulphur and oxygen can also be the ideal cathode choices.[137] First, when the abundant sulphur is applied as the cathode material (**Figure 2.15**a), the theoretical specific capacity can reach as high as 1675 mAh g^{-1}, and the energy density of obtained room-temperature sodium-sulphur (Na-S) batteries can be 1274 Wh kg^{-1} (**Figure 2.15**b).[138] Different from the previously discussed cathode materials, sulphur stores sodium ions based on the conversion mechanism with the formation of Na_2S_x rather than the intercalation/insertion mechanism.[139] However, since the active sulphur is non-conductive, it suffers from sluggish electrochemical reaction kinetics, and the large volume change of sulphur during the sodiation and de-sodiation process can cause severe collapsing of the cathode.[139] In addition, the high solubility of intermediate compounds, namely the sodium polysulphides such as Na_2S_8 and Na_2S_4, can diffuse to the anode side and react with metallic sodium to decrease

the reversibility of its sodium-ion storage capacity, which is called the "shuttle effect".[139] Compared with sulphur cathodes, oxygen cathodes are facing the similar situation. The theoretical energy densities of sodium-oxygen (Na-O_2) batteries can reach 1602 and 1105 Wh kg^{-1}, respectively, according to the formed Na_2O_2 and NaO_2 (**Figure 2.15**d and e).[118] Nevertheless, the slow kinetics of the redox reactions of oxygen including the oxygen reduction and evolution reactions (ORR and OER) can increase the overpotential and decrease the rate performance of sodium-oxygen batteries.[140] Also, oxygen cathodes have mass transport problems because the formed Na_2O_2 and NaO_2 will block the pathways for oxygen gas and electrolyte.[140] To solve these challenges of sulphur and oxygen cathodes, carbon materials have been widely used as versatile functional hosts for them because of their high conductivity, hierarchical pore structures and active sites possibly from embedded electrocatalysts.[141, 142] For sulphur cathodes, carbon functional hosts can restrict the volume change and avoid the "shuttle effect" of polysulphides to some extent (**Figure 2.15**c).[141] For oxygen cathode, carbon functional hosts can accommodate the formed oxides and ensure the pathway for continuous oxygen redox reactions (**Figure 2.15**f).[142] The high conductivity of carbon functional hosts and the embedded electrocatalysts can decrease the polarisation and provide active sites to reduce the energy barriers of electrochemical reactions.[142] The development of both sulphur and oxygen cathodes are in their infancy era, which means more efforts are needed to fabricate high-performance, low-cost and sustainable carbon functional hosts for them.

To sum up, since most cathode materials are non-conductive, the introduction of carbon materials as additives, coating layers or functional hosts is useful and essential for cathode materials. Hence, developing sustainable carbon materials inspired by nature shows great necessity not only for anode materials but also for cathode materials to achieve excellent electrochemical performance.

2.1.2.3 Electrolytes

The literature survey shows that research on electrolytes seems to be neglected currently for sodium batteries. In fact, the conversion of electrolytes from liquid to quasi solid and all solid states is of great necessity and challenge.

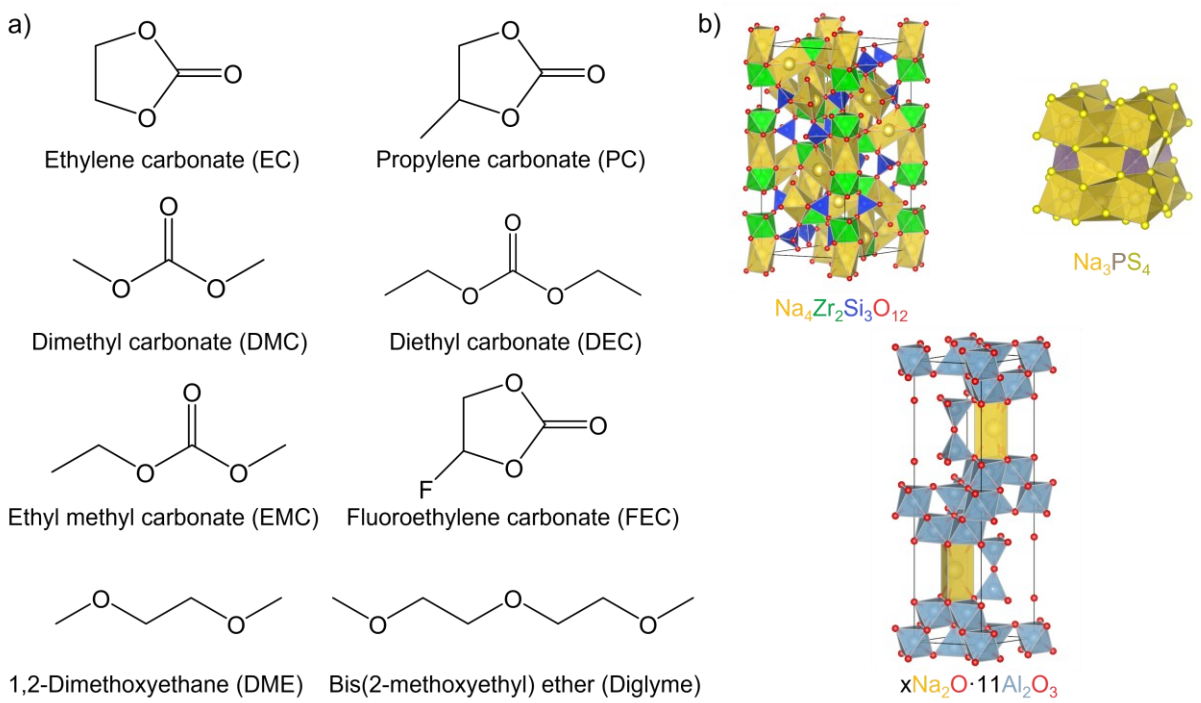


Figure 2.16. a) Molecular structures of solvents for liquid electrolytes; b) Crystal structures of inorganic ceramics for solid electrolytes.

Liquid electrolytes. For conventional sodium batteries, especially sodium-ion batteries, the most common choice of the electrolyte is 1 M sodium salts (*e.g.,* $NaPF_6$, $NaClO_4$, NaTFSI, $NaCF_3SO_3$, *etc.*) in carbonate-based nonaqueous solvents (*e.g.,* EC, PC, DMC, DEC, EMC or a mixture of these solvents, *etc.*) because of its excellent ionic conductivity (~1-10 mS cm^{-1}), suitable cost-effectiveness and outstanding electrochemical stability (up to around 4.5 V vs. Na^+/Na) (**Figure 2.16**a),[143] which is very similar to current commercial lithium-ion batteries based on host materials for lithium-ion storage. At the salt concentration of 1 M, the ionic conductivity often reaches its maximum value.[143] When the salt concentration decreases, the cost and viscosity of electrolytes can be reduced at the same time, but the ionic conductivity usually decreases as well.[144] In contrast, a higher salt concentration can reduce the free solvent molecules, which can broaden the electrochemical stability window.[145]

As mentioned above, the SEI formed during the reduction of carbonate-based electrolytes is composed of the brittle and fragile mixture of organics (*e.g.,* sodium alkyl carbonates, *etc.*) and inorganics (*e.g.,* Na_2CO_3, Na_2O, *etc.*) with heterogeneous ion conductivities, which may be not suitable for alloying anodes or sodium metal anodes. In this situation, fluorinated

additives (*e.g.,* HF, FEC, *etc.*) or glycol ether solvents (*e.g.,* DME, diglyme, *etc.*) can be employed to form dense and flexible SEI layers (**Figure 2.16**a).[99] According to the literature, the SEI layer in the presence of FEC turns into a multilayer structure rather than the mosaic model, in which the inner layer is the organic matrix, while the outside layer is sodium oxides.[146] In addition, the SEI layer derived from glycol ether solvents mainly consists of oligomers.[147] However, ether-based electrolytes have lower anodic decomposition potential and lower ionic conductivity than carbonate-based electrolytes when the salt concentration is similar.[147]

Compared to organic electrolytes with high flammability, aqueous electrolytes with a better safety are also attracting interest from scientists.[102] To overcome the limited electrochemical stability of aqueous electrolytes, one strategy is to develop electrode materials that can work within the redox potential range of aqueous electrolytes, and the other is the utilisation of "water-in-salt" electrolytes with an ultra-high salt concentration (usually around 20 M) which can diminish the free solvent molecules and thus avoid the decomposition of water.[101] Nevertheless, similar to the high-concentration organic electrolytes, the high cost of "water-in-salt" electrolytes, the high-quality requirement of salts and solvents as well as the salt precipitation problems are all challenging for scientists, which needs more efforts to develop low-cost, stable and high-performance aqueous batteries.[145]

Solid electrolytes. Differing from liquid electrolytes, solid-state electrolytes are also promising for achieving next-generation high-energy sodium batteries, especially sodium metal batteries.[148] Solid-state electrolytes can be composed of inorganic ceramics, organic polymers or inorganic-polymer composites, which have been discussed above. For more details, NASICONs, thiophosphates and their derivatives, and Na β-alumina are the most popular inorganic ceramics with suitable ionic conductivities for solid-state electrolytes (**Figure 2.16**b).[104] NASICONs means sodium superionic conductors with the structures of $Na_xA_2B_3O_{12}$ (A: Zr, Hf, Sc, *etc.*; B: Si, P, *etc.*) such as $Na_4Zr_2Si_3O_{12}$ and $Na_{3.4}Sc_{0.4}Zr_{1.6}Si_2PO_{12}$.[149] Moreover, thiophosphate and their relatives represent a series of compounds such as Na_3PS_4 and $Na_{11}Sn_2PS_{12}$.[150] Although the contained pnictogen elements can enhance the ionic conductivity of traditional oxides and sulphides, the electrochemical stability of solid electrolytes can be

reduced at the same time, especially against the sodium metal anode, thus leading to the decomposition of solid electrolytes and the growth of the SEI layer during the reduction process.[13] Therefore, Na β-alumina in the formula of $xNa_2O \cdot 11Al_2O_3$ can be employed as the trade-off with the balanced ionic conductivity and electrochemical stability.[151]

Compared with inorganic ceramics, organic polymers containing sodium salts can also serve as the solid electrolytes with the advantages of higher flexibility and better interface contact with electrodes, but as mentioned above, the ionic conductivity of polymer-based solid electrolytes is usually lower than that of inorganic ceramics.[152] Poly(ethylene oxide) (PEO) is the most conventional matrix choice of polymer-based solid electrolytes, and many other polymers like polycarbonates, polyamines, polynitriles and poly(vinylidene fluoride) (PVDF) have also been explored and used.[153-156] To improve the ionic conductivity of polymer-based solid electrolytes, several strategies such as increasing the operation temperature, adding a limited amount of liquid electrolyte to form a quasi-solid-state gel electrolyte or designing inorganic-polymer composite electrolytes have been widely studied.[106, 157]

Among all these solid electrolytes, inorganic-polymer composite electrolytes can combine the advantages of inorganic and organic solid electrolytes together and diminish their individual disadvantages, being considered the most promising approach to enable the sodium metal anode by avoiding the crack and suppressing dendrite formation.[158] The rational design and large-scale fabrication of solid electrolytes for sodium batteries remain to be investigated for the future industrialisation of solid-state sodium-based energy storage devices.

2.1.2.4 Electrode architecture and cell assembly

For practical applications, the modification of the electrode architecture and cell assembly should also be considered to ensure the electrochemical performance and minimise the cost of cells in tandem.

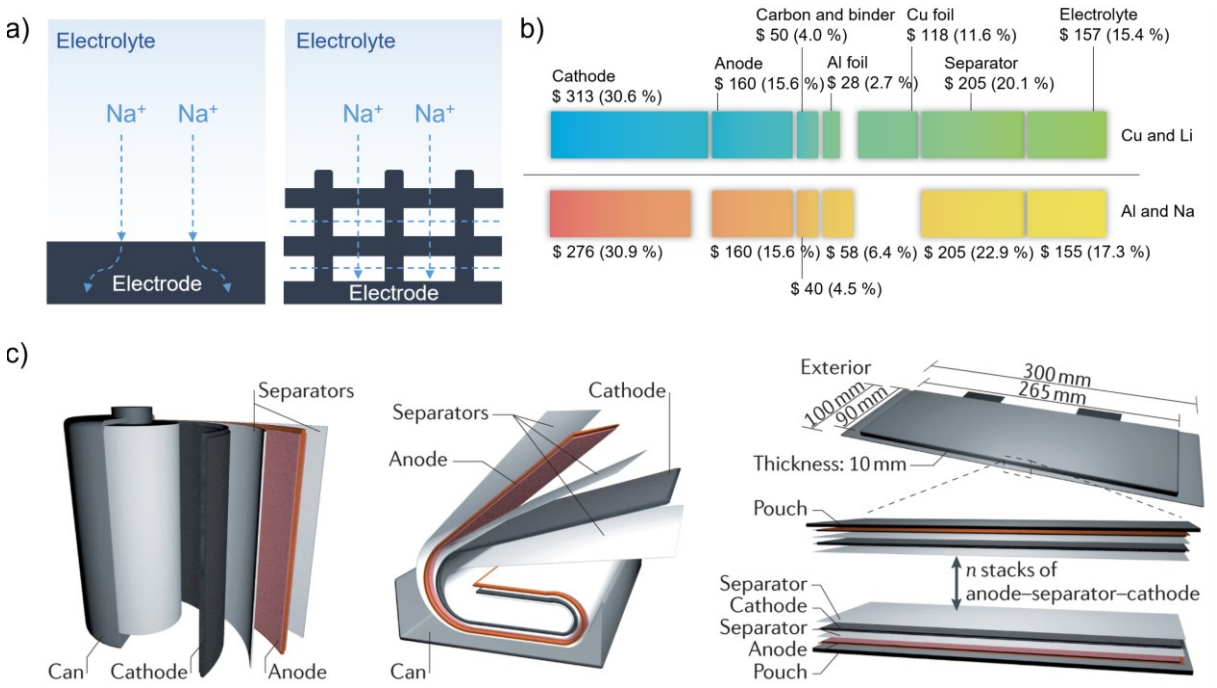


Figure 2.17. a) The comparison between traditional electrode architectures and novel three-dimensional electrode architectures with optimised structures; b) The cost comparison between the commercial lithium-ion battery cell and the future sodium-ion battery cell; c) Schematic illustrations of cylindrical, prismatic and pouch cells (Reproduced with permission from [159], Copyright 2016, Springer Nature).

For most insertion/intercalation-type electrodes, the limited diffusivity of sodium ions is a more crucial factor than the volume changes for large-scale electrodes. Except for improving the inherent sodium-ion diffusivity of materials, the ideal solution in the battery industry is the modification of particle sizes and morphologies of active materials, thus tuning the phase scales of electrodes where sodium ions diffuse and transfer (**Figure 2.17**a).[160] Although the decrease in the length scales can enhance the diffusivity of sodium ions, too small particle sizes of active materials would increase the fabrication costs of electrodes and the requirements of electrode manufacturing techniques.[161] Hence, in future commercial electrodes, more studies on how to optimise the electrode architecture and make a balance between electrochemical performance and cost are needed. Meanwhile, more efforts to develop high-performance, low-cost and sustainable carbon hosts with three-dimensional structures is essential for the architecture of other types of electrodes to solve their problems such as the restricted diffusivity of sodium ions and the uncontrollable volume expansion of active materials (**Figure 2.17**a).[108, 162]

Compared to the commercial lithium-ion batteries based on lithium resources and Cu foil

as the anode current collector, the future sodium-ion battery cell based on the cheaper sodium resource and Al current collectors has the potential to achieve a lower estimated cost.[26] The specific comparison of two kinds of batteries is listed in **Figure 2.17**b, in which we can see the differences in their costs are mainly derived from the cathode and current collector used.[26] The current battery industry adopts three cell types which are cylindrical, prismatic and pouch cells to fulfil the different requirements in various practical applications (**Figure 2.17**c).[159] For other kinds of sodium batteries including sodium metal batteries, more evaluations of their costs are also favoured to assess their possibilities in commercialisation and practical applications, but differing from sodium-ion batteries, their most important aim at the current stage is the systematic development of high-performance and low-cost electrode materials and electrolyte systems.

2.1.3 Sodium capacitors

According to the visualised statistics of keywords in publications related to sodium capacitors (**Figure 2.18**), the electrochemical performance still plays a core role. Meanwhile, various carbon materials exhibit their importance in the research on sodium capacitors because of their dominant frequency of appearance and latest average publication year. The studies on sodium capacitors rise in early 2012 and remain in their infancy stage compared to sodium batteries.[12]

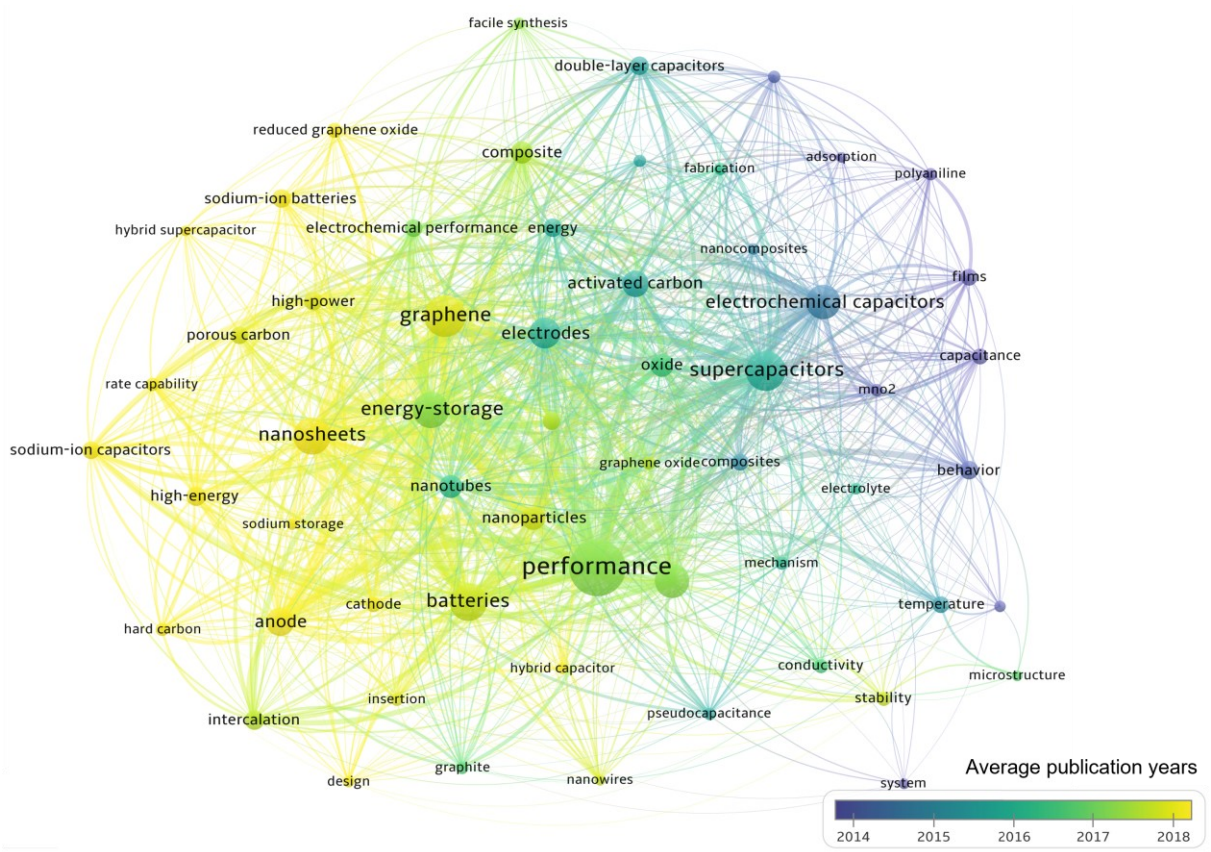


Figure 2.18. The visualised statistics of keywords in publications related to sodium capacitors, where the colour represents the average publication year, the size indicates the reported frequency in the literature.

The main difference between sodium capacitors and sodium batteries is the cathode part. In a sodium capacitor, the cathode stores anions mainly through the physical accumulation of anions on the surface of the cathode, which is a non-Faradic process.[163] Porous carbon materials, therefore, become the essential candidate for the cathode. However, most commercial porous carbon materials are derived from non-renewable fossil fuel-based resources or belong to expensive carbon nanomaterials such as graphene and carbon nanotubes, which do not fit the sustainable standard of sodium-based energy storage devices.[164] At the same time, the micropore structure of commercial porous carbon materials usually limit the electrochemical performance of sodium capacitors.[165] Hence, the rational design of porous carbon materials from renewable precursors is needed for producing high-performance and low-cost sodium capacitors. In this section, I focus on analysing the research progress of carbonaceous materials for sodium capacitors to conclude the design strategies of electrodes and cell assembly principles of sodium capacitors.

2.1.3.1 Electrodes

The anodes of sodium capacitors are similar to those of sodium batteries because the sodium capacitor actually belongs to a hybrid device with an asymmetric configuration, and its anode should be the battery-type anode that can store sodium ions based on the Faradic process.[12] Therefore, for the detailed discussion on the battery-type anode for sodium-ion storage, please refer to the previous section. Here, I only emphasise the discussion on the cathode part of sodium capacitors based on a capacitive or pseudocapacitive storage mechanism.

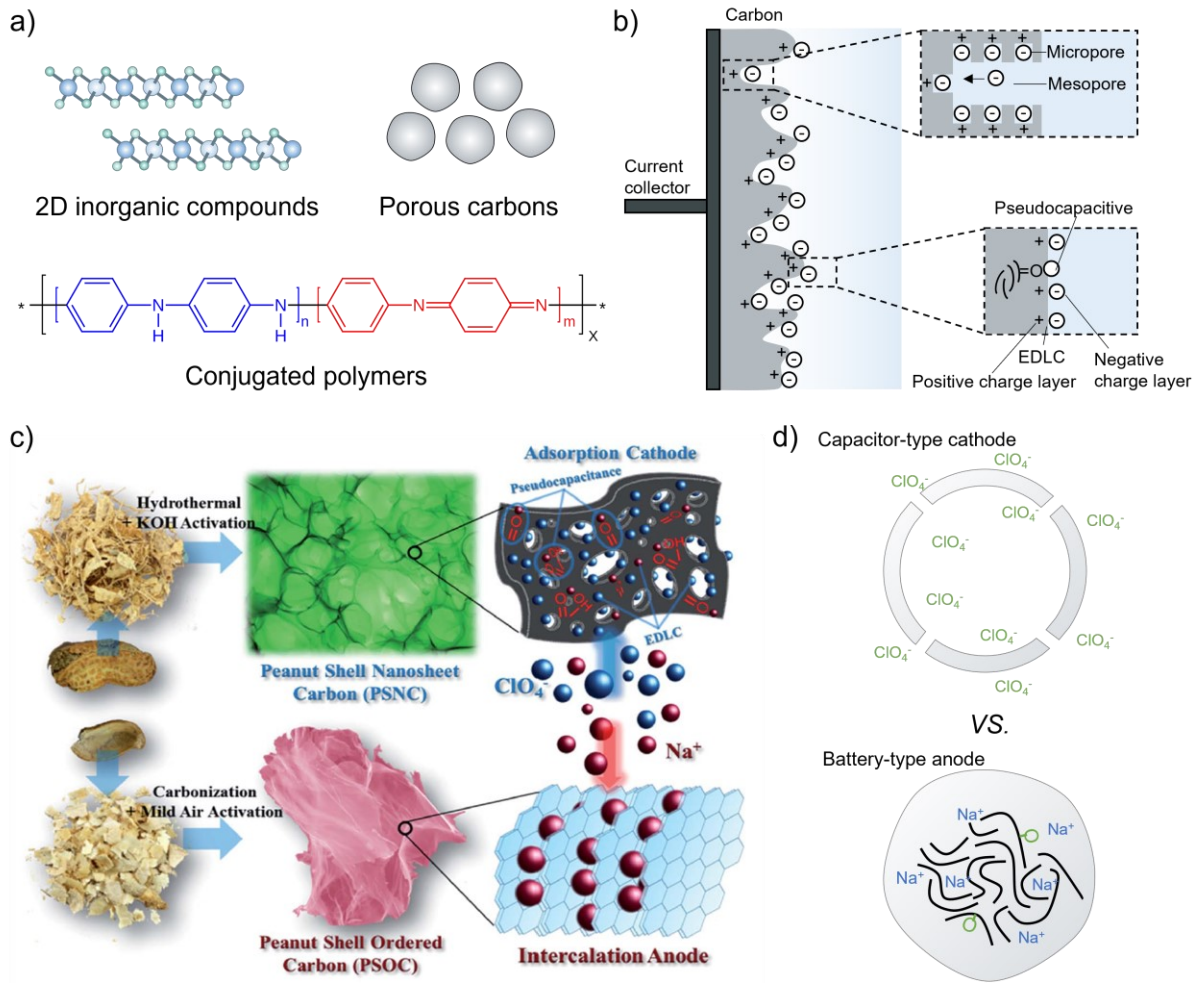


Figure 2.19. a) Schematic diagrams of active materials for cathodes of sodium capacitors; b) Schematic illustration of porous carbon materials as the cathode to store anions through different mechanisms at various active sites; c) Material synthesis process employed for each electrode in sodium capacitors (Reproduced with permission from [166], Copyright 2015, Royal Society of Chemistry); d) Comparison of the relevant cathode/anode charge storage mechanisms in sodium capacitors.

Among various active materials for capacitors including carbonaceous materials, two-

dimensional inorganic compounds and conjugated polymers, porous carbon materials are the most popular choice for the cathode of sodium capacitors (**Figure 2.19**a).[167, 168] Porous carbon materials mainly store the anions through the electrochemical double-layer capacitive (EDLC) mechanism (**Figure 2.19**b),[163] where the anions are moved to the cathode under the electrical field and adsorbed on the surface of carbon materials to form the first charge layer. Meanwhile, the negative surface charge on the surface can attract the positive charge to form the second charge layer underneath the surface, thus becoming the electrical double layers. With no ions across the interface between the two charge layers, EDLC reactions belong to the non-Faradic process.[163] Sometimes, the functional groups on the surface of carbon materials can interact with anions, which is called pseudocapacitive reactions (**Figure 2.19**b).[27] Because the negative ions across the interface between the two charge layers and then combine with positive charges, pseudocapacitive reactions belong to the Faradic process.[27] However, as EDLC and pseudocapacitive reactions occur on the surface or near-surface of carbon materials, they are both surface-controlled reactions with fast kinetics.[169]

Research on sodium capacitors commenced in 2010s when Kuratani K. et al.[170] assembled a sodium capacitor by combining sodium pre-doped hard carbons as the negative electrode and activated carbons as the positive electrode. The working potential window (from 0 to 3.5 V) of the device reported was significantly higher than that of the conventional electrochemical capacitors. Based on the chemical activation or physical activation, activated carbons with porous structures can be achieved. For typically activated carbons, they usually possess a high surface area of around 1000 $m^2 g^{-1}$ with a high degree of microporosity (< 2 nm).[171] Meanwhile, due to the high electrical conductivity and the stable physicochemical properties of typically activated carbons, they are suitable to physically accumulate the active ions on their surface with an excellent stability and reversibility in aqueous electrolytes.[171] However, for sodium capacitors, nonaqueous electrolytes with a higher viscosity and a lower ionic conductivity decrease the electrochemical performance, especially the rate performance, of traditional activated carbons with only micropores. Furthermore, the ionic radius of anions employed in nonaqueous electrolytes such as PF_6^- and ClO_4^- is larger than that of salts in aqueous electrolytes such as OH^- and Cl^-, which further decrease the kinetics of reactions at the cathode part.[172] The high working potential of the cathode part also challenges the stability of traditional

activated carbons. Therefore, the development of porous carbons with hierarchical pore structures (*i.e.,* micropores (< 2 nm) and mesopores (2 – 50 nm)), compact particle configurations and ultralong stability is needed for producing high-performance cathodes.[173] Moreover, most traditional activated carbons are derived from non-renewable fossil fuels, and most high-performance carbon nanomaterials like carbon nanotubes and graphene are expensive.[174] Through "green" activation methods, sustainable porous carbon materials derived from renewable resources can be a promising candidate for the cathode part.[174] For instance, Mitlin D. et al.[166] assembled a peanut shell prepared hierarchical porous carbons for cathodes and ordered non-porous carbons for anodes (**Figure 2.19**c). The outer rough shell was converted into carbon cathodes with hierarchical pore structure *via* KOH-activation method at 800-850 ℃ in argon atmosphere, while the inner shell was chosen to be carbonised directly into carbon anodes at 1200 ℃. The carbon cathodes were tested in a half cell configuration against metallic sodium and delivered a capacitance of 213 F g^{-1} at 0.1 A g^{-1}, while the carbon anodes exhibit a reversible capacity of 315 mAh g^{-1} at 0.1 A g^{-1}. The acquired sodium-ion capacitors with the all-carbon-based asymmetric configuration showed the integrated high energy and high power densities (201 W h kg^{-1} at 285 W kg^{-1}, 50 W h kg^{-1} at an ultrahigh power density of 16,500 W kg^{-1}), as well as good long-term cycling stability (72% of the capacitance retention after 10,000 cycles at the current density of 6.4 A g^{-1}). Although much progress has been achieved in developing nanostructured materials for sodium capacitors, the imbalance of the power capability between anodes and cathodes still inhibits the full energy utilisation of anodes, which results from the difference in kinetics that a non-Faradaic adsorption reaction is faster than a Faradaic insertion process (**Figure 2.19**d). Consequently, more efforts are required to design anodes with higher power and cathodes with higher energy using suitable materials.

2.1.3.2 Electrolytes

Sodium capacitors usually employ a similar electrolyte system with sodium batteries, including the liquid electrolytes, gel electrolytes and solid-state electrolytes. Please refer to the detailed discussion on electrolytes in the section of sodium batteries.

2.2 Summary and perspective

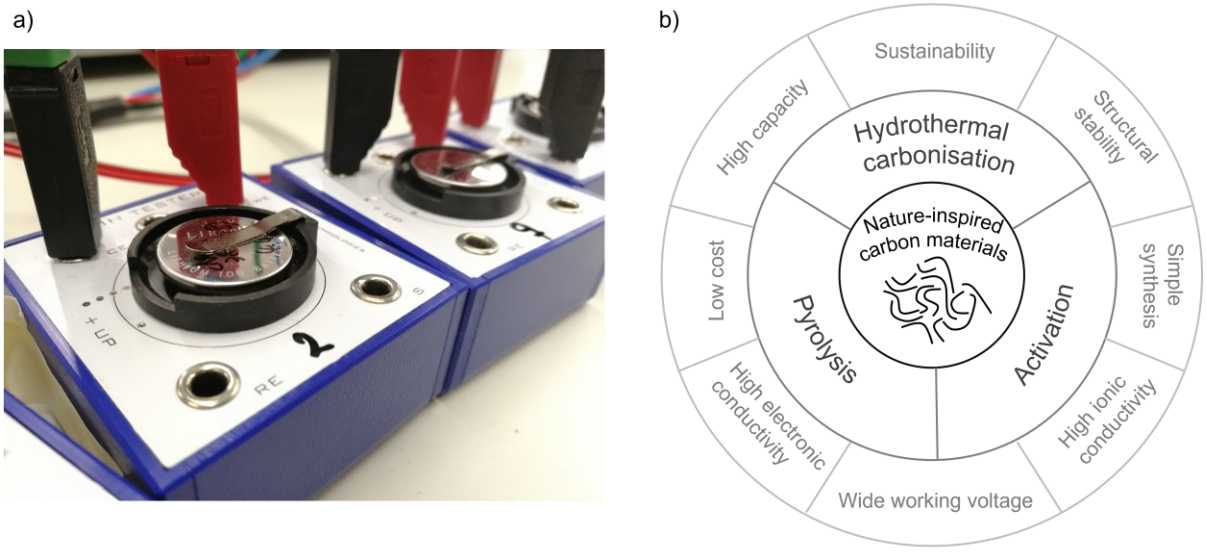


Figure 2.20. a) Photographs of sodium-based energy storage devices in the coin cells; b) Summary of fabrication processes and advantages of nature-inspired carbon materials.

Due to the limited resource and restricted geographical distribution of lithium, the development of post-lithium technologies is highly necessary at the current stage. Sodium-based energy storage technologies including sodium batteries and sodium capacitors can fulfil the various requirements of different applications such as large-scale energy storage or low-speed/short-distance electrical vehicle.[16] Most knowledge and technical chains of current lithium batteries can be easily transferred to the fabrication of sodium-based energy storage technologies (**Figure 2.20**a). Moreover, based on the abundant resource of sodium and the utilisation of cheaper Al current collectors, the cost of sodium-based energy storage technologies can be further decreased. Meanwhile, sodium-based energy storage technologies are more appropriate for the applications in extremely cold environments due to their better capacity retention under a low temperature.[23] However, compared to lithium batteries, the main challenge of sodium-based energy storage technologies is related to their electrochemical performance, especially the energy density, limited by the natural properties of sodium.

As mentioned above, sustainable carbon materials inspired by nature play a tremendously important role in benefiting the development of sodium-based energy storage technologies by serving as active materials, additives or functional hosts because of their low cost, structural stability, high conductivity and outstanding electrochemical performance (**Figure 2.20**b).

Nevertheless, the fabrication process of carbon materials is often linked with high-temperature carbonisation which consumes a large amount of energy with increased carbon emissions.[175] Hence, to truly achieve the sustainability of nature-inspired carbon materials and sodium-based energy storage technologies, the "greener" fabrication processes including hydrothermal carbonisation, pyrolysis and activation are required with decreased carbon emissions and enhanced electrochemical performance. In this thesis, I aim to simultaneously realise the high electrochemical performance of nature-inspired carbon materials and their sustainability for the advancement of novel sodium-based energy storage technologies.

Chapter 3. Materials and methodologies

3.1 Materials

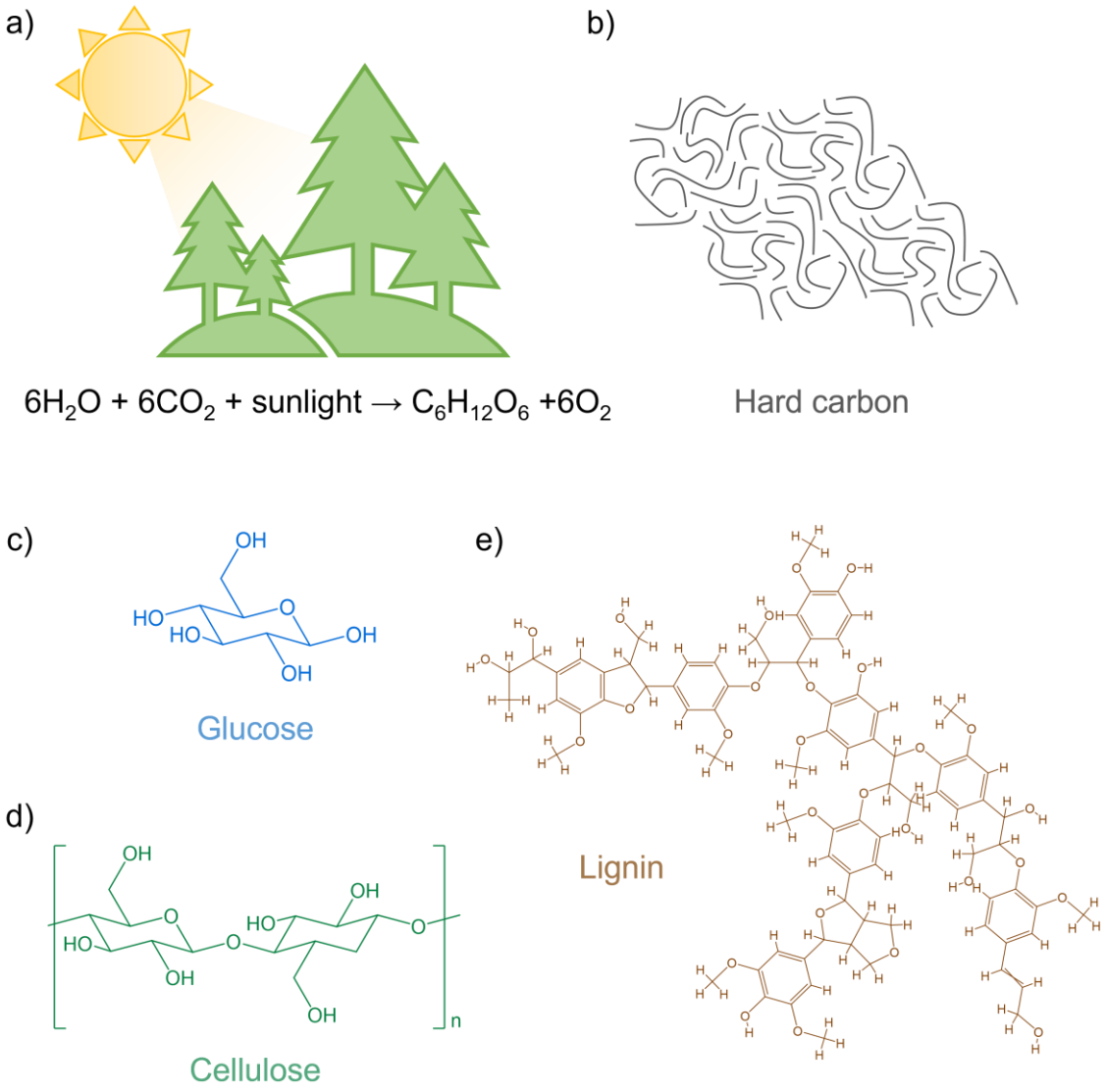


Figure 3.1. a) Schematic diagram of biomass with the photosynthesis process; b) Schematic diagram of the structure of hard carbons; Chemical structure depictions of c) glucose, d) cellulose and e) lignin.

Biomass.[176] As a kind of renewable material derived from plants, biomass is considered as the fourth-generation energy system. Biomass stores chemical energy from the sun through the photosynthesis (**Figure 3.1**a). To avoid carbon emission from the use of non-renewable fossil fuels, biomass fuels can be directly converted into liquid or gas fuels for the power generation. In addition, biomass is an ideal precursor for sustainable hard carbon materials. For instance,

the hierarchical building units of natural woods including glucose, cellulose and lignin can all serve as renewable biomass feedstocks for sustainable hard carbon materials.

Hard carbons.[54] As mentioned above, hard carbons belong to a kind of solid form of carbon materials that cannot be graphitised even at 3000 ºC. Hard carbons usually exhibit long-range amorphous structures and short-range crystalline nanodomains because of the turbostratic stacking of curved graphene layers with enlarged interlayer spacing (**Figure 3.1**b). As the most promising material for sodium-based energy storage technologies, hard carbons can be prepared and tuned using various methods including hydrothermal carbonisation, high-temperature carbonisation, activation and surface modification.[18]

Glucose.[19] As the most abundant monosaccharide on Earth, glucose can be used a kind of renewable precursor for hard carbons. In nature, D-glucose can be produced by plants through the photosynthesis process. The molecular formula of D-glucose is $C_6H_{12}O_6$, which is the repeating unit of cellulose (**Figure 3.1**c).

Cellulose.[177] Cellulose belongs to a kind of polysaccharide with the molecular formula of $(C_6H_{10}O_5)_n$ (**Figure 3.1**d). Therefore, cellulose, as an organic polymer with repeated units, contains both amorphous and crystalline regions. In addition, around 36 cellulose molecular chains form the elementary nanofibrils and then gather together to become cellulose microfibrils. In nature, the cell wall of plants is mainly composed of cellulose. As the most abundant organic polymer on Earth, cellulose can be used as the renewable precursor for hard carbons as well.

Lignin.[178] Except for cellulose and hemicellulose, lignin is another main component in the cell wall of plants. It belongs to a kind of complex organic polymer crossed-linked by phenolic units (**Figure 3.1**e). In the paper industry, since cellulose is extracted from plants as the main source of papers, lignin can be obtained as the by-product at the same time. Lignin is also considered to be the renewable precursor for hard carbons.

3.2 Methodologies

In this section, the methodologies are introduced (**Figure 3.2**).

3.2.1 Synthesis

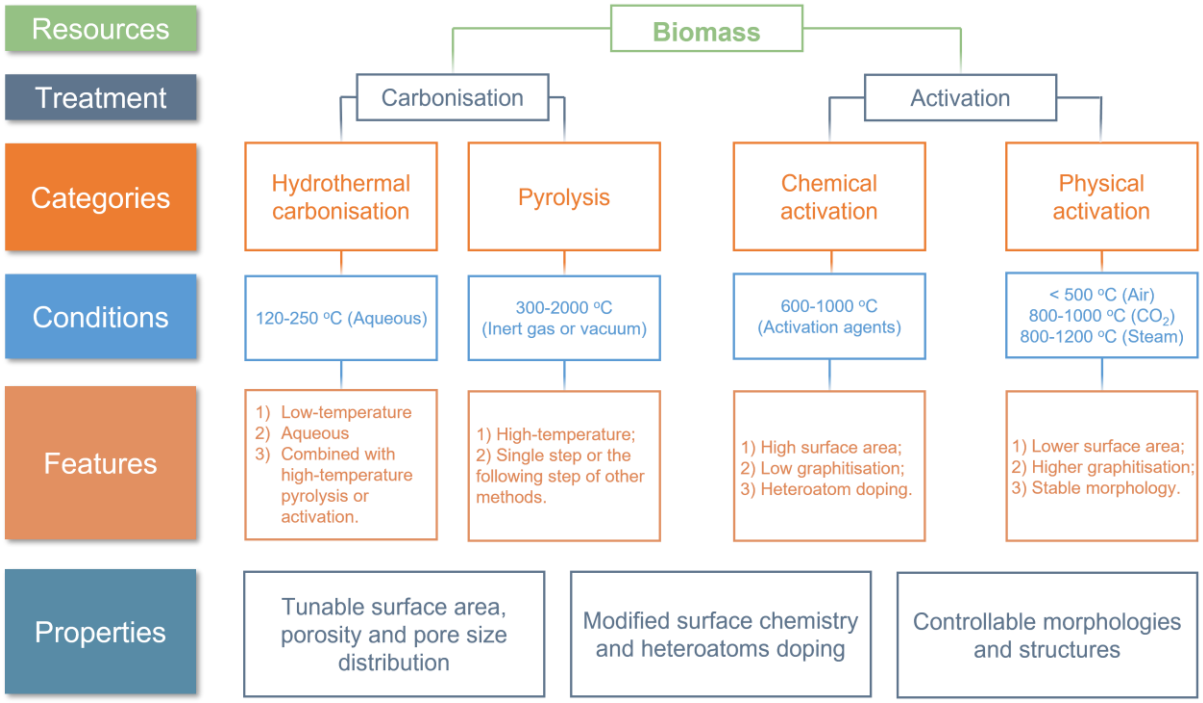


Figure 3.2. Schematic summary of various synthesis methods of sustainable carbon materials.

Hydrothermal carbonisation.[179] Hydrothermal carbonisation is a kind of pre-treatment of biomass feedstocks. It usually happens in the aqueous system at a low temperature of around 200 °C. During the hydrothermal process, biomass gradually dehydrates and then forms carbons in the aqueous phase. The hydrothermal process can stabilise the morphology, increase the carbon yield and enrich the surface functional groups of resulting sustainable carbon materials.

Pyrolysis.[18] Pyrolysis or high-temperature carbonisation usually happens in the inert atmosphere at a relatively higher temperature of around 1000 °C. During the high-temperature carbonisation process, biomass gradually dehydrates and then sinters with the reorganisation of molecular structures. The high-temperature carbonisation process can stabilise the structure and morphology of resulting sustainable carbon materials, while increasing their conductivity with the decrease in their surface functional groups.

Activation.[18] Activation is a method to introduce porosity into carbon materials. For chemical activation, the activation agents such as KOH, NaOH, $ZnCl_2$ and H_3PO_4 are needed to react with the molecules of biomass, thus decomposing their structures and creating porosity. Chemical activation is usually employed using an inert gas flow at around 800 ºC to avoid excessive oxidation of materials. However, for physical activation, it is usually utilised as a post-treatment method within an active gas atmosphere at around 1000 ºC. During the physical activation, the active gas can react with the surface of carbon materials and thus form pores on their surface without destroying their bulk structures and morphologies, which is milder than chemical activation.

Preparation of hard carbon anodes with or without the hydrothermal process.[60] In Chapter 4, for the hydrothermal process, the precursor solution in a Teflon liner was prepared through dissolving glucose (D-(+)-glucose, ≥99.5%, Sigma-Aldrich) in deionized (DI) water with the weight ratio of 10:90 under the continuous magnetic stirring. Afterwards, the liner was sealed using a stainless-steel jacket to become the autoclave reactor, followed by the steady heating of the rector at 200 ºC for 12 h. Subsequently, the sediment at the bottom was separated from the upper supernatant and washed with DI water. The obtained solid phase called biochar was then fully dried in the oven at 80 ºC overnight (**Figure 3.3**a). The biochar was further carbonised in the Carbolite STF furnace at different temperatures including 1000, 1300 and 1500 ºC for 2 h with a heating rate of 5 ºC min^{-1} under an N_2 atmosphere. The yielded hard carbons were named HG1000, HG1300 and HG1500, respectively (**Figure 3.3**b).

In comparison to the HG series, the direct carbonisation of glucose at different temperatures including 1000, 1300 and 1500 ºC was conducted in the same Carbolite STF furnace for 2 h with a heating rate of 5 ºC min^{-1} under an N_2 atmosphere. The resulting hard carbons were noted as DG1000, DG1300 and DG1500, respectively (**Figure 3.3**c)

The obtained hard carbon powers were ground using the mortar and pestle to homogenise the particle size. After that, the hard carbon (*i.e.,* active material) was mixed with the sodium alginate (*i.e.,* binder) in a mass ratio of 90:10 using the mortar and pestle for 30 min, followed by the introduction of a suitable amount of DI water to prepare an aqueous slurry. The hard

carbon electrodes were prepared by coating the mixed slurry onto Al foil (MTI Corporation). Before being cut into pieces for the further assembly of coin cells, the coated Al foil was dried at the room temperature and then dried at 80 °C in a vacuum oven overnight. The loading mass of electrodes was controlled within the range of 1.5-2.0 mg cm^{-2}.

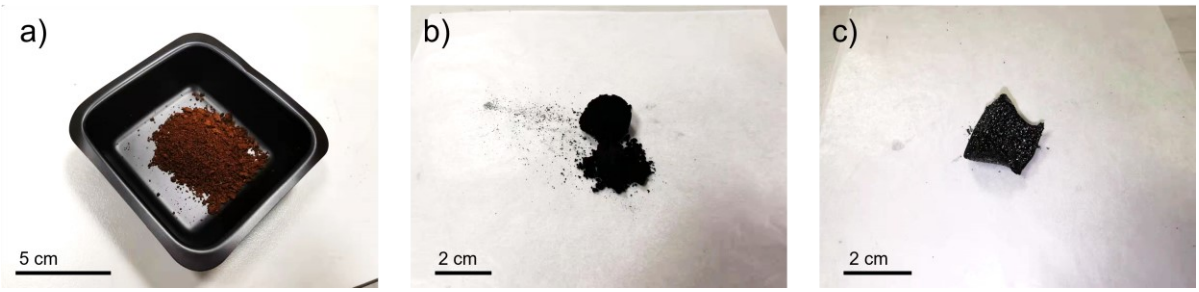


Figure 3.3. The photograph of a) biochar from the hydrothermal process of biomass, b) HG1300, and c) DG1300.

Preparation of $Na_3V_2(PO_4)_3$ (NVP) cathodes. In Chapter 4, the cathode slurry was prepared by mixing commercial NVP powders (MTI Corporation), acetylene black (Sigma-Aldrich), and polyvinylidene difluoride (PVDF, Sigma-Aldrich) in a mass ratio of 60:20:20 within a suitable amount of 1-Methyl-2-pyrrolidinone (NMP, Sigma-Aldrich) solvent under continuous magnetic stirring. Afterwards, the cathode slurry was coated onto Al substrates using a doctor blade (MTI Corporation), followed by the drying at 50 °C in an ambient oven and then at 80 °C in a vacuum oven overnight. Hence, a free-standing and flexible NVP cathode film can be torn from the Al substrate and then cut into the same size as the anode. The mass of each piece of the cathode was tuned to match with the mass of the corresponding anode.

Preparation of cellulose nanocrystals (NC). In Chapter 5, 10 g Cellulose-rich fibres were obtained through the mechanical fibrillation of filter papers (Whatman, WHA10010155) in a biomass grinder, followed by the hydrolysis of filter paper using 87.5 mL home-made 64 % (concentration) sulfuric acid (diluted from 98% sulfuric acid (Sigma-Aldrich)) at 45 °C in a water bath for 50 min. After that, 10-fold deionized (DI) water (around 900 mL) was added to the light-yellow suspension to terminate the reaction. Once staying still at ambient conditions overnight, the supernatant was removed, and then the remaining suspension was centrifuged at 12,000 rpm for 15 min. After the centrifugation, the clear top layer was removed, followed by

the washing of sediments with DI water (*i.e.,* remove the top layer and wash the bottom solids). The centrifugation and washing were repeated until no obvious precipitate appeared after the centrifugation. The aqueous suspensions were then dialyzed against DI water for at least 4 days using dialysis membranes (Spectrum, 12,000-14,000 molecular weight cut-off) until the pH value of the outside water close to 7. **Figures 3.4**a and b exhibit the photography of NC suspensions and the TEM image of NCs.

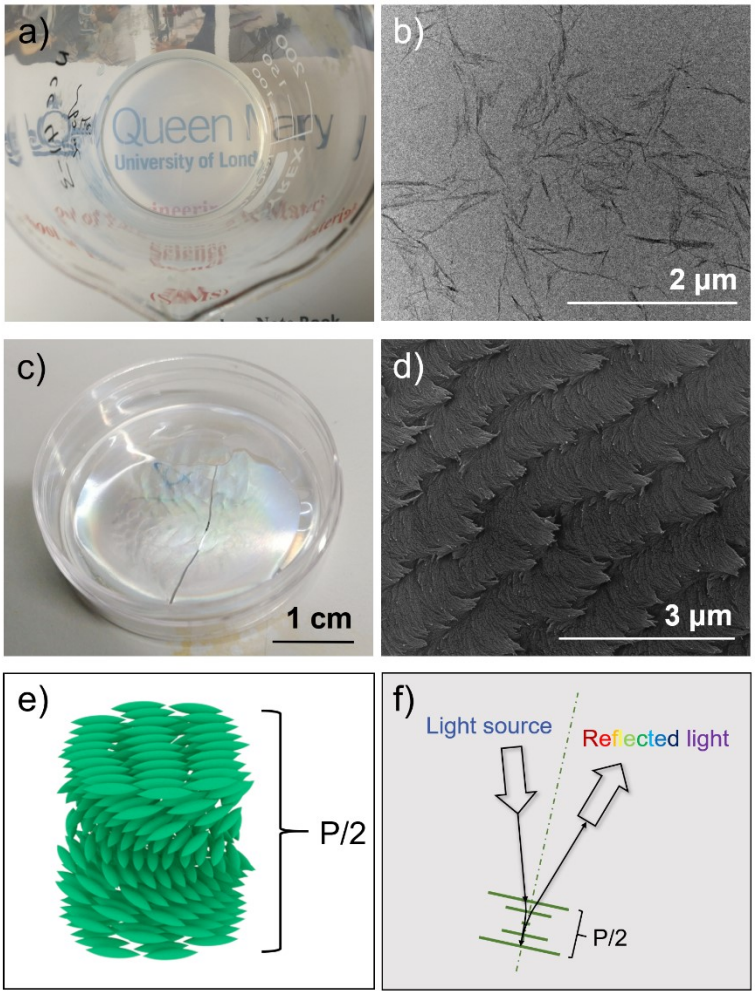


Figure 3.4. a) Photograph and b) TEM image of cellulose nanocrystal (NC) suspensions; c) Photograph and d) SEM images of obtained iridescent NC films with the self-assembled chiral nematic structures; e) Schematic of the chiral nematic ordering present in NC, along with an illustration of the half-helical pitch P/2, and (f) Illustration of the light reflected by a chiral nematic structure.

For cellulose nanocrystals from cellulose-rich resources, **Figures 3.4**e and f show the chiral nematic phase formed *via* evaporation induced self-assembly (EISA), thus resulting in the iridescent colours of the NC films. The peak wavelength (λ_{max}) reflected by the chiral

nematic structure of NC films for incident light normal to the surface can be expressed as: $\lambda_{max}=n_{avg}P$, where n_{avg} is the average refractive index and P is the helical pitch.[180]

Preparation of carbon materials from cellulose nanocrystals (CNC) for anodes. 35 mL of 1 wt% NCC suspension was transferred into a plastic petri dish and dried slowly at the room temperature (**Figures 3.4**c and d). After the evaporation process (*e.g.,* 5 to 7 days), the obtained iridescent NC films were heated to different temperatures (800 ℃, 1000 ℃ and 1300 ℃) with a heating rate of 5 ℃ min^{-1} and dwelling time of 1 h in the N_2 atmosphere. The directly carbonised NCs at different temperatures were denoted CNC800, CNC1000 and CNC1300, respectively.

In order to compare the differences between carbons derived from hierarchical units of cellulose, hard carbons (CMF1000) were obtained by directly carbonisation of cellulose microfibres from filter papers (Whatman, WHA10010155) at 1000 ℃ (5 ℃ min^{-1}, 1 h, N_2 flow).

Then, the carbon anodes were prepared by coating the slurry of the active material and sodium alginate in DI wate with a mass ratio of 95:5. All the coated working electrodes were dried in a vacuum oven at 120 ℃ overnight, and the loading mass of active materials was about 1.5-2 mg cm^{-2}.

Preparation of carbon materials from cellulose microfibrils for cathodes. In Chapter 5, 400 mg of cellulose microfibrils were achieved through the mechanical fibrillation of cotton balls, another cellulose-rich resource (Boots, 100 % cotton), in a biomass grinder. Together with 17.5 mL of DI water, they were then added to a 30mL Teflon-lined stainless-steel autoclaves, followed by the heating process up to 200 ℃ for 12 h in a hydrothermal oven. After the autoclave was cooled to the room temperature, the black-brown solid precipitate, namely the carbonaceous solid, was collected by filtering, and washed using DI water for several times. Afterwards, the biochar was dried at 120 ℃ in the oven. The collected hydrochar, melamine (Sigma-Aldrich) and potassium bicarbonate ($KHCO_3$) (Sigma-Aldrich) were added to 15 mL DI water in a mass ratio of 1:2:4 under the constant magnetic stirring for at least 50 min to ensure a homogenous distribution, before drying the mixture in an oven at 60 ℃. The mixture

was then annealed at 700 ℃ and 800 ℃ with a heating rate of 2 ℃ min^{-1} and held for 1 h under an N_2 flow. Finally, the mixture was washed using homemade 1 M HCl (diluted from 37% HCl (Sigma-Aldrich)) and DI water until the pH value reached around 7, followed by the drying process at 120 ℃ for 12 h. The resulting activated carbons with hierarchical pore structures were labelled CHKM700 and CHKM800.

For the other activation method to create microporosity, the dried biochar from hydrothermal carbonisation was thoroughly mixed with potassium hydroxide (KOH) pellets (Sigma-Aldrich) in a mass ratio of 1:2 using a pestle and mortar, followed by heat treatment of the mixture at 800 ℃ (2 ℃ min^{-1}) for 1 h under an N_2 flow. The KOH-activated carbon (CHK800) was collected after the same washing and drying procedures as the above-activated carbons.

Then, the carbon cathodes were fabricated by coating a mixed slurry of active material, acetylene black (Sigma-Aldrich), and sodium alginate (Sigma-Aldrich) in DI water with a mass ratio of 75:10:15 onto Al foils (MTI Corporation). All the coated working electrodes were dried in a vacuum oven at 120 ℃ overnight, and the loading mass of active materials was about 1.5-2 mg cm^{-2}.

Preparation of cellulose-based membranes for gel polymer electrolytes. In Chapter 5, 200 mg of hydroxyethyl cellulose (HEC) (Sigma-Aldrich, average M_w 380,000), 100 mg of polyethylene oxide (PEO) (Sigma-Aldrich, average M_v 600,000, powder), and 10mg of sodium perchlorate ($NaClO_4$) (Sigma-Aldrich) were dissolved in 15 mL DI water under continuous stirring at 80 ℃ for 4 h using a water bath. 5 mg of silicon dioxide (SiO_2) (Sigma-Aldrich, 10-20 nm particle size, nanopowder) was then added to the solution, followed by the ultrasonication in a bath for 30 min. The solution was transferred into a Teflon petri dish and dried at 40 ℃ overnight to form a cellulose-based membrane (HEC-PEO) with a diameter of 16 mm and a thickness of around 1 mm. Before using the membranes, they were dried at 50 ℃ in the vacuum oven overnight.

Preparation of lignin nanofibre mats. In Chapter 6, the preparation of the carbon nanofibre skeletons was based on the reported studies from our group.[181-183] First, 80 mg of sodium

hydroxide (NaOH, pellets, Fisher Scientific) was dissolved in 4 mL of deionised (DI) water to prepare 0.5 M aqueous NaOH solution. Then, 66.3 mg of polyethylene oxide (PEO, Mw ~600000 g mol^{-1}, Sigma-Aldrich) was added to the mixed solution of 4 mL of home-made 0.5 M NaOH solution and 1 mL of acetone (Sigma-Aldrich), followed by adding 596.7 mg of organosolv lignin (OSL) into the solution. The whole preparation process of the electrospinning solution was kept under continuous magnetic stirring until all the components were well dispersed. The spinning solution was centrifuged for 5 min at 5000 rpm to remove air bubbles before transferring to a syringe with an 18 Gauge needle. Subsequently, the homogenous solution was electrospun at a rate of 1.2 mL h^{-1} under an electric field of 20 kV with a distance of 25 cm from the needle to an aluminium (Al) collector. The whole electrospinning process was performed in a chamber (Nanobox, Plaslab) with a controlled temperature of 25 °C and a controlled humidity of 20%. After spinning 5 mL of solution, the lignin mats (around 100 µm thickness) were collected from the collector and cut into stripes for further utilisation (**Figure 3.5**a).

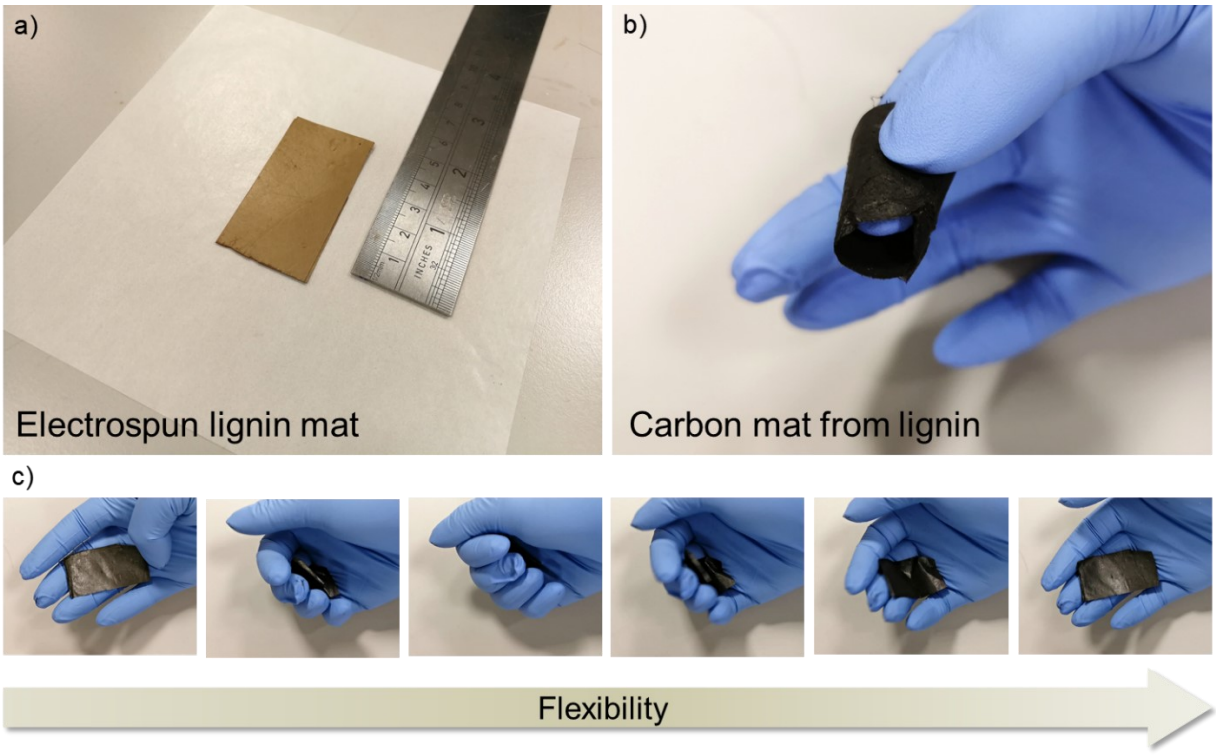


Figure 3.5. a) The photograph of a piece of electrospun lignin mat and b) a non-woven fabric piece of carbonised skeletons. c) Demonstration of the flexibility of lignin-derived carbon mats by bending and releasing.

Preparation of carbon nanofibre skeletons. In Chapter 6, the lignin mats were sandwiched between two ceramic plates, followed by transferring lignin mats to a Carbolite tubular furnace. The lignin mats were then heated to different temperatures (700 °C, 1100 °C and 1500 °C) for 2 h with a ramp rate of 5 °C min^{-1} under an N_2 atmosphere. The carbonised carbon nanofibre skeletons (about 50 μm thickness) were washed in 80 °C DI water for 2 h to remove residual impurities and then dried in an oven at 80 °C for 1 h. Finally, the carbon skeletons were cut into small pieces (8 mm in diameter) and further dried at 80 °C overnight under vacuum. These carbonised lignin mats at different temperatures were noted as L700, L1100 and L1500, respectively (**Figure 3.5**b and c).

Preparation of Na/C composite anodes. In Chapter 6, to test the symmetric cells and full cells, the Na/C composite anodes were prepared by the pre-deposition of a small amount of metallic sodium onto the carbon skeletons at the room temperature. The electrodeposition method can precisely control the amount of metallic sodium on the carbon skeletons by regulating the current density and deposition time, which is beneficial to scientific research and comparison. The deposited metallic sodium is more glassy with enhanced electron and ionic conductivity.[184] A piece of carbon skeleton (8 mm in diameter) and a piece of metallic sodium (8 mm in diameter) were separated by a glass fibre membrane (16 mm in diameter, GF/D Glass microfibre filters, Whatman) soaked in 200 μL of 1 M $NaCF_3O_3$ in diglyme. Stainless steel coin cells (CR2032, MTI Corporation) were pressed using a crimping machine (MTI Corporation). The pre-deposition in the half cell configuration was conducted at a current density of 1.0 mA g^{-1} for 8 h using a LAND CT 3001A battery testing system, followed by the disassembly of the coin cell. The pre-deposited Na/C composite anodes were cleaned by washing with diglyme solvent and dried for further electrochemical testings. The assembly and disassembly of coin cells were both performed in an argon-filled glove box (H_2O, O_2 < 0.5 ppm, MBraun).

Preparation of Prussian blue cathode. In Chapter 6, Prussian blue was prepared based on the method reported by Guo *et al.*[134] 0.968 g of sodium ferrocyanide decahydrate ($Na_4Fe(CN)_6 \cdot 10 H_2O$, Sigma-Aldrich) and 1 mL of hydrochloric acid (37 % HCl, Sigma-Aldrich) were

dissolved in 100 mL of DI water to form a homogenous solution. Then, the solution was under a continuous magnetic stirring at 60 °C for 4 h to form Prussian blue crystals within the solution. Such mixed solution was centrifuged at 10000 rpm for 15 min, after which the supernatant was then removed. The sediments of Prussian blue crystals were washed with DI water. The centrifugation and washing were repeated several times to fully remove the residual impurities. Finally, the yielded sediments of Prussian blue crystals were dried firstly at 120 ºC in an ambient oven for 12 h and then at 100 °C in a vacuum oven overnight. The Prussian blue cathode was prepared by coating a mixed slurry of 60 wt% Prussian blue crystals, 30 wt% acetylene black (Sigma-Aldrich), and 10 wt% polyvinylidene difluoride (PVDF, Sigma-Aldrich) in 1-Methyl-2-pyrrolidinone (NMP, Sigma-Aldrich) onto Al foil (MTI Corporation). Then, the coated foil was dried at 50 ºC in an ambient oven and then at 120 ºC in a vacuum oven overnight, before being cut into pieces of electrodes for further battery assembly. The loading mass of active materials on Al foils was controlled between 2.0 and 2.5 mg cm^{-2}.

Preparation of sulphur cathode. In Chapter 6, the sulphur cathode was prepared based on the method reported by Miao *et al.*[185] The bare sulphur cathodes were prepared by coating a mixed slurry of 60 wt% sulphur, 30 wt% acetylene black (Sigma-Aldrich), and 10 wt% polyvinylidene difluoride (PVDF, Sigma-Aldrich) in 1-Methyl-2-pyrrolidinone (NMP, Sigma-Aldrich) onto Al foils (MTI Corporation). Then, the coated foil was dried at 50 ºC in an ambient oven and then at 50 ºC in a vacuum oven overnight, before being cut into pieces of electrodes for further battery assembly. The loading mass of active materials on Al foils was controlled between 1.0 and 1.5 mg cm^{-2}. For the sulphur/carbon composite cathodes (S/L1500), the mixture of sulphur and L1500 in a mass ratio of 40:20 covered by the Al foil was put into a stainless-steel autoclave which was then heated to 155 ºC for 12 h in a hydrothermal oven to allow the infiltration of sulphur into the porous carbon skeleton. After that, the S/L1500 composite cathodes were prepared by coating a mixed slurry of the yielded mixture, acetylene black (Sigma-Aldrich), and polyvinylidene difluoride (PVDF, Sigma-Aldrich) in 1-Methyl-2-pyrrolidinone (NMP, Sigma-Aldrich) with a mass ratio of 60:30:10 onto Al foils (MTI Corporation) as well. Then, the coated foil was also dried slowly at 50 ºC in an ambient oven and then at 50 ºC in a vacuum oven overnight, before being cut into pieces of electrodes for further battery assembly. The

loading mass of active materials on Al foils was controlled between 1.0 and 1.5 mg cm^{-2} too.

3.2.2 Characterisation

Scanning electron microscopy (SEM).[186] SEM is a kind of electron microscopy technique for the observation of the surface morphology of materials using a focused electron beam to scan the surface of materials. When the focused electron beam touches the surface of materials, the primary electrons are elastically scattered by the atoms on the material surface to form the back-scattered electrons because of the elastic scattering of the primary electrons, while the secondary electrons are emitted by the atoms on the material surface since the radiation of the primary electrons frees the out-layer electrons of those atoms. Therefore, the component information and topography of the surface of materials can be respectively obtained according to the detection of back-scattered electrons and secondary electrons. Here, the morphologies of samples were observed using scanning electron microscopy (SEM, LEO Gemini 1252 FEG-SEM machine). Before the measurement, the powder samples were stuck onto the stainless-steel sample holders using conductive double-sided carbon tapes. In Chapter 6, for the ex-situ SEM testing of cycled samples, the samples were first plated and stripped for 10 cycles, followed by a further plating process, at the current density of 1.0 mA cm^{-2} with a specific capacity of 2.0 mAh cm^{-2} using a LAND CT 3001A battery testing system. The cycled samples were then disassembled in an argon-filled glove box (H_2O, O_2 < 0.5 ppm, MBraun) and loaded onto a sealed tube before being transferred into the testing chamber of SEM to avoid contaminations and oxidation. The element mapping of Na/C composite anodes mentioned above was also conducted using the LEO Gemini 1252 FEG-SEM machine.

Transmission electron microscopy (TEM).[187] TEM is a kind of electron microscopy technique for the observation of the inner structure of materials using a focused electron beam to penetrate an ultrathin piece of material. When the focused electron beam is transmitted across the material, the electrons can interact with its inner structure. Meanwhile, some electrons are lost because of the adsorption by materials and the scattering beyond the observable range of the detector, thus providing the contrast information of the inner structure of materials. Hence, for the inner structures of samples, transmission electron microscopy (TEM, JEOL 2010) was

employed to observe TEM grids (Agar Scientific) loaded with powder samples. When loading the samples on TEM grids, powder samples were first dispersed in the absolute ethanol and then dropped onto the TEM grids. The selected area electron diffraction patterns of samples were also obtained using TEM.

N_2 adsorption and desorption.[188] N_2 adsorption is a kind of physisorption method used to characterise the surface area and the pore structure of materials. According to the van der Waals interaction between N_2 gas and the porous surface of materials, N_2 gas can be physically adsorbed onto the material surface. When the monolayer adsorption of N_2 gas happens to fully cover the porous surface of materials under suitable pressures, the number of N_2 gas molecules required can be calculated according to the multipoint Brunauer–Emmett–Teller (BET) method of the isotherm. Since the cross-sectional area of each N_2 gas molecule is constant, the specific surface area of materials can be achieved. Meanwhile, the pore size distribution can be obtained according to the Non-Local Density Functional Theory (NLDFT) model of the isotherm. This method is suitable for the measurement of opening pores below 50 nm. Hence, the pore structures of samples were characterised using the N_2 adsorption/desorption isotherm tested on the Micromeritics 3 Flex Physisorption at 77 K in Chapter 4 and on the Quantachrome NOVA 4200 system in Chapter 5. Before the testing, the samples were degassed at 200 ºC under vacuum overnight to remove adsorbed water and gas.

Small-angle X-ray scattering (SAXS).[189] SAXS is a kind of X-ray scattering technique used for determining the pore size of materials including closed and opening pores. When the X-ray penetrate the bulk phase of materials, the elastic scattering of X-ray can be detected at the small angles ranging from 0.1 to 10 degrees, thus demonstrating the structure of materials. With the decrease in the scattering angle, the detected structural scale of materials increases. Before the measurement, the samples were filled into a Washer covered by two pieces of Scotch magic tape, followed by mounting them into a sample grid (**Figure A3.1**, Appendix). The small-angle X-ray scattering measurement (SAXS) was measured at the beamline I22 of Diamond Light source (Harwell, UK. Website: www.diamond.ac.uk/Instruments/Soft-Condensed-Matter/small-angle/I22) to further characterise the pore structures of carbon materials,

followed by the fitting of results based on the Porod method using Matlab.[189] The SAXS results have already removed the background. The Porod method was proposed by Stevens and Dahn to probe the pore size of the carbon samples.[189] The equation for carbon materials with rich pore structures is presented as follows:

$$I(q) = \frac{A}{q^a} + \frac{B_1 a_1^4}{\left(1+a_1^2 q^2\right)^2} + D \qquad \text{Equation 3.1}$$

where I(q) is the scattered intensity as a function of the scattering vector q, A is a scale factor for the surface scattering at low Q is proportional to the total surface area of large pores, B_1 is a scale factor for the pore scattering which is proportional to the total surface area of small pores. D is a constant background and a_1 is the characteristic length and associated with the radius of a spherical pore, by $R = a_1 \times \sqrt{10}$. This equation can be further modified by adding an a_1^2 term so that B_2 becomes proportional to the number of pores:[189]

$$I(q) = \frac{A}{q^a} + \frac{B_2 a_1^6}{\left(1+a_1^2 q^2\right)^2} + D \qquad \text{Equation 3.2}$$

For carbon materials with intermediate-sized pores, an additional term can be added with a different characteristic length a_2. Then the equation becomes:

$$I(q) = \frac{A}{q^a} + \frac{B_3 a_2^6}{\left(1+a_2^2 q^2\right)^2} + \frac{C a_3^6}{\left(1+a_3^2 q^2\right)^2} + D \qquad \text{Equation 3.3}$$

where a_2 is the characteristic length of intermediate pores, C is a scale factor for the pore scattering proportional to the total surface area of intermediate pores. I appricate technicians at the beamline I22 of Diamond Light socurse (Harwell, UK) for conducting the SAXS measurement and Mr. Zhenyu Guo for fitting SAXS results which are presented in the Chparter 6.

Raman spectroscopy.[190] Raman spectroscopy is a kind of spectroscopic technique that can be used to measure the bond vibration of materials. When the monochromatic laser source irradiates on the surface of materials, the inelastic scattering of the laser photons called Raman scattering can happen with the changed radiation energy because of the interaction between photons and chemical bonds of materials, together with the elastic scattering called Rayleigh scattering. The obtained shift in the laser energy can help identify the vibrational modes of chemical bonds. The Raman spectra can be fitted based on the Lorentzian model to obtain the

intensity ratio of the D- and G-peaks. After that, the average in-plane distances (L_a) can be calculated from the intensity ratio of the D- and G-peaks. The formula used to determine the average sizes of in-plane (L_a, nm) can be expressed as:[190]

$$L_a = \sqrt{5.4 \times 10^{-2} \times E_L^4 \times \frac{I_D}{I_G}} \qquad \text{Equation 3.4}$$

where E_L (=$\hbar\omega_L$, eV) is the laser excitation energy, and I_D/I_G is the intensity ratio of the D-peak and G-peak. For the light wavelength of 532 nm, E_L is 2.33 eV. For the light wavelength of 633 nm, E_L is 1.95 eV. Therefore, the defect structures of samples were characterised using Raman Spectroscopy (Renishaw inVia Raman instrument) with a laser wavelength of 532 nm. Three individual areas of each sample were detected to average the overall Raman spectra. After that, the obtained Raman spectra were fitted based on the Lorentzian model. The average in-plane distances (L_a) were calculated from the intensity ratio of the D- and G-peaks. The *operando* Raman testing was further performed using the same Raman instrument under the continuous scanning mode. The configuration of the *operando* Raman cell is shown in **Figure A3.10** (Appendix) which was assembled in an argon-filled glove box (H_2O, O_2 < 0.5 ppm, MBraun). During the continuous scanning of the samples, the *operando* Raman cell was simultaneously discharged and charged at a fixed current density using a LAND CT 3001A battery testing system, and the Raman beam was focused on a fixed spot on the surface of carbon materials during testing.

X-ray photoelectron spectroscopy (XPS).[191] XPS is a spectroscopic technique that can reveal the elemental information on the surface of materials. When the X-ray irradiates on the surface of materials, the electrons can be emitted according to the photoelectric effect, and the kinetic energy of electrons can be detected. Since the binding energy of electrons is related to the known energy of X-ray photons and the detected kinetic energy of electrons, the specific elements can be analysed according to the calculated binding energy of electrons. Therefore, the surface conditions and extrinsic defects of carbon materials were characterised using X-ray photoelectron spectroscopy (XPS) (Thermo Fisher K-Alpha* XPS facility) with a monochromated Al-Kα X-ray source. Before the testing, powder samples were stuck onto the specific sample holders using conductive double-sided carbon tapes. The *ex-situ* XPS analysis

was also performed using the same facility to analyse the SEI components upon cycled electrodes. Before the ex-situ XPS testing, the electrodes were pre-discharged and charged using a LAND CT 3001A battery testing system. When transferring samples to the XPS facility, a vacuum transfer capsule (Thermo Fisher) can protect the samples from surface contamination. The XPS spectra were fitted using the Avantage software.

X-ray diffraction (XRD).[192] XRD is a X-ray scattering technique for the analysis of the crystal structure of materials. When the X-ray enters the bulk phase of materials, the X-ray can be elastically diffracted into many specific directions because of the crystal structure of materials. At a suitable incident angle, the intensity of diffracted X-ray can be detected, which can unveil the crystal structures of materials including the interlayer spacing according to Bragg's law. Therefore, the inner structures and intrinsic defects of samples were characterised using X-ray diffraction (XRD) equipment (PANalytical X'Pert PRO) with Cu-Kα source and the power setting of 40 mA and 40 kV. Before the testing, powder samples were placed on the specific sample holders with flat surfaces. XRD patterns were fitted based on the Gaussian model. Afterwards, the average interlayer spacing d (Å) can be calculated based on the Bragg formula as follows:[192]

$$d = \frac{\lambda}{2\sin\theta} \qquad \text{Equation 3.5}$$

where θ (°) is the Bragg angle of peaks, and λ is the X-ray wavelength of 0.154 nm (1.54 Å).

Thermogravimetric analysis (TGA). TGA of HEC-PEO membrane was conducted on a TGA Q500 (TA instruments) (800 ℃, 10 ℃ min^{-1}, N_2 flow). TGA of HEP-PEO membrane and glass fibre membrane absorbing the same amount of liquid electrolyte (5 μL mg^{-1}) was also conducted on it (150 ℃, 5 ℃ min^{-1}, N_2 flow). Before the TGA measurements, membranes were dried at 50 ℃ overnight.

Electrochemical testing. The electrochemical testing was conducted using stainless steel coin cells (CR2032, MTI Corporation) at room temperature, and the cell assembly was completed in an argon-filled glove box (H_2O, O_2 < 0.5 ppm, MBraun). The electrolytes of 1 M $NaClO_4$ in

ethylene carbonate-diethyl carbonate (EC-DMC, 1:1 v%, Sigma-Aldrich) mixed solvents were used in Chapter 4 and Chapter 5. For gel polymer electrolytes in Chapter 5, the cellulose-based membranes were soaked in the liquid electrolyte for 20 min in the glove box to become the gel polymer electrolytes for further testing. For the electrolytes in Chapter 6, the solutions of 1 M $NaCF_3SO_3$ in ethylene carbonate-propylene carbonate (EC-PC, 1:1 v%, Sigma-Aldrich) mixed solvents, ethylene carbonate-diethyl carbonate (EC-DMC, 1:1 v%, Sigma-Aldrich) mixed solvents or diethylene glycol dimethyl ether (diglyme, Sigma-Aldrich) were used (**Figure 3.6**).

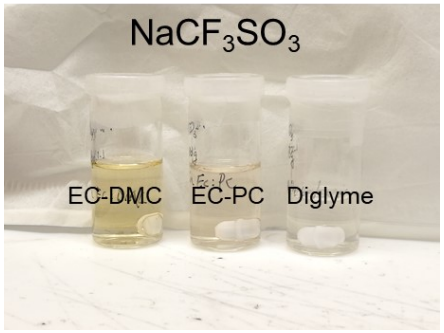


Figure 3.6. The photograph of $NaCF_3SO_3$ in EC-DMC, EC-PC or diglyme.

The half cell and full cell configuration can be employed to characterise the electrochemical performance of materials. In the half cell configuration, a piece of sodium metal foil (10 mm in diameter, Alfa Aesar) was simultaneously used as the counter and reference electrodes. The electrodes were placed against the sodium metal foil having the same size to sandwich the glass fibre separator (16 mm in diameter, GF/D Glass microfibre filters, Whatman) soaked with 200 μL of electrolytes. In the full cell configuration, the anode was placed against the cathode having the same size to sandwich the glass fibre separator (16 mm in diameter, GF/D Glass microfibre filters, Whatman) soaked with 200 μL of electrolyte.

All the galvanostatic charge/discharge (GCD) profiles and rate/cycling performance testing were performed using the LAND CT 3001A battery testing system. According to the GCD profiles, the electrochemical performance including capacity, capacitance, energy and power densities can be determined using Equation 2.1 to 2.4.

In Chapter 4, the half cells of carbons were discharged and charged between 0.001 and 2.5 V vs Na^+/Na at different current densities of 0.1, 0.2, 0.5, 1.0 and 2.0 C (1 C=300 mA g^{-1}) as well as cycled at 0.5 C, while the half cells of NVP were discharged and charged between 2.2 and 3.8 V vs. Na^+/Na at the current densities of 0.3, 0.5, 1.0, 2.0 and 6.0 C (1 C=100 mA g^{-1})

as well as cycled at 1.0 C. The full cells were charged and discharged at 30, 60, 150, 300 and 600 mA g^{-1} from 0 to 3.8 V vs Na^+/Na, and were cycled at 150 mA g^{-1}. The current densities were normalised by the active mass of the carbon anode.

In Chapter 5, the half cells containing carbon anodes were operated within the voltage window of 0-1.5 V vs. Na^+/Na, while those containing carbon cathodes were tested within 1.5-4.2 V vs. Na^+/Na. In the full cell configuration, the capacitor-type carbon cathode, the battery-type carbon anode and the glass fibre membrane were encapsulated together into one coin cell. Before the preparation of full cells, cathodes in the half cells were charged and discharged to a voltage of 1.5 V vs. Na^+/Na with a pulse current at 0.1 A g^{-1} for 30 min followed by a relaxation for 2 h, and anodes in the half cells were discharged and charged to 0.2 V vs. Na^+/Na with the same pulse current. When the full cells were charged, the cathodes positively swung by 2.7 V, and the anodes negatively swung by 0.2 V. Solid-state full cells were further assembled by combining two working electrodes with the cellulose-based quasi-solid-state electrolytes employed as the separator at the same time.

In Chapter 6, in the half cell configuration, sodium metal foil (8 mm in diameter, Alfa Aesar) was used as the counter electrode and the reference electrode at the same time. The carbon mat or other substrates (8 mm in diameter; Al, Ni, Cu and Sn, MTI Corporation; Graphite, Sigma-Aldrich; Carbon mats, Toray) was placed against metallic sodium with the same size, sandwiching the glass fibre membrane as the separator (16 mm in diameter, GF/D Glass microfibre filters, Whatman) soaked with 200 μL of electrolytes. The half cells were kept discharging (plating) and charging (stripping) at the current density of 1.0 mA cm^{-2} with a specific capacity of 2.0 mAh cm^{-2}. The maximum potential limitation of the half cells was set to be 1.5 V vs. Na^+/Na, while the corresponding minimum potential limitation was -5.0 V vs Na^+/Na. In the symmetric cell configuration, two obtained Na/C composite electrodes or two bare metallic sodium foils were placed against each other, sandwiching the glass fibre membrane as the separator (16 mm in diameter, GF/D Glass microfibre filters, Whatman) soaked with 200 μL of electrolytes. The symmetric cells were kept discharging (plating) and charging (stripping) at different current densities including 0.1, 0.2, 0.5, 1.0 and 2.0 mA cm^{-2} for 0.5 h per (dis-)charge process, and were cycled at 1.0, 2.0 and 3.0 mA cm^{-2}. The maximum and minimum potential limitations of the symmetric cells were set to be 5.0 V and -5.0 V vs.

Na^+/Na, respectively. In the full cell configuration, the Na/C composite anode or bare metallic sodium foil (8 mm in diameter) was placed against the cathode with the same size, sandwiching the glass fibre membrane as the separator (16 mm in diameter, GF/D Glass microfibre filters, Whatman) soaked with 200 μL of electrolytes. For the full cells with Prussian blue cathode, the full cells were charged and discharged at 30, 60, 150, 300, 600 and 1200 mA g^{-1} between 2.0 to 4.2 V vs Na^+/Na, and were cycled at 30 mA g^{-1} between 2.0 to 4.2 V vs Na^+/Na. For the full cells with the sulphur cathode, the full cells were charged and discharged at 167.5 mA g^{-1} between 1.5 to 3.0 V vs Na^+/Na.

Electrochemical impedance spectroscopy (EIS) from 100 kHz to 0.01 Hz was conducted on an Autolab PGSTAT204 electrochemical workstation to analyse the resistance and fitted using Zview software. Before the measurement, the half cells were pre-discharged and charged back to different states such as open circuit (around 2.5 V vs Na^+/Na), sodiated state at the first cycle (0 V vs Na^+/Na), de-sodiated state at the first cycle (1.5 – 2.5 V vs Na^+/Na), de-sodiated state after cycling, with a fixed current densities.

For the galvanostatic intermittent titration technique (GITT) testing, the half cells were pre-discharged and charged using the LAND CT 3001A battery testing system, followed by the discharging of half cells using a pulse current for a fixed time and then relaxation for a fixed time until the potential went to 0.001 V vs Na^+/Na. Combined with GITT, the diffusion coefficient of Na^+ ions (D_{Na+}, cm^2 s^{-1}) can be calculated based on Fick's second law:[193]

$$D_{Na^+} = \frac{4}{\pi\tau}\left(\frac{m_B V_m}{M_B S}\right)^2\left(\frac{\Delta E_s}{\Delta E_\tau}\right)^2 \qquad \text{Equation 3.6}$$

where τ (s) is the pulse duration, m_B, M_B and V_M are the mass (g), the molar mass (g mol^{-1}) and the molar volume (mL mol^{-1}) of the active materials, and S is the active surface area (cm^2) of the working electrodes. ΔE_S (V) is the potential difference of two adjacent steady states, and $\Delta E\tau$ (V) is the potential change owing to the pulse current. was also conducted. In Chapter 4, the half cells were pre-discharged and charged at 0.1 C, followed by the discharging of half cells using a pulse current at 0.1 C for 30 min and then relaxation for 3 h until the potential went to 0.001 V vs Na^+/Na. In Chapter 6, the half cells of L700 were pre-discharged and charged at 1.0 mA cm^{-2} with the capacity of 2.0 mAh cm^{-2}, followed by the discharging of half cells using a pulse current at 1.0 mA cm^{-2} for 5 min and then a relaxation for 1 h until the

potential went to the plating potential.

Cyclic voltammetry (CV) measurements of hard carbons in the half cell configuration at different scan rates were conducted using Biologic VSP-300 potentiostat to investigate the detailed electrochemical reactions and their corresponding kinetics. In Chapter 4, CV measurements of hard carbons in the half cell configuration from 0.1 to 5.0 mV s^{-1} were conducted.

According to the Power law, the response current at a fixed potential is linearly or exponentially related to the applied scan rate:[32]

$$\mathrm{i} = \mathrm{a}v^{\mathrm{b}} \qquad \text{Equation 3.7}$$

where i (mA) is the response current measured at a fixed potential using a specific scan rate, v (mV s^{-1}) is the applied scan rate, a and b are variable parameters. The change of b-value from 0.5 to 1.0 represents the type of the electrochemical reaction varies from diffusion-controlled to surface-controlled, which can be used to analyse the kinetics of electrochemical reactions qualitatively. Therefore, using the power law, the overall response current i (mA) can be further quantified into the surface- and diffusion-controlled currents as follows:[32]

$$\mathrm{i} = \mathrm{a}_1 v + \mathrm{a}_2 v^{0.5} \qquad \text{Equation 3.8}$$

where $a_1\nu$ and $a_2\nu^{0.5}$ respectively refer to the response currents from the surface- and diffusion-controlled reactions because the surface-controlled current is linearly related to the applied scan rate v (mV s^{-1}) at a fixed potential, while the diffusion-controlled one is exponentially related.

Equation 3.8 can be rearranged into:

$$\frac{\mathrm{i}}{v^{0.5}} = \mathrm{a}_1 v^{0.5} + \mathrm{a}_2 \qquad \text{Equation 3.9}$$

By fitting Equation 3.9, the a_1 and a_2 can be obtained to determine the surface- and diffusion-controlled currents.

3.2.3. Theoretical modelling and simulations.

Molecular modelling. In Chapter 4, The molecular modelling of solvent molecules was conducted using ArgusLab based on the models of free EC and DMC solvent molecules. First, the standard models of solvent molecules with fixed bonding angles were built up. After that, the electrostatic mapping of a single molecule can be obtained from the software. In Chapter

6, the molecular level modelling of solvent molecules was conducted using ArgusLab based on the models of free EC, PC, DMC and diglyme solvent molecules. First, the standard models of solvent molecules with fixed bonding angles were built up. After that, the electrostatic mapping and the electron cloud distribution of HOMO/LUMO of a single molecule can be obtained from the software.

Finite element modelling. In Chapter 4, The finite element modelling was conducted using Ansys Maxwell to analyse the electric field distribution at the interface between electrolytes and electrodes during the discharge process. Two-dimensional and three-dimensional models with different surface situations (carbon spheres vs carbon blocks) were built up and compared. The ionic conductivities of the ester-based electrolyte were set to be 1.0 S m^{-1}. The diameters of sample models were set to be 1.0 μm and 5.0 μm. The conductivity of the sample model was set to be 10000 S m^{-1}. The overpotential of 0.1 V was utilized as the voltage excitation from the edge of the electrolyte to the edge of the sample model. The boundary of finite elements was set to be the Bolloon type during the simulation. As a result, the electric field distributions and corresponding differential vector profiles of different sample models during the discharge process can be obtained. In Chapter 6, the finite element modelling was conducted using Ansys Maxwell to analyse the electric field distribution at the interface between electrolytes and electrodes during deposition. For the deposition onto the metallic sodium, two-dimensional models with the same surface morphology (only bulging nuclei) were firstly built up to compare the difference between the ester- and ether-based electrolyte. The ionic conductivities of the ester- and ether-based electrolyte were set to be 1.0 and 0.5 S m^{-1}, respectively. The length and height of the entire model were set to be 100 and 50 μm, respectively. The conductivity of metallic sodium was set to be 2.1 x 10^7 S m^{-1}. The overpotential of 0.1 V was utilised as the voltage excitation from the top edge of the electrolyte to the bottom edge of the electrode. The boundary of finite elements was set to be the Bolloon type during the simulation. Hence, the electric field and ion flux distribution during the deposition onto the metallic sodium can be obtained. Two-dimensional models with the different surface morphologies (bulging nuclei and concave nuclei) on the metallic sodium were also built up in the ether-based electrolyte for further comparison. For the deposition onto the carbon skeleton, three-

dimensional models of carbon skeleton with nanofibre structures in the ether-electrolyte were built up as well. The conductivity of the carbon skeleton was set to be 10000 S m^{-1}. The length, width and height of the entire model were set to be 100, 50 and 50 μm, respectively. The overpotential of 0.1 V was utilised as the voltage excitation from the top face of the electrolyte to the bottom face of the electrode. The boundary of finite elements was set to be the Bolloon type during the simulation. Then, the three-dimensional electric field distribution and its differential vector profile of the deposition onto the carbon matrix can be obtained.

Life cycle assessment. The life cycle assessment of the two different systems in Chapter 4 was conducted based on the ISO 14040:2006 guideline using the openLCA software.[194] The life cycle impact assessment (LCIA) was also performed to obtain five main environmental impacts including global warming potential (GWP), human toxicity potential (HTP), photochemical oxidants creation potential (POCP), acidification potential (AP), and eutrophication potential (EP) using the CML 2001 method.[195] The databases of Product Environmental Footprints (PEF) and Ecoinvent were used, and the inventory data is summarized in **Table A1.1** (Appendix). The values of commercial graphite for lithium-ion batteries are also obtained from Ecoinvent.

Density functional theory (DFT) computations. In Chapter 6, all DFT computations at the atomic level were performed by Mr. Ruixuan Chen with the aid of Gaussian 09 package.[196] Hybrid generalised gradient approximation (GGA) functional B3LYP[197, 198] was applied throughout the computation. The structure optimisation and subsequent vibrational analysis were carried out at the basis set level of 6-31G(d) with quadratic self-consistent field convergence criterion. The structures were shown in the figures with pyridinic, pyrrolic and quaternary nitrogen doping at different positions (*i.e.,* centre and edges 1 to 3). A control group without nitrogen doping (plain) was also considered. The binding energy was calculated according to the vibrational analysis results. The charge density and spin density were calculated under the scope of natural bond orbital (NBO)[199] analysis. The binding energies between the sodium atom and idealised graphene layer (E_b) were defined as follows:

$$E_b = E_{total} - E_{sub} - E_{Na} \qquad \text{Equation 3.7}$$

where E_b, E_{sub}, E_{Na} were the energies of graphene layer models with sodium atom, pure

graphene layer models, and a sodium atom in a sodium crystal, respectively.

Chapter 4. From glucose to sodium-ion batteries

- *The role of hydrothermal carbonisation in sustainable sodium-ion battery anodes*

As mentioned above, although hard carbons derived from biomass precursors are considered to be an ideal anode candidate for the sodium-ion storage, the energy consumption and carbon emissions of their fabrication process have also aroused wide attention during this rapid growth period of sodium-ion batteries. Therefore, developing the strategy to make the anode fabrication process more sustainable deserves more effort from scientists whilst enhancing the electrochemical performance of hard carbon anodes. Therefore, I look into the functions and energy consumptions of the hydrothermal pre-treatment method and analyse its role in the sustainable sodium-ion battery anodes.

In this chapter, hard carbons were prepared either by the direct high-temperature carbonisation of glucose or the hydrothermal pre-treatment of glucose followed by the high-temperature carbonisation, establishing a comprehensive comparison platform. The structures and electrochemical performance of obtained hard carbons were characterised and correlated to unveil the sodium-ion storage mechanism and electrode-electrolyte interface properties, combined with electrochemical kinetic calculations, *operando* Raman spectroscopy, *ex-situ* X-ray photoelectron spectroscopy and multi-scale modelling (*i.e.*, molecular modelling and finite element simulation). It is important to note that *operando* Raman characterisation of hard carbons during the electrochemical sodium-ion storage, including the low-frequency Raman shift region, are complicated to perform due to their broad characteristic peaks with low intensities and the intense background caused by the Rayleigh scattering at the low-frequency Raman shift region.[200] Despite this, the *operando* Raman cell with increased sealing pressure has a remarkable resolution, making significant breakthroughs in achieving a real-time fine spectrum analysis of hard carbons. Meanwhile, through an innovative combination of life cycle assessment with experimental testing of sodium-ion battery technologies, we can look across the different life-stages of hard carbon anodes from the supply chain of raw materials to the preparation of products and recycling of waste, thus assessing the differences in the

sustainability of hard carbons with and without hydrothermal pre-treatment.[201] The hydrothermal pre-treatment confers more active sites (*e.g.*, defects, closed nanovoids, *etc*.) into hard carbons to store sodium ions. The morphology of the hydrothermal carbon is spherical with hierarchical pore structures that facilitate a uniform ion flux and charge transfer. Also, the surface functional groups can help make the solid electrolyte interphase more homogenous, boosting the overall electrochemical performance. Moreover, the hydrothermal carbonisation process can pre-stabilise the morphologies and structures of carbon materials to simultaneously increase the total carbon yield, specific capacity and thus decrease the carbon emission, overturning the traditional but unverified understanding that the hydrothermal pre-treatment as an additional step would increase the cost and carbon emissions of hard carbon anodes. Overall, I provide a systematic study to critically analyse and understand the contribution of hydrothermal pre-treatment to the electrochemical performance and sustainability of hard carbon anodes for sodium-ion storage, which can provide guidance for rationally fabricating sustainable, high-performance sodium-ion batteries in the future. Only when sustainability exists at each stage can we achieve a promising battery technology towards carbon neutrality.[202]

4.1 Synthesis and structural characterisation of bio-derived hard carbons

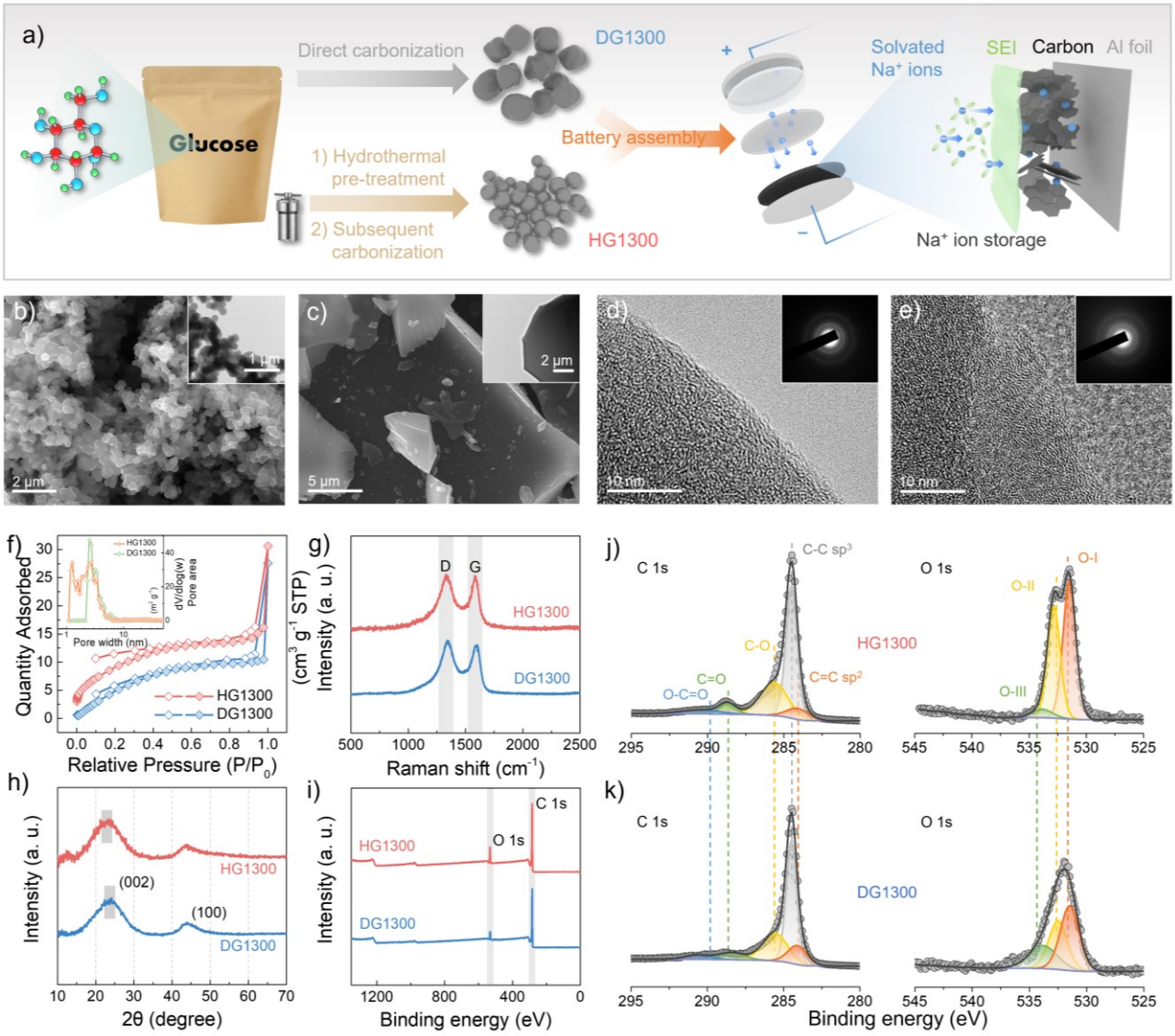


Figure 4.1. Material characterisation. a) The schematic illustration of the two synthesis routes of glucose-derived hard carbons. One is the direct carbonisation of glucose (DG), and the other is the hydrothermal pre-treatment of glucose at 200 °C (HG) followed by the high-temperature carbonisation; SEM images with inserted TEM images of b) HG1300 and c) DG1300; HRTEM images with SAED patterns of d) HG1300 and e) DG1300; f) N_2 adsorption and desorption isotherms with the corresponding pore distributions, g) Raman spectra, h) XRD patterns, and i) XPS surveys, of HG1300 and DG1300; Fitted C 1s and O 1s core-level XPS spectra of j) HG1300 and k) DG1300.

As illustrated in **Figure 4.1**a, hard carbons were prepared using the hydrothermal pre-treatment of glucose at 200 °C for 12 h, followed by the high-temperature carbonisation at 1000, 1300 or 1500 °C for 2 h under N_2 atmosphere, which has been well-optimised based on our group's previous research experience.[60] The as-obtained carbon samples are denoted as HG1000,

HG1300 and HG1500. In comparison, directly carbonised samples from the same precursor at different temperatures including 1000, 1300 and 1500 ºC for 2 h are denoted as DG1000, DG1300 and DG1500, respectively.

First, the resulting carbons obtained through the hydrothermal pre-treatment and subsequent carbonisation exhibit a uniform spherical morphology. The carbon spheres all have a similar diameter around 200 nm (**Figure 4.1**b and **Figure A1.1**, Appendix). During the hydrothermal process, the glucose molecules gradually dehydrate to form 5-hydroxymethylfurfural which polymerises, nucleates and form spherical hydrothermal carbons in the aqueous phase.[203] The subsequent carbonisation further introduces the conductivity and stabilises the morphology. The compact packing density resulting from the unique spherical morphology can contribute to shorter diffusion pathways for ions and electrons (**Figure A1.1**, Appendix).[58] On the other hand, the directly carbonised carbons show a completely different morphology of irregular particles with different particle sizes according to the scanning electron microscopy (SEM) images (**Figure 4.1**c and **Figure A1.1**, Appendix). The direct high-temperature carbonisation firstly results in the rapid foaming and expansion of precursors, followed by sintering, which finally produces disconnected carbon blocks. The morphological differences in obtained electrodes will be inherited from the carbon materials (**Figure A1.1**, Appendix) to affect their electrochemical performance. Based on the high-resolution transmission electron microscopy (HRTEM) images (**Figures 4.1**d and e, and **Figure A1.2**, Appendix) and the corresponding selected area electron diffraction (SAED) patterns, the inner structures of carbon materials display both turbostratic and amorphous features, which means they are categorized as hard carbons.

N_2 adsorption and desorption isotherms can be employed to characterise the porosity of carbons. According to the isotherms in **Figure 4.1**f, the Brunauer–Emmett–Teller (BET) specific surface areas (S_{BET}) of HG1300 and DG1300 are 34.4 and 28.0 $m^2\ g^{-1}$, respectively. The pore size distributions analysed using the non-local density functional theory (NLDFT) method are inserted in **Figure 4.1**f, where hierarchical pore structures including micro- and meso-pores of HG1300 can be beneficial to mass transportation and ion diffusion.[204] In contrast, dominant mesopores but few micropores can be observed from directly carbonised DG1300. This phenomenon can also be seen from the isotherms of DG1000 and HG1000 (**Figure A1.3**,

Appendix), where the surface area of HG1000 (338.8 $m^2 g^{-1}$) with abundant micropores is much larger than that of DG1000 (85.1 $m^2 g^{-1}$) with fewer micropores. Therefore, it can be concluded that the hydrothermal pre-treatment method can generate more micropores within carbons and thus increase the overall surface area when the carbonisation temperature is constant.[205] With the carbonisation temperature increasing from 1000 to 1500 ºC, for each type, the surface areas of carbons decrease, while their average pore diameters increase (**Table 4.1**). The difference in surface areas between 1000 and 1300 ºC is the most prominent, indicating that the carbonisation temperature of 1300 ºC is a critical factor in decreasing the surface area due to the closure of most micropores at this temperature (**Table 4.1**).[204] Consequently, HG1300 can possess more closed nanovoids than DG1300 (**Figure A1.3**, Appendix), which has also been confirmed in our previous studies using small-angle X-ray scattering (SAXS) and ^{23}Na solid-state nuclear magnetic resonance (NMR) spectroscopy of hydrothermal carbons.[39, 60]

The defect structures of carbons can be studied with Raman spectroscopy, X-ray diffraction (XRD) and X-ray photoelectron spectroscopy (XPS). Raman spectra of HG1300 and DG1300 **(Figure 4.1**g) exhibit typical broad D- and G-peaks, further demonstrating they belong to disordered hard carbons classified as Stage II in the three-stage Raman model proposed by A. C. Ferrari *et al.*[190, 206-208] In contrast to ordered graphitic carbons in Stage I such as graphite, graphene and carbon nanotubes,[208] the intensity ratio of D- to G-peaks (I_D/I_G) of hard carbons in Stage II increases when the defect concentration of the curved graphene layers of hard carbons decreases.[207] Therefore, the lower I_D/I_G value of HG1300 compared to that of DG1300 (**Table 4.1** and **Figure A1.4**, Appendix) indicates more defective graphene planes in HG1300, suggesting that, the hydrothermal pre-treatment is responsible for the formation of more defects within carbons. With the increase in the carbonisation temperature from 1000 to 1500 ºC, the I_D/I_G value increases, indicative of a less defective carbon structure (**Table 4.1** and **Figure A1.4**, Appendix). Furthermore, the defect structures described before can be further categorised into intrinsic and extrinsic defects.[209] XRD patterns (**Figure 4.1**h) can be used to selectively study the intrinsic defects caused by turbostratic graphene nanosheets. At the same time, XPS spectra can analyse the extrinsic defects created by the presence of heteroatom dopants on carbon surfaces (**Figure 4.1**i). XRD patterns of HG1300 and DG1300 both display two broad peaks located at $2\theta \approx 24°$ and 44°, attributed to the expanded (002) and (100) planes

as well as the distortion and dislocation of lattices inside carbons. However, HG1300 is more disordered than DG1300; from the analysis of its calculated average interlayer spacing of (002) planes (d_{002}) being wider than that of DG1300 (**Table 4.1**). In addition, the broader full width at half maximum of (002) planes ($FWHM_{002}$) of HG1300 also indicates less uniform carbon interlayer spacing (**Table 4.1**). As the carbonisation temperature increases from 1000 to 1500 ^{o}C, the carbon structure becomes more ordered because of the smaller corresponding values of d_{002} and $FWHM_{002}$ (**Table 4.1** and **Figure A1.5**, Appendix). Meanwhile, according to XPS surveys (**Figure 4.1**i) and fitted core-level XPS spectra (**Figure 4.1**j and k), the atomic amount of oxygen doping inside HG1300 and DG1300 can reach 9.8 at. % and 6.8 at. %, respectively, in which C=O carbonyl groups (O-I) and C–OH hydroxyl or C-O-C ether groups (O-II) dominate. Besides, O-III represents the O=C-OH carboxyl groups. When the carbonisation temperature increases from 1000 to 1500 ^{o}C, the amount of oxygen doping decreases (**Table 4.1** and **Figure A1.6**, Appendix). To sum up the observations from experimental characterisation, the hydrothermal pre-treatment leads to more defects (*e.g.,* intrinsic carbon dislocation and vacancies, extrinsic oxygen doping, *etc*.) into hard carbons.

Hence, the discrepancy in electrochemical results can be reliably ascribed to these physicochemical properties including the morphological, structural and compositional variations of carbons and obtained electrodes, and the detailed characterisation can provide deep insights into the role of hydrothermal carbonisation processes in sustainable sodium-ion battery anodes.

Table 4.1. Physical parameters of carbon materials.

	S_{BET}[a] ($m^2\ g^{-1}$)	V_t[b] ($cm^3\ g^{-1}$)	D_A[c] (nm)	I_D/I_G[d]	L_a[e] (nm)	d_{002}[f] (nm)	$FWHM_{002}$[g] (°)	C (at%)	O (at%)
HG1000	338.8	0.19	2.3	1.00	1.26	0.391	8.8	84.7	15.3
DG1000	85.1	0.048	2.2	1.05	1.29	0.388	7.8	90.2	9.8
HG1300	34.4	0.024	2.9	1.08	1.31	0.385	8.1	90.2	9.8
DG1300	28.0	0.016	2.3	1.12	1.34	0.378	7.4	93.2	6.8
HG1500	26.1	0.019	3.3	1.12	1.34	0.377	7.6	97.0	3.0
DG1500	22.6	0.014	2.3	1.39	1.49	0.357	5.5	95.7	4.3

[a] Brunauer–Emmett–Teller (BET) specific surface area,
[b] Total pore volume,
[c] Average pore diameter,
[d] Intensity ratio of D-peak to G-peak,
[e] Average in-plane distance of the graphene layer,
[f] Calculated average interlayer spacing of graphene layers,
[g] Fitted full width at half maximum of (002) peaks.

4.2 Electrochemical testing in the half cell configuration

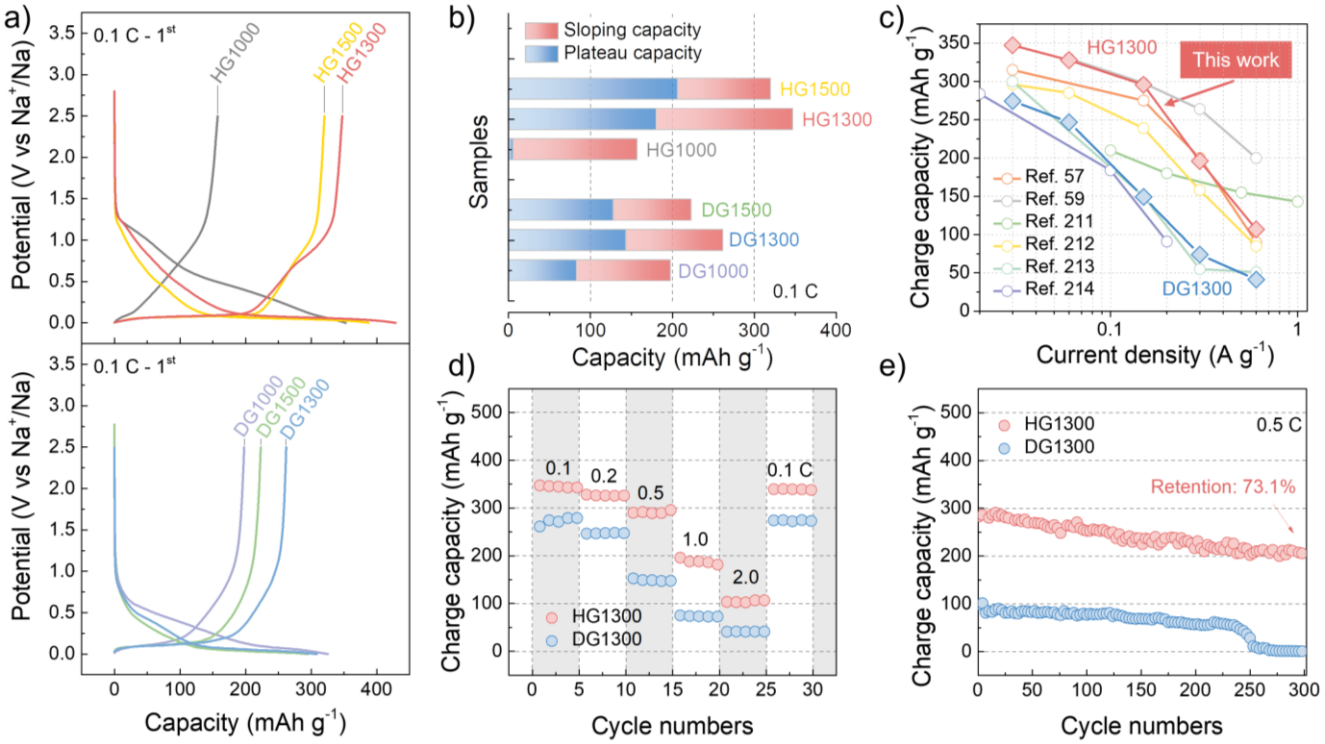


Figure 4.2. Electrochemical testing. a) The first cycle of GCD curves of different samples including HG1000, HG1300, HG1500, DG1000, DG1300 and DG1500 at 0.1 C (1 C = 300 mA g^{-1}) within the potential range of 0.001-2.5 V vs Na^+/Na using 1 M $NaClO_4$ in EC-DMC; b) The contributions of sloping and plateau capacities in each sample; c) Specific capacities of HG1300 and DG1300 in comparison to reported carbon anodes for sodium-ion batteries; d) Rate performance at different current densities including 0.1, 0.2, 0.5, 1.0 and 2.0 C, and e) Cycling performance at 0.5 C, of HG1300 and DG1300.

The half cell configuration can be applied to investigate the ability of hard carbons to store sodium ions. In this two-electrode configuration, the hard carbon electrode is utilised as the working electrode and placed against a piece of metallic sodium used as both the reference and counter electrodes. The half cells were tested from 0.001 to 2.5 V vs Na^+/Na using 1 M $NaClO_4$ in ethylene carbonate (EC) and dimethyl carbonate (DMC) (1:1 in volume) as the electrolyte.

The first cycles of galvanostatic charge/discharge (GCD) curves of hard carbons are shown in **Figure 4.2**a. Among them, HG1300 delivers the highest reversible charge capacity of 347.4 mAh g^{-1} at 0.1 C with both obvious plateau and sloping regions.[60] In comparison, the reversible charge capacity of DG1300 is only 261.3 mAh g^{-1}, which ranks the highest among the DG series. Hence, HG1300 and DG1300 from two different synthesis routes will be studied in detail as the most promising samples in each series from a performance perspective. Besides,

since carbonates' lowest unoccupied molecular orbital (LUMO) is lower than the energy level (μ_A) of hard carbons, the electrons will transfer from μ_A of hard carbons to LUMO of carbonates, leading to the reduction and decomposition of the electrolyte during the initial discharge process.[36] As a result, a passivation layer known as the solid electrolyte interphase (SEI) will be formed to fully cover the hard carbon surface as a barrier that prevents direct electron transfer with carbonates.[34] The SEI formation mainly results in the irreversible capacity during the first cycle, thus leading to a decrease in the initial Coulombic efficiency (ICE). The ICE of HG1300 and DG1300 both can reach as high as 85 %. However, the ICE is much lower for HG1000 and DG1000 which were carbonised at the relatively low temperature of 1000 °C because of extensive SEI formation on the abundant open pores described previously (**Table 4.1**). In a full cell, a higher ICE means less consumption of sodium ions from the cathode to form excessive SEI at the anode side, which can therefore reduce the mass of the cathode needed in the full-cell configuration.[210]

In **Figure 4.2**b, the sloping capacity of each sample is distinguished from its plateau capacity. When the carbonisation temperature increases from 1000 to 1500 °C, the decrease in the contribution of sloping regions can be correlated to fewer defect sites in carbons for either HG or DG series, indicating that the sloping region may correspond to the adsorption of sodium ions at defect sites, in good agreement with our and others' previous observations.[39, 56, 57, 60] Meanwhile, the samples of HG series carbonised at over 1300 °C have higher plateau capacities than the DG series, which is consistent with more closed nanovoids in HG1300 and HG1500 as described above.[60] A more detailed discussion on the sodium-ion storage sites in the different carbon materials will be presented in the following section using kinetic analysis, advanced characterisation and simulations. As the most promising hard carbon material in this study, the capacity of HG1300 is also highly competitive to other reported carbonaceous materials for sodium-ion storage (**Figure 4.2**c), ranking within the top level of state-of-the-art carbon anodes.[57, 59, 211-214] For the rate performance (**Figure 4.2**d) ranging from 0.1 C to 2.0 C, the retention of the capacity of spherical HG1300 at 2.0 C is 31.1%, which is much higher than that of DG1300 (14.7%). Thus, the imbalance between the kinetics of anodes and cathodes will be exacerbated by the poor rate performance of DG1300. When the current density returns to 0.1 C, the capacity of HG1300 is able to recover to its original level, further proving the

reversibility and stability of the HG material. For the cycling performance at 0.5 C (**Figure 4.2**e), HG1300 with an average decay rate below 0.09 % each cycle has higher capacity retention after 300 cycles than DG1300 whose cell fails after around 250 cycles. Furthermore, the half cell of HG1300 with an ultra-long lifetime can run for about 1000 cycles at 0.5 C (**Figure A1.7**, Appendix). Detailed electrochemical performance of all samples is presented in **Figure A1.8** (Appendix). In brief, the defects and closed nanovoids of HG1300 provide more sodium-ion storage sites, and the hierarchical pore structure of HG1300 and its compact packing density based on spherical particles enhances the mass and charge transfer. These beneficial properties are a direct result of the hydrothermal pre-treatment, enabling the excellent electrochemical performance of HG1300.

4.3 Electrochemical kinetic calculation and analysis

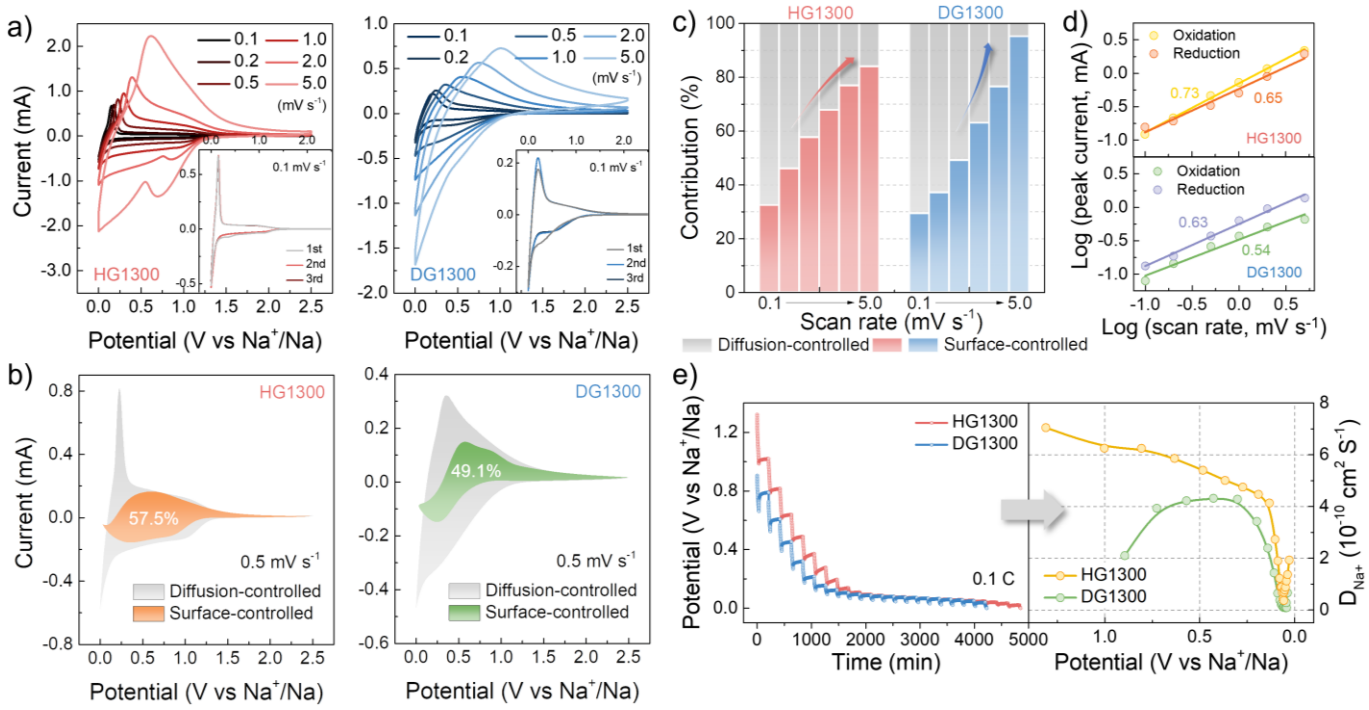


Figure 4.3. Kinetic analysis. a) CV curves of HG1300 and DG1300 at different scan rates of 0.1, 0.2, 0.5, 1.0, 2.0 and 5.0 mV s^{-1} (the second cycle at each scan rate), inserted with the very first three cycles of CV curves of HG1300 and DG1300 at 0.1 mV s^{-1}; b) The surface-controlled current separated from the diffusion-controlled one at each potential in CV curves of HG1300 and DG1300 at 0.5 mV s^{-1}; c) Calculated contributions of the surface- and diffusion-controlled proportions varying from 0.1 to 5.0 mV s^{-1} in HG1300 and DG1300; d) Linear relationship between log (peak current) and log (scan rate) of HG1300 and DG1300 for calculating the exponent (b values) in half cells; e) and f) GITT profiles of HG1300 and DG1300 (left) by discharging the half cells with a pulse current at 0.1 C for 30 min followed by an interval for 3

h, and calculated D_{Na+} (right) at different potentials.

Cyclic voltammetry (CV) measurements of hard carbons in the half cell configuration from 0.1 to 5.0 mV s^{-1} can be employed to investigate the detailed electrochemical reactions and their corresponding kinetics based on Equation 3.7 and 3.8. At the start of the electrochemical assessment, the formation of SEI introduces irreversibility in the CV profiles from the first cycle (insets in **Figure 4.3**a). In Figure 4.3a, HG1300 and DG1300 exhibit different CV curves at increased scan rates because the electrochemical kinetics of HG1300 differ from DG1300. With the increase in scan rates, DG1300 has more potential shift of redox peaks and polarisation of CV profiles than HG1300. Under 5.0 mV s^{-1}, the CV curve of HG1300 still displays sharp redox peaks, while redox peaks of DG1300 become broad and tend to diminish. Furthermore, the redox peak in CV curves (**Figure 4.3**a) corresponds to the plateau region in GCD curves (**Figure 4.2**a). In comparison to DG1300, the sharper redox peaks in the CV curves of HG1300 (**Figure 4.3**a) represent the lower potential range of the plateau region in the GCD curves of HG1300 (*e.g.*, below 0.1 V vs Na^+/Na at 0.1 C) (**Figure 4.2**a), which means a higher average working voltage in the full cell configuration using HG1300.

To understand these differences in CV curves, the currents contributed by surface- or diffusion-controlled reactions are calculated (**Figure 4.3**b). The response currents in the sloping region are mainly composed of the surface-controlled currents, and the diffusion-controlled currents dominate in the plateau region. From a kinetic point of view, the surface-controlled reaction in the sloping region with a faster kinetic is similar to the pseudocapacitive process due to the adsorption of sodium ions on the surface or near-surface active sites in the form of defects.[204] In contrast, the diffusion-controlled reaction in the plateau region is attributed to the diffusion and storage of cations in the carbon bulk phase with slower kinetics.[204] According to **Figure 4.3**c, most of the capacity (around 70 %) at a low scan rate (0.1 mV s^{-1}) is provided by the diffusion-controlled reactions in the plateau region, which is a typical feature of high-energy battery-type hard carbon anodes. During a faster charge-discharge process, the loss of capacity is manifested by the decrease in diffusion-controlled reactions in the plateau region, which simply do not have time to occur. As the scan rate increases from 0.1 to 5.0 mV s^{-1}, the contribution of surface-controlled reactions in HG1300

slowly rises from 32.4 to 84.0 %, but that in DG1300 rapidly grows from 29.4 to 95.2 % (**Figure 4.3**c). Together with the more obvious disappearances of DG1300 redox peaks at an increased scan rate, this tendency can also be related to the poorer rate performance of DG1300 described before. Furthermore, the b-values of the reduction and oxidation peaks of HG1300 are 0.65 and 0.73, respectively, both higher than those of DG1300 (0.63 and 0.54) (**Figure 4.3**d); hence, the kinetics of diffusion-controlled reactions in HG1300 are faster than those in DG1300, which explains the better rate performance of HG1300. Overall, the hydrothermal pre-treatment not only produces more active sites to enhance the surface- and diffusion-controlled capacities but also creates interconnected spherical morphologies and hierarchical pore structures in HG1300 to facilitate the ion and electron diffusion, thus enabling excellent electrochemical kinetics.

To further understand the electrochemical kinetics of hard carbons, the galvanostatic intermittent titration technique (GITT) can be utilised to evaluate the diffusion coefficient of sodium ions (D_{Na+}) in the electrode during the second discharge process using Equation 3.6. In **Figure 4.3**e, the calculated D_{Na+} of HG1300 slightly decreases in the sloping region of the sodiation process, followed by a rapid decrease in the plateau region. This situation also validates that when the potential decreases from the sloping region to the plateau region, the electrochemical reactions switch from surface-controlled to diffusion-controlled. Compared with HG1300, the average D_{Na+} of DG1300 in the sloping region is not notably higher than that in the plateau region, although differences in the two regions still exist. Similar trends can also be observed in the GITT profiles of other samples at different carbonisation temperatures (**Figure A1.10**, Appendix). The kinetics of their electrochemical reactions in sloping and plateau regions elucidated here can, therefore, attest that the sloping region is based on the faster adsorption of sodium ions on the superficial active sites like defects.[193] In contrast, the plateau region refers to the slower diffusion and storage of sodium ions at active sites like closed nanopores within the bulk phase of carbons.[57]

4.4 Fundamental mechanistic insights into sodium-ion insertion behaviours and interfacial phenomena

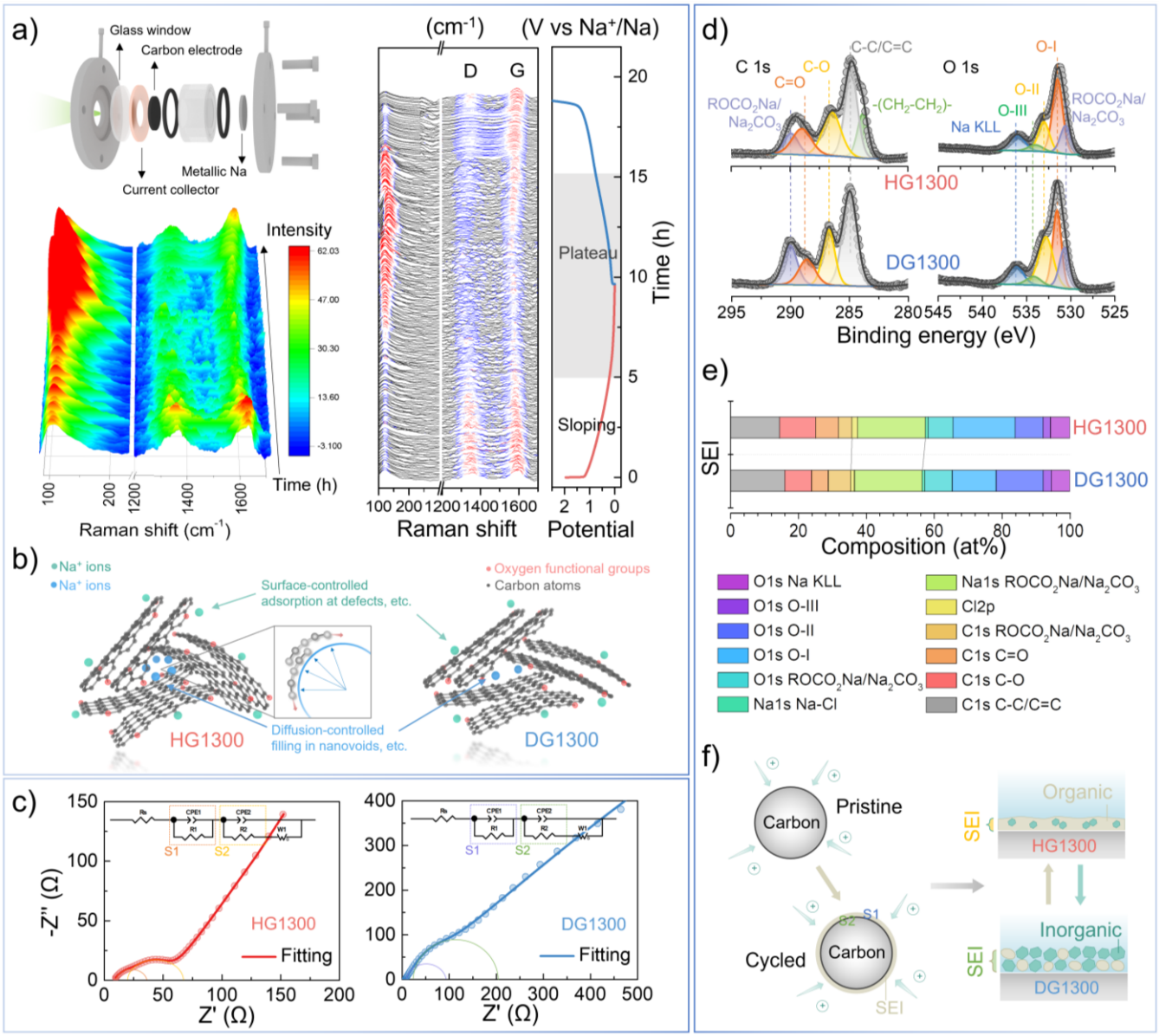


Figure 4.4. *Operando* and *ex-situ* characterisations. a) *Operando* Raman spectra of HG1300 and the corresponding 3D mapping image during the second discharge-charge process using the illustrated *operando* Raman cell; b) Schematic illustrations of the sodium-ion storage behaviours in HG1300 and DG1300 with different structural features; c) Fitted EIS of cycled HG1300 and DG1300 at the same de-sodiated state based on the modified equivalent circuits with two charge-transfer resistances in two interphases (S1 and S2); d) Fitted C 1s (left) and O 1s (right) core level XPS spectra of HG1300 and DG1300 after the first discharge-charge process; e) Corresponding composition contributions of the interphase upon de-sodiated HG1300 and DG1300; f) Schematic diagrams of the interface conditions of cycled carbons (left) with detailed illustrations of possible SEI compositions upon cycled HG1300 and DG1300 (right).

To further evaluate the relationship between active sites in hard carbons and electrochemical behaviours, high-resolution *operando* Raman spectroscopy including characteristic peaks and the low-frequency Raman shift region was conducted to understand the detailed sodium-ion storage mechanisms in HG1300 (**Figure 4.4**a and **Figure 4.5**a). The *operando* Raman spectroscopy setup is presented in **Figure 4.4**a and **Figure 4.5**a, where the Raman beam (532 nm) was continuously focused on a fixed particle of HG1300 during the discharge-charge process. The first Raman spectrum of HG1300 has typical broad D- and G-peaks (**Figure 4.4**a), which is the same as **Figure 4.1**g. Likewise, the low-frequency Raman signal cannot be observed at the very beginning of the electrochemical sodium-ion storage process, and the basic intensity here is the background signal caused by the Rayleigh scattering. In detail, the first-order Raman scattering from a phonon in the plane of crystalline graphene layers leads to the G-peak at ~1580 cm^{-1}, which is also called the E_{2g} in-plane bond-stretching motion of pairs of sp^2 carbon atoms (**Figure 4.5**b).[215] The D-peak at ~1350 cm^{-1} refers to the A_{1g} breathing mode of sp^2 carbon atoms (**Figure 4.5**c).[190] The relative motion of graphene planes (*i.e.,* the distortion and dislocation of graphene planes) from the shear mode will lead to changes in low-frequency Raman signal below 200 cm^{-1}.[200]

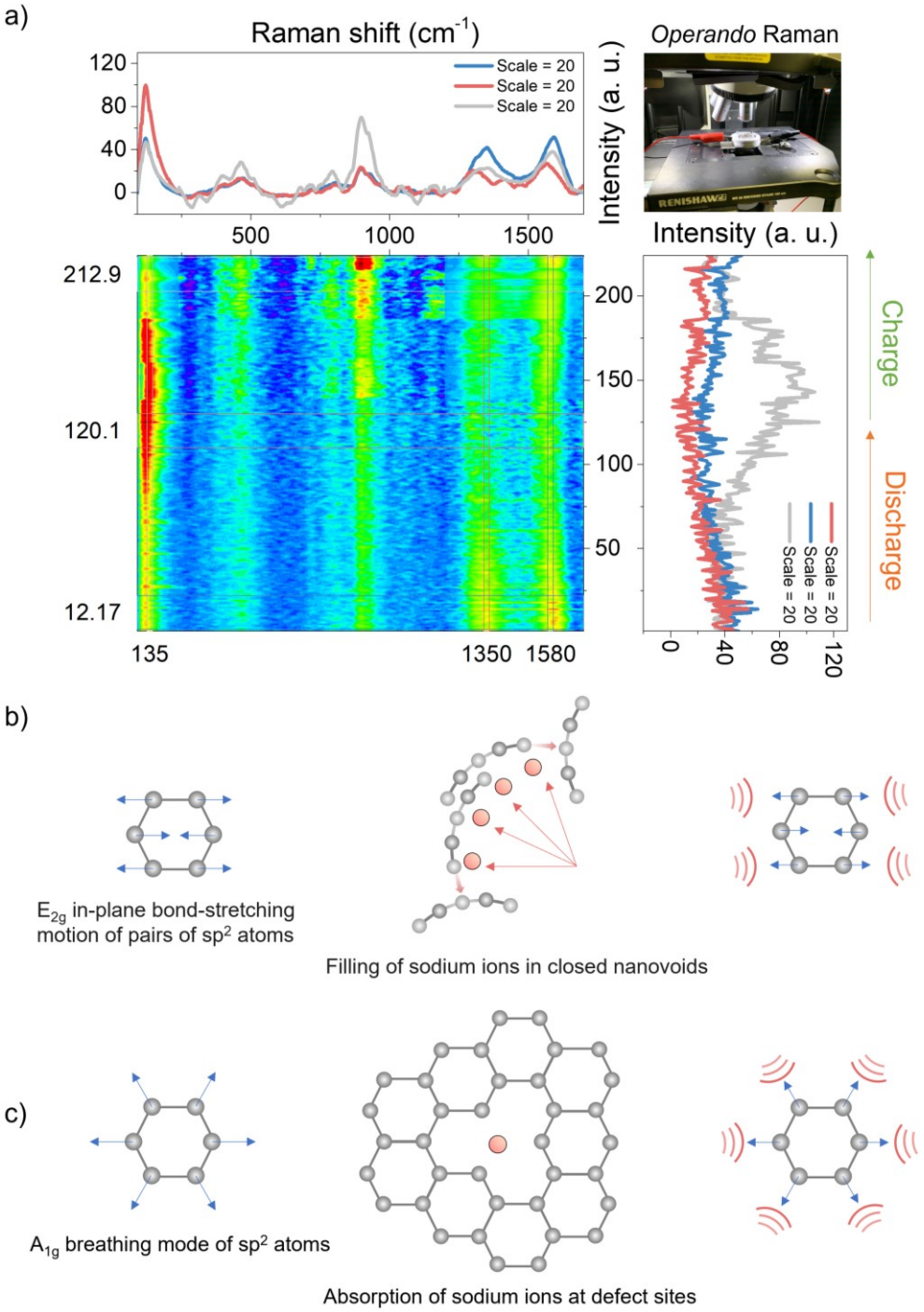


Figure 4.5. a) Full-range *operando* Raman spectra with detailed spectrum at the specific discharge-charge state or at the specific Raman shift of HG1300 in the *operando* cell during the discharge-charge process; b) Schematic illustrations of the pristine E_{2g} in-plane bond-stretching motion of pairs of sp^2 atoms and suppressed G stretching mode by the filling of sodium ions in closed nanovoids enclosed by curved graphene layers; c) Schematic illustrations of the pristine A_{1g} breathing mode of sp^2 atoms of the benzene rings and restricted D breathing mode by the absorption of sodium ions at defect sites.

In the sloping region (> 0.1 V vs Na^+/Na), the D-peak becomes broader and slightly shifts to a lower wavenumber, which indicates sodium ions are interacting with defect sites (*e.g.*,

carbon vacancies, substitutional and interstitial impurities, *etc*.), thus restricting A_{1g} breathing mode of D-band (**Figure 4.5**c).[216] The position of the G-band peak remains almost unchanged in this region, suggesting no sodium ion significantly reacts with sp^2 carbon atoms because the E_{2g} stretching mode of G-band is highly sensitive to ion doping.[217] Meanwhile, the low-frequency Raman signal responsive to the plane de-coupling is still not observed, further implying that sodium ions' interaction with defect sites belongs to the adsorption mode without any evident inner shearing (**Figure 4.4**b).[200] Consequently, the adsorption mode of sodium ions at defect sites as the surface-controlled reaction dominates in the sloping region, and the fast electrochemical kinetics in this region can also be explained by this phenomenon.

During the plateau region (< 0.1 V vs Na^+/Na), the D-peak becomes broader and shifts to a lower wavenumber. This implies that the interaction between sodium ions and defect sites still exists.[216] As observed above, the surface-controlled currents in this region can also be correlated to the existence of adsorbing sodium ions at defect sites. Nevertheless, the decrease in the G-band peak position can be observed along with an increase in its width in the plateau region, which means the length of the C-C bonds is changed by the charge transfer from sodium atoms to π^* antibonding orbitals of carbon atoms.[217] Namely, sodium ions diffuse to suitable inner voids enclosed by curved graphene layers and interact with sp^2 carbon atoms, thus affecting the E_{2g} stretching mode of the G-band (**Figure 4.5**b).[215] Notably, the sharp low-frequency Raman feature is now observed. During the plateau region, the intensity of the low-frequency Raman signal becomes stronger, and its position also increases by 15 cm^{-1}. This trend provides further evidence that the reaction of sodium ions within closed nanovoids *via* a kind of filling and expansion mode by interacting with more accessible sp^2 carbon atoms; this reaction increases the inner shearing stress and disordered degree of the carbon bulk phase *via* the dislocations of graphene planes (insets in **Figure 4.4**b).[200] As this reaction continues in the filling mode, the E_{2g} stretching mode of G-band is eventually significantly suppressed (**Figure 4.5**b). By linking the structural changes observed in this section with the previous kinetic analysis, I can conclude that this filling mode of sodium ions into closed nanovoids needs to overcome large energy barriers, and proceeds with slow kinetics as the diffusion-controlled reaction.

For the duration of the de-sodiation process, D- and G-band peaks both gradually shift

back towards their original position, and the low-frequency Raman signal decreases, combined with the steady recovery of their widths, which suggests the reversibility of the sodium-ion storage behaviours as well as the structural stability of HG1300. In **Figure 4.4**b, compared with HG1300, DG1300 which is less defective with narrower nanovoids, hence, can accommodate fewer sodium ions.

In addition to *operando* Raman spectra, electrochemical impedance spectroscopy (EIS) (**Figure 4.4c**) and *ex-situ* X-ray photoelectron spectroscopy (XPS) **(Figures 4.4**d and e) of cycled HG1300 and DG1300 at the same de-sodiated state are used to analyse the interface conditions. For EIS analysis, the obtained Nyquist plots can be separately represented by the specific resistor and capacitor elements in a Randles equivalent circuit presented as follows:[33]

$$Z = R_S + \frac{1}{j\omega C_{dl} + \frac{1}{R_{ct1}}} + \frac{1}{j\omega C_{dl} + \frac{1}{R_{ct2} + W_o}} \qquad \text{Equation 4.1}$$

where Z (Ω), R_s (Ω), R_{ct} (Ω) are the impedance, inner resistance (*e.g.,* intrinsic electrical resistances of electrode materials, electrolyte, current collector, *etc.*) and charge-transfer resistance, respectively. The equivalent series resistance (ESR) can be calculated according to the sum of R_s and R_{ct} (Ω). Furthermore, C_{dl}, C_l and W_o represent the double-layer capacitance, low-frequency mass capacitance and Warburg constant-phase element respectively. With the frequency changing from 0.01 Hz to 100 kHz, the dynamics of detected processes vary from slow (*e.g.,* diffusion in liquid) to fast (*e.g.,* charge transfer, electron migration, *etc*.).[31] In the low-frequency region, the long sloping line corresponds to the ion diffusion in liquid and capacitive accumulation on the surface. According to the slope differences in the low-frequency regions of HG1300 and DG1300, the ion diffusion in liquid and capacitive accumulation on HG1300 are faster.[31] At the de-sodiated state, as SEI fully covers the carbon surface, the charge must transfer through two interphases before reaching the current collector. One is the transfer within SEI (S1), and the other is the transfer within carbons (S2) (**Figure 4.4**f). Therefore, the small curved feature is composed of two separate semicircles in the high-frequency region.[218] By fitting the Nyquist plot, two different charge-transfer resistance parts of HG1300 can be individually achieved (**Table 4.2**), whose values are both smaller than those of DG1300. In addition, the HG series all have smaller ESR than the DG series (**Figure A1.11**, Appendix). The smaller R_{ct} of S2 of HG1300 results from its spherical morphology and hierarchical pore

structures resulting from the hydrothermal pre-treatment. Especially, the smaller R_{ct} of S1 of HG1300 suggests the thinner SEI layer upon HG 1300 with the better ionic conductivity, compared with DG1300.

Table 4.2. Fitted elements of EIS of HG1300 and DG1000 at the same de-sodiated state.

	Rs	CPE1-T	CPE1-P	Rct1	CPE2-T	CPE2-P	Rct2	W1-R	W1-T	W1-P
HG1300	8.4	3.7×10^{-5}	0.69	24.3	1.6×10^{-5}	0.99	24.8	768.1	1.90	0.60
DG1300	6.6	8.2×10^{-6}	1.1	33.2	3.8×10^{-5}	0.72	76.1	2719	0.83	0.41

Unit: Ω

Furthermore, the ionic conductivity of SEI is related to its composition, which is evaluated by *ex-situ* XPS here. The *ex-situ* XPS study was performed after the first discharge-charge process. A vacuum transfer capsule was used to load the samples from the glovebox to the XPS facility to protect the samples from surface contamination. After fitting C 1s, O 1s, Na 1s and Cl 2p core-level XPS spectra of the cycled samples (**Figure 4.4**d and **Figure 4.6**, Appendix), the atomic composition of the SEI layer is unveiled (**Figure 4.4**e). The peaks of C-C/C=C (~284.8 eV), C-O (~287.0 eV), C=O (~288.6 eV) and Na_2CO_3/$ROCO_2Na$ (~290.0 eV) can be observed in both HG1300 and DG1300. Secondly, the peaks of O-I (~531.5 eV), O-II (~532.5 eV), O-III (~535.5 eV) and Na_2CO_3/$ROCO_2Na$ (~530.5 eV) can be identified in O 1s core-level XPS spectra. For the SEI layers on the surface of HG1300 and DG1300 (**Figure 4.4**e), both are the mixture of organics and inorganics. However, the calculated proportions of organics (~ 66.3 at%), are dominant in the SEI layer of HG1300 according to fitted XPS spectra, which is higher than that of DG1300 (~ 58.1 at%). As a result, the formed SEI on HG1300 may be expected to exhibit better flexibility. Such a kind of SEI layer model supported by the organic phase (**Figure 4.4**f) can enhance the interface stability and, reasonably, the ionic conductivity upon cycling,[38, 219] which can be correlated with the better cycling performance of HG1300 described before. In contrast, composed of more inorganic components, a kind of mosaic model can be established for the SEI of DG1300 whose extra inorganic compositions with more ceramic features are fragile and brittle during cycling (**Figure 4.4**f).[219, 220]

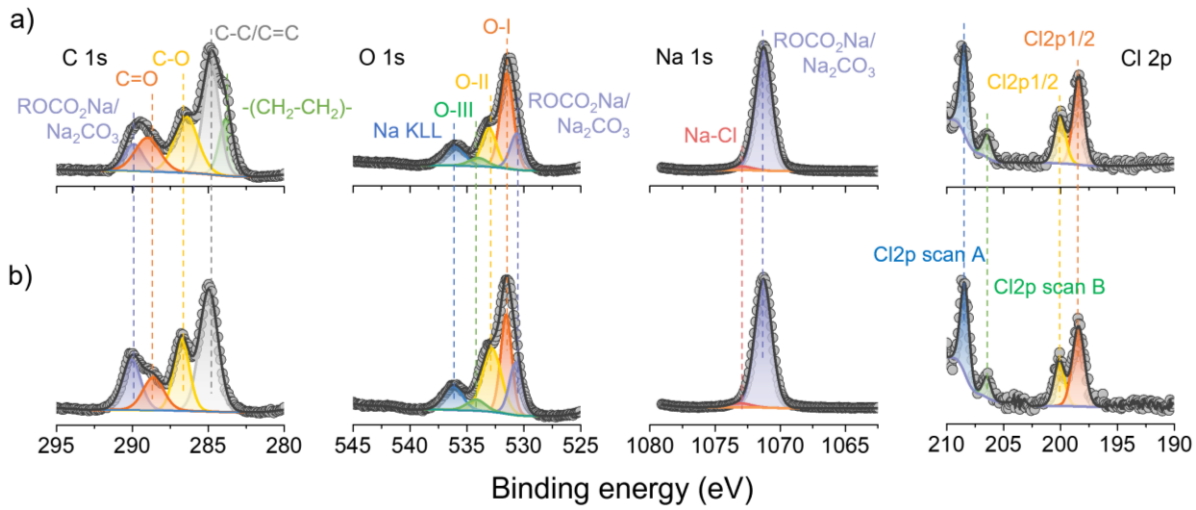


Figure 4.6. Fitted C 1s, O 1s, Na 1s and Cl 2p core-level XPS spectra of a) HG1300 and b) DG1300 after the first discharge-charge process.

In the same electrolyte, the discrepancies in the SEI components can be attributed to the differences in the electrostatic interactions of carbon surfaces with the solvent molecules, which can be estimated using molecular modelling. The obtained electrostatic potential maps of electrolyte molecules (**Figure 47**a) show that the negative charge region (red) is mainly concentrated on the oxygen atoms of C=O groups of EC, followed by the polarization of EC into a local dipole.[221] At the same time, oxygen atoms in the functional groups can de-localise the charges on carbon atoms to form a positive charge region, namely another local dipole. Based on the previous XPS characterisation, HG1300 has more enriched oxygen functional groups than DG1300. Therefore, HG1300 has more possibility to form the local dipoles. These local dipoles between carbons and organic solvent molecules can strongly interact with each other (**Figure 4.7**a) to induce a more homogenous decomposition of organic solvent molecules on the surface of HG1300.[221]

In addition, the finite element simulation taking material morphologies into account was also performed to assess the uniformity of the ion flux, which can affect the electrolyte decomposition and sodium ion diffusion (**Figure 4.7**b). The 2D electric field distributions around HG1300 and DG1300 are first presented in **Figure 4.7**c. The blue substrates represent carbons with two different surface scenarios, and the colourful areas surrounding the substrate are defined as the changes of the electric field distributions. Hence, the electric field distribution can represent the voltage change rate with various ion flux densities. In **Figure 4.7**c, the spherical morphology of HG1300 can homogenise the ion flux to stabilise the

interface condition. At the same time, the sharp tips on the irregular morphology of DG1300 can lead to uneven electric field distributions,[222] which will be very dangerous during the fast charge-discharge process. The concentrated ion flux around DG1300 can result in the precipitation and random nucleation of metallic sodium during the fast charge-discharge process, thus forming uncontrollable sodium dendrites in the end.[216] Moreover, the 3D electric field distributions and voltage changes around HG1300 are further simulated to comprehensively predict the ion flux of HG1300 (**Figure 4.7**d). The grey substrate represents HG1300 in the 3D simulation. Differing from the ideal 2D model, the ion flux will concentrate on the top of HG1300 spheres to some extent in the 3D model under a vertically applied voltage. In short, the homogenous ion flux and uniform voltage change can be still observed in **Figure 4.7**d, which benefits from the spherical morphology of HG1300. A more ordered morphology leads to a more predictable ion flux. The 3D model further proves the advantages of structural pre-stabilisation using the hydrothermal pre-treatment.

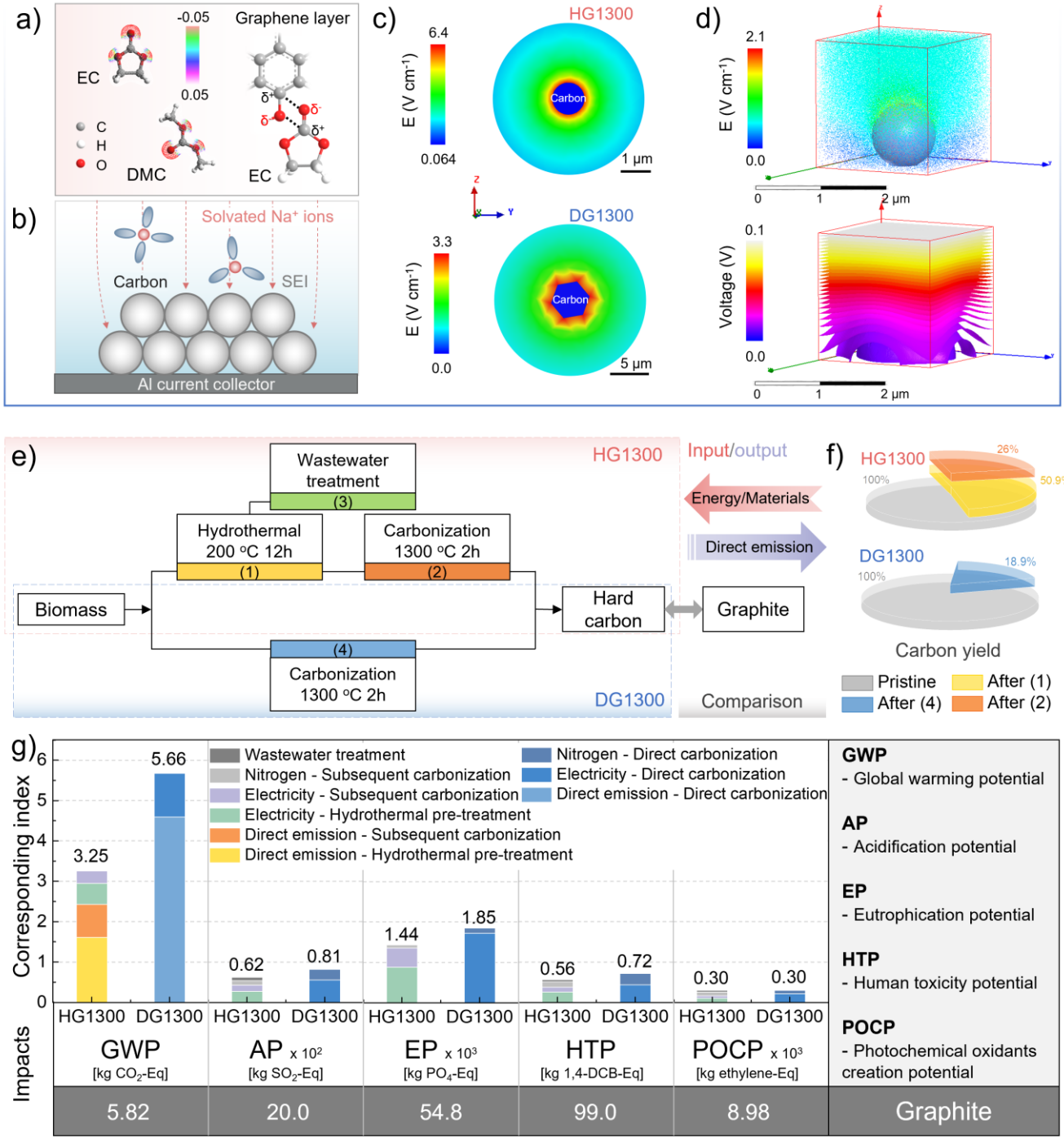


Figure 4.7. Modelling and assessment. a) Electrostatic potential mapping of EC and DMC with the dipole-dipole interaction between EC and oxygen functional groups of carbons; b) The schematic illustration of the uniform sodium-ion flux from the electrolyte to carbon spheres; c) 2D electric field distribution vector profiles of the sodium-ion flux from the electrolyte to spherical HG1300 and lumpy DG1300 under a constant electric field of 0.1 V; d) The 3D electric field distribution vector profile and voltage change profile of the sodium-ion flux from the electrolyte to spherical HG1300 under a constant electric field of 0.1 V. e) The life cycle diagram of the preparation of hard carbons from the same precursor *via* two different routes for sodium-ion batteries, compared with graphite for lithium-ion batteries; f) The measured carbon yields at different stages of routes for HG1300 and DG1300; g) The calculated

environmental impacts of hard carbons including HG1300 and DG1300 from two different routes for sodium-ion batteries, compared with those of graphite for lithium-ion batteries.

4.5 Life cycle assessment of hard carbon anodes for sodium-ion storage

I have shown that the hydrothermal pre-treatment can improve the performance and stability of hard carbons for sodium-ion batteries. In addition to the electrochemical performance, it is equally of great significance to evaluate the sustainability of hard carbons from the hydrothermal process for sodium-ion batteries. Life cycle assessment (LCA) studies have been widely used to study the hydrothermal process of different feedstocks for applications like bioenergy production, heat and electricity production.[223, 224] However, the LCA study on hydrothermal carbons for energy storage is non-existent and urgently needed, in particular for sodium-ion batteries. Hence, based on the standard of ISO 14040:2006 and the databases of Product Environmental Footprints (PEF) and Ecoinvent,[194] an innovative LCA study can be conducted using openLCA software to demonstrate the sustainability of the hydrothermal process of biomass for the battery technology beyond lithium. The detailed inventory data used for LCA are listed in **Table A1.1** (Appendix).

As shown in **Figure 4.7**e, the hydrothermal process, the subsequent carbonisation and the wastewater treatment are individually defined in the route for HG1300. Meanwhile, the direct carbonisation is also defined in the route for DG1300. According to **Figure 4.2**a and **Figure 4.7**f, the additional hydrothermal process not only enhances the specific capacity from 261.3 to 347.4 mAh g^{-1} but also increases the carbon yield from 18.9 to 26.0 %, which makes a significant impact at larger scales. Here, the life cycle impact (LCI) assessment is calculated to show the five main environmental impact factors of the two different scenarios at the kilogram (kg) level, including global warming potential (GWP), acidification potential (AP), eutrophication potential (EP), human toxicity potential (HTP) and photochemical oxidants creation potential (POCP), using the CML 2001 method.[195] First of all, the theoretical specific capacity of graphite anodes in lithium-ion batteries is 372 mAh g^{-1}. Hence, the capacity of 1 kg of graphite anodes for lithium (372 Ah) is equal to the capacity of 1.07 kg of HG1300 or 1.42 kg of DG1300 for sodium according to their measured specific capacities, which enables us to normalise and standardise the comparison between my samples and commercial graphite.

Furthermore, based on their carbon yields, the glucose resource required by HG1300 and DG1300 are 4.12 and 7.51 kg, respectively, for the production of hard carbons with the standard capacity of 372 Ah.

Figure 4.7g and **Table A1.2** (Appendix) show the calculated environmental impact factors of HG1300 and DG1300 for sodium-ion batteries. The GWPs of HG1300 and DG1300 are 3.25 and 5.66 kg CO_2 eq/kg, respectively. Among them, the direction carbon emissions per kg of HG1300 (2.43 kg CO_2 eq/kg) are much lower than those of DG1300 (4.59 kg CO_2 eq/kg). Moreover, the GWPs generated by the electricity of the hydrothermal process (0.52 kg CO_2 eq/kg) and subsequent carbonisation (0.30 kg CO_2 eq/kg) for HG1300 are also lower than that for DG1300 (1.08 kg CO_2 eq/kg). Hence, even though the hydrothermal pre-treatment represents an extra step in the preparation of HG1300, its energy consumption and resulting carbon emissions are lower than those of the one-step carbonisation for DG1300. These trends all result from the increased carbon yield and enhanced specific capacity of HG1300 contributed by the hydrothermal pre-treatment. In addition, compared with the GWP of graphite (5.82 kg CO_2 eq/kg),[194] HG1300 can also deliver the same capacity with lower GWP (3.25 kg CO_2 eq/kg). Therefore, introducing the hydrothermal pre-treatment into the synthesis route makes the preparation of HG1300 more sustainable when it comes to the GWP factor. In terms of other impact factors such as AP, EP, HTP and POCP, these impact factors can be mainly ascribed to the input of electricity, implying that a higher energy input usually leads to a higher calculated environmental impact factor. Still, compared to graphite, the impact factors of the two scenarios are all reduced by over 95%, which further proves the importance of using renewable precursors and waste recycling towards carbon neutrality in the future. Combined with our reported LCA studies of the hydrothermal process of other feedstocks (*e.g.,* cellulose, *etc*.) for sodium-ion batteries,[194] It can be concluded that the hydrothermal process is a necessary step to pre-treat biomass for sodium-ion batteries, which will result in better environmental impacts than the direct carbonisation of biomass or the production of commercial graphite at scale.

4.6 Practical applications of sodium-ion full cells

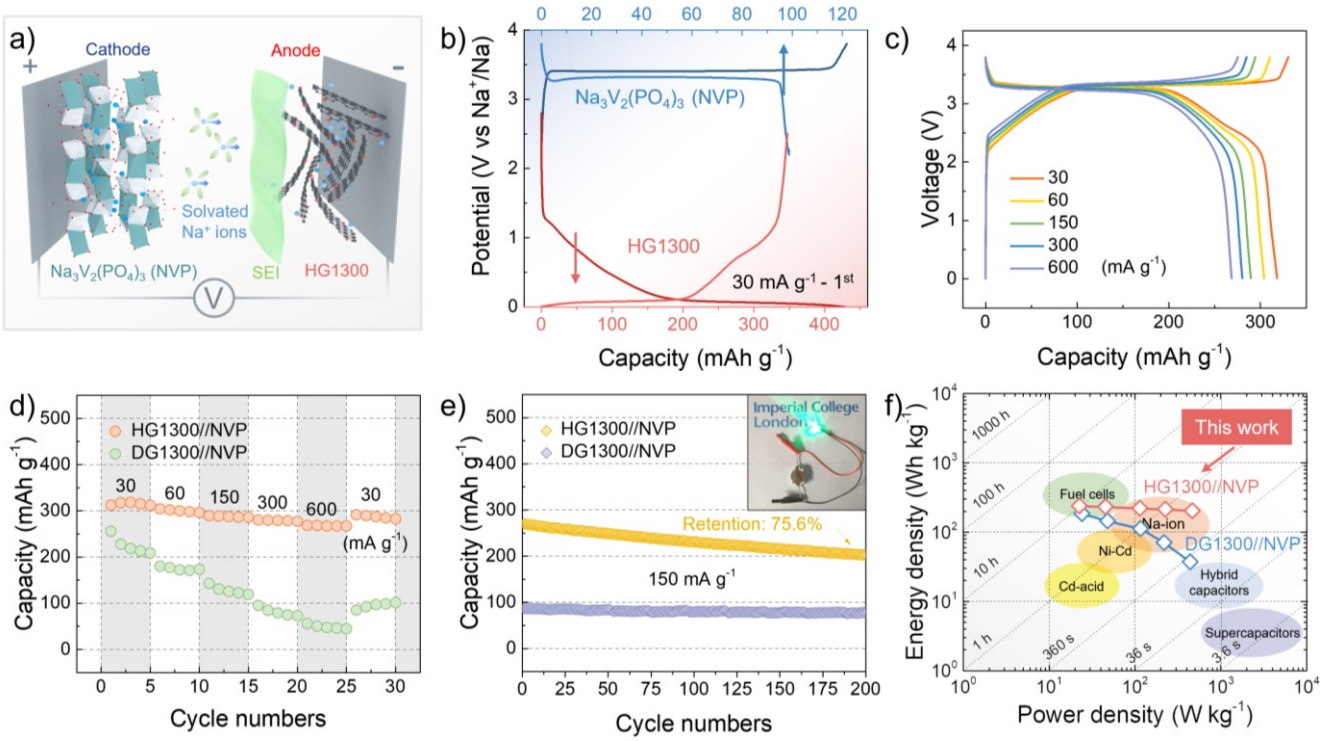


Figure 4.8. Full cells. a) The schematic illustration of the full configuration, where the hard carbon anode is coupled with the $Na_3V_2(PO_4)_3$ cathode during the charge process; b) The first charge-discharge cycles of the hard carbon anode and the $Na_3V_2(PO_4)_3$ cathode in their half-cell configurations at the same current density; c) GCD curves of the full-cell using the HG1300 anode and the $Na_3V_2(PO_4)_3$ cathode (HG1300//NVP) at the current densities of 30, 60, 150, 300, 600 mA g^{-1}, whose capacities are normalized by the active mass of the anode; Comparison of d) the rate performance at the current densities of 30, 60, 150, 300, 600 mA g^{-1}, and e) the cycling performance at 150 mA g^{-1}, between HG1300//NVP and DG1300//NVP whose capacities are normalized by the active mass of the anode, with an inserted image of a LED light powered by the full cell of HG1300//NVP; f) The Ragone plot to compare the energy and power densities of the full cells with other types of energy storage devices, where the energy and power densities are normalised by the overall active mass of both the anode and cathode.

To fully evaluate the potential of my hard carbon anodes in practical applications, sodium-ion full cells were also assembled by coupling the hard carbon anode with a $Na_3V_2(PO_4)_3$ (NVP) cathode (**Figure 4.8**a). From **Figure 4.8**b in the half cell configurations, the specific discharge capacity of HG1300 is 420 mAh g^{-1}, while the specific charge capacity of NVP is 120 mAh g^{-1}. Therefore, the active mass of electrodes is adjusted to make the capacity ratio of the negative to positive electrodes (N/P ratio) around 1.1, which can maximize the energy and power of full-cells and the stability,[41] When a good balance between HG1300 anode and NVP cathode is

achieved, a full cell made of HG1300//NVP with the highest capacity can be fabricated, where the reversible capacity of the full cell is 318.2 mAh g^{-1} at the current density of 30 mA.g^{-1} normalized by the active mass of the anode (**Figure 4.8**c). The average working voltage is 3.5 V. The shape of the GCD curves of HG1300//NVP (**Figure 4.8**c) reflects the combination of synergetic electrochemical reactions between HG1300 and NVP, where the plateau and sloping regions of the full cell correspond to the plateau and sloping regions of HG1300. Along with increased current densities of 60, 150, 300 and 600 mA g^{-1}, the capacity of the full-cell becomes 304.1, 289.5, 280.2 and 268.5 mAh g^{-1}, respectively (**Figure 4.8**d), suggesting an excellent rate performance and ability to fast-charge. When the current density is reversed back to 30 mA g^{-1}, the capacity shows excellent reversibility and reaches the original value. In comparison, the full cell of DG1300//NVP exhibits a lower initial capacity of 255.7 mAh. g^{-1} and an inferior rate performance with a capacity retention of only 17.4 % (**Figure 4.8**d and **Figure A1.12**, Appendix) as a result of the poor electrochemical performance of DG1300. Additionally, when the current density returns to 30 mA g^{-1}, the capacity cannot recover to the initial value. After 200 cycles at 150 mA g^{-1}, the capacity retention of the HG1300//NVP full cell is 75.6 % (**Figure 4.8**e). From the inset in **Figure 4.8**e, the green LED light can be successfully powered by an HG1300//NVP full cell even after 200 cycles, which further demonstrates the full cell's excellent stability. Finally, the calculated energy and power densities of HG1300//NVP and DG1300//NVP are presented in **Figure 4.8**f. For HG1300//NVP, the energy densities can reach 237.8, 230.2, 219.4, 211.9 and 201.5 Wh kg^{-1} when the power densities are 22.6, 45.6, 114.5, 227.8 and 468.6 W kg^{-1}, respectively, which are much higher than those of DG1300//NVP. The full cell configuration therefore further confirms the importance of the hydrothermal pre-treatment for bio-derived carbon anodes. In addition, the energy and power densities of HG1300//NVP are superior to other energy devices, while also being very competitive with those state-of-the-art sodium-ion batteries (**Table 4.3**). Generally, this work successfully paves the way for the next-generation sodium-ion batteries using the hydrothermal bio-derived carbons. By coupling my anode with a sodium layered metal oxide cathode, the energy and power of the full cell can be further enhanced close to the commercial lithium-ion batteries.

Table 4.3. Comparison of energy densities of sodium-ion batteries.

Sodium batteries (Anode-Cathode)	Energy density (Wh kg^{-1})	References
HCT//$Na_{0.9}[Cu_{0.22}Fe_{0.30}Mn_{0.48}]O_2$[57]	207	*Adv. Energy Mater.* **2016**, 1600659
CCD//$NaNi_{1/3}Fe_{1/3}Mn_{1/3}O_2$[34]	248	*J. Mater. Chem. A*, **2019**, 7, 27567
HC//$Na_{0.72}[Li_{0.24}Mn_{0.76}]O_2$[123]	270	*Joule*, **2019**, 3, 503
$Na_2Ti_3O_7$//$VOPO_4$[225]	220	*Energy Environ. Sci.* **2016**, 9, 3399
HG1300//NVP	238	This work

4.5 Conclusions

In this chapter, for the first time, I provide a comprehensive understanding of the critical role played by the hydrothermal carbonisation process in designing sustainable sodium-ion battery anodes by comparing two different scenarios with and without a hydrothermal pre-treatment. By correlating the structural differences in hard carbons with their electrochemical sodium-ion storage behaviours, the extra active sites including defects and nanovoids introduced by the hydrothermal pre-treatment are responsible for the enhanced electrochemical performance in sodium-ion batteries. Based on the electrochemical kinetic analysis and *operando* measurements, a modified sodium-ion storage mechanism in hard carbons is unveiled in detail. Precisely, the adsorption mode of sodium ions at defect sites in the whole region, especially in the sloping region, can be confirmed. In contrast, the filling mode of sodium ions at nanovoids in the plateau region can be demonstrated through *operando* Raman spectroscopy of hard carbons. Using a combination of *ex-situ* characterisation and multi-scale modelling, I also obtain fundamental insights into sodium-ion diffusion behaviours and interfacial phenomena including the SEI compositions, which confirm the benefits of the spherical morphology and hierarchical pore structures to the uniform ion flux as well as the functions of surface oxygen groups for the homogenous interface characteristics. Along with the exceptional performance metrics, the sustainability of material synthesis and battery application is also considered from a life cycle perspective. The life cycle assessment is innovatively used to quantify the superior

sustainability of bio-derived hard carbons for sodium-ion batteries. The hydrothermal carbonisation process is shown to pre-stabilise the carbon morphologies and structures, increasing the overall carbon yield and decreasing the carbon emission simultaneously. In conclusion, the hydrothermal carbonisation process is a necessary step to pre-treat biomass and produce high-performance hard carbons with real sustainability for sodium-ion batteries, thereby providing a promising opportunity for the development of next-generation sustainable batteries beyond lithium.

Chapter 5. From cellulose to sodium-ion capacitors

- All-cellulose-based quasi-solid-state sodium-ion hybrid capacitors enabled by structural hierarchy

Sodium-ion hybrid capacitors based on the capacitor-type carbon cathode and the battery-type anode can fill the technology gap between high-energy batteries and high-power supercapacitors. However, the traditional activated carbons for the cathode part of sodium-ion capacitors are prepared from non-renewable fossil fuel-based resources. Meanwhile, most high-performance hard carbons for the anode part of sodium-ion capacitors require high-temperature annealing (over 1000 ºC) during the preparation process, which consumes a huge amount of energy. Therefore, I look into a kind of sustainable and high-performance sodium-ion capacitor whose compositions are all derived from cellulose through the energy-saving fabrication processes (~ 1000 ºC).

In this chapter, I proposed the facile and sustainable strategies to develop NIC anodes and cathodes from cellulose nanocrystals and microfibrils, respectively. Low-temperature pyrolysis of cellulose nanocrystals was employed to prepare carbon nanorods with self-assembled 3D structures as anodes in NICs, while hydrothermal carbonisation (HTC) and co-activation of cellulose microfibrils were used to prepare coral-like hierarchically porous carbons as cathodes for NICs. The unique multiscale structures were designed to mimic biological materials in order to fabricate high power-energy carbon electrodes, thus optimizing the energy and power density of the full cells. In comparison to less complex morphologies, hierarchical structures can promote fast ion transport through their ordered frameworks with hierarchical pores or efficient ion storage in the active sites including defects and nanopores.[226] Besides the individual characteristic performances of my carbon electrodes, the main factor affecting the performance of full cells is the imbalance of kinetics between diffusion-controlled processes and surface-controlled behaviours, since the Faradic reactions in anodes are much slower than the non-Faradic reactions in cathodes.[163] Consequently, the kinetics of anodes and cathodes in half cell configurations were investigated to select the best voltage windows for the asymmetric configuration. Moreover, I have fabricated renewable membranes from modified cellulose as

hosts for gel polymer electrolytes to build an all-cellulose-based quasi-solid-state system, which could exhibit good performance in terms of the high operating voltage from 1.3-4.2 V. During the fabrication of my electrodes and electrolytes, eco-friendly binders and solvents rather than toxic and expensive ingredients were used.

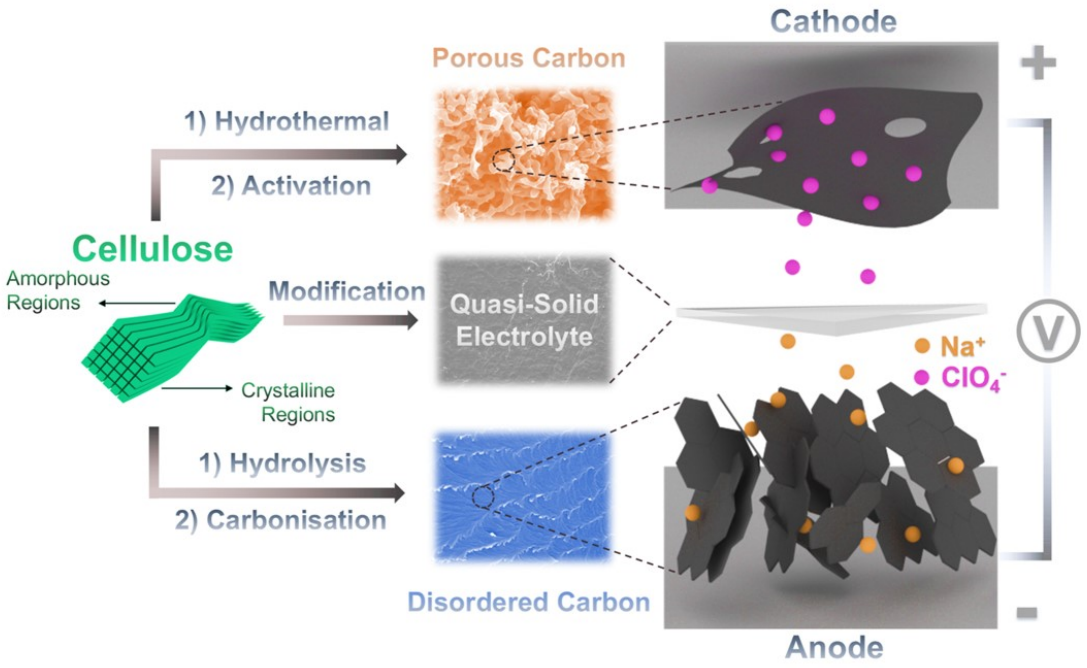


Figure 5.1. Schematic diagram illustrating the 'one-for-all' synthesis processes of electrodes and electrolytes as well as the asymmetric configuration of NICs.

In nature, cellulose always appears as a hierarchical assembly of building blocks rather than a single molecule. As shown in **Figure 5.1**, the elementary fibril of cellulose comprised of individual cellulose molecules can pack into larger units including micro- and macro-fibres.[177] Cellulose microfibrils can be obtained from natural materials using the mechanical fibrillation. Furthermore, the cellulose biopolymer possesses both amorphous and crystalline domains which have different kinetics of acid hydrolysis; therefore, the cellulose microfibres can be further converted into either nanofibres or nanocrystals.[22, 180, 227] These different components isolated from cellulose represent ideal precursors for hierarchical carbon materials. For NICs, on the anode side, nonporous hard carbons with structural hierarchy were obtained through direct thermal pyrolysis of cellulose nanocrystals (NC) at different temperatures (800, 1000 and 1300 °C) (CNC800, CNC1000 and CNC1300). In order to directly probe the influence of hierarchy on their electrochemical performance, I have also produced hard carbons *via* the direct carbonisation of cellulose microfibres at 1000 °C (CMF1000). For cathodes,

coral-shape nitrogen-doped carbons (CHKM800) with a hierarchically porous architecture were prepared by $KHCO_3$ and melamine co-activation of hydrochars from cellulose microfibres at 800 °C. Again, to probe the influence of hierarchy on the cathode performance I also produced microporous only carbon (CHK800) *via* the KOH activation at 800 °C. To prepare the gel electrolyte, the hydroxyethyl cellulose (HEC) which is soluble in water but insoluble in most organic solvents has been used as the host for gel polymer electrolytes. The asymmetric configuration of NICs is also shown in **Figure 5.1**. During the charge process, the Na^+ ions move into the carbon anode, while the counter ions are adsorbed onto the carbon cathode.

5.1 Carbon anodes from cellulose nanocrystals

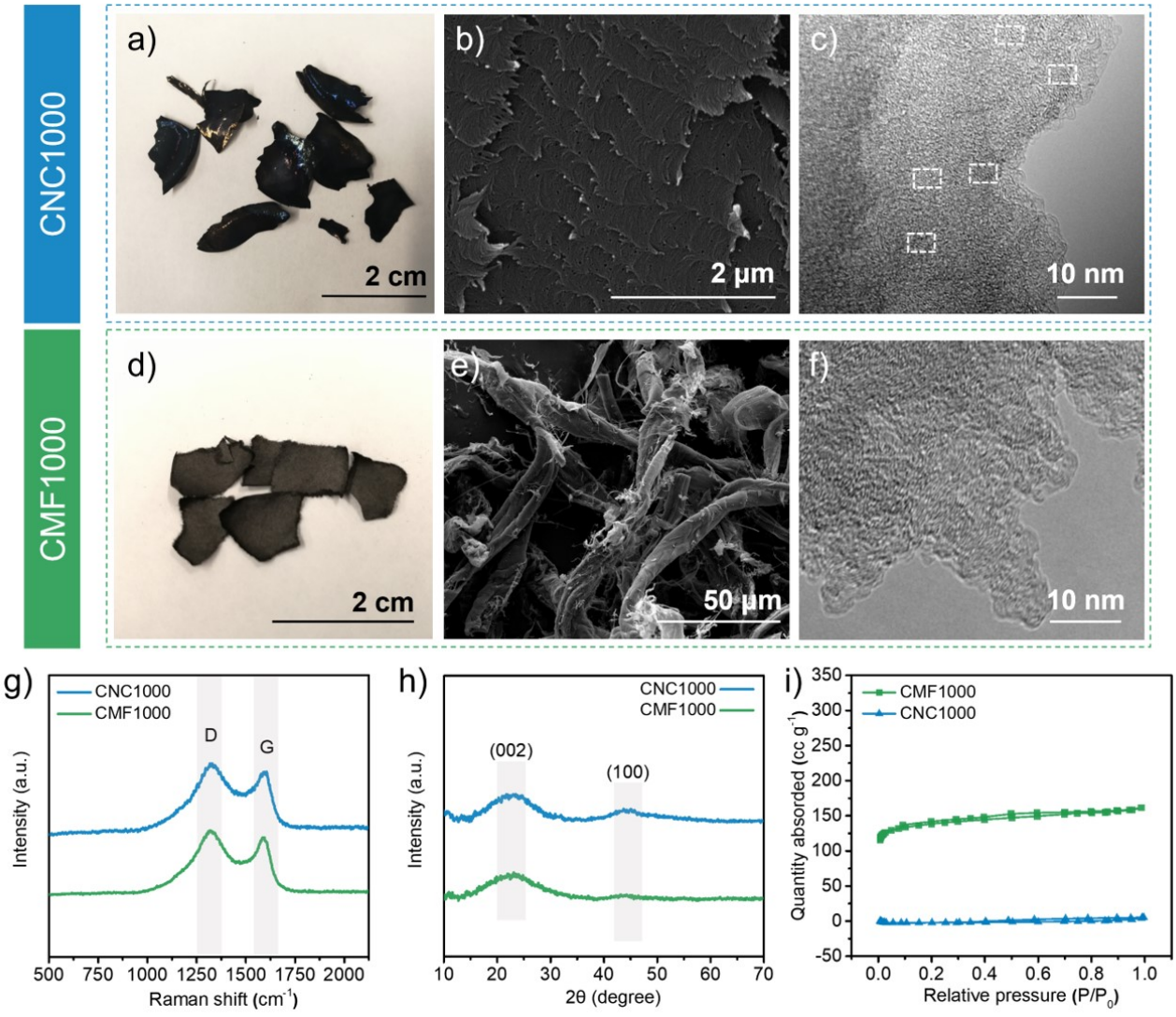


Figure 5.2. Material characterisation of carbon anodes. a) Photograph, b) SEM image and c)

TEM image of CNC1000; d) Photograph, e) SEM image and f) TEM image of CMF1000 g) Raman spectra, h) XRD patterns, and i) N_2 adsorption/desorption isotherms (77 K) of CNC1000 and CMF1000.

After the acid hydrolysis, the cellulose microfibres can be separated into NCs. Upon carbonisation at 1000 ºC, as observed from **Figure 5.2**a, CNC1000 forms a free-standing but brittle film. The scanning electron microscope (SEM) image (**Figure 5.2**b) shows that the carbon film is hierarchically nanostructured, being formed of carbonised NC units which could maintain their morphology after the high-temperature carbonisation. From the transmission electron microscope (TEM) image of CNC1000 (**Figure 5.2**c), both amorphous and short-range ordered (white-squared areas) regions are identified, which belongs to the features of hard carbons. The ordered nanodomains are beneficial to the fast electronic and ion transport, while the turbostratic regions could provide more active sites to store sodium ions (Na^+).[228] Compared with CNC1000, the morphology of CMF1000 consists of a disordered arrangement of fibrils (**Figures 5.2**d and e). From **Figure 5.2**f, CMF1000 also shows a typical pseudographitic structure. The Raman spectra of CNC1000 and CMF1000 both show broad D- and G- peaks (**Figure 5.2**g), as the typical disordered stage II materials described by Ferrari *et al.*, [190, 206-208] in which the intensity ratio of D-band to G-band (I_D/I_G) increases with a decrease in the density of defects among graphite layers. Based on the calculated values of I_D/I_G, the graphene planes of CMF1000 are more defective than those of CNC1000. In addition, with the increase in the carbonisation temperature, the I_D/I_G and average in-plane distance (L_a) increases (**Table 5.1**), which means the structures of hard carbons prepared at the higher temperatures have fewer defects within graphene layers. For X-ray diffraction (XRD) studies (**Figure 5.2**h), two peaks located at $2\theta \approx 24°$ and 44° can be detected, attributed to the (002) and (100) planes of expanded graphene layers. In the hard carbons, the calculated average interlayer spacing of graphene layers (d_{002}) is larger than 3.35 Å (**Table 5.1**).[229] According to the N_2 adsorption/desorption isotherms (**Figure 5.2**i), the specific surface area of CMF1000 is much higher (536 $m^2\ g^{-1}$) than that of CNC1000 (21 $m^2\ g^{-1}$). It is worth noting that unlike traditional nanomaterials with high surface areas, the cellulose nanocrystals orderly stack together during the drying process to form an iridescent film with a relatively low surface area as a result of the unique self-assembly of hierarchical layer structures in the long-range.

Table 5.1. Physical parameters of the carbon materials for anodes.

Anode	d_{002}[a] (Å)	$FWHM_{002}$[b] (°)	I_D/I_G[c]	L_a[d] (nm)	S_{BET}[e] ($m^2\ g^{-1}$)
CMF1000	3.87	10.7	1.30	1.02	536
CNC800	3.88	9.6	1.29	1.01	32
CNC1000	3.90	9.5	1.40	1.06	21
CNC1300	3.86	9.1	1.59	1.13	17

[a] d_{002}: Calculated average interlayer spacing of graphene layers by Bragg formula,
[b] $FWHM_{002}$: Fitted full width at half maximum of (002) peaks based on Gaussian models,
[c] I_D/I_G: Intensity ratio of D-peaks to G-peaks,
[d] L_a: Average in-plane distance of the graphene layer.
[e] S_{BET}: Specific surface areas calculated using the multipoint Brunauer-Emmett-Teller (BET) method.

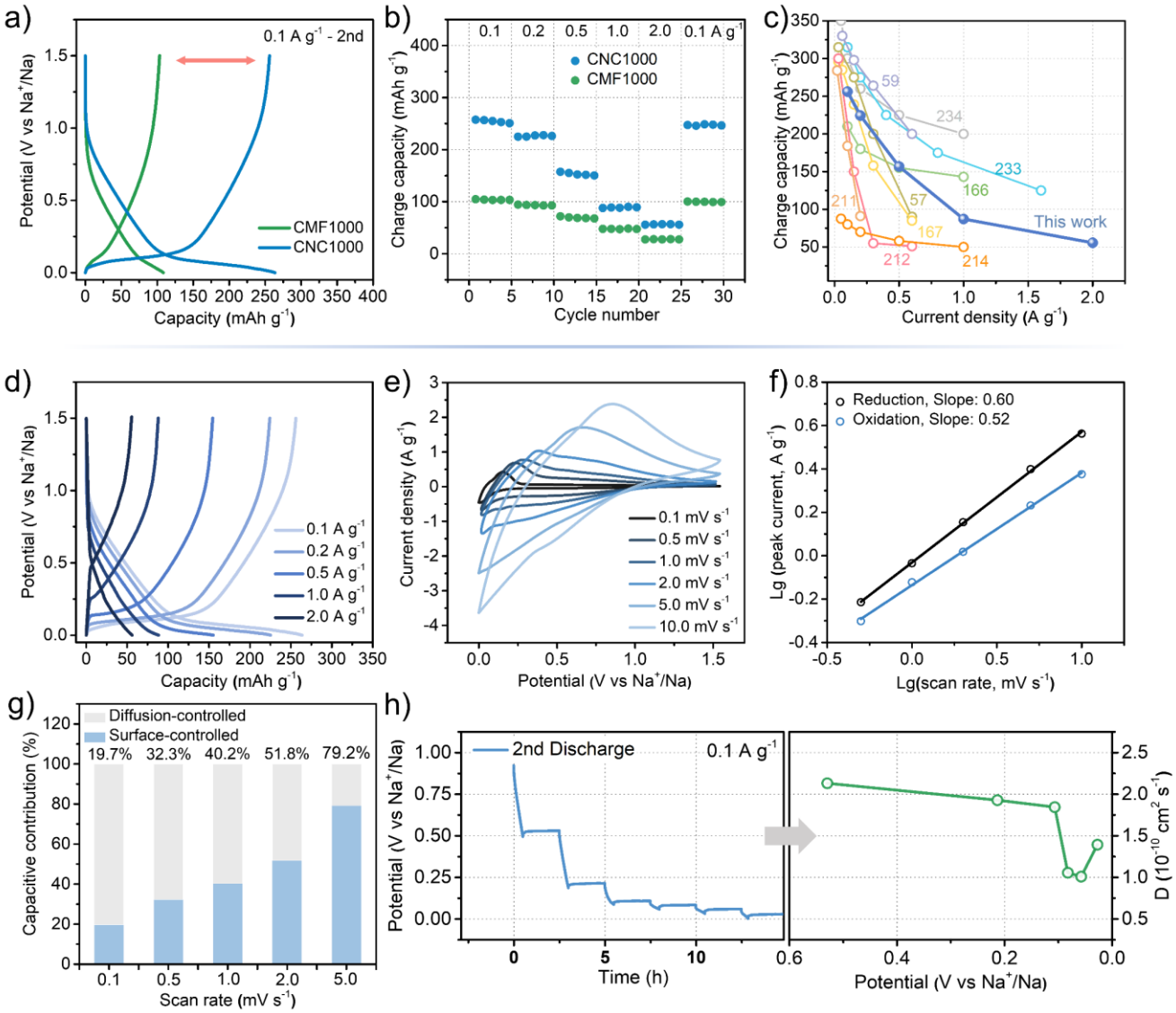


Figure 5.3. Electrochemical testing of carbon anodes in half cells. Comparison of a) Specific capacities and b) Rate performance of charge capacities of CNC1000 and CMF1000; c) Specific capacities of CNC1000 in comparison to reported anodes in NICs; d) GCD curves of CNC1000 at 0.1 to 2.0 A g^{-1} (the second cycle of each rate current); e) CV curves of CNC1000 at 0.1 to 10.0 mV s^{-1} (the second cycle of each sweep rate); f) Linear relationship between log i and log ν of CNC1000 at different potentials; g) Calculated contribution proportions of the surface- and diffusion-controlled processes at 0.1 to 5.0 mV s^{-1} in CNC1000; and h) GITT profiles of CNC1000 (left) and calculated D_{Na+} (right).

In order to investigate the sodium-ion storage ability of the carbon anodes, half cells were assembled with liquid electrolytes (1 M $NaClO_4$ in ethylene carbonate (EC) and dimethyl carbonate (DMC) (1:1 in volume)) and tested within 0-1.5 V vs. Na^+/Na. **Figure 5.3**a shows the galvanostatic charge/discharge (GCD) curves of different carbon anodes in the second cycle, where CNC1000 can deliver the highest reversible charge capacity of 256.9 mAh g^{-1} at the current density of 0.1 A g^{-1} with an apparent plateau region. In contrast, the charge capacity of

CMF1000 is barely half that of CNC1000 at the same current density. The low initial Coulombic efficiency (ICE) of CMF1000 (33 %) at 0.1 A g^{-1} from 0 to 1.5 V vs Na^+/Na can be related to the extensive formation of solid electrolyte interface (SEI) which is proportional to the surface area and porosity of carbon anodes, thus dramatically increasing the irreversible charge capacity in the first cycle (**Table 5.1** and **Table 5.2**).[230] The unique hierarchical layered structure of cellulose nanocrystals greatly reduces the surface area and the number of the opening pores available for the SEI formation, thereby improving the reversible capacity.[231, 232] In addition, with carbonisation temperatures increasing, the decrease of ratios of sloping regions (**Table 5.2**) is correlated to fewer defect sites based on the report from Titirici, Hu *et al.* where the sloping region corresponds to the adsorption of sodium in defects.[39, 57] For the rate performance, although the almost all-sloping-type charge-discharge feature of CMF1000 can bring a better retention of 27 % at 2.0 A g^{-1}, CNC1000 still has a higher energy at the same current density (**Figure 5.3**b and **Table 5.2**). Whilst CNC1000 and CNC1300 have similar charge capacities at 0.1 A g^{-1}, the poor performance of CNC1300 at higher rates could exacerbate the imbalance between the kinetics of anodes and cathodes (**Figure A2.4**, Appendix). Compared with the previously reported carbonaceous materials[57, 59, 166, 167, 211, 212, 214, 233, 234] where high carbonisation temperatures are used, CNC1000 can deliver a good electrochemical performance after the carbonisation at only 1000 ºC (**Figure 5.3**c). Hence, CNC1000 is the best choice for anodes in the full cell configuration here. Limited power is a common case for high energy battery-type anodes, so the combination with capacitor-type cathodes can be of great benefit to the overall power density of full cells.

Table 5.2. Specific electrochemical performance of the half cells of anodes.

Anode	RCC[a] (mAh g^{-1}, 0.1 A g^{-1})	ICE[b] (%)	RSC[c] (%)	RPR[d] (%, 0.1->2.0 A g^{-1})	CR[e] (%, 2.0 A g^{-1}, 200 cycles)
CNC800	181.3	58	55.4	19	79
CNC1000	256.9	67	41.8	22	91
CNC1300	247.0	76	35.5	5	72
CMF1000	103.2	33	65.2	27	84

[a] RCC: Reversible charge capacity,
[b] ICE: Initial Coulombic efficiency,
[c] RSC: Ratio of sloping region (> 0.2 V vs Na^+/Na) to whole region at charging part of the2nd cycle,
[d] RPR: Rate performance retention,
[e] CR: Cycling retention.

Kinetic analysis of the anodes in half cells reveals that the plateau regions of the GCD curves (< 0.2 V, **Figure 5.3**d) correspond to the redox peaks in the cyclic voltammetry (CV) profiles (< 0.2 V, **Figure 5.3**e), and that the redox peaks in **Figure 5.3**e become broader as the sweep rates increase from 0.1 to 10.0 mV s^{-1}, corresponding to the disappearance of the plateau region in **Figure 5.3**d with increased current densities. The currents in CV curves follow the power law (Equation 3.7 and 3.8). The b-value close to 0.5 means that the electrochemical reaction is based on a diffusion-controlled process, while the b-value approaching 1.0 implies that the electrochemical reaction is a surface-controlled behaviour. In **Figure 5.3**f, the b-values of the reduction and oxidation peaks are 0.60 and 0.52; hence, the capacity at the peak voltage mostly comes from diffusion-controlled processes. Furthermore, since the current response at an applied sweep rate could change in accordance with whether the electrochemical reaction is surface-controlled or diffusion-controlled, the current response can be qualitatively separated into surface-controlled currents (k_1v) and diffusion-controlled currents ($k_2v^{1/2}$) (Equation 3.8). By fitting and calculating k_1 and k_2 (**Figure A2.5**, Appendix), each part of the response current at each specific voltage can be determined, thus distinguishing the diffusion-controlled fraction from the surface-controlled one. When the sweep rate increases from 0.1 to 5.0 mV s^{-1}, the

contribution of diffusion-controlled reactions sharply decreases from 80.3 to 20.8 %, which is a typical phenomenon of high-energy but low-power battery-type anodes (**Figure 5.3**g). From a kinetic point of view, the electrochemical reaction in the sloping region of the GCD curves is similar to a fast-capacitive process, which can also be proved by the fact that the lower-temperature carbons with larger sloping regions have better rate performance. During the faster charge-discharge processes, the loss of capacity is manifested by a decrease in the plateau regions of the GCD curves where the phase transformations with slow kinetics happen. Their slow kinetics result from the relatively slow diffusion of cations in the bulk phase of anodes.

To further study the kinetics of the carbon anodes in half cells, the galvanostatic intermittent titration technique (GITT) was employed to determine the diffusion coefficient of Na^+ ions (D_{Na+}) in the second cycle of the discharge (charge) process (Equation 3.6). CNC1000 was discharged (charged) with a pulse current at 0.1 A g^{-1} for 30 min followed by an interval for 2 h. As shown in **Figure 5.3**h, during the sodiation process, the calculated D_{Na+} slightly decreases in the sloping region, and then sharply decreases in the plateau region, which also confirms that the kinetics of the electrochemical reactions in the sloping region are faster. However, the Faradic reaction in the plateau region provides the majority of the energy within the whole potential range. In order to maximise the energy density of full cells, the capacity from the plateau region should be fully taken advantage of. Faradic reactions in the bulk phase are essential in the battery side, where the electrons transfer across the double layers. The sodium-ion storage mechanism of carbon materials is still under debate, but the kinetics of their electrochemical reactions in sloping and plateau regions clarified here may contribute to the future research on it.

5.2 Carbon cathodes from cellulose microfibrils

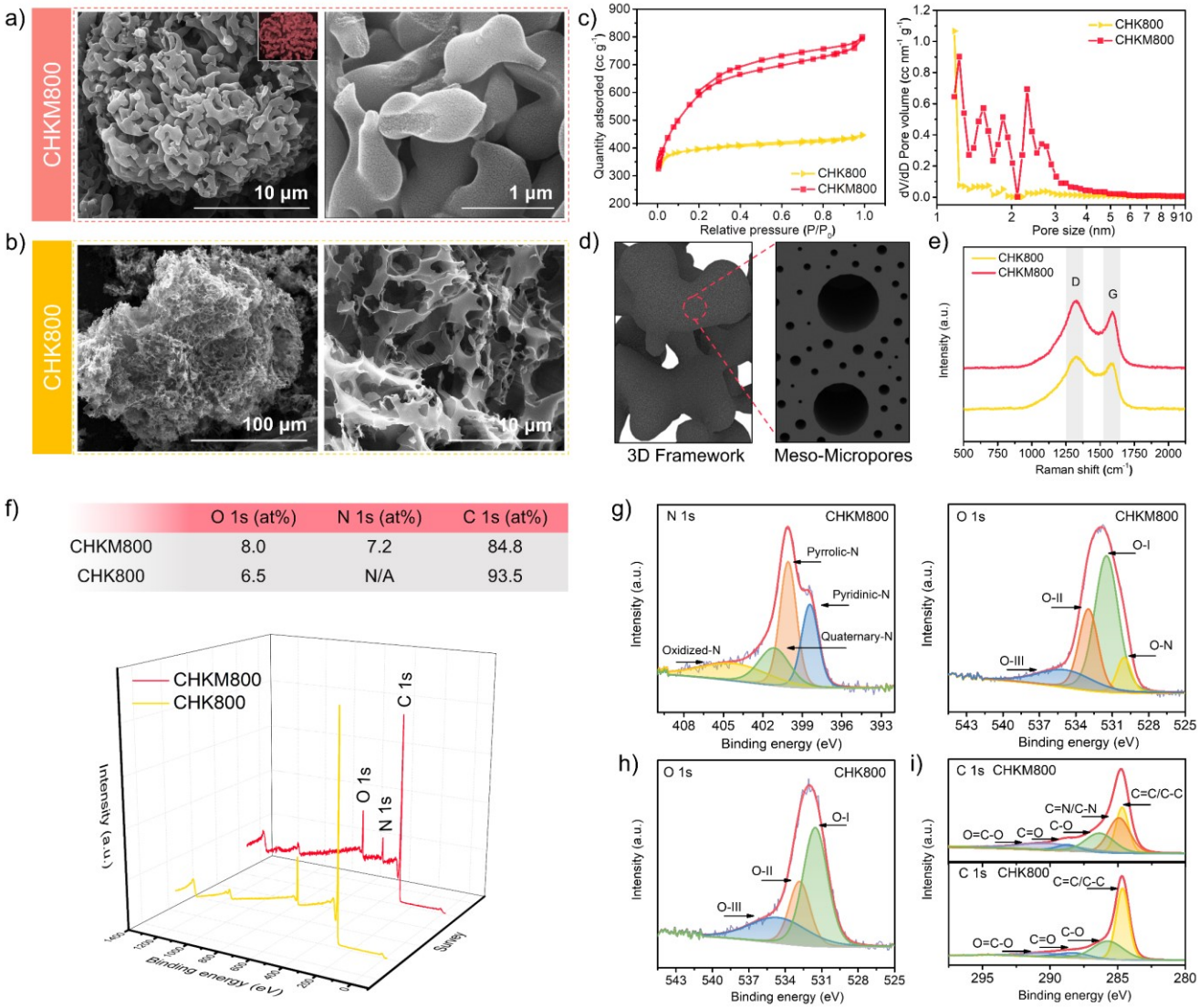


Figure 5.4. Material characterisation of carbon cathodes. a-b) SEM images of CHKM800 with an inserted picture of coral and CHK800; c) Left: N_2 adsorption/desorption isotherms at 77 K, Right: Pore size distributions obtained from the adsorption isotherms based on non-local density functional theory (NLDFT) method, of CHKM800 and CHK800; d) Schematic illustration of the hierarchical pores of CHKM800; e) Raman spectra and f) XPS survey spectra with the atomic percentage of different elements, of CHKM800 and CHK800; g) Fitted N 1s (left) and O 1s (right) core level XPS spectra of CHKM800; h) Fitted O 1s spectrum of CHK800; and i) Fitted C 1s spectra of CHK800 and CHKM800.

The SEM images of the cathode material CHKM800 prepared by $KHCO_3$ and melamine co-activation at 800 °C (**Figure 5.4**a) show coral-shaped 3D networks with a length of the carbon skeletons of about 2 μm. During the co-activation, the carbon skeleton (**Figure A2.6**, Appendix) obtained *via* the hydrothermal carbonisation of cellulose microfibrils shrinks and agglomerates,

thus forming the carbon network. Compared with the co-activation, KOH activation at 800 °C totally destroys the morphology of the carbon microtubes and converts them into sponge-like structures (**Figure 5.4**b) due to the fast gas release during the activation, thus resulting in the lack of interconnections between carbon sponges (CHK800). Instead, the co-activation enables a spherical morphology of carbons, which leads to more compact packing and shorter diffusion paths for ions and electrons compared with the KOH-activated one.[173, 235] Based on the N_2 adsorption/desorption isotherms in **Figure 5.4**c, CHKM800 has the highest specific surface area of 2137 m^2 g^{-1} and the largest total pore volume (V_t) of 1.1 cm^3 g^{-1}, while the specific surface area of CHK800 is 1560 m^2 g^{-1} with the total pore volume of 0.6 cm^3 g^{-1}. **Figure 5.4**c also shows CHKM800 has standard micropores and mesopores where micropores only occupy 68% of the total surface area. Therefore, at the same temperature, co-activation can create larger surface areas and hierarchical pore structures based on the same ratio of activation agent to biochar compared with KOH-activation. XRD and Raman spectroscopy were employed to further investigate the structures of the carbon materials for cathodes. In the Raman spectra (**Figure 5.4**e), the broad D-band and G-band can be observed in all samples, where the D-band and G-band are located at around 1350 cm^{-1} and 1580 cm^{-1} respectively. The XRD patterns (**Figure A2.7**, Appendix) of these carbon samples all have very broad (002) peaks, which means the activated carbons have a high degree of amorphous character. In addition, in accordance with the full width at half maximum (FWHM) of peaks in XRD and Raman spectra (**Table 5.3**), the KOH-activated material (CHK800) is more disordered than the co-activated carbon (CHKM800), proving that co-activation is a milder process.

The functional groups on the near-surface of CHKM800 and CHK800 were characterised to understand the potential pseudocapacitive reactions with anions. The X-ray photoelectron spectroscopy (XPS) spectrum of CHKM800 demonstrates that the amount of nitrogen- and oxygen-doping can reach 7.2 at% and 8.0 at%, respectively (**Figure 5.4**f), while CHK800 contains no nitrogen heteroatoms as shown in Figure 5.3f, where no C-N bonds can be fitted in CHK800 (**Figure 5.4**i). As the activation temperature decreases, the co-activation method can provide more nitrogen-doping (*i.e.,* the amount of nitrogen-doping in CHKM700 is 9.2 at% (**Figure A2.7**, Appendix)). Figure 5.3g reveals four types of nitrogen sites including pyridinic- (N-6, 398.4 eV), pyrrolic- (N-5, 400.1 eV), quaternary- (N-Q, 401.2 eV) and oxidized nitrogen

(404.7 eV) in CHKM800. The pyrrolic- and pyridinic-nitrogen can provide lone pair electrons, thus improving the charge mobility in the carbon matrix.[236] The O 1s spectrum of CHKM800 as shown in **Figure 5.4**g indicates four types of oxygen functional groups containing O-N bonds (530.0 eV), C=O carbonyl groups (O-I, 531.5 eV), C–OH hydroxyl or C-O-C ether groups (O-II, 532.5 eV), and O=C-OH carboxyl groups (O-III, 534.5 eV), where the O-I and O-II groups dominate on the near-surface of CHKM800. The same three types of oxygen functional groups are also observed in CHK800 except for the O-N bonds (**Figure 5.4**h). During the charge process, the lone pair electrons at nitrogen or oxygen sites are easy to be removed by oxidation; therefore, the positively charged functional groups can interact with perchlorates on the near-surface including surface (surface-controlled) and shallow bulk (diffusion-controlled), which is no more a pure physical adsorption of anions.[237]

Table 5.3. Physical parameters of the carbon materials for cathodes.

Cathode	d_{002}[a] (Å)	$FWHM_{002}$[b] (°)	I_D/I_G[c]	L_a[d] (nm)	S_{BET}[e] ($m^2\ g^{-1}$)	V_t[f] ($cm^3\ g^{-1}$)	Micropores (%)
CHK800	2.81	13.6	1.38	1.05	1560	0.607	84
CHKM800	3.25	11.8	1.47	1.08	2137	1.091	68
CHKM700	3.46	10.2	1.54	1.11	1519	0.604	78

[a] d_{002}: Calculated average interlayer spacing of graphene layers by Bragg formula,
[b] $FWHM_{002}$: Fitted full width at half maximum of (002) peaks based on Gaussian models,
[c] I_D/I_G: Intensity ratio of D-peaks to G-peaks,
[d] L_a: Average in-plane distance of the graphene layer,
[e] S_{BET}: Specific surface areas calculated using the multipoint Brunauer-Emmett-Teller (BET) method,
[f] V_t: Total pore volume.

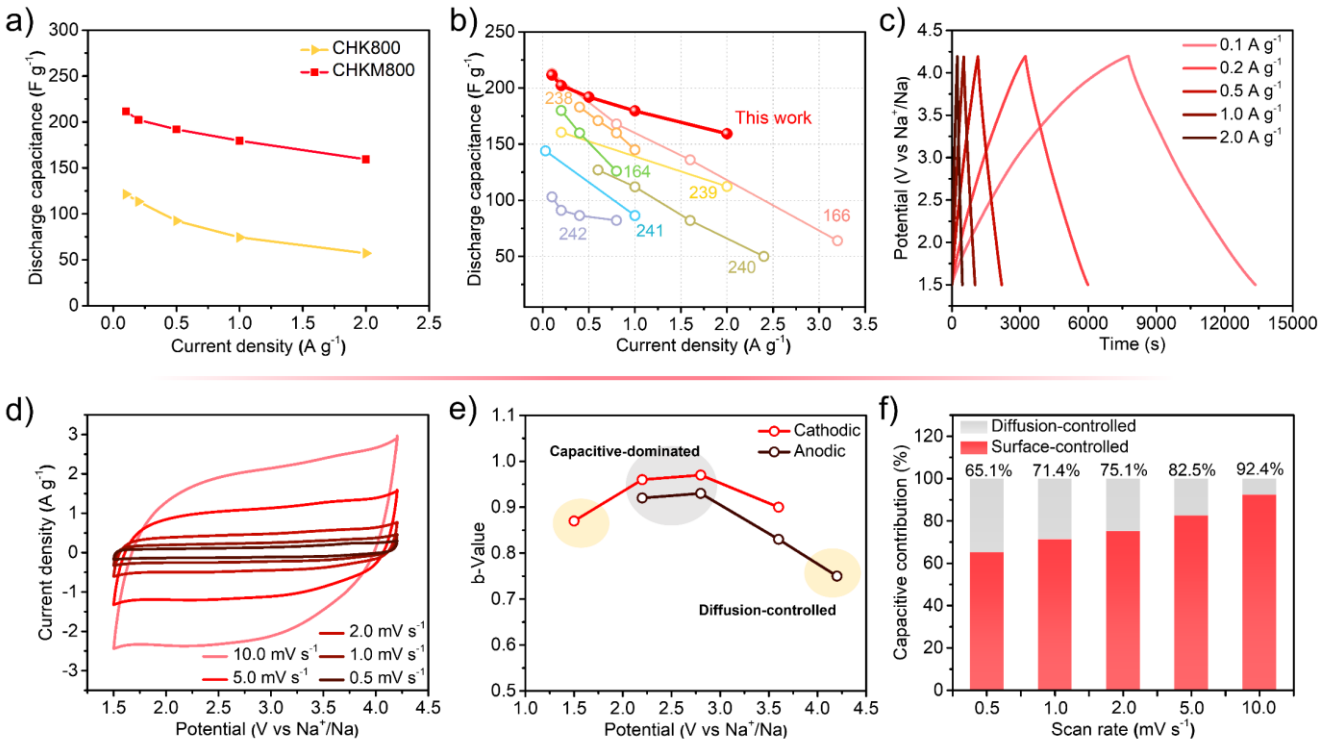


Figure 5.5. Electrochemical testing of carbon cathodes in half cells. a) Comparison of specific capacitances of CHKM800 and CHK800; b) Specific capacitances of CHKM800 with the comparison to published cathodes in NICs; c) GCD curves of CHKM800 at 0.1 to 2.0 A g^{-1} (the second cycle of each rate current); d) CV curves of CHKM800 under 0.5 to 10.0 mV s^{-1} (the second cycle of each sweep rate); e) The b-values of CHKM800 at different measured potentials; and f) Calculated contribution proportions of the surface- and diffusion-controlled processes at 0.5 to 10.0 mV s^{-1} in CHKM800.

Electrochemical characterisation of the carbon cathodes was carried out to investigate their suitability for perchlorate anion storage. The carbon cathodes were tested in a half cell configuration against sodium foil as both the counter and reference electrode within the voltage window of 1.5-4.2 V vs. Na^+/Na. This potential range was chosen to maximise the operating voltage window while preventing the electrolyte decomposition as well as the insertion of cations into the cathode, as the open-circuit voltage (OCV) for carbon materials in half cells is normally around 1.5-2.5 V vs. Na^+/Na.[166] Figure 5.4a shows the comparison of the electrochemical performance of diverse carbon cathodes. The CHKM800 delivers the highest discharge capacitance of 212.4 F g^{-1} which can be converted into 158.7 mAh g^{-1} at the current density of 0.1 A g^{-1}, while the capacitances of CHKM700 (co-activated at 700 °C) and CHK800 are 134.4 and 122.3 F g^{-1}, respectively (**Figure A2.8**, Appendix). When the current density increases to 2.0 A g^{-1}, the capacity retention for CHKM800 is 76% which is also the best among

the different carbon cathodes (**Figure 5.5**a). In addition, GCD curves in **Figure 5.5**c show that even at a high current density of 2.0 A g^{-1}, the IR_{drop} of CHKM800 (0.13 V) is still insignificant, also indicative of good rate performance.

Table 5.4. Specific electrochemical performance of the half cells of cathodes.

Cathode	DC[a] (mAh g^{-1}, 0.1 A g^{-1})	RPR[b] (%, 0.1->2.0 A g^{-1})	CR[c] (%, 2.0 A g^{-1}, 200 cycles)
CHK800	91.2	45	82
CHKM800	158.7	76	77
CHKM700	100.4	70	84

[a] DC: Discharge capacity,
[b] RPR: Rate performance retention,
[c] CR: Cycling retention.

The interconnected coral-like carbon frameworks containing multiscale meso-micropores can provide enough charge storage sites as well as lead to short diffusion lengths and good multiphase contact, thus greatly improving the performance of the EDLC (**Figure 5.4**d), while Faradic charge-transfer reactions with the functional groups can contribute towards pseudocapacitance, thus also increasing the overall energy density of the carbon cathodes. Moreover, compared with the KOH-activated carbon (CHK800), the introduction of the hierarchical pore structure and heteroatom doping to the co-activated carbons (CHKM700) effectively improves the rate performance of CHKM700 in spite of their similar surface areas (both around 1500 m^2 g^{-1}) (**Table 5.3** and **Table 5.4**). Among all the prepared cathodes, CHKM800 is a very promising candidate to be used in carbon cathode for NICs, being also very competitive with other carbons from the literature as cathodes for NICs (**Figure 5.5**b).[164, 166, 238-242]

CV measurements of the carbon cathodes were employed at different scan rates to explore the electrochemical reactions, especially the diffusion-controlled insertion pseudocapacitive contributions, as well as their kinetics. The electrochemical reactions in the cathode are dominated by a double layer effect as suggested by the nearly rectangular shape of CV curves

(**Figure 5.5**d), but diffusion-controlled reactions also exist, especially at the two sides of the voltage window where the b-value is not around 1.0 (**Figure 5.5**e). However, broad and continuous curvature instead of distinct peaks appears. Compared with the Faradic reactions at the battery side, the interactions between anions and functional groups at the capacitor side are much faster, because they happen on the near-surface rather than in the deep bulk phase. **Figure A2.5** (Appendix) shows the CV curve of the capacitive current (red area) in comparison with the response current of insertion pseudocapacitance (grey area), where 71.4 % of the whole capacitance in CHKM800 is derived from surface-controlled capacitance including EDLC and surface-pseudocapacitance at the sweep rate of 1.0 mV s^{-1}. As the sweep rate increases from 0.5 to 10.0 mV s^{-1}, the contribution of surface-controlled capacitance also increases from 65.1 % to 92.4 % because the pseudocapacitive reactions in the shallow bulk phase do not have enough time to happen (**Figure 5.5**f). Most of the capacitance in the cathodes is achieved by surface-dominated reactions, especially the physical adsorption of anions. This means that in the full cell configurations, the fast kinetics of capacitor-type cathodes could speed up the energy storage process in battery-type anodes since the charge balance ($Q^+ = Q^-$) have to be always kept.[32] Overall, the high surface area, hierarchical pore structure and compact 3D framework based on spherical units permit the excellent electrochemical performance of CHKM800.

5.3 Full cells with liquid electrolytes

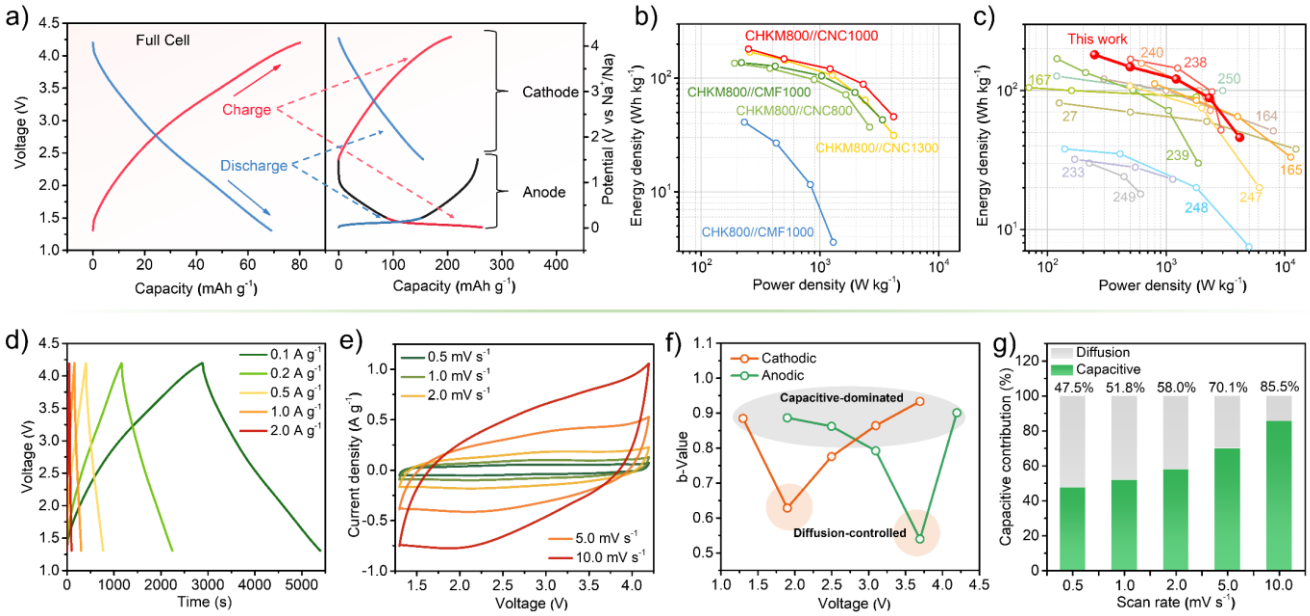


Figure 5.6. Electrochemical testing of NICs with different configurations. a) Illustration of the corresponding charge-discharge processes in cathodes and anodes during NICs operation; b) Ragone plot comparing a device based on different combinations of CHKM800//CNC1000, CHKM800//CNC1300, CHKM800//CNC800, CHKM800//CMF1000 and CHK800//CMF1000; c) Energy–power density performance comparison of NICs *versus* reported carbon-based hybrid capacitor systems; d) GCD curves at 0.1 to 2.0 A g^{-1} (the second cycle of each rate current), e) CV curves under 0.5 to 10.0 mV s^{-1} (the second cycle of each sweep rate), of CHKM800//CNC1000; f) The related b-values at different measured voltages; and g) Calculated contribution proportions of the surface- and diffusion-controlled processes at 0.5 to 10.0 mV s^{-1} in CHKM800//CNC1000. (All the parameters in the full cell configuration are normalised by the total active mass of both anode and cathode.)

Figure 5.6a illustrates the corresponding charge-discharge processes in the CHKM800 cathode and the CNC1000 anode when NICs (CHKM800//CNC1000) are charged and discharged. During the charge process in full cells, anodes are sodiated, while cathodes adsorb the counter ions. The charge capacities of CNC1000 and CNC1300 from the plateau regions (< 0.2 V vs. Na^+/Na) in half cells are close to the discharge capacity of 158.7 mAh g^{-1} in CHKM800 cathodes; therefore, in order to balance the charges passing through the electrodes ($Q_{cathode}=Q_{anode}$), carbon anodes were discharged and charged to 0.2 V vs. Na^+/Na with a pulse current in half cells prior to the assembly of full cells, thus not only making it easier to adjust the ratio of the active mass in anodes and cathodes ($m_{cathode}:m_{anode}$ is closed to 1:1), but also getting full use of the capacity from the plateau regions. In addition, the pre-sodiation treatment

of carbon anodes can activate the materials, and reduce side reactions including the formation of SEI.[243-246] Carbon cathodes were also charged and discharged to 1.5 V vs. Na^+/Na with a pulse current for balancing the charges, stabilizing the electrode surface and ensuring the voltage windows of full cells (1.3-4.2 V). However, when CMF1000 and CNC800 were employed as anodes in full cells, they were discharged and charged to 1.5 V vs. Na^+/Na, because their charge capacities from the whole potential range in half cells are close to the discharge capacities in CHKM800 and CHK800 (**Table 5.4**). Furthermore, there is no obvious plateau region in their GCD curves, in other words, only sloping regions of these anodes can provide energy for full cells (**Figure A2.4**, Appendix).

When CHKM800 and CNC1000 with the best half-cell electrochemical performance among the electrodes were used as the cathode and anode of full cells respectively, the NICs with the highest energy-power density were achieved, where the discharge capacity is 72.3 mAh g^{-1} (0.1 A g^{-1}) (**Figure A2.9**, Appendix). As the current density increases from 0.1 to 2.0 A g^{-1}, the energy densities are 181, 148, 121, 89 and 46 Wh kg^{-1} when the power densities are 250, 498, 1216, 2313 and 4173 W kg^{-1}, respectively (red line in **Figure 5.6**b). Additionally, the effect of the electrochemical performance of anodes and cathodes on the energy-power densities of full cells are studied. The energy and power densities of NICs would vary according to the energy-power performance of the selected anode or cathode. If one anode (cathode) has good power (energy) performance, then the NIC has proportionally good power (energy) performance (**Figure 5.6**b and **Table 5.5**).

Table 5.5. Specific electrochemical performance of full cells.

Full cell	DC[a] (mAh g^{-1}, 0.1 A g^{-1})	RPR[b] (%, 0.1->2.0 A g^{-1})	CR[c] (%, 2.0 A g^{-1}, 200 cycles)
CHKM800//CNC1000	72.3 (1.3-4.2 V)	34	64
CHKM800//CNC1300	66.2 (1.3-4.2 V)	24	49
CHKM800//CMF1000	66.3 (0-4.2 V)	41	65
CHK800//CMF1000	20.0 (0-4.2 V)	18 (0.1->1.0 A g^{-1})	68 (1.0 A g^{-1})
CHKM800//CNC800	70.2 (0-4.2 V)	35	50

[a] DC: Discharge capacity,
[b] RPR: Rate performance retention,
[c] CR: Cycling retention.

The NICs listed in **Figure 5.6**c include various carbon-based systems [27, 164, 165, 167, 233, 238-240, 247-250]. The system based on the configuration CHKM800//CNC1000 possesses a promising energy-power performance as well as a low-cost and easy fabrication process. In **Figure 5.6**d, GCD curves can no longer be recognised as the perfect linearity in corresponding to the CV curves in **Figure 5.6**e with the appearance of broad Faradic peaks which also can be seen in **Figure A2.5** (Appendix), because in the full cells, the existence of Faradic reactions in battery-type anodes causes the disproportionation of the stored charges (ΔQ) to the applied voltage (ΔU). In addition, 34% of the discharge capacity is retained when the current density increases from 0.1 to 2.0 A g^{-1}, which is greatly improved in comparison to the rate performance of batteries in general (**Figure A2.9**, Appendix).

In order to further understand the energy storage mechanism of NICs, the kinetics of the full cell configuration were studied. The b-values in full cells decrease close to 0.5 when the voltage approaches 1.9 and 3.7 V, implying that diffusion-controlled reactions (including the interaction between anions and functional groups in the shallow bulk phase of carbon cathodes, and especially the interaction between cations and carbon anodes in the body phase) exists at these specific voltages (**Figure 5.6**f). When the current density increases from 0.1 to 2.0 A g^{-1}, the surface-controlled contribution increases from 47.5 to 85.5 % (**Figure 5.6**g). To sum up, in

cathodes, anions mainly adsorb-desorb at micropores, while mesopores could provide ion path and improve the rate performance, which has been proved above. In addition, the capacitance of cathodes consists of both EDLC (a physical adsorption process mainly happening at micropores on the surface) and pseudocapacitance (an extra contribution of capacitance based on the interaction between anions and functional groups on the surface and in the shallow body phase). EDLC is a non-Faradic reaction that is faster, while pseudocapacitive behaviour is a slower Faradic process. The kinetic of the battery side is much slower than the cathode side because the Faradic reaction of cations which can provide more energy happens in the bulk phase not only on the surface. The attributes of the capacitor-style cathode and battery-style anode are successfully combined in a NIC which exhibits an impressive electrochemical behaviour with fast dynamics, and thus an optimised energy to power performance. The perchlorate-based electrolyte needs to be further considered in the future. With better electrolyte salts, the electrochemical performance of devices would be further improved.

5.4 Full cells with cellulose-based gel electrolytes

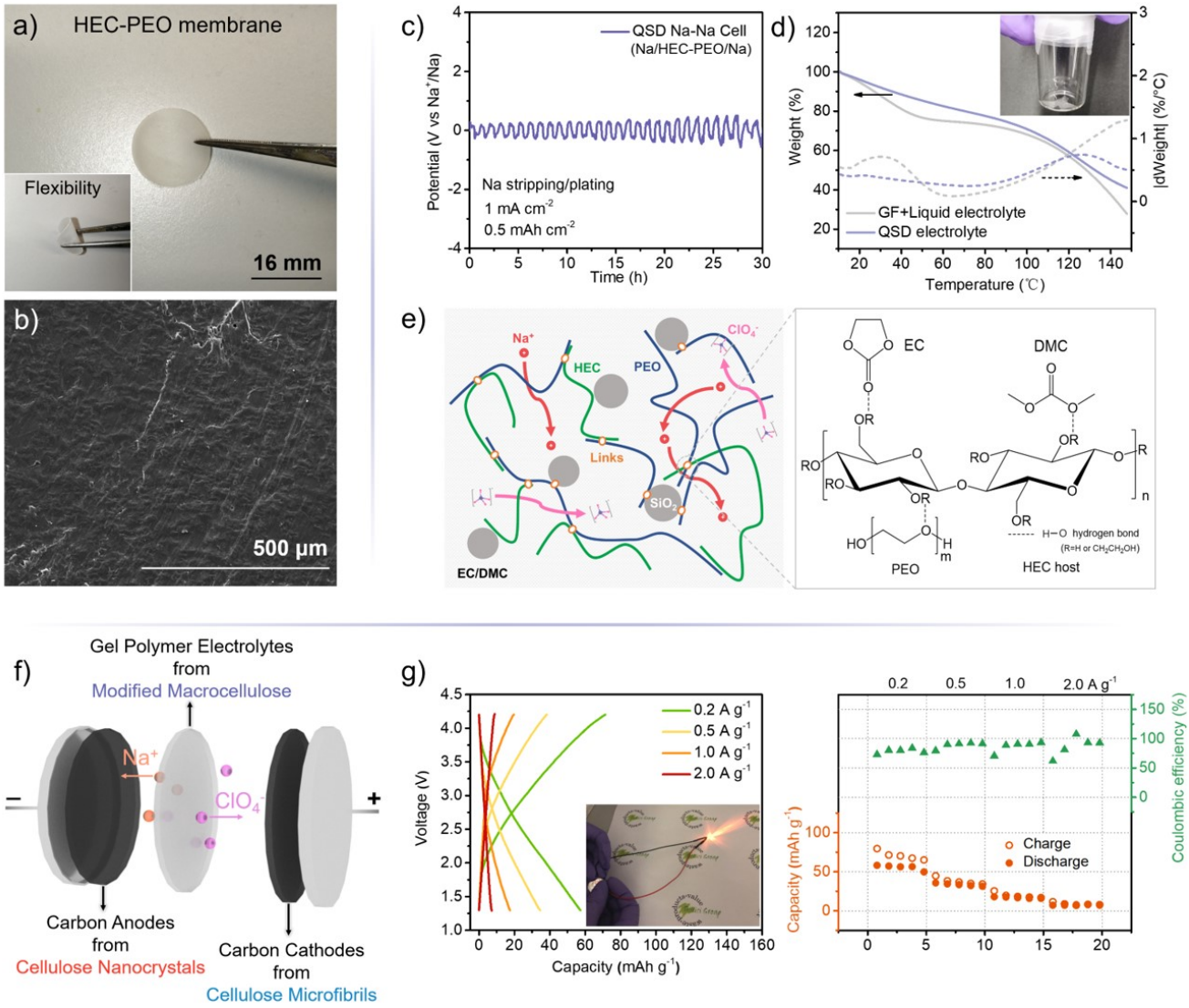


Figure 5.7. Gel polymer electrolytes and QSD NICs: schematics, performance and mechanisms. a) Photographs of HEC-PEO composite membrane with an insert photo illustrating its flexibility; b) SEM image of HEC-PEO composite membrane; c) Voltage profiles at room temperature for sodium stripping/plating in a symmetric Na/HEC-PEO/Na cell at 1 mA cm^{-2}; d) TGA curves of HEC-PEO membrane and glass fibre membrane absorbing the same amount of electrolyte (150 °C, 5 °C min^{-1}, N_2 flow) with an inserted photograph of QSD gel electrolyte; e) Schematic of the transport of anions and cations inside the polymer network of HEC-PEO formed by the hydrogen binding effect (left), and schematic illustration of the interactions of hydroxyl groups in HEC with PEO and EC/DMC organic electrolytes (right); f) Schematic of all-cellulose-based QSD NICs; g) GCD curves (the second cycle of each rate current) and rate performance at 0.2 to 2.0 A g^{-1}, of the QSD device (CHKM800/HEC-PEO/CNC1000) with an inserted photograph of the LED powered by the NIC.

Finally, cellulose-based solid electrolytes were developed to build an all-cellulose-based quasi-solid-state (QSD) system (**Figure 5.7**a). Hydroxyethyl cellulose (HEC), a renewable and

biocompatible derivative of cellulose, was selected as the matrix for the gel polymer electrolyte. The functional groups of HEC can form hydrogen bonds with carbonate-based organic electrolytes, so HEC could be a suitable host for gel polymer electrolytes based on the interaction with liquid electrolytes as well as the absorption in pores.[251] In addition, polyethylene oxide (PEO) was introduced to the polymer matrix to improve flexibility and the formation of the membrane as well as the porosity, which is also beneficial for the absorption of the liquid electrolyte into the membrane/separator.[155]

The surface morphology of the HEC-PEO composite membrane is smooth (**Figure 5.7**b) which can ensure good contact between all the components. The Na/Na symmetric cells were assembled to investigate the behaviour of sodium stripping and plating in the gel polymer electrolyte. **Figure 5.7**c shows that the overpotential of the symmetric cell is stable, which means sodium ions can reversibly move through the QSD electrolyte, and the interfaces remain stable.[252] The possible explanations of its reversible performance are listed as follows (**Figure 5.7**e): 1) The intermolecular hydrogen bonds formed in the polymer matrix allow the polymer chains to be more disordered and thus benefit the ion migration;[253] 2) The addition of SiO_2, an inorganic filter, can decrease the degree of crystallinity of the polymer matrix, thus also improving ionic conductivity.[156, 254] To further prove the good interphase contact between electrodes and gel polymer electrolytes, the Nyquist plots of full cells with liquid and QSD electrolyte have been measured (**Figure A2.11**, Appendix) and fitted based on Equation 5.1:

$$Z = R_s + \frac{1}{j\omega C_{dl} + \frac{1}{R_{ct}+W_o}} + \frac{1}{j\omega C_l + \frac{1}{R_{leak}}} \qquad \text{Equation 5.1}$$

where Z (Ω) is the impedance, R_s (Ω) is the inner resistance, R_{ct} (Ω) is the charge-transfer resistance. The sum of R_s and R_{ct} is the equivalent series resistance (**ESR**) of the device. Furthermore, C_{dl}, C_l, W_o and R_{leak} respectively represent the double-layer capacitance, the low-frequency mass capacitance, the Warburg element and the low-frequency leakage resistance.

The series resistance (ESR) of QSD full cells is very similar to that of full cells with liquid electrolytes, demonstrating that the QSD electrolyte also has a good wettability and interface contact. For the retention ability of QSD electrolyte, HEC-PEO membranes absorbing the same amount of liquid electrolyte (5 μL mg^{-1}, 1 M $NaClO_4$ in EC/DMC) with a glass fibre membrane were heated to 150 ^oC under N_2 *via* thermogravimetric analysis (TGA). From **Figure 5.7**d, we

can see the cellulose-based QSD electrolyte has better retention ability than commercial glass fibre membrane because the interaction between organic electrolytes and polymer chains enables the good stability of the gel polymer electrolyte (**Figure 5.7**e). For the electrochemical performance of QSD full cells in the configuration of CHKM800/HEC-PEO/CNC1000 (Figure 5.6f), the discharge capacity can reach 58.2 mAh g^{-1} at 0.2 A g^{-1} (**Figure 5.7**g). The energy density can reach 139, 80, 39, 12 Wh kg^{-1} at the power density of 478, 1126, 2149, 3240 W kg^{-1}, respectively. Figure 5.6g also shows that QSD NICs in the coin cells can power a red LED after charging with the current density of 2.0 A g^{-1} in a few seconds.

5.5 Conclusions

In summary, sustainable hybrid capacitors with excellent electrochemical performance were demonstrated based on an all-cellulose-based configuration and a cheap Na-based dual-ion energy storage process for the first time. Carbon electrodes were designed according to the understanding of the multiscale building blocks of cellulose, and their electrochemical performance was optimised by utilizing the hierarchical structures of carbon materials inspired by nature, where structural hierarchy is one of the most important features in plants. Moreover, cellulose-based QSD electrolytes not only ensure that the device is cheaper and safer, but also lay a foundation for the preparation of flexible energy storage devices in the future.[255] The kinetics of the electrochemical reactions inside the hybrid capacitors have also been studied to acquire the optimised configuration of the full cells with maximized energy-power density. This ‘one-for-all’ strategy has enabled superior performance in both, the individual electrodes as well as the full device which was assembled using a gel electrolyte, all made by translating the cellulose hierarchical features into bioinspired materials, thus making NICs feasible for grid-scale energy storage with a lower levelized cost of electricity storage. [256]

Chapter 6. From lignin to sodium-metal batteries

- Homogenous metallic deposition regulated by defect-rich skeletons for sodium metal batteries

Towards the next-generation battery technologies, sodium metal batteries with a high energy density can be a promising alternative to commercial lithium-ion batteries. Nevertheless, the metallic anode part suffers from the dendrite formation and relative safety issues. Among the possible solutions to these issues, the carbon functional hosts for metallic anodes have been developed, but most commercial carbon mats or fabrics have a poor interface contact with sodium metal anodes. Therefore, I look into the rational design strategy of lignin-derived sustainable carbon functional hosts for dendrite-free sodium metal anodes.

In this chapter, sustainable carbon skeletons with rich defects and negligible pores have been rationally synthesized by one-step annealing at a low temperature (only 700 ^{o}C) from electrospun lignin mats, and then were employed as three-dimensional (3D) hosts for metallic sodium anodes. Multiscale modelling from atoms to macroscale in concert with *operando* and *ex-situ* characterisation have been conducted to deepen the fundamental understanding of metallic sodium deposition behaviour and electrochemical interfaces formed onto the carbon skeletons. I have successfully demonstrated for the first time in the literature that defects in carbon materials play a more important role in facilitating the nucleation and deposition of metallic sodium than pores. In addition, I have investigated different electrolytes and revealed that diglyme in combination with low-cost and stable $NaCF_3SO_3$ salt can regulate the ionic conductivity and increase the lowest unoccupied molecular orbital (LUMO) energy of the electrolyte,[38, 101, 136] which additionally contributes to a uniform metallic sodium deposition. To authenticate the potential of the lignin-derived carbon mats in practical applications for the concept of “anode-less” sodium metal batteries, I have coupled them with various cathodes such as Prussian blue (PB) crystals or sulphur (S). The lignin-derived carbon skeletons with a 3D structure play an important role in reducing electrochemical polarisation by improving the ion and mass diffusion in electrodes. In this chapter, I not only developed and studied novel carbon skeletons with rich defects for stable metallic sodium anodes, but also optimised the

whole system from electrodes to electrolytes to help the development of sodium metal batteries with enhanced sustainability, thus paving the way for the future improvement of next-generation energy storage devices beyond lithium-ion battery technologies.

6.1 Synthesis and structural characterisation of carbon skeletons

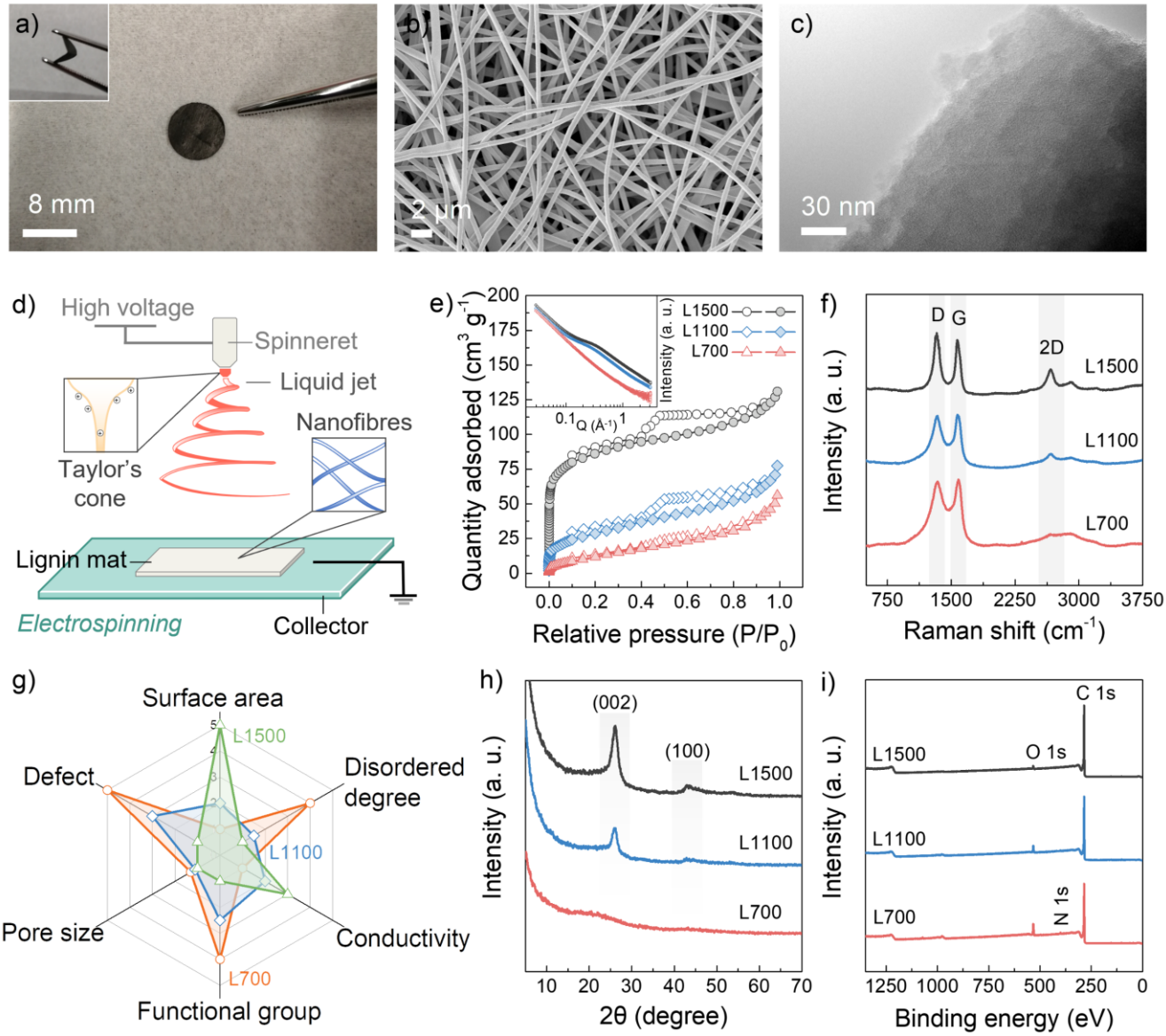


Figure 6.1. Material Characterisation. a) Photograph of L700 with an inserted illustration of its flexibility. b) SEM image and c) TEM image of L700. d) Schematic diagram illustrating the electrospinning process of lignin nanofibres. e) N_2 adsorption and desorption isotherms (77 K) with inserted SAXS patterns. f) Raman spectra, g) Rada curve of structural properties, h) XRD patterns, and i) XPS survey, of L700, L1100 and L1500.

The carbon skeletons were synthesized *via* the aqueous electrospinning of lignin, followed by

the low-temperature pyrolysis (700 °C) under a nitrogen gas atmosphere. To tune defect and pore structures of carbon skeletons, the pyrolysis temperatures were also increased to 1100 °C and 1500 °C. These samples are annotated as L700, L1100 and L1500 depending on their carbonisation temperatures of 700 °C, 1100 °C and 1500 °C, respectively. **Figure 6.1**a show that obtained carbon skeletons can maintain a free-standing and flexible format, in which a non-woven fabric with a 3D structure formed by interconnected nanofibres can be observed according to the scanning electron microscopy (SEM) image in **Figure 6.1**b. Such 3D morphology results from the inherent properties of the electrospinning method. After the Taylor cone is formed because of the polarisation of the spinning solution, the lignin nanofibres are pulled out from the prepared aqueous spinning solution under a high-voltage field (**Figure 6.1**d). During the electrospinning process, the volatilised solvent randomly deposits on a collector as single nanofibres, forming a 3D skeleton.[257, 258] The inner structure of the carbon skeleton is identified with the help of the transmission electron microscopy (TEM) (**Figure 6.1**c) from which the turbostratic nanostructure, a characteristic amorphous feature of biomass-derived hard carbons, can be observed.

Table 6.1. Physical parameters of L700, L1100 and L1500.

	d_{002}[a] (nm)	$FWHM_{002}$[b] (°)	I_D/I_G[c]	L_a[d] (nm)	S_{BET}[e] ($m^2\ g^{-1}$)	V_t[f] ($cm^3\ g^{-1}$)	D_A[g] (nm)
L700	0.396	7.92	0.94	1.22	50.4	0.081	6.2 (2.34)
L1100	0.345	2.25	0.97	1.24	103.6	0.083	5.4 (2.09)
L1500	0.343	1.98	1.04	1.29	282.3	0.141	4.8 (1.79)

[a] d_{002}: Calculated average interlayer spacing of graphene layers from XRD patterns,
[b] $FWHM_{002}$: Fitted full width at half maximum of (002) peaks from XRD patterns,
[c] I_D/I_G: Intensity ratio of D-peak to G-peak based on fitted Raman spectra,
[d] L_a: Average in-plane distance of the graphene layer from Raman spectra,
[e] S_{BET}: Specific surface areas calculated using the multipoint Brunauer-Emmett-Teller (BET) method,
[f] V_t: Total pore volume from N_2 adsorption and desorption isotherms,
[g] D_A: Average pore diameter from N_2 adsorption and desorption isotherms based on NLDFT method (out of brackets) and from SAXS patterns based on Porod method (within brackets).

The pore structures of the carbon skeletons are investigated with the help of the N_2 adsorption and desorption isotherms (**Figure 6.1**e). From the isotherms, the obtained Brunauer–Emmett–Teller (BET) specific surface area (S_{BET}) of L700 (50.4 m^2 g^{-1}) is lower than those of L1100 (103.6 m^2 g^{-1}) and L1500 (282.3 m^2 g^{-1}). The pore size distribution based on the non-local density functional theory (NLDFT) method is also shown in **Figure A3.1** (Appendix). The average diameter of pores decreases with the increase in carbonisation temperatures (**Table 6.1**), which means that higher carbonisation temperatures create more micropores (< 2 nm, diameter). Small-angle X-ray scattering (SAXS) is utilised as a complementary technique to further probe the pore structure, which can corroborate the BET and NLDFT results. From the inserted image in Figure 6.1e, a plateau region from 0.1 to 1 $Å^{-1}$ in SAXS patterns become more obvious with the increase in carbonisation temperatures. Based on SAXS patterns fitted by Stevens and Dahn's Porod method,[34, 189] L700 depicts a lower surface area and negligible pore structures than L1500 (**Figure A3.1** and **Table A3.1**, Appendix).

To characterise the defects, Raman spectroscopy, X-ray diffraction (XRD) and X-ray photoelectron spectroscopy (XPS) are utilised. The Raman spectra of L700, L1100 and L1500 show broad characteristic D- and G- peaks (**Figure 6.1**f), indicating they are all disordered hard carbons categorised as Stage II in a three-stage model proposed by Ferrari *et al.*,[190, 206-208] which is different from ordered graphitic carbons such as graphite, graphene and carbon nanotubes. In Stage II of this model, the intensity ratio of D- to G-peaks (I_D/I_G) of hard carbons increases when the defect concentration among graphene layers within hard carbons decreases. According to the calculated values of I_D/I_G from the fitted Raman spectra (**Table 6.1** and **Figure A3.2**, Appendix), the graphene planes of L700 are more defective than those of L1100 and L1500. Additionally, the 2D peaks become broader with a decrease in the carbonisation temperatures, which also proves the stacks of graphene planes become more disordered. The uniformity of defect sites of L700 can be recognised based on the TEM image and multi-point Raman scanning of L700 in **Figure A3.2** (Appendix). The defect structures demonstrated in the Raman spectra can further be categorised into intrinsic defects and extrinsic defects. [209, 259] The trends of intrinsic defects derived from turbostratic nanostructures can be clarified by the XRD analysis (**Figure 6.1**h),[260] and the extrinsic defects caused by heteroatom doping on the

surface of carbon skeletons can be further confirmed by XPS (**Figure 6.1**i).[261] From XRD patterns (**Figure 6.1**h), two peaks attributed to the (002) and (100) planes of expanded inner structures can be observed at 2θ ≈ 24° and 44° in L1100 and L1500, while L700 shows two wider peaks whose full width at half maximum of (002) planes ($FWHM_{002}$) can reach 7.92°. The calculated average interlayer spacing of graphene layers (d_{002}) of hard carbons decreases when carbonisation temperatures increase (**Table 6.1**). L700, therefore, is more disordered than L1100 and L1500, suggesting more intrinsic defect sites. XPS survey (**Figure 6.1**i) and the fitted C 1s, N 1s and O 1s core-level XPS spectra (**Figure 6.2**) show that the atomic amount of nitrogen- and oxygen-doping of L700 can reach 2.3 at% and 9.6 at%, respectively (**Table 6.2**). As the carbonisation temperatures increases, the amount of doping in L1100 and L1500 decreases (**Table 6.2**). In general, L700 has rich defects and negligible pores compared with L1500 possessing abundant pores and few defects.

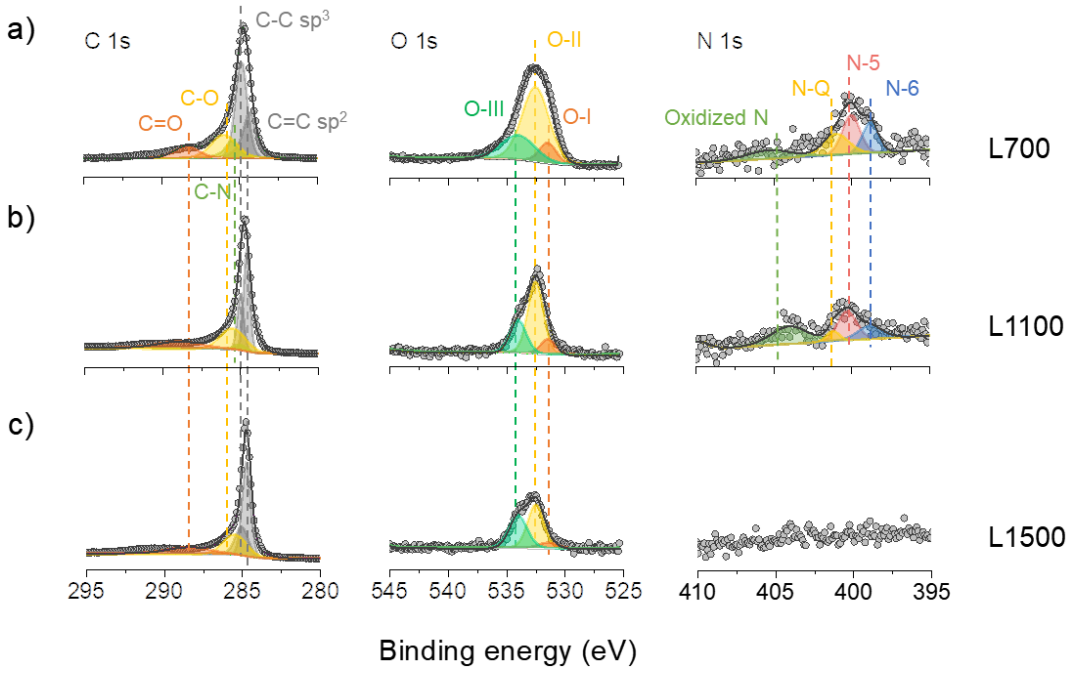


Figure 6. 2. Fitted C 1s, N 1s and O 1s core-level XPS spectra of a) L700, b) L1100 and c) L1500

It is worth noting that in this study, the pore and defect structures of lignin-derived carbon materials show reverse trends with the presence of the activation agents when the carbonisation temperatures increase. The reasons for this phenomenon are listed as follows: (1) differing from the linear molecular chain of cellulose consisting of repeated units of D-glucose, lignin belongs

to phenolic polymers. The degree of order and defective structures of carbon skeletons from lignin are sensitive to temperatures because a large number of benzene rings exist, which has also been discussed in detail in our reported studies;[181, 182] (2) the electrospinning process under high-voltage can orient the inherently amorphous polymer chains of lignin, thus allowing the increase in the ordered degree of lignin materials; and (3) the amount of activation agents (NaOH) used in this study is one-tenth of that in traditional chemical activation of biomass to avoid the excessive oxidisation and achieve the appropriate pore-forming at 1100 and 1500 ºC rather than 700 ºC. These rational experimental designs all contribute to the successful implementation of the reverse trend between defect structures and pore structures (**Figure 6.3**g) with the change of carbonisation temperatures, enabling deep insights and a good platform for the current mechanism study.

Table 6.2. The atomic percentage of different elements (C, N, O) in L700, L1100 and L1500.

at %[a]	**C 1s**				**N 1s**					**O 1s**		
	sp2	sp3	C-O	C=O	C-N	N-6	N-5	N-Q	Ox-N[b]	O-I	O-II	O-III
L700	18.99	32.84	18.10	9.19	9.06	0.52	0.75	0.58	0.40	1.05	6.09	2.43
L1100	35.81	19.70	22.49	12.21	2.90	0.34	0.58	0.11	0.55	0.59	3.09	1.48
L1500	42.12	15.58	24.64	14.75	-	-	-	-	-	0.22	1.45	1.24

[a] at %: Atomic %
[b] Ox-N: Oxidised N

6.2 Electrochemical performance in half cell configurations

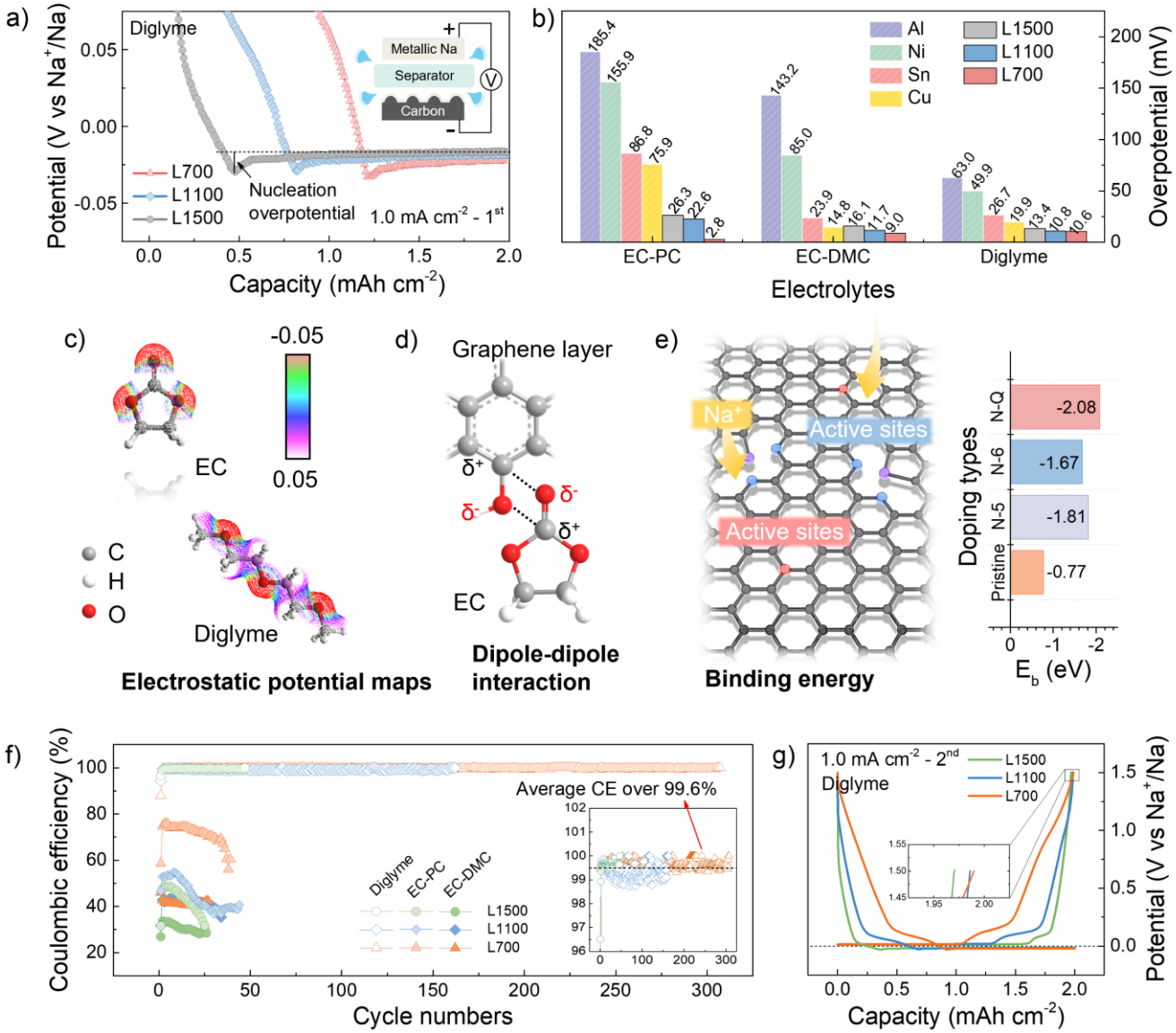


Figure 6.3. Electrochemical Characterisation. a) The potential-capacity profiles (the 1st cycles) showing the initial nucleation overpotentials of sodium deposition on L700, L1100 and L1500 at 1.0 mA cm^{-2} using 1 M $NaCF_3SO_3$ in diglyme. b) The overview of nucleation overpotentials of sodium deposition on different substrates (Al, Sn, Ni, Cu, L700, L1100 and L1500) in different electrolytes (1 M $NaCF_3SO_3$ in EC-PC, EC-DMC or diglyme) at 1.0 mA cm^{-2}. c) The electrostatic potential maps of EC and diglyme, where the red regions represent the negative charge, and the white regions represent the positive charge. d) The schematic illustration of the dipole-dipole interaction between EC and oxygen functional groups of L700. e) Left: the schematic illustration of the interaction between the nitrogen-doped graphene layer with sodium atoms, and Right: the calculated binding energy (E_b) of sodium atoms with the nitrogen-doped graphene layers. f) The Coulombic efficiencies of sodium plating and stripping on L700, L1100 and L1500 in different electrolytes (1 M $NaCF_3SO_3$ in EC-PC, EC-DMC or diglyme) at 1.0 mA cm^{-2} with a specific charge and discharge capacity of 2.0 mAh cm^{-2}. g) The specific GCD curves (the 2nd cycle) of metallic sodium plating and stripping on L700, L1100 and L1500 at 1mA cm^{-2} using 1 M $NaCF_3SO_3$ in diglyme.

To correlate the structure of the carbon skeletons and the sodium deposition behaviour, sodium plating and stripping experiments were carried out in a half cell in which the carbon skeletons were placed against a piece of metallic sodium with the same size (Inserted image in **Figure 6.3**a) using 1 M $NaCF_3SO_3$ in ethylene carbonate-propylene carbonate (EC-PC, 1:1 v%) mixed solvents, ethylene carbonate-diethyl carbonate (EC-DMC, 1:1 v%) mixed solvents or diethylene glycol dimethyl ether (diglyme) as electrolytes. I selected $NaCF_3SO_3$ because of its lower cost, lower fluorine content, high solubility (9.26 M in non-aqueous electrolytes)[262] and good stability[263] compared with traditional salts like $NaPF_6$ and NaTFSI for sodium batteries. Commercial current collectors including aluminium (Al), nickel (Ni), tin (Sn) and copper (Cu) were also employed as substrates for comparison (**Figure A3.3**, Appendix). The galvanostatic charge and discharge (GCD) of the cell was operated using a constant current density of 1.0 mA cm^{-2} with a fixed specific charge and discharge capacity of 2.0 mAh cm^{-2}.

A potential dip (< 0 V vs Na^+/Na) can be observed in the potential-capacity profiles, followed by a plateau region of potential representing the sodium deposition process (**Figure 6.3**a). The sodium nucleation overpotentials are first determined by the difference between the bottom value of the potential dip and the value of the plateau region potential. A smaller initial nucleation overpotential represents a lower energy barrier of the nuclei formation needed to be overcome, thus helping identify the sodiophilic properties of a substrate.[264, 265] Compared with other commercial substrates, the carbon skeletons always show smaller initial nucleation overpotentials (**Figure 6.3**b), which means the sodiophilic properties of carbon skeletons are much better than other substrates no matter in what electrolytes. Moreover, L700 always has the smallest initial nucleation overpotentials of 2.8 mV in EC-PC, 9.0 mV in EC-DMC and 10.6 mV in diglyme, indicating the best sodiophilic properties of L700. Actually, the initial nucleation overpotentials of the various commercial substrates shown in Figure 2b are almost incomparable with the lignin-derived carbon skeletons because of the different surface situations even under the same constant current density of 1.0 mA cm^{-2} and with a fixed specific charge and discharge capacity of 2.0 mAh cm^{-2}. Namely, the surface conditions of substrates can make a big difference on the initial nucleation overpotentials.

For the same substrate, the electrostatic interaction between solvent molecules and the heteroatom doping in carbon skeletons can be simulated to understand the influence of electrolytes on nucleation overpotentials.[221] According to the electrostatic potential maps of solvent molecules (**Figure 6.3**c), the negative charge region (red) are mostly localised on the oxygen atoms of C=O groups of EC, thus polarizing the solvent molecules into a local dipole. Meanwhile, in L700, the charges on the carbon atoms are delocalized by nitrogen and oxygen atoms in the functional groups of L700, and a positive charge region can be formed, which represents the formation of another local dipole. These local dipoles in L700 and ester solvent molecules can strongly interact with each other (**Figure 6.3**d).[266] However, based on the electrostatic potential maps of diglyme, the negative charge regions (red) are distributed more uniformly because of its molecular structure, which means no strong dipole-dipole interaction can exist between L700 and ether solvent molecules. Therefore, ester solvent molecules have stronger dipole-dipole interactions with the enriched functional groups on the L700 surface, so the initial nucleation overpotentials of L700 in ester-based electrolytes are smaller than those in ether-based electrolytes. Even so, L700 in diglyme still performs better for long cycling testing, which will be discussed and explained in the following parts.

In the same electrolytes, L700 shows better sodiophilic properties than L1500 since the initial nucleation overpotentials of L700 are smaller than those of L1500 (**Figure 6.3**b). According to the literature, porous structures, especially micropores, are beneficial to the nucleation process,[267] but the importance of defects in carbon materials cannot be distinguished from pores. In this study, the benefits of defects to the nucleation process can be independently recognised by comparing the discrepancy in structural features of L700 and L1500 with their nucleation overpotentials. Based on our reported studies on the sodium storage mechanism in hard carbons using ^{23}Na nuclear magnetic resonance (NMR), X-ray and neutron scattering,[39, 57, 60] we proved that defects within hard carbons formed by tortuous and imperfect graphene layers can lead to the sloping regions in the GCD curves, where defects serve as active sites to enhance the capacitive interaction with sodium ions. As observed from **Figure 6.3**g and **Figure A3.5** (Appendix), the GCD curves of L700 always have higher sloping capacities, which can be correlated with rich defects in the L700.[260] In this study, DFT calculations were further conducted to clarify the beneficial role of defects for nucleation. According to the XPS data

displayed in **Figure 6.2**, L1500 has no nitrogen content. Therefore, idealised models can be created to symbolise the most obvious difference in defect structure between L700 and L1500. The single pristine graphene layer represents L1500, while the single graphene layer with different types of nitrogen doping signifies L700 (**Table A3.2**, Appendix). Here, L700 with nitrogen-containing functional groups exhibit relatively higher binding energies with sodium atoms than L1500 (**Figure 6.3**e), validating the stronger interaction between sodium atoms and defect sites. Among different types of nitrogen doping including pyridinic nitrogen (N-6), pyrrolic nitrogen (N-5) and quaternary nitrogen (N-Q), the quaternary nitrogen-doped L700 has the largest binding energy of -2.1 eV. Meanwhile, it can be confirmed that nitrogen-containing functional groups of L700 are dominated by quaternary nitrogen based on XPS fitting analysis (**Table 6.2**). In comparison to L1500, the local charge densities between sodium atoms and quaternary nitrogen-doped L700 increase because of the stronger interaction between sodium atoms and defect sites (**Figure A3.6**, Appendix). Combined with the binding energy simulations reported in the literature,[60, 113, 268-271] it can be attested that defects including extrinsic heteroatom-doped sites and intrinsic carbon defects can all offer binder sites for sodium nucleation by enhancing the binding energy of sodium ions and the defective carbon substrates.

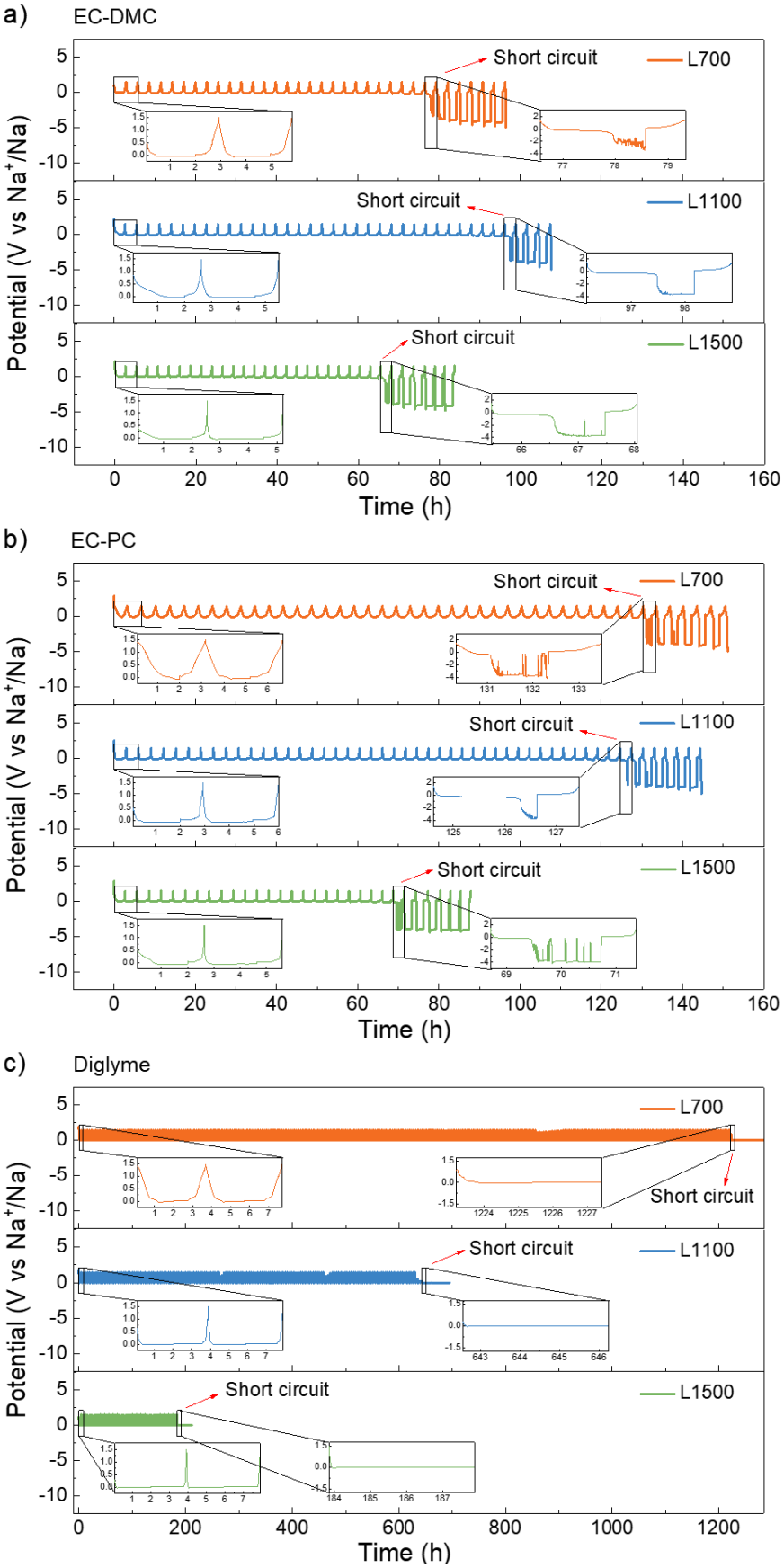


Figure 6.4. The GCD of the plating/stripping of metallic sodium onto/from L700, L1100 and L1500 using 1 M $NaCF_3SO_3$ in a) EC-DMC, b) EC-PC or c) diglyme, respectively.

The cycling performance of L700, L1100 and L1500 was tested in a half cell at a current density of 1.0 mA cm^{-2} with a specific charge and discharge capacity of 2.0 mAh cm^{-2} (**Figure 6.4**). Upon cycling, metallic sodium kept plating onto and stripping from carbon skeletons. The lower Coulombic efficiency means more irreversible capacity, which mostly results from the formation of so-called "dead sodium" including the sodium consumed in solid electrolyte interphase (SEI) and isolated metallic sodium.[35] In the ether-based electrolyte, L700 exhibits the most stable plating and stripping process of over 1200 h (4 h per cycle, over 300 cycles) with the highest average Coulombic efficiency of over 99.6% and the highest last cycle Coulombic efficiency of over 99.9% at the same time (**Figure 6.3**f and **Figure 6.4**c), which is one of the best carbon substrates for metallic sodium deposition.[108, 114] The initial Coulombic efficiencies of L700, L1100 and L1500 for sodium plating and stripping are 87.9 %, 94.4 % and 96.2 %, respectively. Differing from the traditional hard carbon anode for sodium-ion batteries with a low initial Coulombic efficiency (usually below 80 %),[39] the carbon mats have quite high initial Coulombic efficiencies during the first cycle of sodium plating and stripping because of fewer irreversible reactions like SEI formation. In ester-based electrolytes, although EC-PC and EC-DMC both deliver poor cycling performance (which will be explained in the following parts), L700 still shows the highest Coulombic efficiency and lowest IR_{drop} compared with L1100 and L1500 (**Figure 6.4**). These results all identify that the defective structures of L700 can significantly improve the reversibility of metallic sodium deposition rather than porous structures of L1500. In addition, I have applied carbon mats from Toray and commercial graphite from Sigma-Aldrich and which both feature negligible defects and few pores as the comparison samples in sodium metal batteries. Please see **Figure 6.5**a and c of Raman spectra as the proofs of the highly ordered structures of carbon mats and graphite. In **Figure 6.5**b and d, we can see that the initial overpotentials of Toray carbon fabric and graphite are 16.4 and 33.4 mV, respectively, which are much larger than that of L700 (10.6 mV) with rich defects and negligible pores in the same electrolyte. The corresponding reversibility and efficiencies are obviously worse than those of L700 as well, where efficiencies of L700 are all over 99.0% starting from the second cycles. Combined with the comparison of the carbon mats to commercial defect-free carbon samples, it can be further proved that defects play a beneficial role when metallic sodium deposits onto carbon materials (**Figure 6.5**).

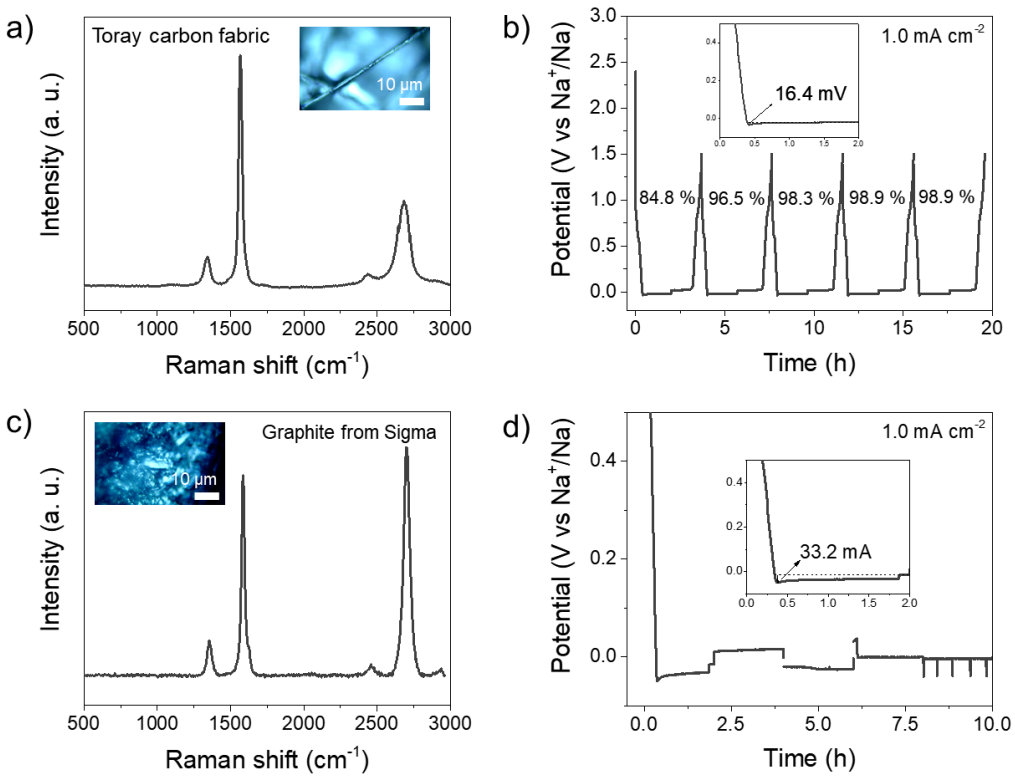


Figure 6.5. a) Raman spectrum of carbon mats from Toray with the inserted photography of the sample; b) The charge-discharge curves of carbon mats from Toray in the half cell configuration for sodium plating and stripping using 1 M $NaCF_3SO_3$ in diglyme; c) Raman spectrum of commercial graphite substrate from Sigma-Aldrich with the inserted photography of the sample; b) The charge-discharge curves of commercial graphite substrate from Sigma-Aldrich in the half cell configuration for sodium plating and stripping using 1 M $NaCF_3SO_3$ in diglyme.

6.3 Fundamental mechanism insights into interfacial phenomena and deposition behaviours

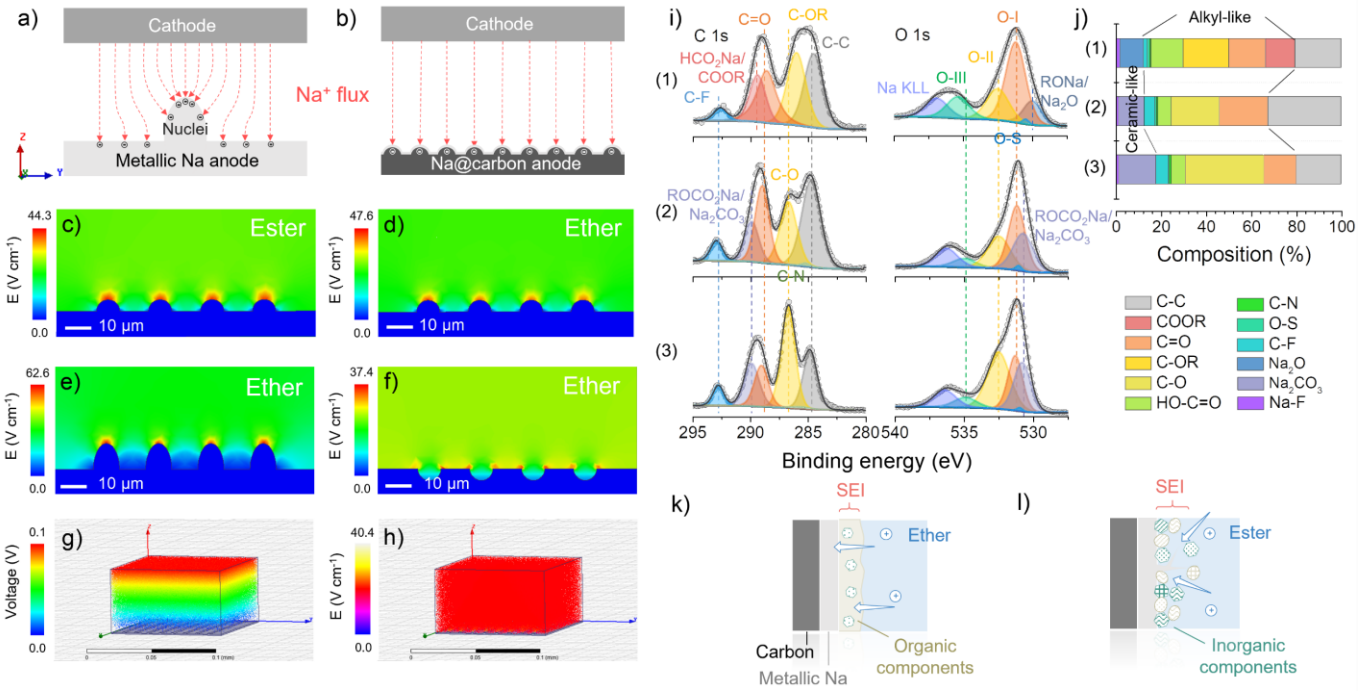


Figure 6.6. Interface analysis. Schematic diagrams of sodium deposition onto a) bare metallic sodium with obvious nuclei, leading to non-uniform ion flux, and b) carbon matrix with homogenous ion flux. Two-dimensional electric field distribution vector profiles of the metallic electrodeposition onto the metallic sodium with the same surface situation in c) the ester-based electrolyte, and d) the ether-based electrolyte under a constant electric field of 0.1 V. Two-dimensional electric field distribution vector profiles of the metallic electrodeposition onto the metallic sodium with e) bulging nuclei, and f) concave nuclei, in the ether-based electrolyte under a constant electric field of 0.1 V. g) Three-dimensional electric field distribution, and h) its differential vector profile of the metallic electrodeposition onto the carbon matrix in the ether-based electrolyte under a constant electric field of 0.1 V. i) Fitted C 1s (left) and O 1s (right) core level XPS spectra of plated L700 using (1) 1 M $NaCF_3SO_3$ in diglyme, (2) 1 M $NaCF_3SO_3$ in EC-PC, and (3) 1 M $NaCF_3SO_3$ in EC-DMC after the first cycle of metallic deposition at 1.0 mA cm^{-2} with a specific discharge capacity of 2.0 mAh cm^{-2}. j) The corresponding composition calculations of the interface upon the metal/carbon composite anode using (1) 1 M $NaCF_3SO_3$ in diglyme, (2) 1 M $NaCF_3SO_3$ in EC-PC, and (3) 1 M $NaCF_3SO_3$ in EC-DMC. Schematic illustration of possible SEI situation upon the metal/carbon composite anode in k) the ether-based electrolyte, and l) the ester-based electrolyte.

As mentioned before, with the same substrate, the difference in metallic deposition is caused by the properties of electrolytes used. Finite element simulation is employed to study the electric field distribution and corroborate the superior uniformity of ion flux when employing carbon skeletons in the ether-based electrolytes (**Figure 6.6**a and b). First, in **Figure 6.6**c-f, the

substrate (blue) on the bottom is defined as metallic sodium with the same nuclei on the surface. The colours above the substrate represent the differences in the electric field distribution, which indicates the change rate of voltage and the density of ion flux. The tip induction of ion flux is observed both in **Figure 6.6**c and d, but the density of ion flux in the ester-based electrolyte is more concentrated at the tip of nuclei than that in the ether-based electrolyte because the higher ionic conductivity of ester-based electrolyte facilitates the rapid metallic deposition to form sharper dendrites on the surface.[147] The initial ionic conductivity of electrolytes can be confirmed by electrochemical impedance spectroscopy (EIS) of half cells before cycling (**Figure A3.7**, Appendix), where the charge transfer resistance in ester-based electrolytes is smaller than that in the ether-based electrolyte at the beginning. Combined with the modelling of the other two surface scenarios in the ether-based electrolyte (**Figure 6.6**e and f), it can be verified that the rough surface can strengthen the ion flux and then accelerate the dendrite formation, which causes a short lifetime and severe safety problems.[272] In comparison to the bare metallic sodium, carbon mats are replaced as the substrate (grey) in the simulation, where the homogenous ion flux and uniform voltage change can be observed in **Figure 6.6**g and h. The identical electric field distribution can validate the controlled nucleation and deposition dynamics of carbon skeletons at the macro-level in the ether-based electrolyte.[273] Hence, the utilisation of carbon skeletons and ether-based electrolytes theoretically support the prevention of dendrite formation, providing the opportunity for stable sodium metal anode (**Figure A3.8**, Appendix).

Ex-situ XPS is used to analyse the interface of the cycled electrodes, in particular the differences in the solid electrolyte interphase (SEI) "composition" formed in various electrolytes. The XPS analysis was conducted after the initial deposition onto the carbon skeletons at 1.0 mA cm^{-2} with a specific discharge capacity of 2.0 mAh cm^{-2}. During the transfer process from the glovebox to the XPS facility, a vacuum transfer capsule was used to load the samples, preventing surface contamination. According to the fitted C 1s, O 1s and Na 1s core-level XPS spectra of plated L700 (**Figure 6.6**i and **Figure A3.9**, Appendix), the percentage of composition of SEI layers in different electrolytes is revealed (**Figure 6.6**j). First, the peaks of C-C (284.8 eV), C-OR (~286 eV), C=O (~288.6 eV), O=C-O (~289 eV) and C-F (~292 eV) can be observed in **Figure 6.6**i(1). Differing from **Figure 6.6**i(1), the peaks of C-O

(~287 eV) and CO_3 (~289.9 eV) can be seen in **Figure 6.6**i(2) and (3). Secondly, the peaks of C=O carbonyl groups (O-I, ~531.5 eV), C-OH hydroxyl or C-O-C ether groups (O-II, ~532.5 eV), and O=C-OH carboxyl groups (O-III, ~535.5 eV) can be spotted in all three samples. Furthermore, the presence of Na_2O can be stated when 1 M $NaCF_3SO_3$ in diglyme is used, while the Na_2CO_3 can be detected when 1 M $NaCF_3SO_3$ in EC-PC or EC-DMC is employed. For the ether-based electrolytes, the formed SEI is dominated by organic components (~ 68 at%), leading to the establishment of a continuous phase with more flexibility.[147] Besides, inorganic components (~ 12 at%) are dispersed in the dominated continuous organic phase, which finally becomes a uniform and compact mixture of organics and inorganics on the surface of electrodes (**Figure 6.6**k).[38] Such an SEI layer is beneficial to enhanced stability during the repeated platting and stripping process, which has been demonstrated in our reported work.[43] Meanwhile, the two ester-based electrolytes decompose to form a relatively higher proportion of inorganics (~ 18 at%), thus forming more ceramic features, e. g., a fragile and brittle non-uniform mixture of inorganics and fewer organics (**Figure 6.6**l).[220]

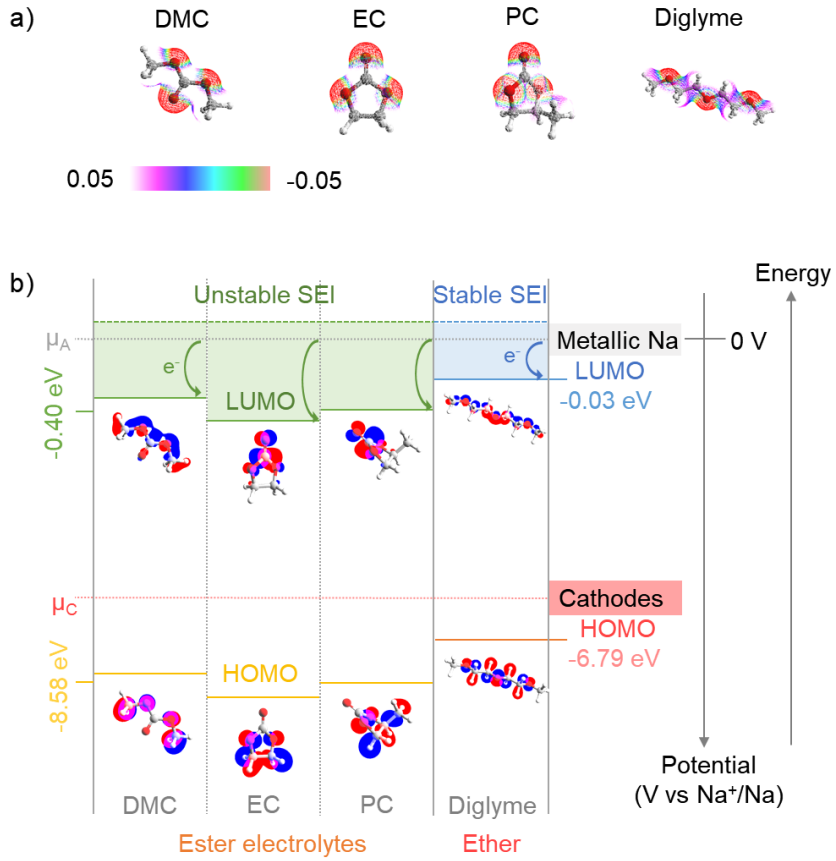


Figure 6.7. a) The electrostatic potential maps of DMC, EC, PC and diglyme (Red colour means the negative charge, and white colour means the positive charge); b) Schematic

illustration of energy states of electrodes, ester-based electrolytes and ether-based electrolytes, where the lowest unoccupied molecular orbital (LUMO), the highest occupied molecular orbital (HOMO) levels and their corresponding electron cloud distribution of free electrolyte solvent molecules (*i.e.,* DMC, EC, PC and diglyme) are presented as well.

When the energy level (μ_A, chemical potential) of metallic sodium is higher than the LUMO of solvent molecules, the electrons can transfer from μ_A of metallic sodium to the LUMO of solvent molecules, thus reducing the electrolyte to decompose and form a passivation solid electrolyte interphase (SEI) layer on the surface of metallic sodium as a barrier to block the further transfer of an electron from μ_A of metallic sodium to the LUMO of solvent molecules.[36] Combined with molecular modelling, the lowest unoccupied molecular orbital (LUMO) and the highest occupied molecular orbital (HOMO) levels of EC, DMC, PC and diglyme molecules are also compared since the LUMO and HOMO levels are related to the electrochemical redox potentials (**Figure 6.7**). Because the LUMO levels of solvent molecules are lower than the energy level of metallic sodium (Na^+/Na), SEI layers confirmed by the XPS analysis can be attributed to the spontaneous decomposition of electrolytes. In addition, free ester molecules like EC, DMC and PC have much lower LUMO levels (average around -0.40 eV) than free diglyme molecules (around -0.03 eV).[99] Hence, ester molecules can obtain electrons from the energy level of metallic sodium, which means ester-based electrolytes are more likely to be reduced by metallic sodium during the plating process. However, ether molecules have a less pronounced reduction tendency, resulting in a less pronounced electrolyte decomposition and a thinner SEI layer (**Figure 6.6**k).[274]

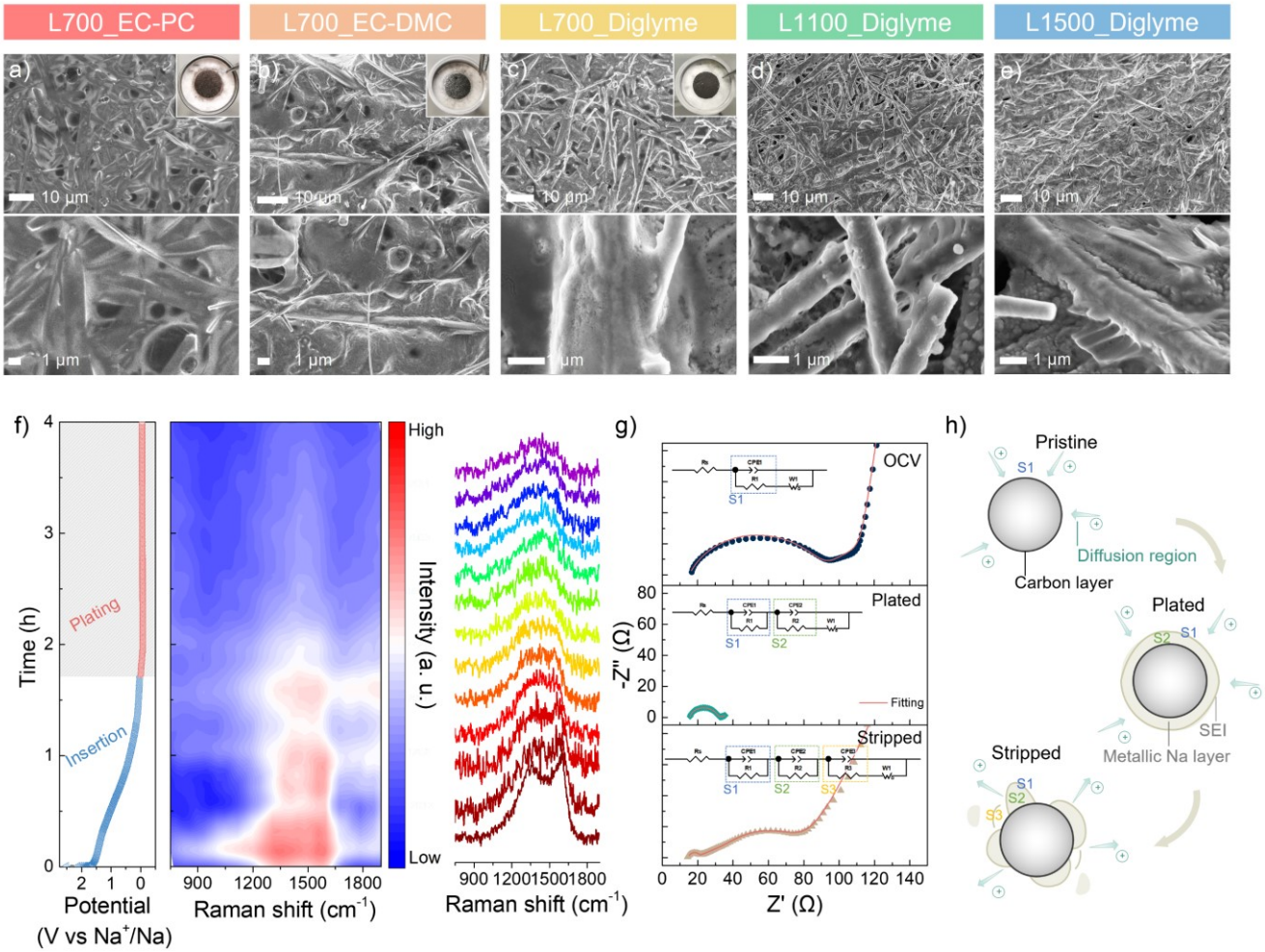


Figure 6.8. Deposition behaviour study. *Ex-situ* SEM morphology evolution of the surface conditions of a) plated L700 in 1 M $NaCF_3SO_3$ in EC-PC, b) plated L700 in 1 M $NaCF_3SO_3$ in EC-DMC, c) plated L700 in 1 M $NaCF_3SO_3$ in diglyme, d) plated L1100 in 1 M $NaCF_3SO_3$ in diglyme, and e) plated L1500 in 1 M $NaCF_3SO_3$ in diglyme, after 10 cycles at 1.0 mA cm^{-2} with a specific discharge capacity of 2.0 mAh cm^{-2}, with inserted photography of the cycled coin cells. f) *Operando* Raman spectra of L700 during the first plating process in 1 M $NaCF_3SO_3$ in diglyme, with the corresponding plating electrochemical curve (left), the mapping of the intensity of Raman spectra (middle), and the specific Raman spectra at different plating stages (right). g) EIS of L700 at OCV, plated stage and stripped stage of the first cycle, with fitted EIS and corresponding equivalent circuits. h) The schematic diagrams of the interface conditions of carbon fibre at OCV, plated stage and stripped stage.

To visualise the metallic sodium deposition behaviour on the carbon skeletons, the morphology evolution is analysed *via ex-situ* SEM. After 10 cycles of platting and stripping at 1.0 mA cm^{-2} with a specific discharge capacity of 2.0 mAh cm^{-2}, the morphologies of a series of carbon skeletons in different electrolytes at a plated state are shown in **Figures 6.8**a-e. An inhomogeneous surface and spherical nuclei can be directly observed on L700 in the ester-based electrolytes (**Figures 6.8**a and b), with the random metallic sodium and exfoliated carbon

dust in the cycled coin cells (Inserted photograph in **Figures 6.8**a and b), which is consistent with the cycling performance and finite element simulation results. In comparison, all carbon skeletons show smoother surfaces in the ether-based electrolyte owing to the electrochemical stability of ether-based electrolytes explained above. However, in **Figures 6.8**d and e, numerous small spherical nuclei can still be observed on both the plated L1100 and L1500. L700 exhibits the smoothest and most homogenous surface without any noticeable spherical nuclei in the ether-based electrolyte (**Figure 6.8**c), with the "clean" separator and electrode surface after cycling (Inserted photograph in **Figure 6.8**c), which can additionally identify the more beneficial role of defects for uniform metallic deposition.

To further correlate defects and metallic sodium deposition, *operando* Raman spectroscopy is performed to analyse the electrochemical behaviour in the different regions of the GCD curve at 0.5 mA cm^{-2} with a specific discharge capacity of 2.0 mAh cm^{-2} (**Figure 6.8**f). The set-up of the *operando* Raman spectroscopy is shown in **Figure A3.10** (Appendix). Raman beam (532 nm) was continuously focused on a fixed spot on the surface of L700 during testing. The first Raman spectrum of L700 before discharging has broad characteristic D- and G-peaks (**Figure 6.8**f). Specifically, the G-peak (~1580 cm^{-1}) refers to the first-order Raman scattering from a phonon in the plane of crystalline graphene layers, while the D-peak (~1350 cm^{-1}) corresponds to the disordered scatting.[190] During the whole sodiation (*i.e.,* insertion) (> 0 V vs Na^+/Na) process in the discharge curve, the insertion of Na^+ ions into the carbon bulk phase happens, where the intensities of D- and G-peaks both slightly decrease. For the main sloping region of sodiation (> 0.1 V vs Na^+/Na), both peaks are found to become broader, while the D-peak is gradually shifting to a higher wavenumber, meaning that in this region, Na^+ ions are forming chemical bonding with atoms at in-plane defect sites such as carbon vacancies, substitutional impurities, interstitial impurities.[217, 275] These findings can also support that the longest sloping region in the GCD curve of L700 results from the interaction of Na^+ ions with defect sites. The position of the G-peak remains almost unchanged during the main sloping region of sodiation, suggesting no significant electrochemical interaction of Na^+ ions with the graphitic bands since the G-peak position and width are highly sensitive to electron or ion doping.[217] When the potential is close to 0 V vs Na^+/Na, the decrease of G-peak position can be measured concomitant with an increase in its width because Na^+ ions are interacting with

graphitic bands in this region. The transfer of charge from the sodium atoms to π* antibonding orbitals of carbons affects the length of the C–C bonds.[217] Upon the first sodiation, the formation of SEI also contributes to the slight decrease in the intensities of both peaks.

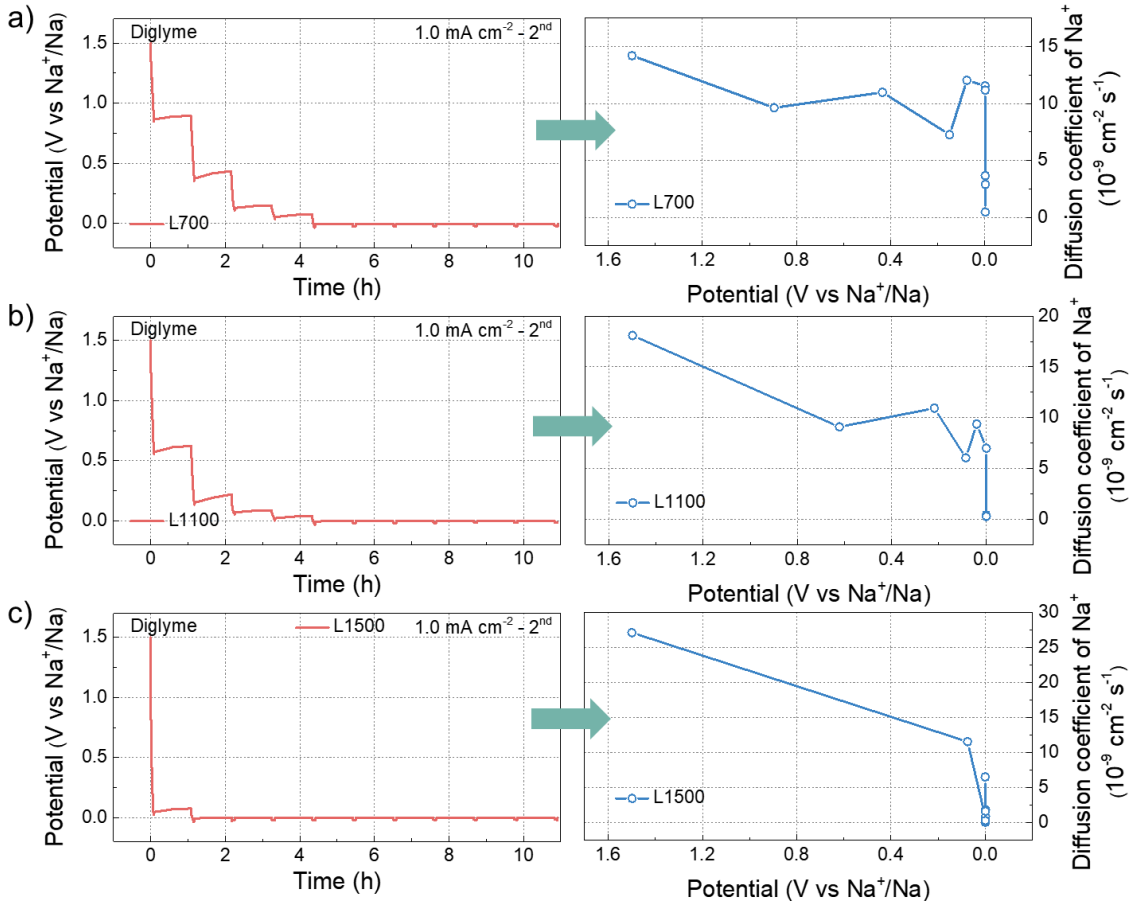


Figure 6.9. GITT profiles of a) L700, b) L1100 and c) L1500 using 1 M $NaCF_3SO_3$ in diglyme (left) and their calculated diffusion coefficient of Na^+ ions (right).

From the perspective of reaction kinetics, the diffusion coefficient of Na^+ ions (D_{Na+}) can be calculated according to the galvanostatic intermittent titration technique (GITT) testing (**Figure 6.9**).[204] During the main sloping region of sodiation (> 0.1 V vs Na^+/Na), the interaction of Na^+ ions with defect sites as a surface-controlled pseudocapacitance takes place first, showing a higher average D_{Na+} and faster kinetics. However, the interaction of Na^+ ions with graphitic bands is hindered by the diffusion-controlled reaction including insertion into graphitic layers and pore filling with lower average D_{Na+} and slower kinetics, which happens at the left region of sodiation (0 - 0.1 V vs Na^+/Na). Compared with L1100 and L1500, the diffusion coefficients of L700 exhibits a lower decrease rate because of the larger insertion capacity. Therefore, combining the material characterisations of L700, L1100 and L1500, it

can be concluded that the existence of rich defects in L700 can significantly contribute to the larger insertion capacity rather than the abundant pores in L1500, which is identical to the explanation on *operando* Raman spectra at the sloping region of sodiation (> 0.1 V vs Na^+/Na). Meanwhile, the insertion behaviour at the defect sites with a faster kinetic than plating process can be further confirmed.

During the whole plating process in the discharge curve (< 0 V vs Na^+/Na), D- and G-peaks finally merge into a single peak as the deposition of metallic sodium onto carbon surfaces starts to happen with the lowest D_{Na+} and slowest kinetics. In the meantime, a continuous decrease in the intensities of D- and G-peaks can be detected. After plating for 30 min, the intensity reduces to around half of the initial value because the surface of carbon skeletons has been partially covered by metallic sodium. When the discharge capacity reaches 2.0 mAh cm^{-2}, the D- and G-peaks disappear as the carbon features on the surface are fully covered with metallic sodium. In this region, the steady decrease in the signal intensity reveals the uniform ion distribution at the interface and the even deposition of metallic sodium.[273] Therefore, it can be further confirmed that the largest sloping capacity (*i.e.,* insertion capacity) of L700 results from its abundant defects. Meanwhile, the sodiophilic properties and durability of L700 for sodium plating and stripping can be enhanced since the stronger interaction between Na^+ ions and defect sites of L700 is beneficial to the uniform nucleation and deposition process,[276, 277] as mentioned above.

Besides *operando* Raman spectra, electrochemical impedance spectroscopy (EIS) from 100 kHz to 0.01 Hz of L700 at the initial open-circuit voltage (OCV), plated and stripped states of the first cycle are employed to understand the sodium plating and stripping behaviour. The specific parts of the obtained Nyquist plots are correlated to the resistor and capacitor elements in Randles equivalent circuits with different charge-transfer resistance parts, thus illustrating the interface condition between the electrolyte and electrode.[218] According to typical Randles circuits, the Nyquist plot can be fitted:[218]

$$Z = R_s + \frac{1}{j\omega C_{dl} + \frac{1}{R_{ct1} + W_o}} + \frac{1}{j\omega C_l + \frac{1}{R_{leak}}} \qquad \text{Equation 6.2}$$

$$Z = R_s + \frac{1}{j\omega C_{dl} + \frac{1}{R_{ct1}}} + \frac{1}{j\omega C_{dl} + \frac{1}{R_{ct2} + W_o}} + \frac{1}{j\omega C_l + \frac{1}{R_{leak}}} \qquad \text{Equation 6.3}$$

$$Z = R_s + \frac{1}{j\omega C_{dl} + \frac{1}{R_{ct1}}} + \frac{1}{j\omega C_{dl} + \frac{1}{R_{ct2}}} + \frac{1}{j\omega C_{dl} + \frac{1}{R_{ct3} + W_o}} + \frac{1}{j\omega C_l + \frac{1}{R_{leak}}} \quad \text{Equation 6.4}$$

where Z (Ω) is the impedance, R_s (Ω) is the inner resistance, R_{ct} (Ω) is the charge-transfer resistance. The sum of R_s and R_{ct} is the equivalent series resistance (ESR) of the device (**Table 6.3**). Furthermore, C_{dl}, C_l, W_o and R_{leak} respectively represent the double-layer capacitance, the low-frequency mass capacitance, the Warburg element and the low-frequency leakage resistance. All the equivalent circuits inserted in **Figure 6.8**g are simplified to mainly focus on the ESR part, thus facilitating the following discussion on the interface conditions at different states. At the low-frequency region (close to 0.01 Hz), processes like ion diffusion with relatively slow dynamics can be detected. In the high-frequency region (close to 100 kHz), processes like ion reaction and migration with relatively faster dynamics can be discovered. At the maximum frequency (starting point of the semicircle), the electron migration with the fastest dynamic can be measured.

First, the EIS tested at OCV is a typical Nyquist plot that shows a semicircle at the high-frequency region and a long sloping line at the low-frequency region (**Figure 6.8**g). At the low-frequency region (close to 0.01 Hz), the decrease in the frequency is accompanied by an increase in capacitance.[31] The long sloping line corresponds to the ion diffusion in liquid and capacitive accumulation at the opening surface of carbon skeletons, thus forming a diffusion layer on the surface (**Figure 6.8**h).[31] In the high-frequency region (close to 100 kHz), the semicircle represents the ion and charge transfer in the intermediate phase (S1), namely the diffusion layer (**Figure 6.8**h).[31] Based on this region, the charge-transfer resistance can be obtained (Equation 6.2). At the maximum frequency, the starting point of the semicircle refers to the inner resistance. Differing from the EIS at OCV, the EIS tested at the plated state shows a shorter sloping line and a smaller semicircle (**Figure 6.8**g). As the carbon surface is fully covered by metallic sodium at the plated state, the diminished opening surface of carbon and negligible diffusion layers both contribute to the considerable reduction of the sloping line. Hence, the ion and charge need to transfer in two new intermediate phases before reaching the carbon (**Figure 6.8**h). One is the SEI layer (S1), and the other is the metallic sodium layer (S2).[218] Along with the decreased charge transfer resistance, the smaller semicircle composed of two individual semicircles suggests the increased charge transfer abilities in metallic sodium

(S2) and SEI layer (S1), which can be perfectly fitted by Equation 6.3 with two charge-transfer resistance sections. Finally, at the stripped state, a long sloping line appears again at the low-frequency region (**Figure 6.8**g) since the stripping of metallic sodium exposes the opening surface of carbon skeletons. Because of the accumulated ions on the exposed opening surface of carbon, the diffusion layer is built up again. Also, a little metallic sodium is inactive and remains on the surface of carbon. Consequently, a small semicircle and a big semicircle consisting of two individual semicircles can be observed at the high-frequency region, which correspond to the ion and charge transfer in the SEI layer (S1), residual metallic sodium layer (S2) and diffusion layer (S3), respectively (**Figure 6.8**h and Equation 6.4).[218]

Table 6.3. Fitted elements of EIS of L700 at OCV, plated state and stripped state.

	R_s	R_{ct1}	R_{ct2}	R_{ct3}
OCV	15.3	74.4	N/A	N/A
Plated	4.6	10.8	15.2	N/A
Stripped	14.4	4.6	5.7	51.2

Unit: Ω

6.4 Practical applications of sodium metal batteries

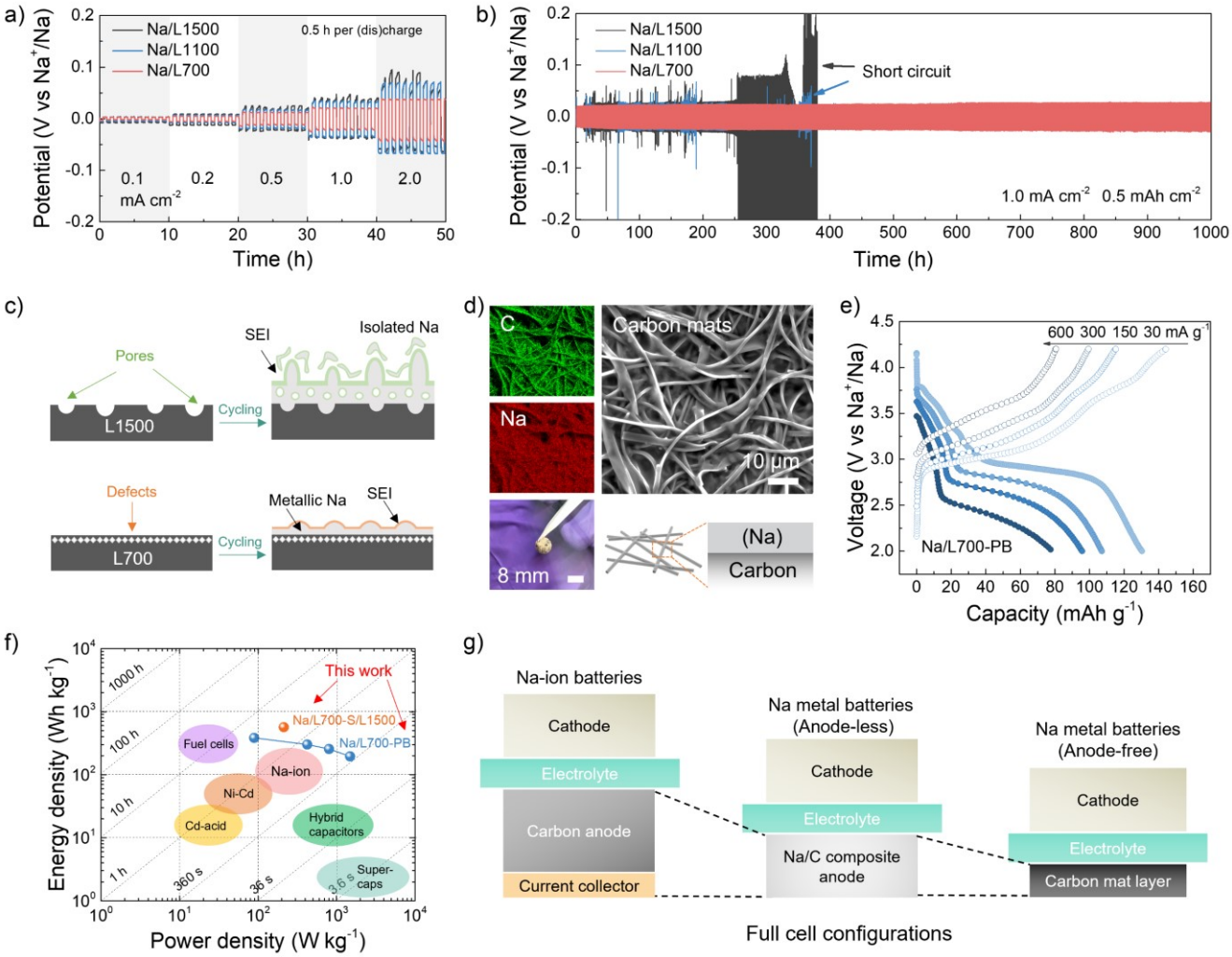


Figure 6.10. Practical applications. a) Rate performance of the Na/C composites in the symmetrical cell at current densities of 0.1, 0.2, 0.5, 1.0 and 2.0 mA cm^{-2} for 0.5 h per (dis-)charge process using 1 M $NaCF_3SO_3$ in diglyme. b) Cycling stability of Na/C composite anodes in the symmetrical cell at current densities of 1 mA cm^{-2} with a specific capacity of 0.5 mAh cm^{-2} using 1 M $NaCF_3SO_3$ in diglyme. c) Illustration images of L700 with defect structures and L1500 with pore structures before and after cycling. d) SEM image, element mapping, photography and schematic illustration of the obtained Na/L700 composite anodes with a certain amount of plated metallic sodium (8 mAh cm^{-2}). e) GCD curves of the Na/L700 composite anode in a full cell at current densities of 30, 150, 300 and 600 mA cm^{-2}, based on the active mass of the coupled Prussian blue cathode. f) Ragone plot of the full cell with the Na/L700 composite anode and Prussian blue cathode, the full cell with the Na/L700 composite anode and sulphur/L1500 cathode, and their comparison with other kinds of energy devices (the energy density and power density of the full cell are normalised by the total mass of active materials in both electrodes). g) Schematic illustration of the design idea of the current "anode-less" sodium metal batteries and future "anode-free" sodium metal batteries, in comparison to the traditional sodium-ion batteries.

In addition to understanding the fundamentals governing the deposition behaviour of metallic sodium on carbon skeletons, the potential for practical application of the Na/C composite anode is also evaluated. The rate and cycling performance of the Na/C composite anodes in a symmetric cell with two identical electrodes is shown in **Figures 6.10**a and b. Before assembling the symmetric cells using 1 M $NaCF_3SO_3$ in diglyme, a certain amount of metallic sodium (8.0 mAh cm^{-2}) was initially pre-deposited on carbon skeletons at a fixed current density of 1.0 mAh cm^{-2} for 8 h in the same electrolyte to fabricate Na/C composite anodes including Na/L700, Na/L1100 and Na/L1500,[184] followed by disassembly of the plated carbons from coin cells. For the rate performance, the composite electrodes in the symmetric cell were repeatedly stripped and plated between each other at 0.1, 0.2, 0.5, 1.0 and 2.0 mA cm^{-2} for 0.5 h per (dis-)charge process. As shown in **Figure 6.10**a, when the current density increases to 2.0 mA cm^{-2}, the potential hysteresis of Na/L1100 and Na/L1500 start to fluctuate, indicating uncontrolled sodium dendrite growth. However, Na/L700 exhibits the most stable potential hysteresis with the lowest overpotentials (< 50 mV) at different current densities. For the cycling performance, the composite electrodes in the symmetric cell were tested at 1.0 mA cm^{-2} with a specific capacity of 0.5 mAh cm^{-2}. The potential hysteresis of Na/L1100 and Na/L1500 obviously fluctuates after just around 350 h of cycling (**Figure 6.10**b). Especially for Na/L1500 with few defects but abundant pores, its potential hysteresis varies a lot, and a significant increase in the plating/stripping overpotentials can be seen because of the formation of dendrite and isolated sodium after cycling (**Figure 6.10**c). However, for the Na/L700 with rich defects but negligible pores, the plating and stripping overpotentials remain stable without any noticeable increase even after 1000 h of cycling, which can also prove the more important role played by defects for uniform metallic deposition. No obvious fluctuation of working potentials can be observed in the Na/L700 symmetric cells after over 100 cycles at the higher current densities (2 and 3 mA cm^{-2}) (**Figure A3.11**, Appendix), which can successfully prove the excellent stability of L700 for fast sodium plating and stripping. In addition, compared with the cycling performance of bare metallic sodium symmetric cells (**Figure 6.11**), the enhanced cycling stability due to the existence of carbon skeletons can be further verified. The SEM image, elemental mapping, photograph and schematic illustration of the Na/L700 composite anodes with a certain amount of plated metallic sodium (8.0 mAh cm^{-2}) are respectively shown

in **Figure 6.10**d from which the uniform distribution of metallic sodium on the carbon skeletons can be recognised.

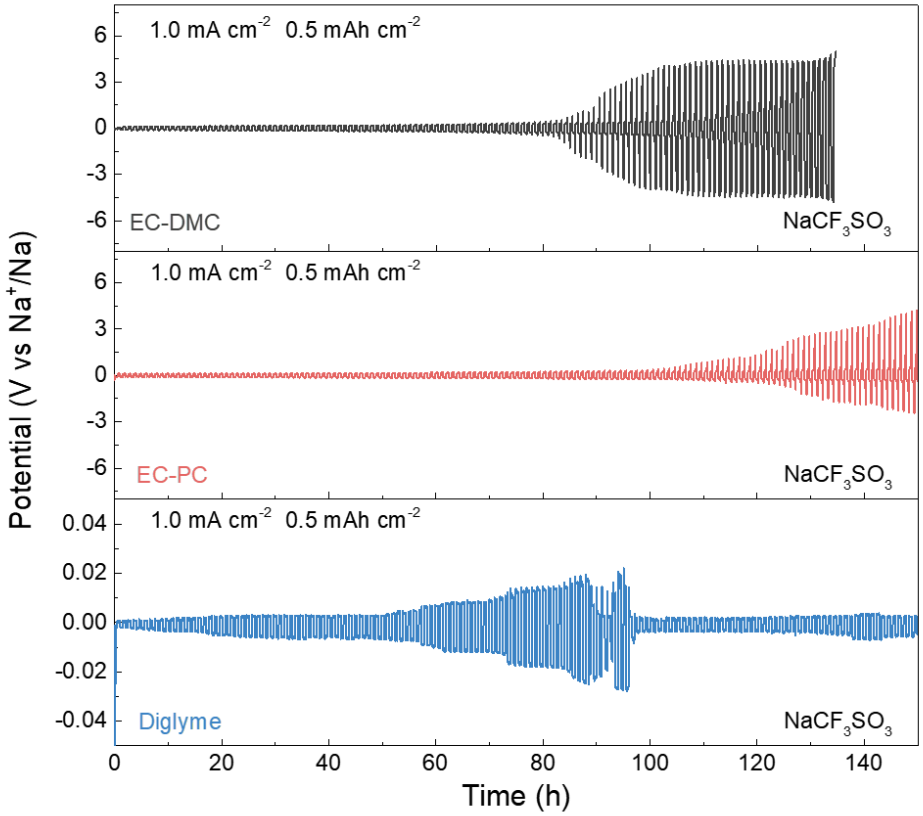


Figure 6.11. The potential hysteresis of the plating and stripping of bare metallic sodium symmetric cells using 1 M $NaCF_3SO_3$ in EC-DMC, 1 M $NaCF_3SO_3$ in EC-PC and 1 M $NaCF_3SO_3$ in diglyme during cycling at 1.0 mA cm^{-2} with a specific capacity of 0.5 mAh cm^{-2}.

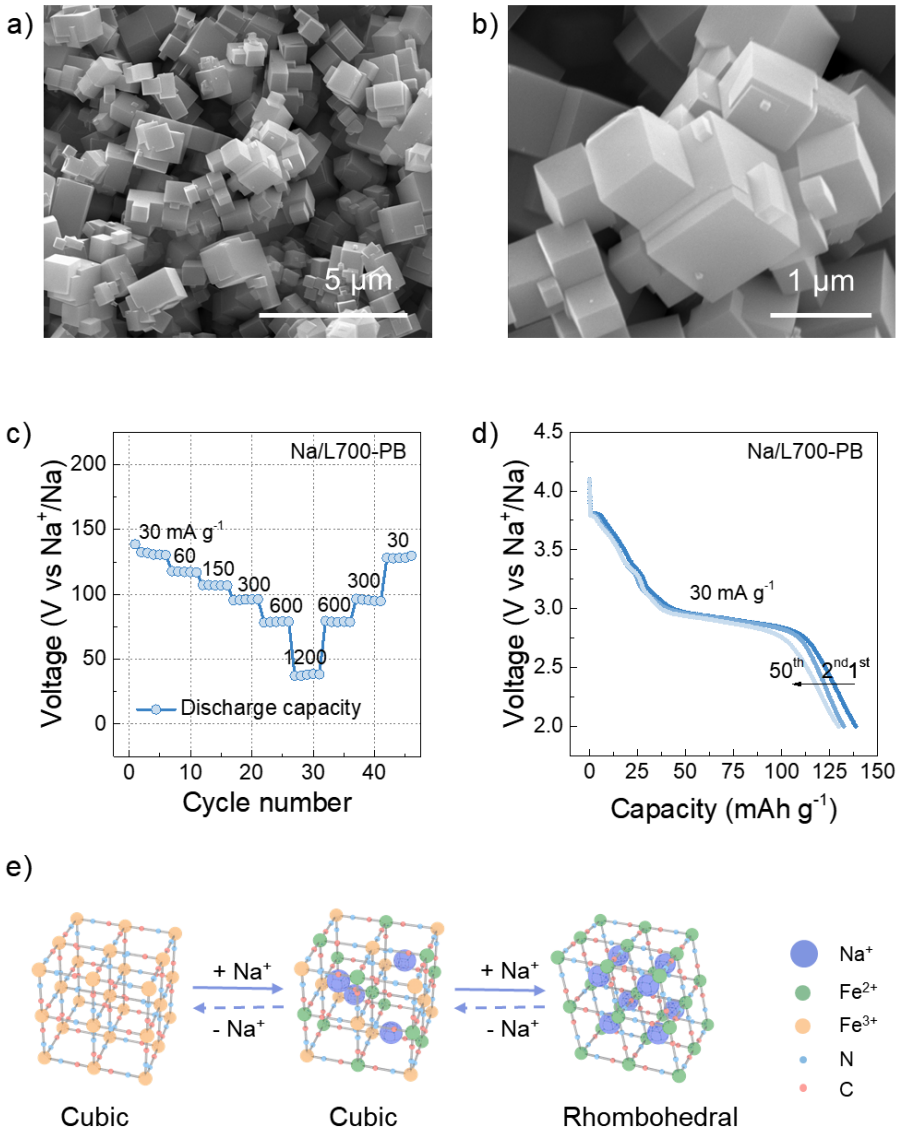


Figure 6.12. a) and b) SEM images of synthesized Prussian blue; c) Rate performance and d) cycling performance of sodium metal batteries with the Prussian blue cathode; e) Schematic illustration of the Na^+ ion storage mechanism of Prussian blue $Fe^{III}Fe^{III}(CN)_6$.

Subsequently, the Na/L700 composite anodes can be applied in a full cell to fabricate sodium metal batteries, coupled with various cathodes including the Prussian blue cathode (**Figure 6.12**a and b) and sulphur cathode (**Figure 6.13**a and b). In the Na/L700 composite anodes, the free-standing carbon skeletons can act as a protection matrix and current collector at the same time, eliminating a large amount of bulk metallic sodium and heavy aluminium or copper current collectors at the anode side compared with a bare sodium metal anode. Therefore, the so-called "anode-less" sodium metal batteries has the potential to decrease the cost of the whole battery and achieve a higher energy density.[41] In the sodium metal batteries

with the Prussian blue (PB) cathode (**Figure 6.10**e), the full cell (Na/L700-PB) can deliver a reversible capacity of 130.3 mAh g^{-1} at 30 mA g^{-1} based on the active mass of the cathode. When the current densities increase to 150, 300 and 600 mA cm^{-2}, the reversible capacities can maintain at 107.1, 95.7 and 77.5 mAh g^{-1}, respectively (**Figure 6.12**c). After 50 cycles of the full cell at 30 mA g^{-1}, a stable cycling performance with no obvious loss of reversible capacity can be achieved (**Figure 6.12**d). Prussian blue was prepared based on the reported method in literature.[134] In principle, the Prussian blue cathode provides the capacity through a two-electron redox reaction where the cubic $Fe^{III}Fe^{III}(CN)_6$ is converted into cubic $NaFe^{III}Fe^{II}(CN)_6$ and further into rhombohedral $Na_2Fe^{II}Fe^{II}(CN)_6$ with the insertion of Na^+ ions (**Figure 6.12**e).[132] We note that, although the low-temperature synthesis methods of Prussian blue cathodes based on aqueous systems are energy-saving , the working potential and Coulombic efficiency of Prussian blue cathodes need to be further improved due to the possible existence of coordinated or interstitial water in Prussian blue cathodes.[23]

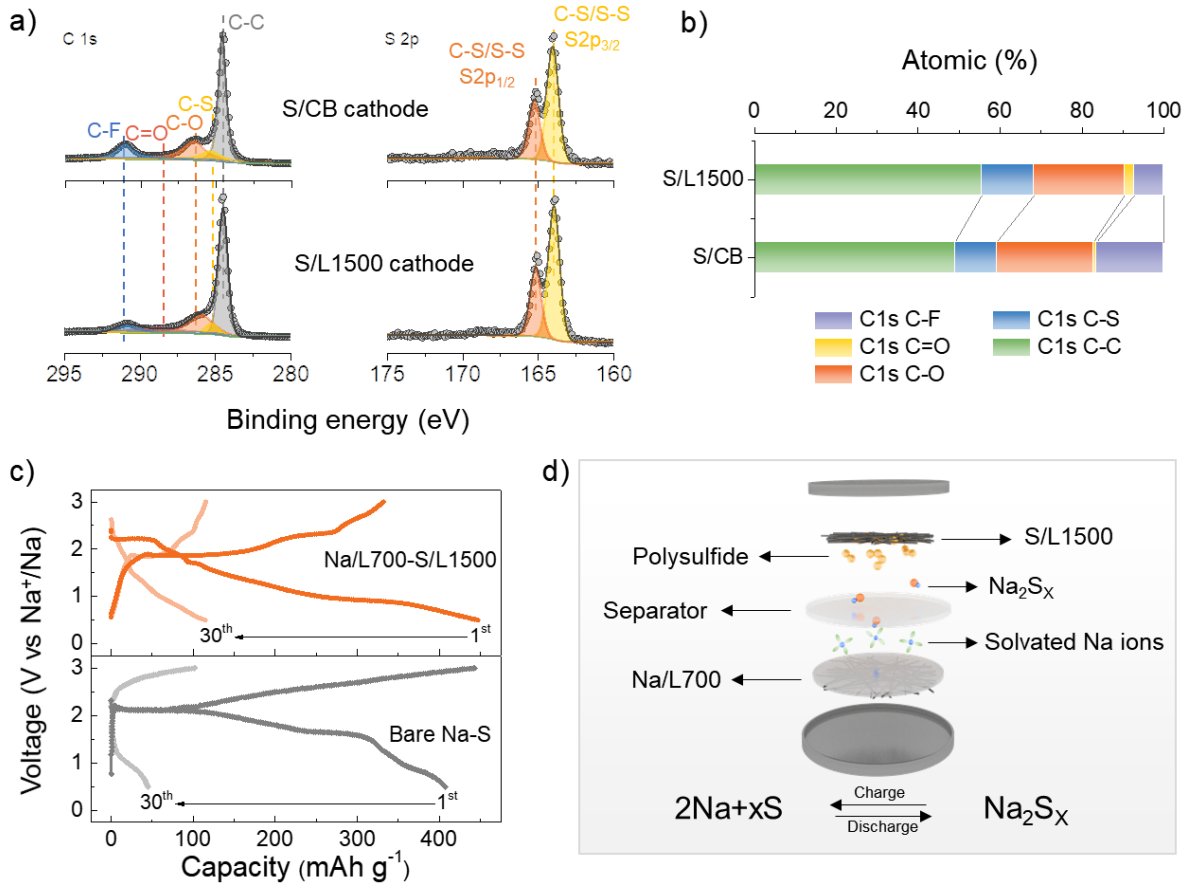


Figure 6.13. a) Fitted C 1s and S 2p core-level XPS spectra of the bare sulphur cathode (S/CB) and sulphur/L1500 cathode (S/L1500), and b) their corresponding atomic percentage; c) GCD curves of the full cells of Na/L700-S/L1500 and bare Na-S before and after cycling at 167.5

mA g^{-1}; d) Schematic illustration of sodium-sulphur batteries with the configuration of Na/L700 anode and sulphur/L1500 cathode (Na/L700-S/L1500).

Moreover, proof-of-concept sodium metal batteries with sulphur cathodes are also studied. The full cell with the configuration of Na/L700 anode and sulphur/L1500 cathode (Na/L700-S/L1500) is compared with the full cell based on the bare metallic sodium anode and sulphur/carbon black cathode (bare Na-S) (**Figure 6.13**). The sulphur cathode was prepared based on the reported method in the literature.[185] The obtained full cell with the supporting of carbon skeletons can exhibit a discharge capacity of 447.3 mAh g^{-1} at 167.5 mA g^{-1}, while the full cell without the carbon skeletons can only display a discharge capacity of 407.1 mAh g^{-1} at the same current density. Besides, the on-set potential of the full cell with the supporting of carbon skeletons (1.8 V vs Na^+/Na) is much lower and smoother than that of the full cell without carbon skeletons (2.2 V vs Na^+/Na), which refer to less polarisation of electrochemical reaction as a result of the utilisation of carbon skeletons. After 30 cycles of the full cells at 167.5 mA g^{-1}, a more pronounced polarisation in the full cell without carbon skeletons can be observed (**Figure 6.13**c), which further substantiates the importance of carbon skeletons to improve the electrochemical performance.[139] At the anode side, the defective structure of L700 facilitates the uniform plating and stripping of metallic sodium, while at the cathode side, the porous structure of L1500 allows the conversion reaction of insulative sulphur (**Figure 6.13**d).[278, 279] Both metallic sodium and sulphur are effectively confined in the 3D structure of carbon skeletons with enhanced conductivity of the whole electrode. The retention of the cycling performance still needs further efforts to be enhanced. The loss of capacity is mainly derived from the shuttle effect of the sulphur cathode.

Finally, the calculated energy and power densities of Na/L700-PB and Na/L700-S/L1500 are displayed in Figure 5f. For Na/L700-PB, the energy densities can reach 384.0, 300.9, 255.8 and 195.4 Wh kg^{-1} at the power densities of 89.1, 423.0, 802.2 and 1490.3 W kg^{-1}, respectively, while for Na/L700-S/L1500, the energy density is 567.2 Wh kg^{-1} when the power density is 212.4 W kg^{-1}. For comparison, the energy and power densities of the "anode-less" sodium metal batteries are superior to other kinds of energy devices (**Table 6.4**).[7, 34, 183, 204] Moreover, the defect-rich carbon skeletons have a promising application potential for the next generation "anode-free" sodium metal batteries without using any metallic sodium or pre-deposition

process during the cell assembly (**Figure 6.10**g). A sodium-containing cathode is placed against a piece of the carbon protection layer for sodium deposition only. The stable metallic sodium deposited on the carbon protection layer all originates from the cathode at a suitable voltage.[5, 280] Hence, this "anode-free" design can accomplish the excellent volumetric and gravimetric cell energy density. Besides, Na^+ ions from the cathode will not be wasted to form excessive SEI because of the high initial Coulombic efficiencies of the carbon mats, thus reducing the production costs of the "anode-free" cells. Overall, this work successfully paves the way for the future preparation of "anode-free" sodium metal batteries. However, real devices using this concept will require further optimisation and demonstration in pouch cells which will be the focus of future studies in our research group.

Table 6.4. Comparison of energy densities of sodium batteries.

Sodium batteries (Anode-Cathode)	Energy density (Wh kg^{-1})	References
HCT-$Na_{0.9}[Cu_{0.22}Fe_{0.30}Mn_{0.48}]O_2$[57]	207	*Adv. Energy Mater.* **2016**, 1600659
CCD-$NaNi_{1/3}Fe_{1/3}Mn_{1/3}O_2$[34]	248	*J. Mater. Chem. A*, **2019**, 7, 27567
HC-$Na_{0.72}[Li_{0.24}Mn_{0.76}]O_2$[123]	270	*Joule*, **2019**, 3, 503
Na/L700-PB	384	This work
Na/L700-S/L1500	567	This work

6.5 Conclusions

In this chapter, I have presented the preparation and application of sustainable carbon nanofibre skeletons from the renewable precursor as a free-standing and flexible host for the protection of metallic sodium anodes. Specifically, the tunable microstructures of carbon skeletons are designed and compared to understand the role of various carbon structural features in the electrochemical processes. According to this study, defects in carbon skeletons play a more important role than porosity for inducing uniform metallic deposition. Using a combination of advanced characterisation and multi-scale modelling, the fundamental insights into interfacial phenomena, SEI composition and deposition behaviour in defect-rich carbon structures using

different electrolytes can be obtained. Defects in carbon structure can enhance sodiophilic properties of carbon skeletons by promoting the interaction with Na^+ ions. The utilisation of diglyme with stable $NaCF_3SO_3$ salts can regulate the ionic conductivity and increase the lowest unoccupied molecular orbital (LUMO) energy level of the electrolyte system, which all contribute to suppressing the dendrite formation during cycling. The "anode-less" sodium metal batteries exhibited here represent an initial proof-of-concept towards circumventing the safety hazards while exhibiting high energy densities (384.0 Wh kg^{-1} at 89.1 W kg^{-1}), demonstrating their potentials for flexible or structural energy storage systems in electric vehicles (EVs) and large-scale electrical grids.[18] In addition to the excellent performance metrics, the sustainability of material synthesis and battery manufacturing should also be considered from the entire technological scale,[175] where my approach utilises renewable and abundant resources, eco-friendly aqueous spinning method, relatively low carbonisation temperature (only 700 ºC) and low-cost electrolytes. In conclusion, this work provides new insights into the fundamental understanding of defect-induced metallic deposition mechanism in sustainable carbon skeletons for high-performance sodium metal anodes, which are of great importance to assist with the rational design of cost-effective carbon protection layers for sodium metal batteries in the future.

Chapter 7. Summary and outlook

For sodium-based energy storage technologies, hard carbons exhibit great importance not only directly as the active material to store ions but also as the functional material to stabilise active materials such as metallic sodium. In this thesis, I have demonstrated the development of hard carbons derived from the hierarchical building blocks of natural biomass and prepared through 'green' nature-inspired methods. The rational design of microstructures of biomass-derived hard carbons have been realised based on the nature-inspired methods, thus successfully improving the sustainability and enhancing the performance of emerging sodium-based energy storage devices.

1) In the project of sodium-ion batteries, optimised hydrothermal carbonisation has been studied as a versatile pre-treatment method of glucose to produce high-performance, sustainable hard carbon anodes with a reversible capacity of 347.4 mAh g^{-1} at the current density of 30 mA g^{-1}. Furthermore, innovatively combining life cycle assessment (LCA) with experimental characterisation and theoretical modelling, I present clear evidence for the important role of hydrothermal carbonisation in sustainable sodium-ion batteries by quantifying both their enhanced sustainability and performance. The hydrothermal carbonisation process can pre-stabilise the carbon morphologies and structures, increasing the overall carbon yield and decreasing the carbon emission simultaneously. Meanwhile, I make breakthroughs in achieving a real-time fine spectrum analysis of hard carbons using *operando* Raman techniques. Combined with these advanced characterisation and simulation, the modified sodium-ion storage mechanism in hard carbon anodes is unveiled, which can aid the development of hard carbon anodes for sodium-ion storage. Precisely, the adsorption mode of sodium ions at defect sites in the whole region, especially in the sloping region, can be confirmed. In contrast, the filling mode of sodium ions at nanovoids in the plateau region can be confirmed. In the future, by coupling the hard carbon anodes with a better sodium layered metal oxide cathode, the energy and power of the full cell will be further enhanced close to the commercial lithium-ion batteries. More than that, real devices using the hard carbon anodes at a scale-up level will require further

optimisation in pouch cells.

2) In the project of sodium-ion capacitors, the "all-cellulose-based" quasi-solid-state sodium-ion capacitor has been demonstrated, which ticks all the boxes in terms of novel synthesis, novel electrodes, novel electrolytes possessing improved overall sustainability. The structural hierarchy is introduced into sodium-ion capacitors by utilising the hierarchical forms of cellulose as a bioresource. This all-cellulose-based quasi-solid-state sodium-ion capacitor consists of a capacitor-like cathode from cellulose microfibrils, a battery-type anode from cellulose nanocrystals and a modified cellulose-based gel electrolyte, which are biocompatible and biodegradable. The electrochemical performance of the anodes and cathodes has been evaluated separately in half cells using in-depth characterisation methods as well as their electrochemical kinetics and possible mechanisms. After that, a comprehensive and systemic set of structural and electrochemical characterisation methods have been used to make clear structure-performance correlations for the whole device, which paves the way for the future fabrication of sodium-ion capacitors. In the future, the modification of cellulose-based electrolytes will be needed to realise an all-solid-state sodium-ion capacitor. Meanwhile, the pouch cell configuration will be employed to test the large-scale capacity sodium-ion capacitors for practical applications.
3) In the project of sodium-metal batteries, the structural features of sustainable carbon skeletons have been rationally designed from lignin to unveil the individual roles of defects and pores for metallic deposition. The benefits of defects to the metallic deposition process can be independently identified by comparing the discrepancy in carbon structural features with the corresponding electrochemical performance. The obtained carbon skeletons with rich defects and negligible pores exhibit the best performance when applied to protect metal anodes, indicating that defects in carbon materials play a more important role in facilitating the metallic deposition than pores. Advanced characterisation methods and multi-scale modelling are also employed to elucidate the roles of defects versus pores and provide new insights into the fundamental understanding of defect-induced metallic deposition on carbon skeletons. Combined with different types of cathodes, "anode-less" sodium metal batteries with

enhanced electrochemical performance are also established in terms of sustainability. In the future, I will directly employ the carbon mats as the cost-effective carbon protection layers to realise the idea of "anode-free" sodium metal batteries. At the same time, real devices using this "anode-free" concept will be further demonstrated in pouch cells with enhanced flexibility.

All in all, nature-inspired carbon materials will play important roles in the emerging sodium-based energy storage technologies. I hope this thesis can provide some guidance for the rational design of sustainable, high-performance carbon materials inspired by nature for the emerging sodium-based energy storage technologies in the near future.

Appendix

- *Supplementary information*

A1. Supplementary figures and tables for Chapter 4

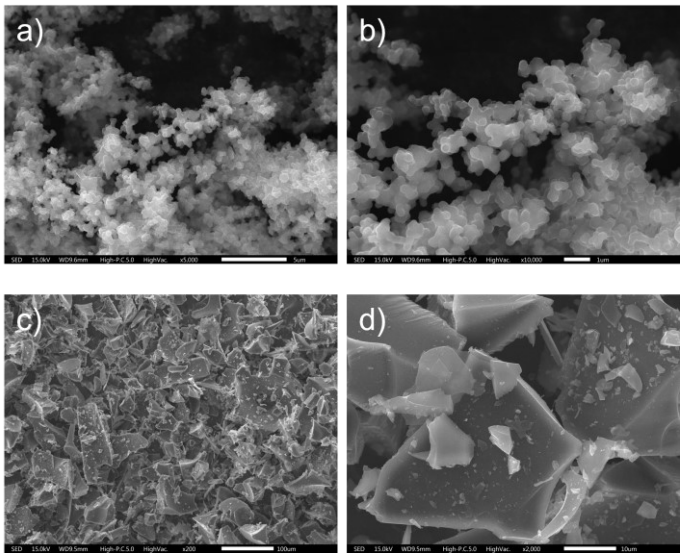


Figure A1.1. a) and b) SEM images of HG1300 at different magnifications; c) and d) SEM images of DG1300 at different magnifications. More SEM images of coated electrodes of hydrothermal carbons can be referred to our previous study.[281] (Scale bar: (a) 5 μm, (b) 1 μm, (c) 100 μm, (d) 10 μm)

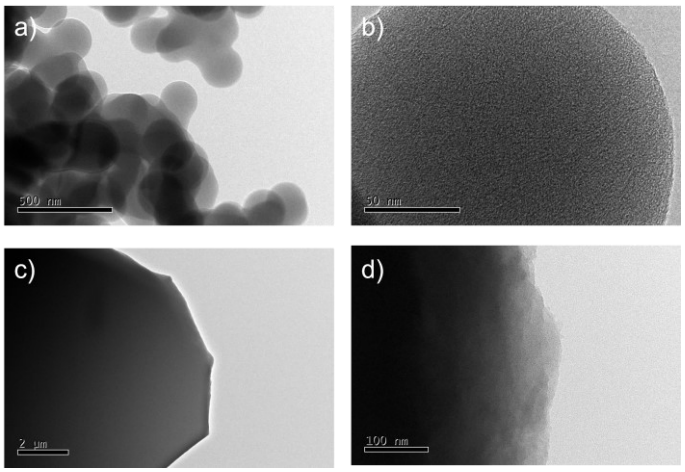


Figure A1.2. a) and b) TEM images of HG1300 at different magnifications; c) and d) TEM images of DG1300 at different magnifications.

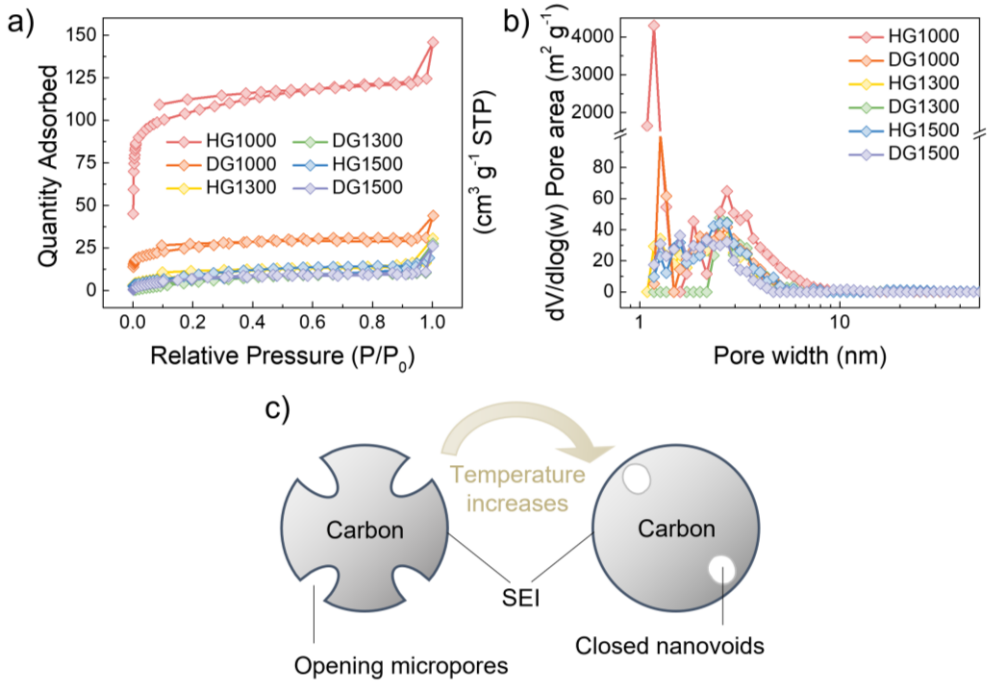


Figure A1.3. a) N_2 adsorption and desorption isotherms, b) the corresponding pore size distributions, of HG1000, DG1000, HG1300, DG1300, HG1500 and DG1500; c) Schematic illustration of the closure of micropores to form closed nanovoids when the carbonisation temperature increases.

HG1500 has a larger plateau capacity than HG1300, while DG1500 has a fewer plateau capacity than DG1300, because the hydrothermal process introduces more micropores (< 2nm) that can be closed at over 1300 ºC into carbons. When the temperature reaches 1300 ºC, the few micropores in DG series samples have all been converted into closed nanovoids, so the plateau capacity of DG series samples reaches the peak value at 1300 ºC. With the further increase in temperature to 1500 ºC, there is no more micropore that can be closed, and the closed nanovoids become narrower, thus decreasing the plateau capacity of DG1300. In contrast, HG series samples have plenty of initial micropores. As the temperature rises to 1300 ºC, part of micropores can be converted into closed nanovoids, hence the plateau capacity of HG1300 increases. With the increase in temperature to 1500 ºC, the left microspores are further closed, which leads to the increased plateau capacity of HG1300.

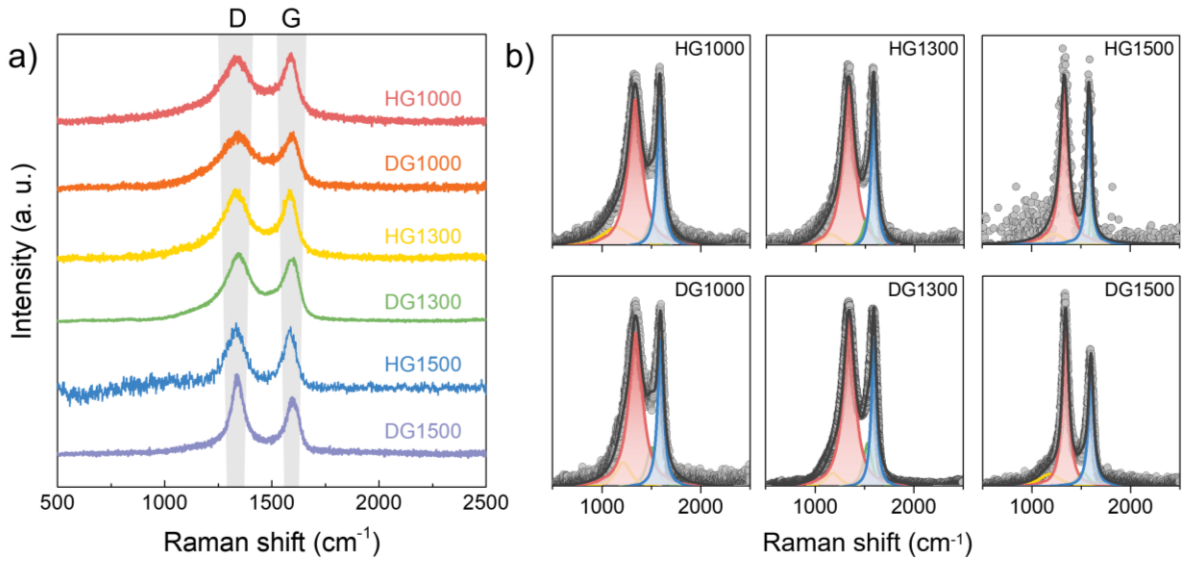


Figure A1.4. a) Raman spectra of HG1000, DG1000, HG1300, DG1300, HG1500 and DG1500; b) Fitted Raman spectra of HG1000, DG1000, HG1300, DG1300, HG1500 and DG1500.

As mentioned in the main text, the sloping capacity of samples keeps decreasing with the increase in temperatures because the increased temperatures result in the decrease of defect structures. Meanwhile, the hydrothermal process can introduce defects into carbons, so the HG series samples always have a larger sloping capacity than DG series samples at the same carbonisation temperature.

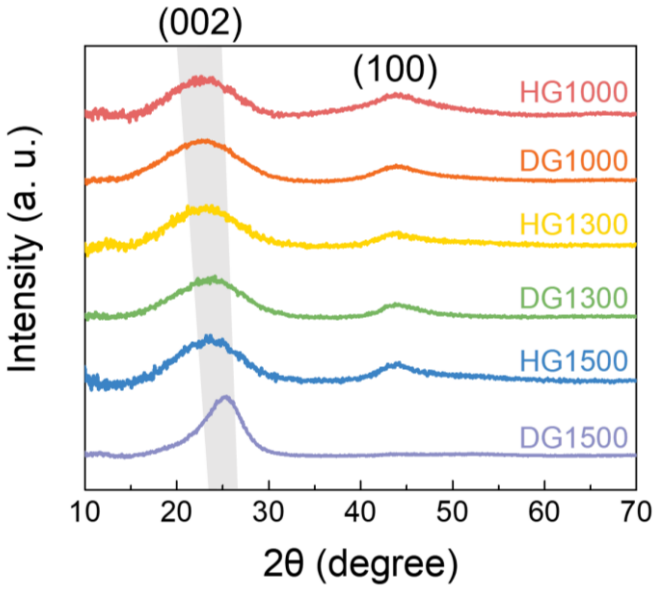


Figure A1.5. XRD patterns of HG1000, DG1000, HG1300, DG1300, HG1500 and DG1500.

By correlating the d-spacing with the plateau capacity in each sample, I can analyse whether the plateau capacity is caused by the insertion of sodium ions into the space between two expended graphene layers. When the temperature increases from 1000 ºC to 1300 ºC, the d-spacing between two expended graphene layers decreases, but the plateau capacity increases, implying that the plateau capacity is not related to the expended d-spacing. If the plateau capacity resulted from the insertion of sodium ions into the space between two expended graphene layers, HG1000 or DG1000 with the broadest d-spacing would have the largest plateau capacity with numerous sodium ions inserting into the space between two expended graphene layers. In fact, HG1000 and DG1000 have the smallest plateau capacity, which indicates the proposed hypothesis is not correct. The plateau capacity should be derived from other sodium-ion storage behaviours like the filling of sodium ions into nanovoids.

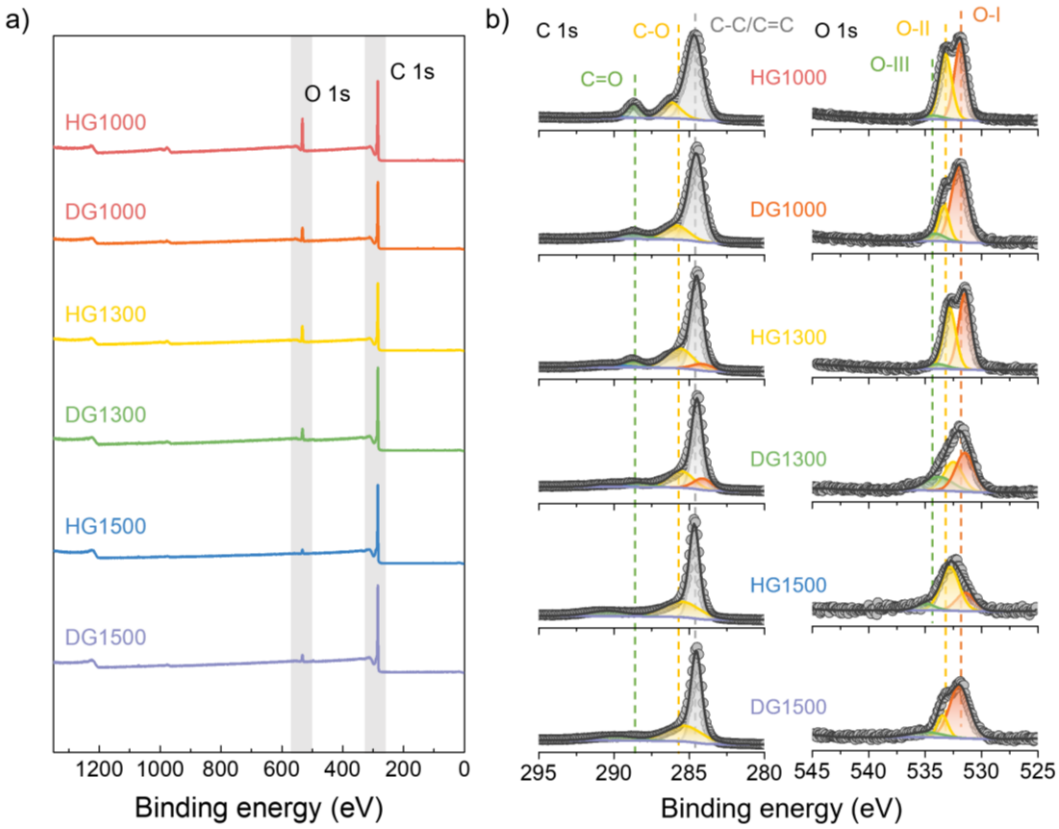


Figure A1.6. a) XPS surveys, and b) Fitted C 1s and O 1s core-level XPS spectra, of HG1000, DG1000, HG1300, DG1300, HG1500 and DG1500.

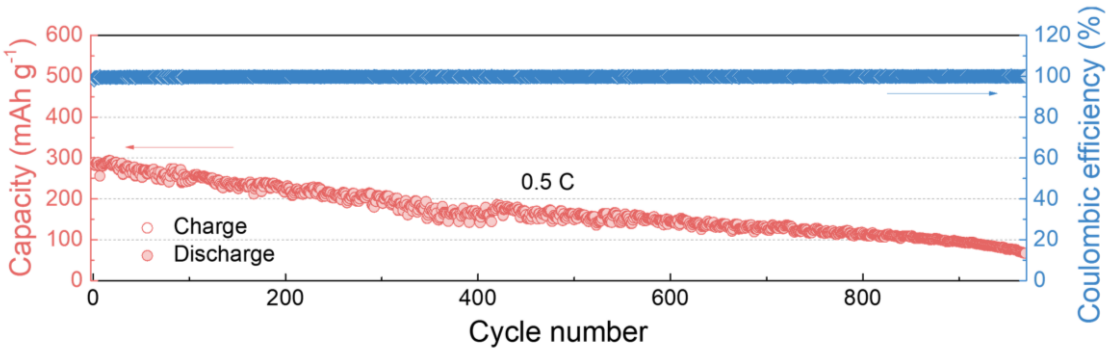


Figure A1.7. Ultra-long cycling performance of HG1300 in the half cell configuration at 0.5C.

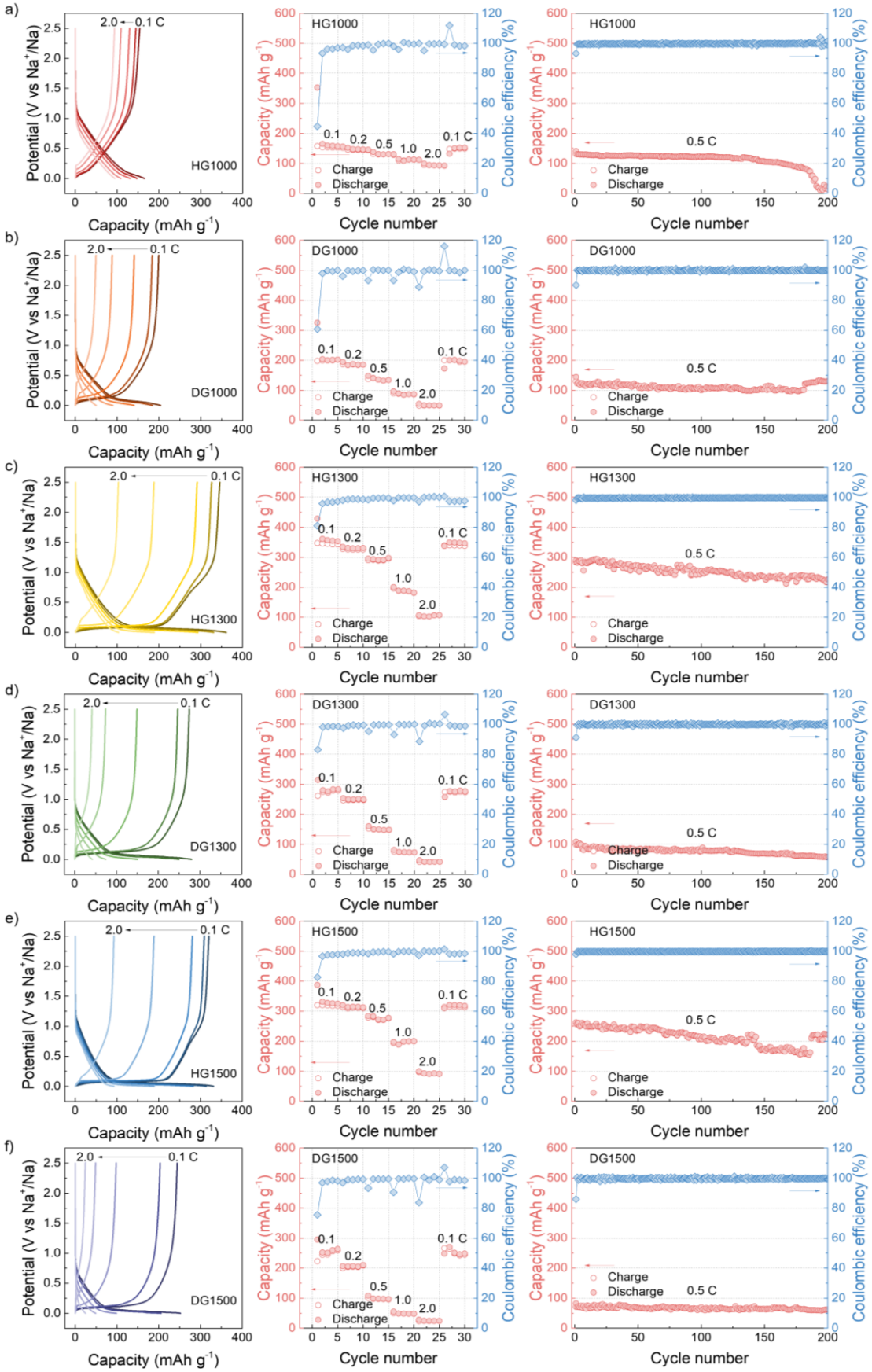


Figure A1.8. GCD curves, rate and cycling performance of a) HG1000, b) DG1000, c) HG1300, d) DG1300, e) HG1500 and f) DG1500

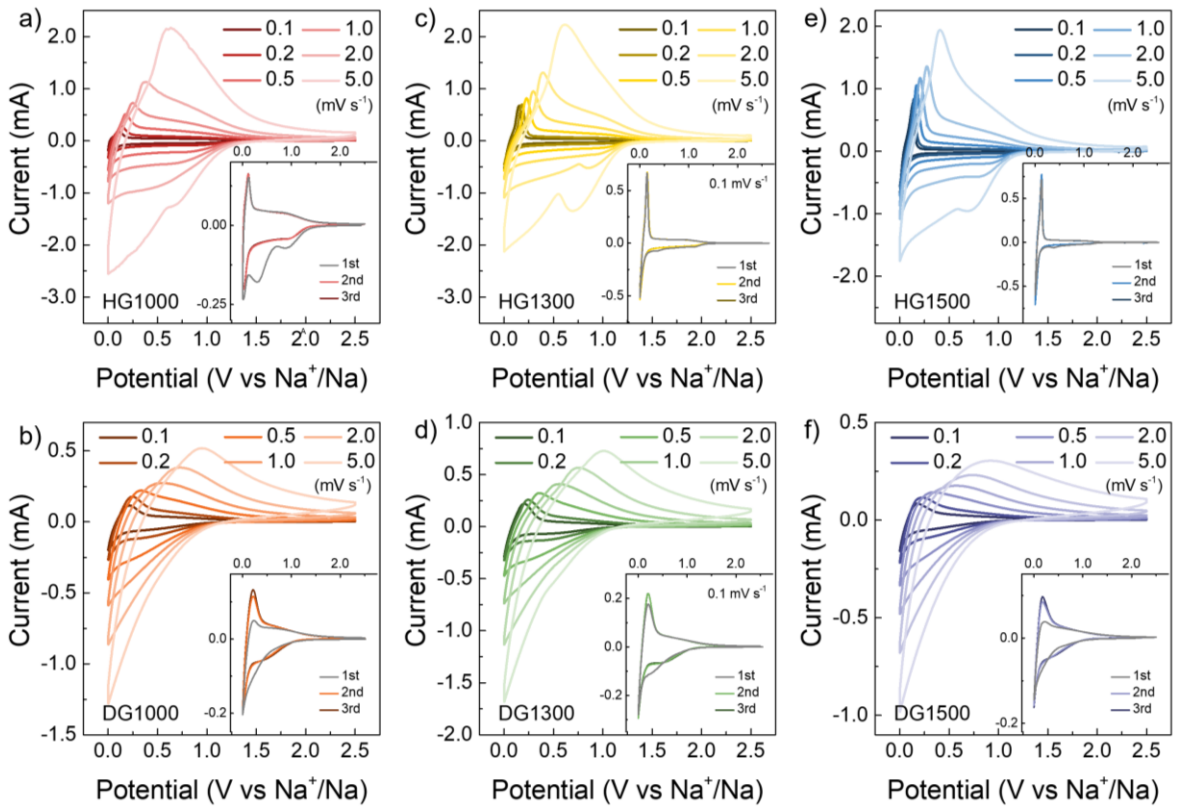


Figure A1.9. CV curves at different scan rates of 0.1, 0.2, 0.5, 1.0, 2.0 and 5.0 mV s^{-1} (the second cycle of each scan rate), inserted with the very first three cycles of CV curves at 0.1 mV s^{-1}, of a) HG1000, b) DG1000, c) HG1300, d) DG1300, e) HG1500 and f) DG1500.

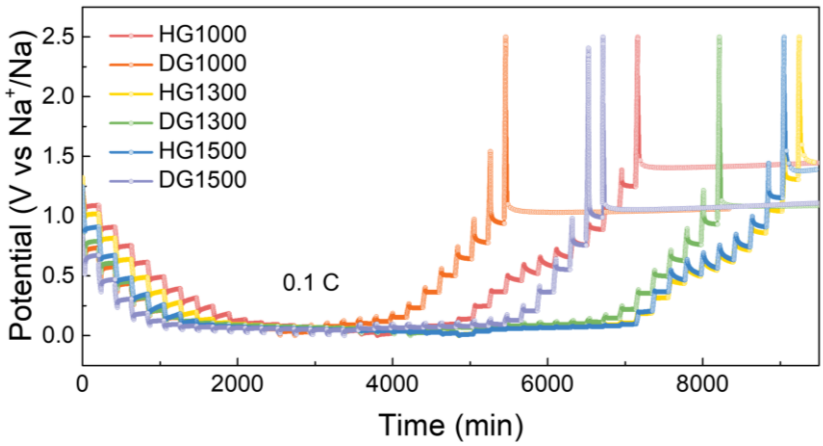


Figure A1.10. GITT profiles by discharging and charging the half cells with a pulse current at 0.1 C for 30 min followed by an interval for 3 h, of HG1000, DG1000, HG1300, DG1300, HG1500 and DG1500. The discharge time decides how many steps and points of diffusion coefficients that can be obtained, while the interval time should be 5 to 10-fold of the discharge time to make sure that sodium ions have enough time to relax and diffuse automatically.

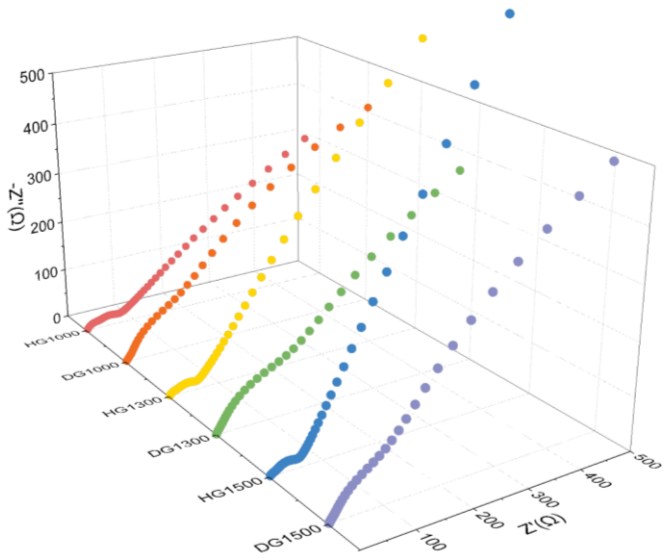


Figure A1.11. EIS of HG1000, DG1000, HG1300, DG1300, HG1500 and DG1500 at the same de-sodiated state.

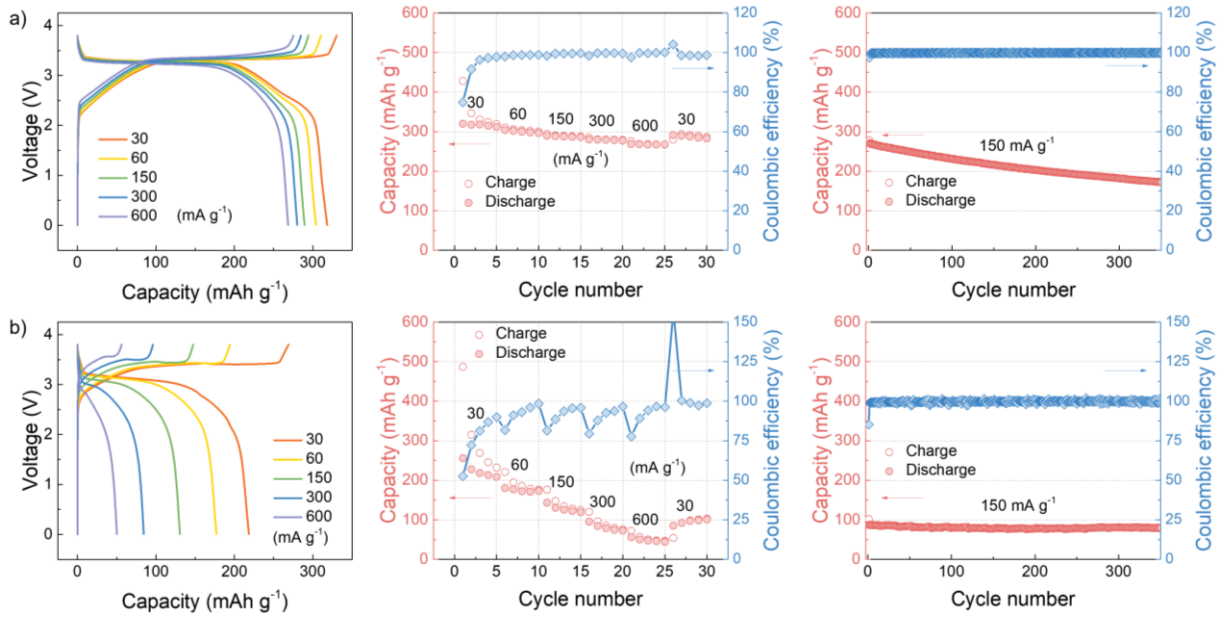


Figure A1.12. GCD curves, rate and cycling performance of a) HG1300//NVP and b) DG1300//NVP (capacities are normalized by the active mass of the anode).

Table A1.1. Inventory data of LCA of HG1300 and DG1300.

Inputs		**Unit**	**HG1300**	**DG1300**
Hydrothermal process	Biomass	kg	4.12	N/A
	Electricity	kwh	0.94	
	Water	kg	37.09	
Carbonisation	Biochar	kg	2.10	N/A
	Biomass	kg	N/A	7.51
	Electricity	kwh	0.57	2.04
	N_2	kg	0.090	0.31
Outputs		**Unit**	**HG1300**	**DG1300**
Hydrothermal process	Biochar	kg	2.10	N/A
	Direct CO_2	kg	1.61	
	Wastewater	kg	37.51	
Carbonisation	Carbon	kg	1.07	1.42
	Direct CO_2	kg	0.82	4.59
	Steam	kg	0.21	1.50
Normalized capacity		Ah	372	372

Table A1.2. Environmental impact results of System A and System B for sodium-ion batteries.

Impact	Scenario	Unit	Step					
			Hydrothermal		Carbonisation			Wastewater
			Direct emission	Electricity	Direct emission	Electricity	N_2	
GWP	HG1300	[kg CO_2-Eq]	1.61159	0.5216	0.81823	0.30204	0.00216	7.29×10^{-4}
	DG1300		N/A		4.59054	1.07892	0.00394	N/A
AP	HG1300	x 10^2 [kg SO_2-Eq]	N/A	0.27274	N/A	0.15526	0.1049	0.0887
	DG1300		N/A			0.55321	0.26083	N/A
EP	HG1300	x 10^3 [kg PO_4-Eq]	N/A	0.87447		0.48203	0.07157	0.01201
	DG1300		N/A			1.72175	0.13036	N/A
HTP	HG1300	[kg 1,4-DCB-Eq]	N/A	0.25387		0.12063	0.13847	0.04721
	DG1300		N/A			0.43192	0.28696	N/A
POCP	HG1300	x 10^3 [kg ethylene-Eq]	N/A	0.10501		0.05939	0.08853	0.04561
	DG1300		N/A			0.21221	0.08345	N/A

A2. Supplementary figures and tables for Chapter 5

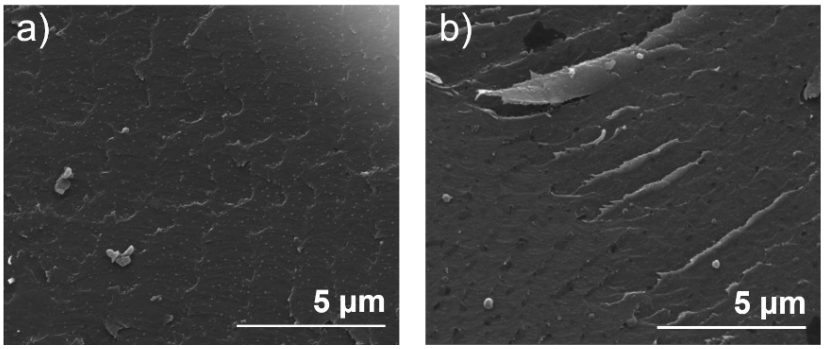


Figure A2.1. SEM images of a) Carbon films (CNC800) with structural hierarchy by direct carbonisation of cellulose nanocrystals at 800℃, and b) CNC1300.

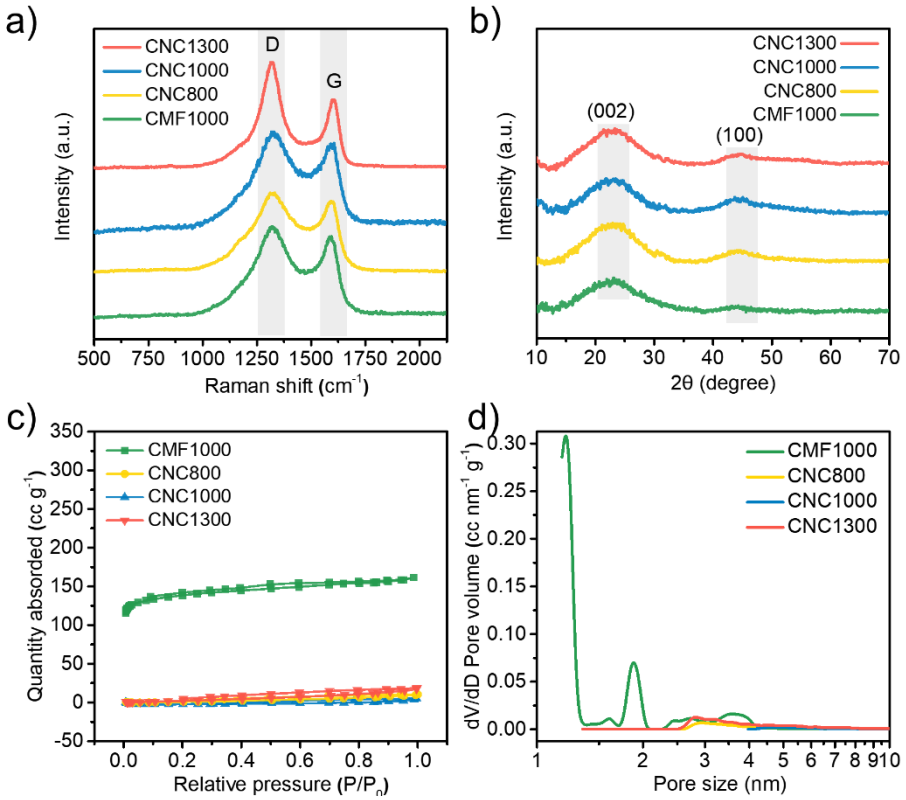


Figure A2.2. a) Raman spectra, b) XRD patterns, c) N_2 adsorption/desorption isotherms (77 K), and d) Pore size distributions obtained from the adsorption isotherms based on non-local density functional theory (NLDFT) method, of different samples (CMF1000, CNC800, CNC1000 and CNC1300). Using the non-local density functional theory (NLDFT) model from the adsorption part of the isotherm, the average pore sizes of CNC1000 and CMF1000 can be obtained. The average pore sizes of CNC1000 and CMF1000 are 4.7 nm and 1.2 nm; therefore, in comparison to CMF1000 with many micropores responsible for the extensive formation of the solid electrolyte interface (SEI), CNC1000 only possesses a few mesopores which could contribute to the ion diffusion without much consumption of Na^+ ions.

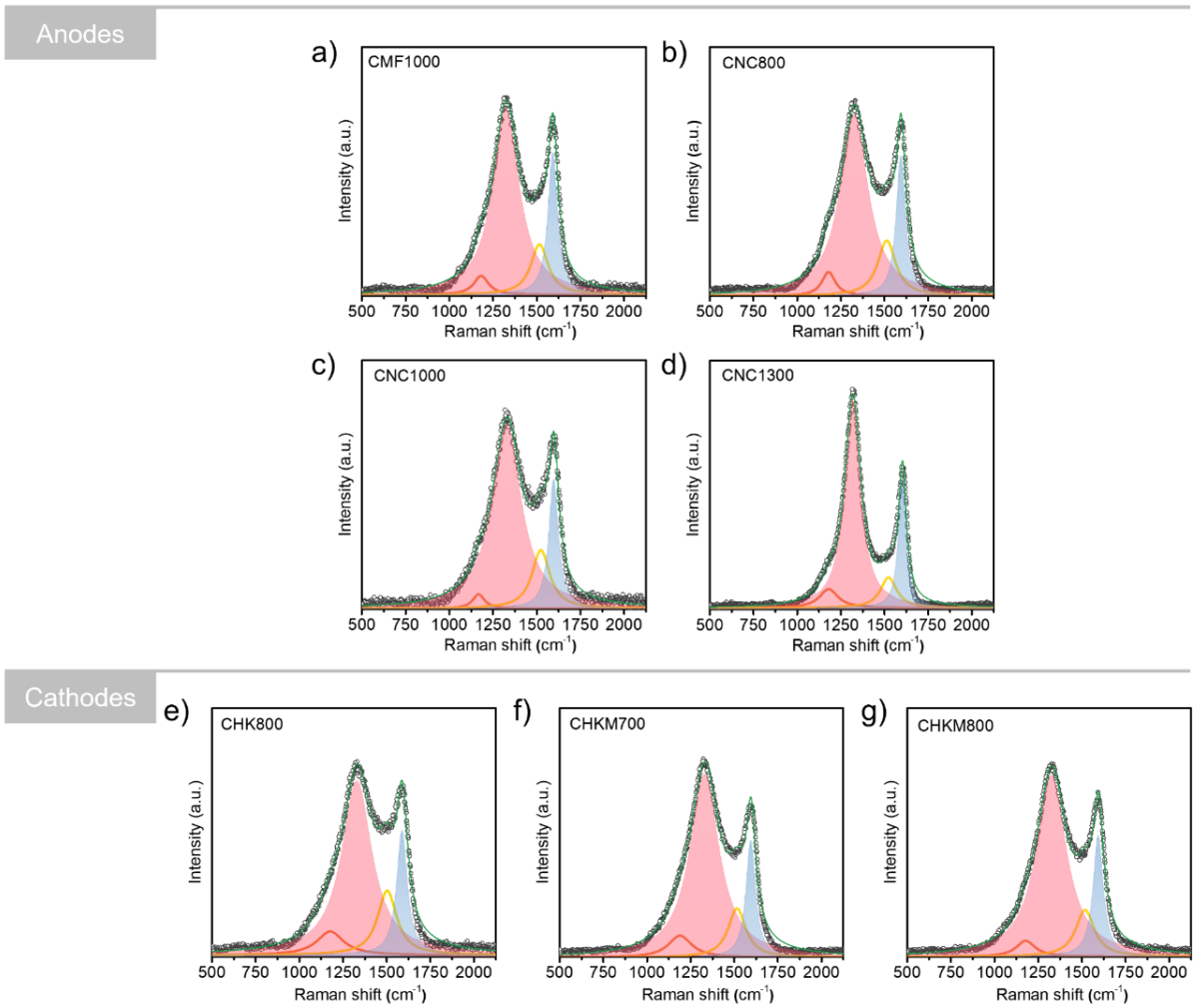
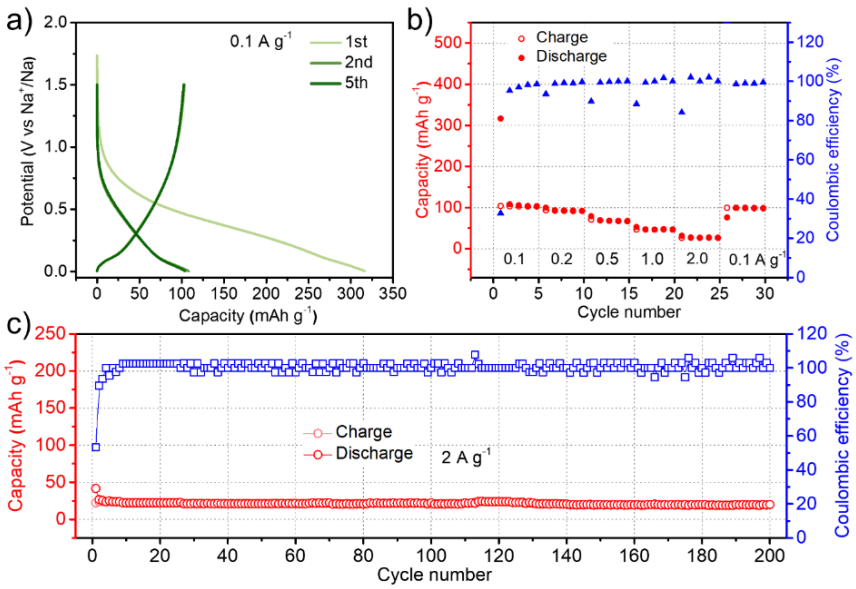
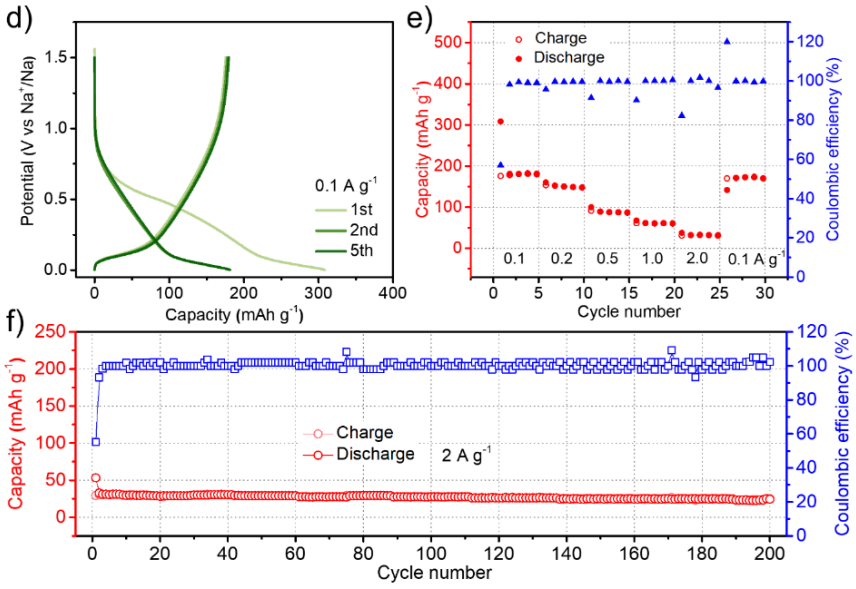


Figure A2.3. a-d) Fitted Raman spectra of CMF1000, CNC800, CNC1000 and CNC1300; e-g) Fitted Raman spectra of CHK800, CHKM700 and CHKM800, respectively (Peak Fitted by Lorentz models).

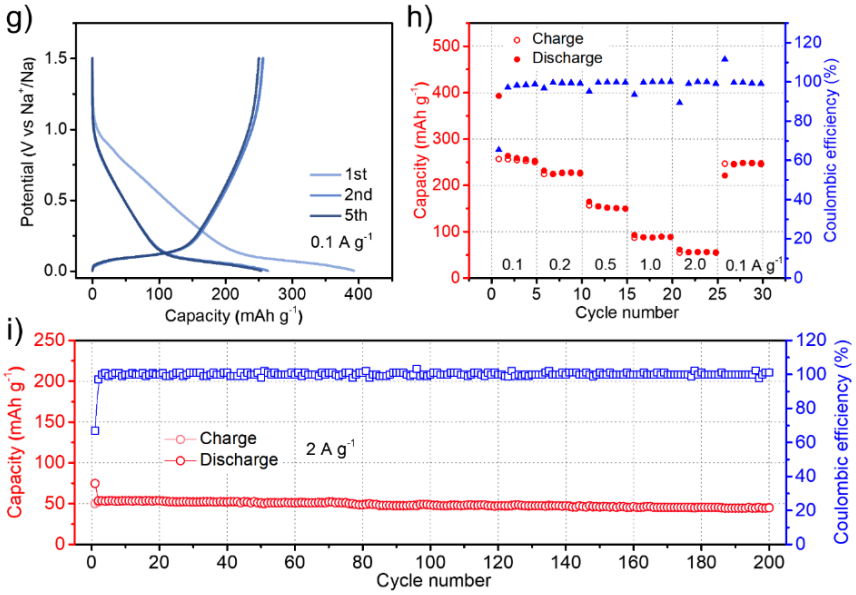
CMF1000



CNC800



CNC1000



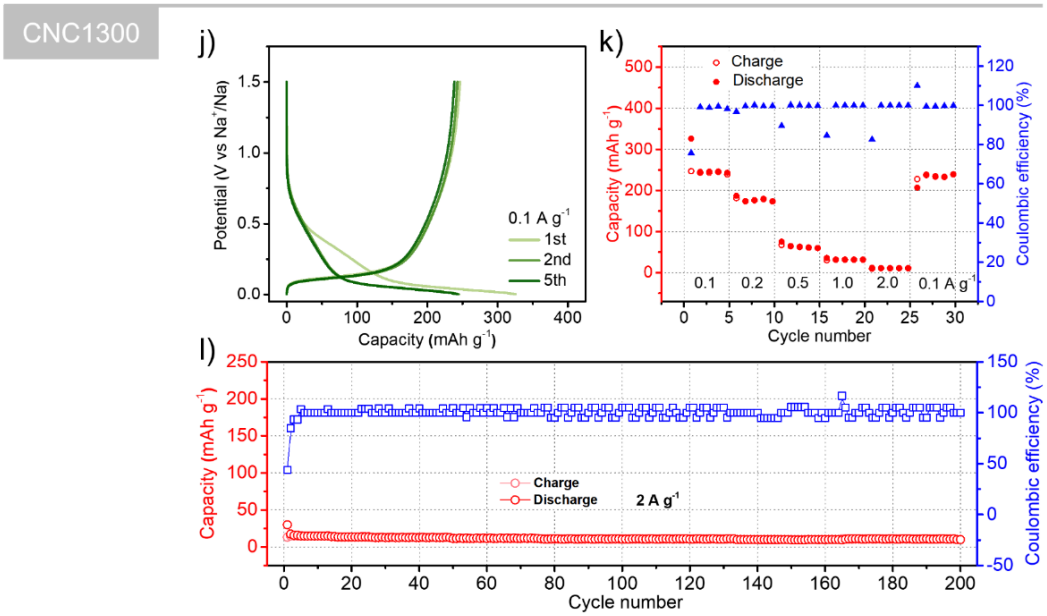


Figure A2.4. Electrochemical performance (GCD curves, rate and cycling performance) of a-c) CMF1000, d-f) CNC800, g-i) CNC1000, and j-l) CNC1300. For carbon anodes, different carbonisation temperatures of cellulose nanocrystals do not result in significant changes in surface areas of carbon samples (CNC800, CNC1000 and CNC1300), all being below 35 m^2 g^{-1}.

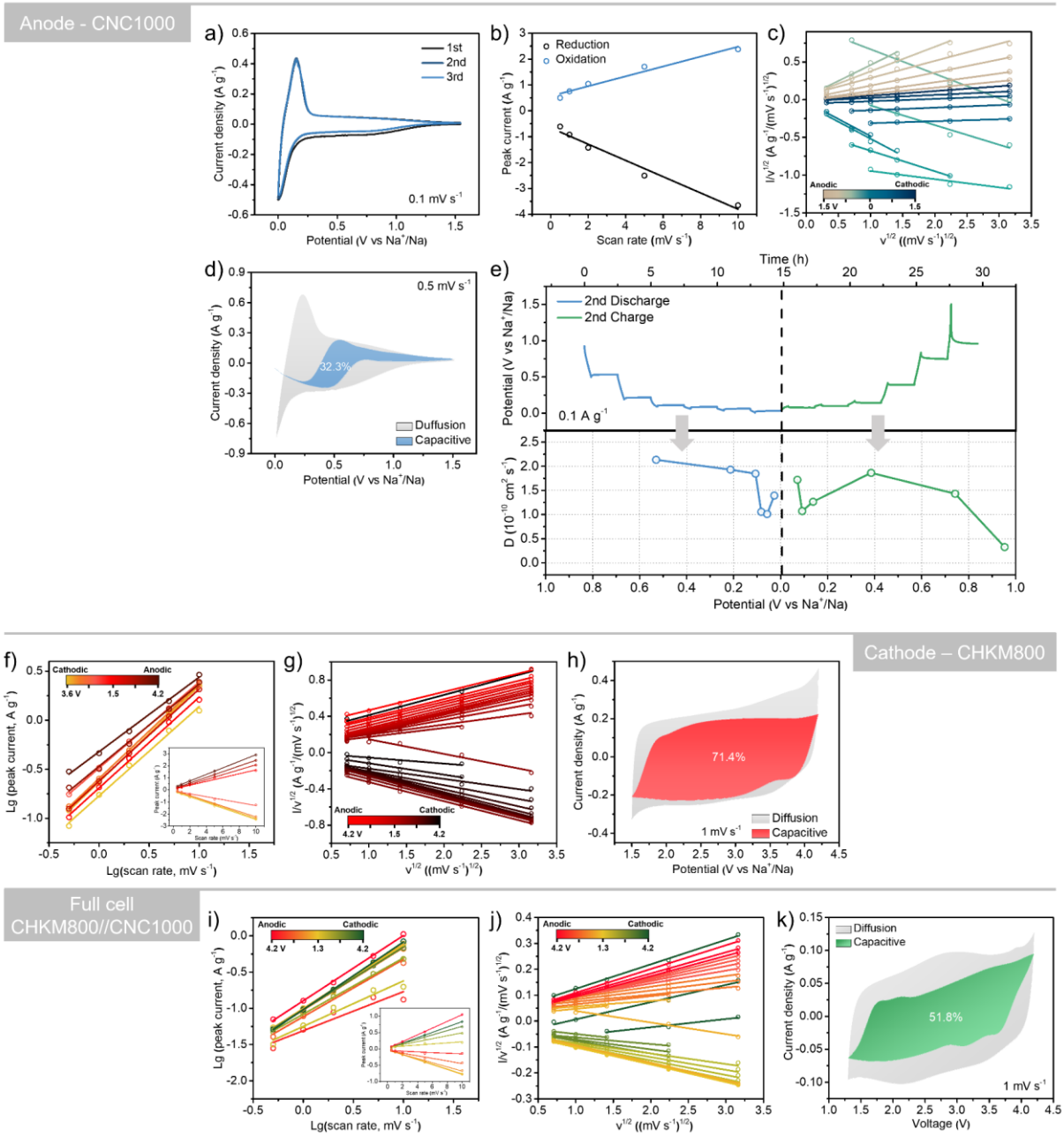


Figure A2.5. a) The first three cycles of CV curves of CNC1000 at 0.1 mV s^{-1}; b) Linear fitting plots of scan rates vs. peak currents for calculating constants b of CNC1000 in half cells; c) Linear fitting plots of $v^{1/2}$ vs. $i/v^{1/2}$ used for calculating constants k_1 and k_2 of CNC1000 in half cells at different potentials; d) Separation of the capacitive and diffusion currents in CNC1000 anodes; e) GITT profiles of CNC1000 (upper) and calculated Na-ion diffusion coefficients (bottom); f) Linear relationship between lg i and lg v of CHKM800 in half cells at different measured potentials; g) Linear fitting plots of $v^{1/2}$ vs. $i/v^{1/2}$ used for calculating constants k_1 and k_2 of CHKM800 in half cells at different potentials; h) Separation of the capacitive and diffusion currents in CHKM800 cathodes; i) Linear relationship between lg i and lg v of CHKM800//CNC1000 in full cells at different measured potentials; j) Linear fitting plots of $v^{1/2}$ vs. $i/v^{1/2}$ used for calculating constants k_1 and k_2 of CHKM800//CNC1000 in full cells at different potentials; and k) Separation of the capacitive and diffusion currents in full cells of

CHKM800//CNC1000.

The formation of SEI gives rise to the irreversible areas in the CV profile of the first cycle (**Figure A2.5**a). For the desodiation process, the same phenomenon with sodiation process can be observed, where the D_{Na+} in the sloping region is apparently larger than D_{Na+} in the plateau region (**Figure A2.5**e). However, during the high potential region, the decrease of the coefficient may result from the slow diffusion process when charging near the cut-off voltage, which is similar to the previously reported results.[57]

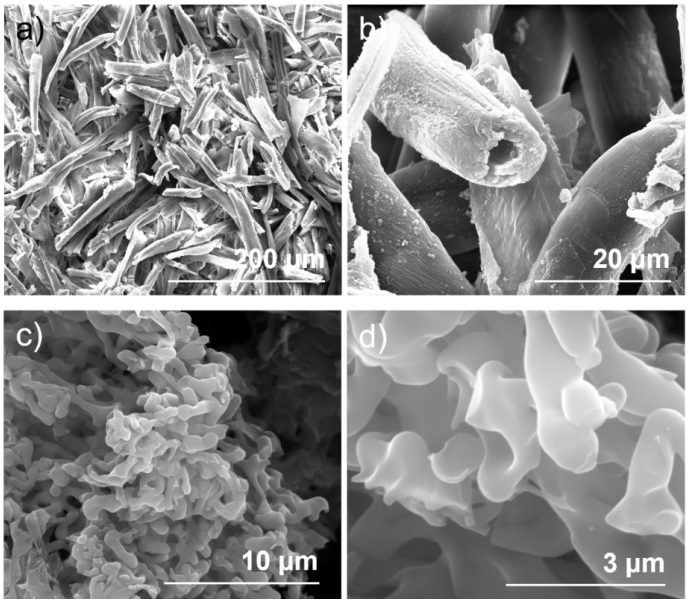


Figure A2.6. a) and b) SEM images of carbon microtubes derived from cellulose microfibrils *via* hydrothermal treatment; c) and d) SEM images of coral-shape nitrogen-doped carbon materials (CHKM700) with a hierarchically porous architecture prepared by $KHCO_3$ and Melamine co-activation at 700°C. Cellulose microfibrils as the carbon precursor can maintain the cross-linked networks of hierarchically porous carbons after thermal treatment and chemical co-activation.

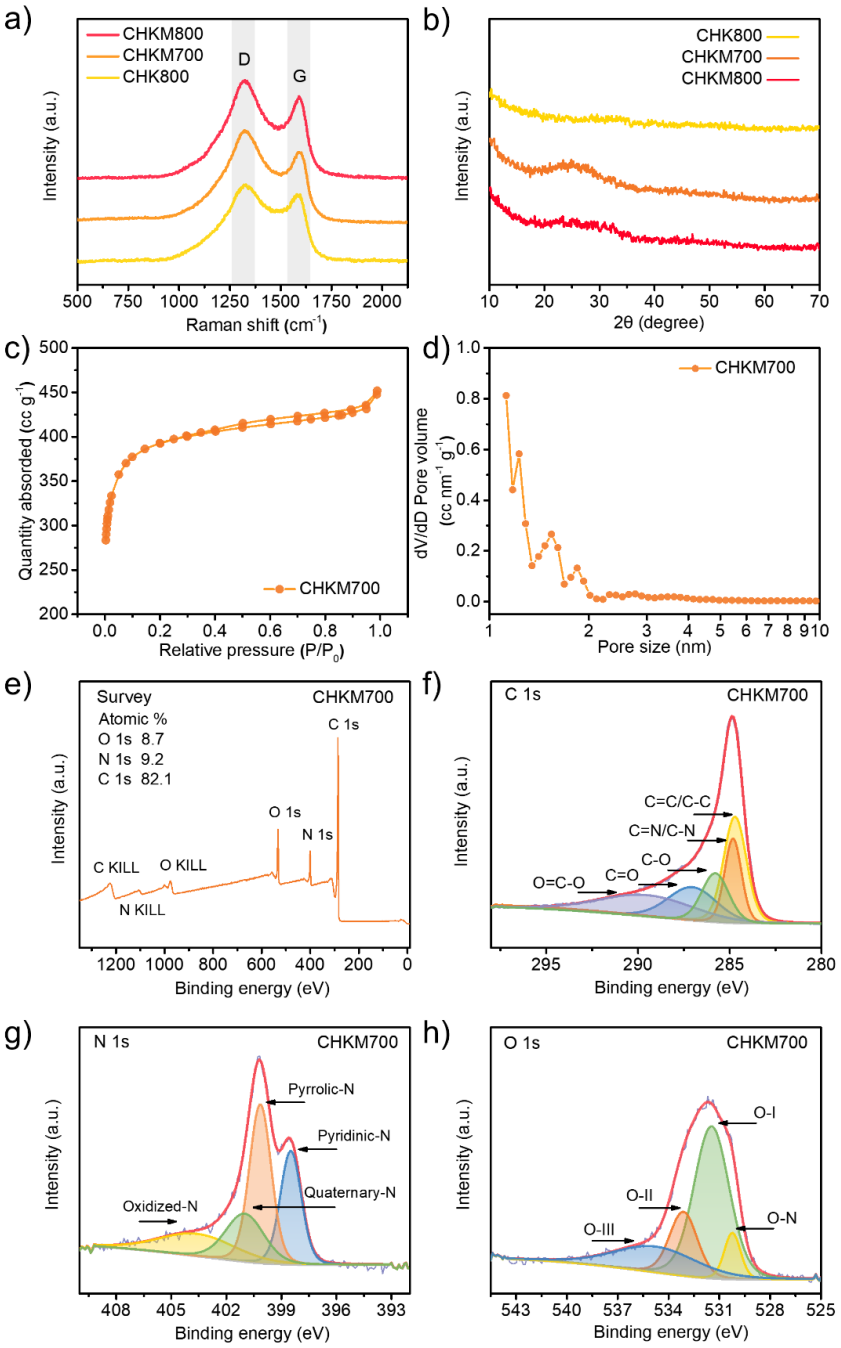


Figure A2.7. a) Raman spectra, and b) XRD patterns of carbon cathodes (CHKM800, CHKM700 and CHK800); c) N2 adsorption/desorption isotherms at 77 K, and d) Pore size distributions calculated from the adsorption isotherms using NLDFT method, of CHKM700; e) XPS survey spectra of CHK700 with the atomic percentage of different elements; f) C 1s, g) N 1s and h) C 1s core level XPS spectra of CHKM700.

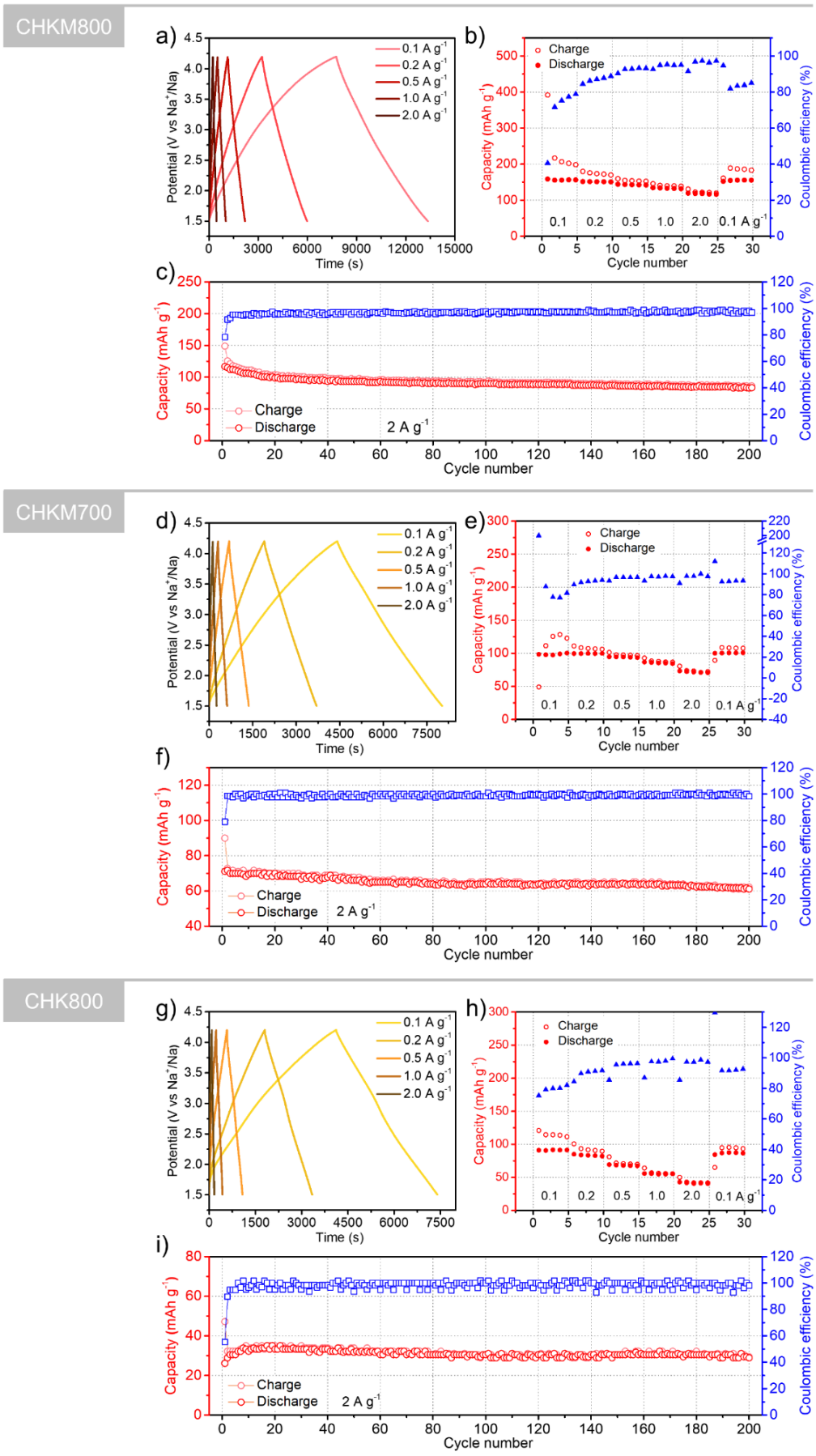
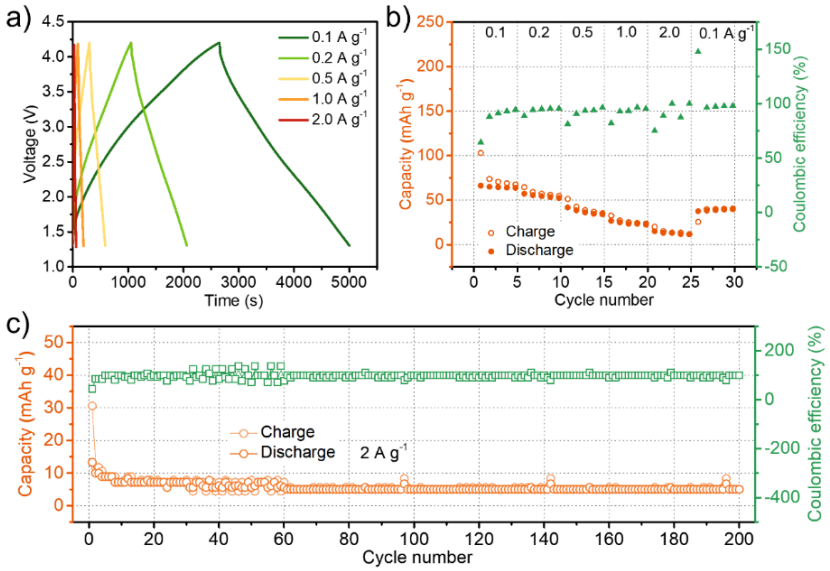


Figure A2.8. Electrochemical performance (GCD curves, rate and cycling performance) of a-

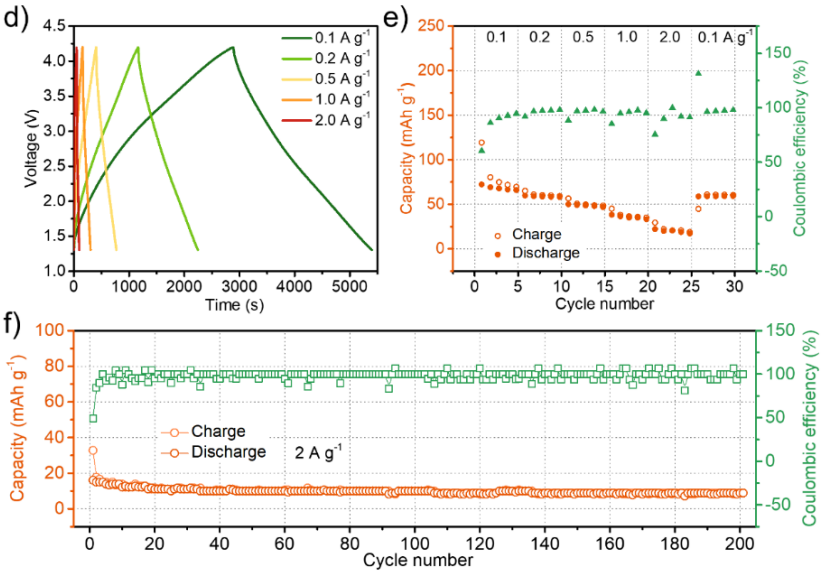
c) CHKM800, d-f) CHKM700 and g-i) CHK800.

For carbon cathodes, with the increase of co-activation temperatures, the porosity developed will increase, but there is a critical temperature after which the structure of the carbons will collapse, and heteroatoms will escape as gases. Based on the experiments, when the co-activation temperature rises to 900 ºC, the yield of co-activated carbons decreases sharply to below 5 %, thus greatly increasing the difficulty of their practical applications in real devices.[171]

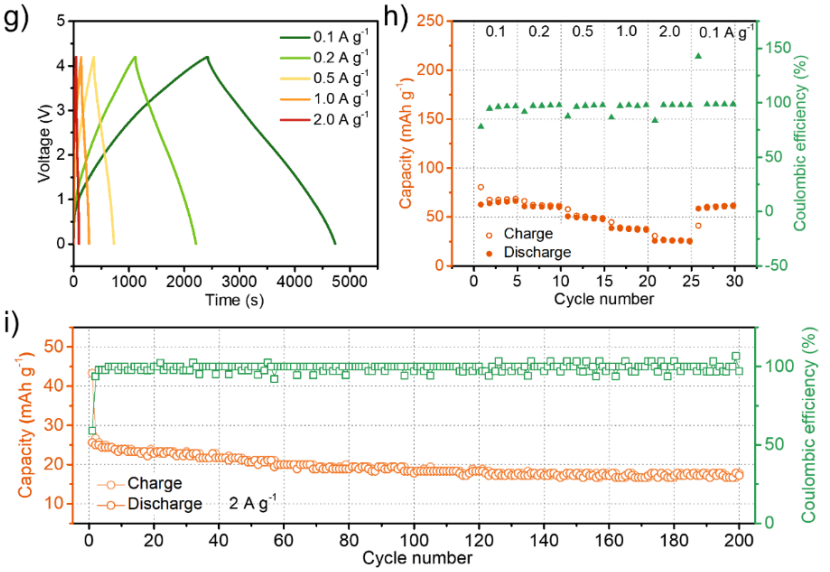
CHKM800//CNC1300



CHKM800//CNC1000



CHKM800//CNC800



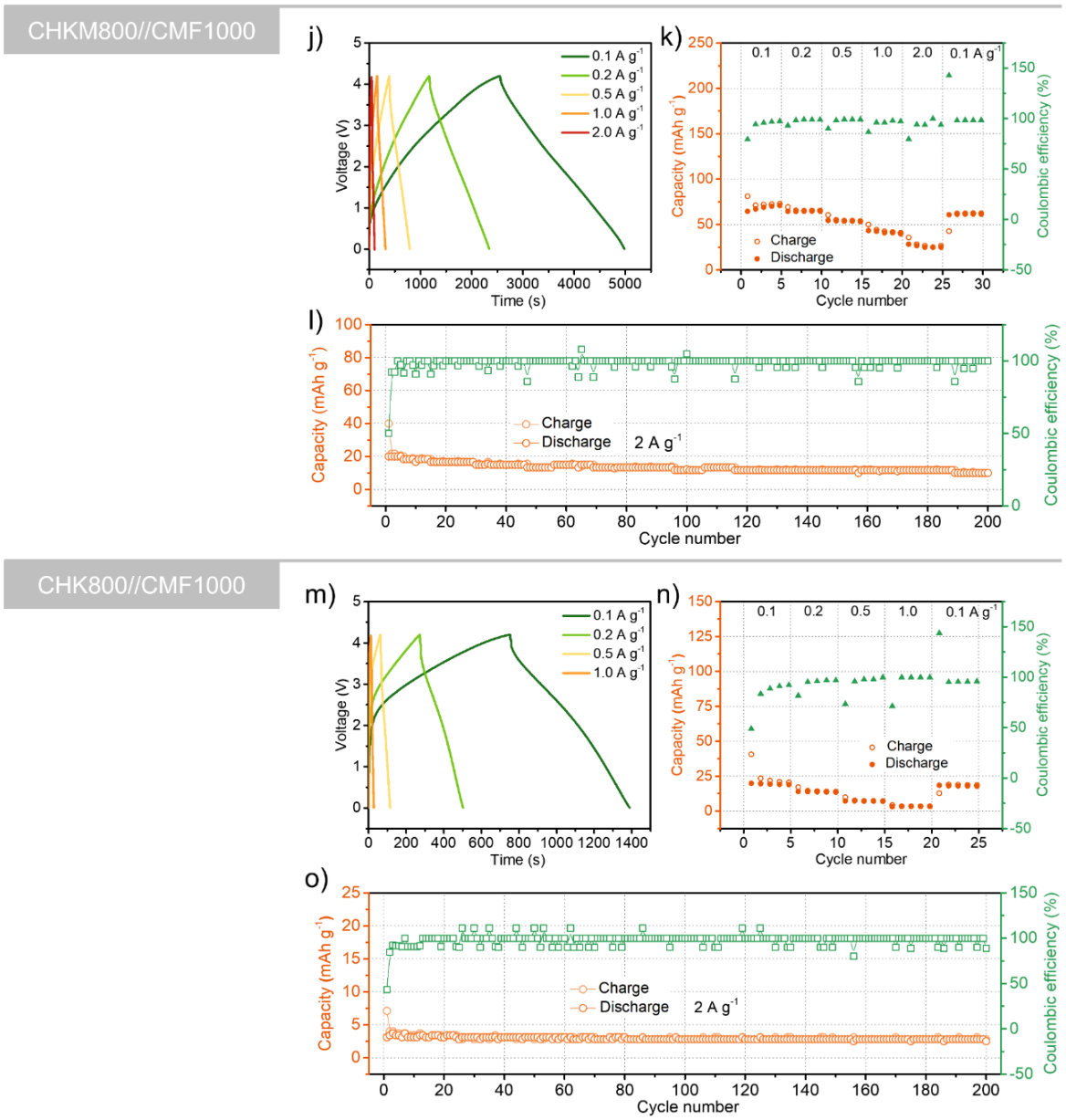


Figure A2.9. Electrochemical performance (GCD curves, rate and cycling performance) of a-c) CHKM800//CNC1300, d-f) CHKM800//CNC1000, g-i) CHKM800//CNC800, j-l) CHKM800//CMF1000, and m-o) CHK800//CMF1000. (All the parameters in the full cell configuration are normalized by the total active mass of both anode and cathode.)

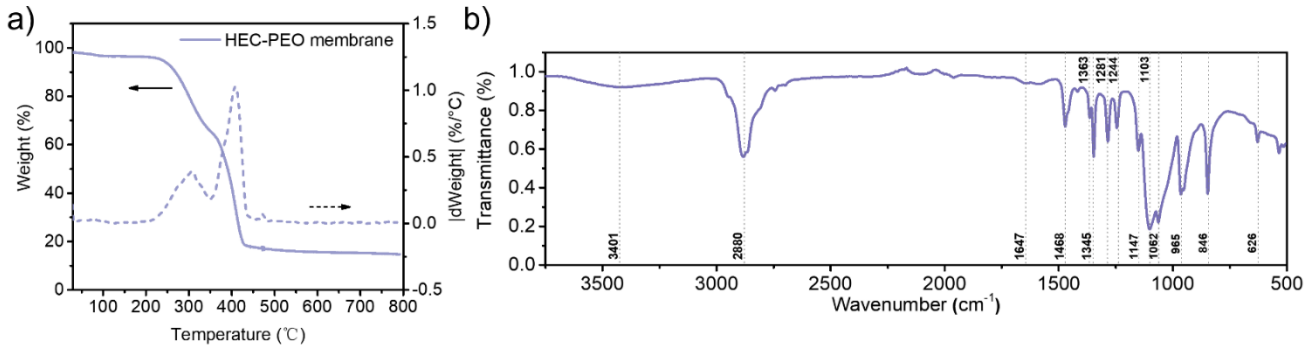


Figure A2.10. a) TGA curve of HEC-PEO composite membrane (800 °C, 10 °C min^{-1}, N_2 flow); b) FTIR spectra of HEC-PEO composite membrane.

The thermogravimetric analysis (TGA) was conducted with specific heating programs under N_2 flow to test the thermal stability of the HEC-PEO composite membrane. The HEC-PEO has no obvious weight loss before 300ºC, and the main decomposition happens at about 400 ºC (**Figure A2.10**a). Fourier transform infrared spectroscopy (FTIR) was carried out using an Agilent Cary 630 FTIR spectrometer.

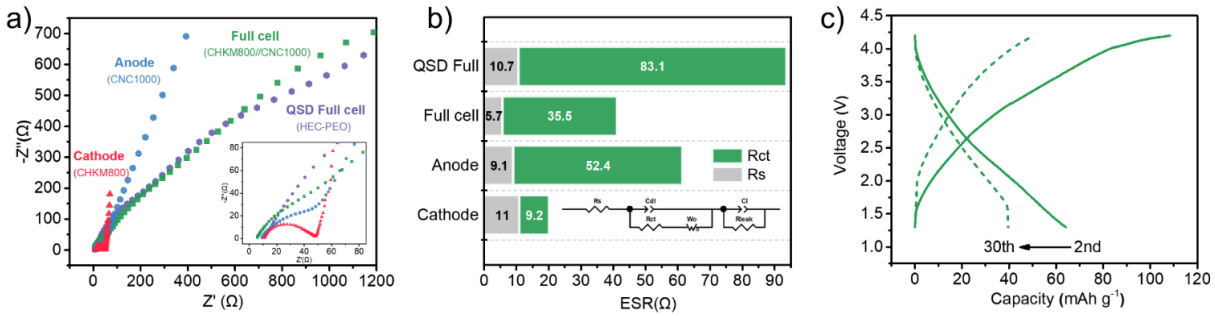


Figure A2.11. a) Impedance curves of CHKM800, CNC1000 in half cells and CHKM800//CNC1000, CHKM800/HEC-PEO/CNC1000 in full cells; and b) Equivalent series resistance (ESR) of the half cells and full cells consisting of the internal resistance (R_s) and the charge-transfer resistance (R_{ct}); and c) Cycling performance of CHKM800/HEC-PEO/CNC1000 in full cells tested at 0.1 A g^{-1} after 30 cycles (All the parameters in the full cell configuration are normalized by the total active mass of both anode and cathode).

After charging/discharging for 30 cycles at 0.1 A g^{-1}, the retention of discharge capacity is 62 %, which is promising in terms of the high working voltage since such high working voltage could cause some side reactions including the decomposition of many binders and nonaqueous electrolytes.

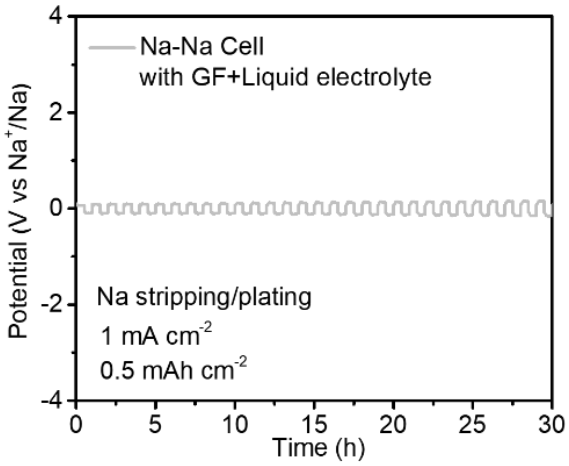


Figure A2.12. Voltage profiles at room temperature for sodium stripping/plating in a symmetric Na//Na cell with glass fibre membrane in liquid electrolyte at 1 mA cm^{-2}.

Table A2.1. The vibration modes of each peak in FTIR spectra of HEC-PEO.

Wavenumbers (cm^{-1})	**Vibration mode**
3401	O-H stretching
2880	C-H stretching
1647	C-C ring stretching
1468, 1363, 1345, 1281, 1244, 965, 846	C-H different types of bending
1147, 1103, 1062	C-O-C stretching
626	ClO_4^- stretching

A3. Supplementary figures and tables for Chapter 6

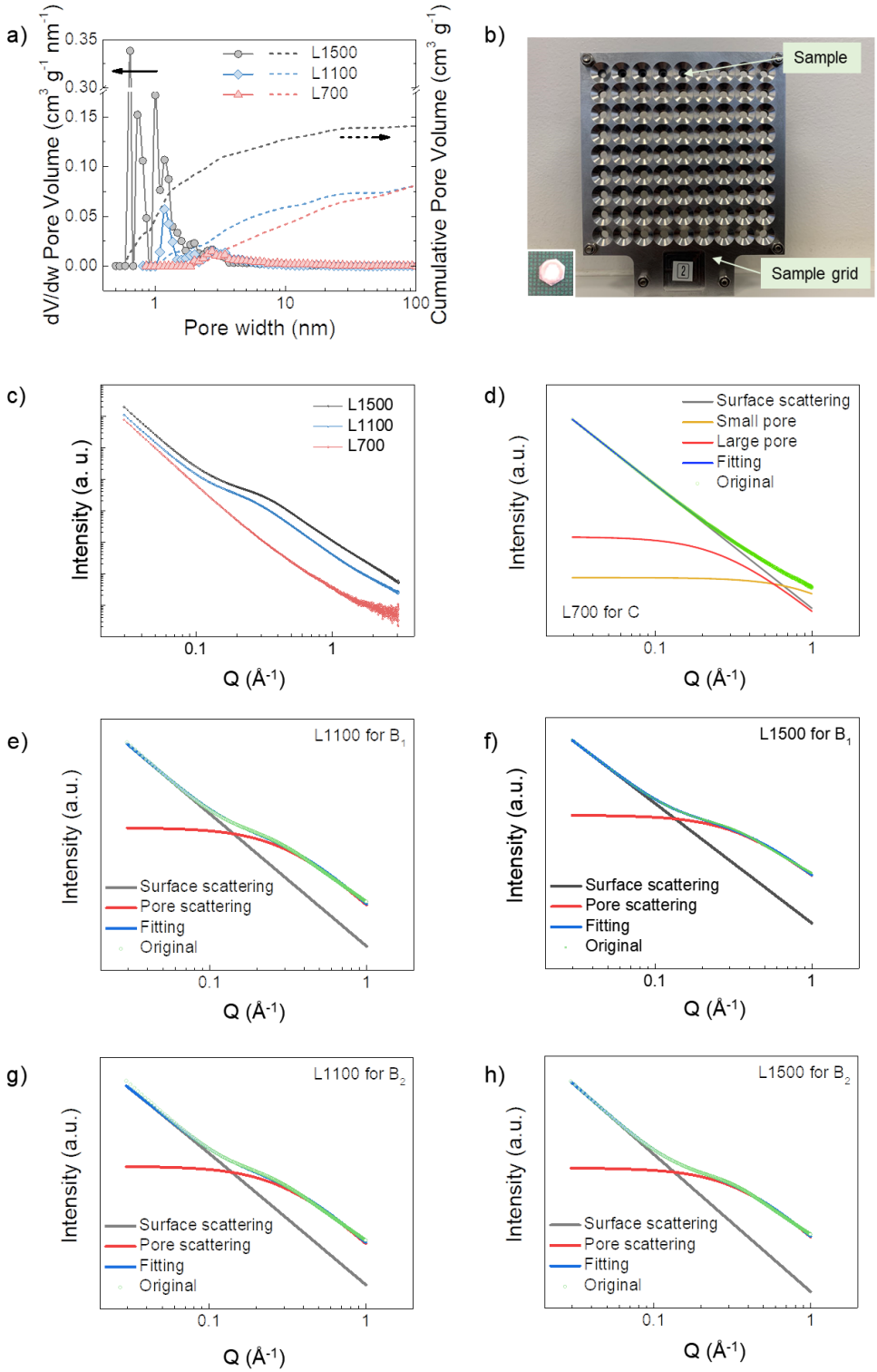


Figure A3.1. a) The pore size distribution based on the non-local density functional theory (NLDFT) method L700, L1100 and L1500; b) The photograph of sample grid for SAXS measurement with an inserted photograph of a washer used to fix the samples. c) The small-angle X-ray scattering (SAXS) patterns of L700, L1100 and L1500; d) Fitted SAXS patterns of L700 based on Equation S5 for the value of C; Fitted SAXS patterns of e) L1100 and f) L1500 based on Equation S3 for the value of B_1; Fitted SAXS patterns of g) L1100 and h)

L1500 based on Equation S4 for the value of B_2; (The SAXS results have already removed the background)

The SAXS pattern of L700 shows the negligible pore structures of L700.[189] Furthermore, the SAXS patterns of L1100 and L1500 can be fitted based on Equation 3.1 and 3.2, while the SAXS pattern of L700 can be fitted based on Equation 3.3. B_1 for L1100 and L1500 is a scale factor for the pore scattering which is proportional to the total surface area of small pores, while C for L700 is a scale factor for the pore scattering proportional to the total surface area of intermediate pores. B_2 becomes proportional to the number of pores.[60] According to these results, with the increase of carbonisation temperatures, the pore structures in carbon skeletons including the total surface area of pores and the number of pores increase. This trend is consistent with the conclusions from N_2 adsorption and desorption results.

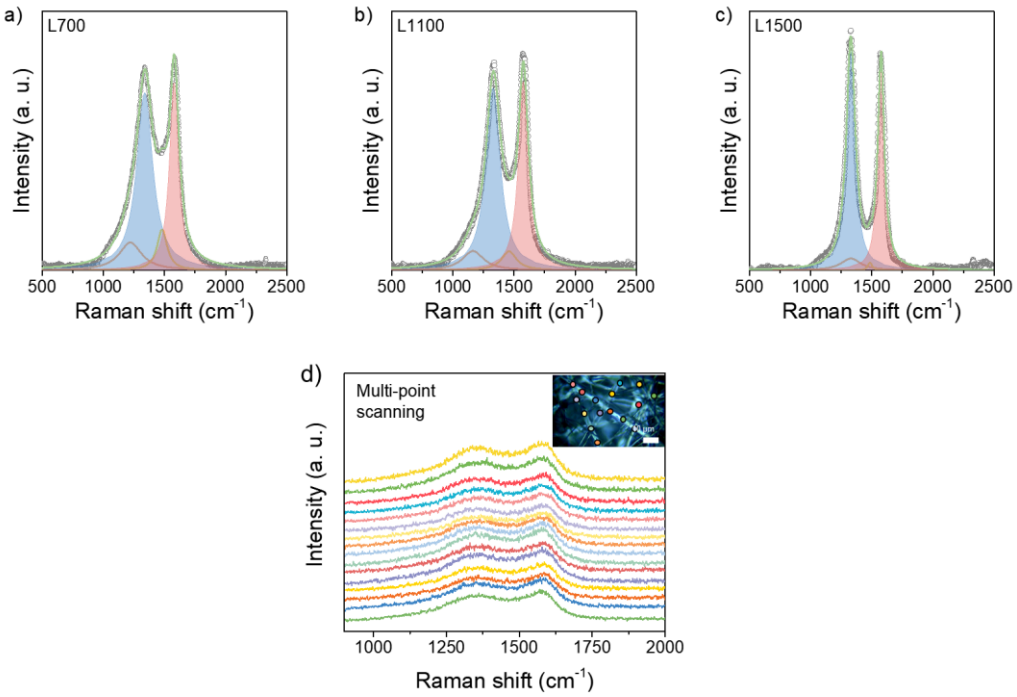


Figure A3.2. Fitted Raman spectra of a) L700, b) L1100 and c) L1500 using the Lorentzian methods; d) Raman spectra of an area of L700 through the multi-point scanning model, which is conducted to further prove the uniformity of defect sites of L700. With the uniformly distributed defect sites, L700 can prevent the dendrite growth as a protection skeleton for sodium metal anodes.

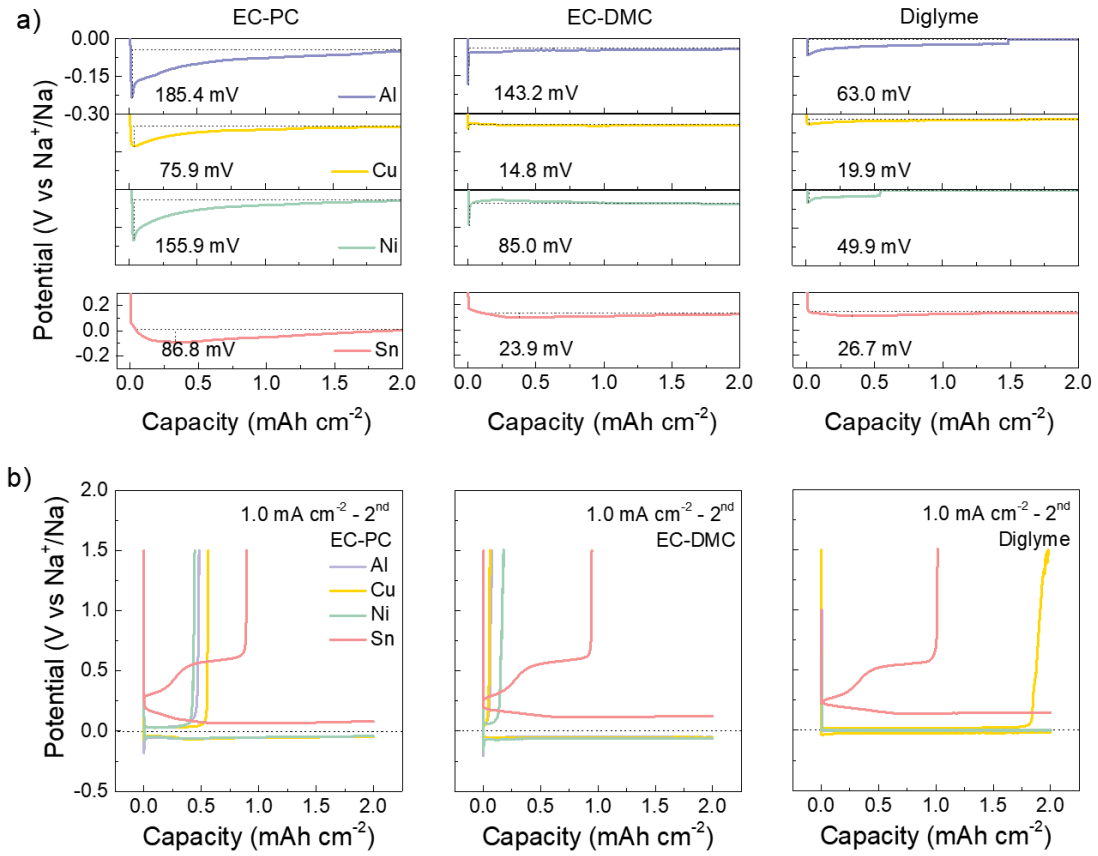


Figure A3.3. a) The potential-capacity profiles (the 1st cycle) showing initial nucleation overpotentials of sodium deposition on Al, Cu, Ni and Sn at 1 mA cm^{-2} using 1 M $NaCF_3SO_3$ in EC-PC (left), EC-DMC (middle) or diglyme (right); b) The specific GCD curves (the 2nd cycle) of sodium plating/stripping on Al, Cu, Ni and Sn at 1mA cm^{-2} using 1 M $NaCF_3SO_3$ in EC-PC (left), EC-DMC (middle) or diglyme (right).

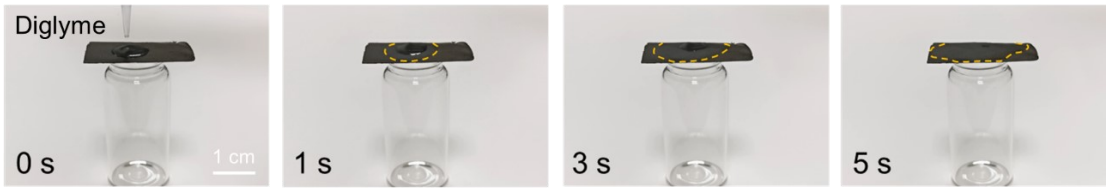


Figure A3.4. The wettability testing of L700 with diglyme, where the 100μL diglyme can be fully absorbed in a piece of L700 since no diglyme can penetrate the L700.

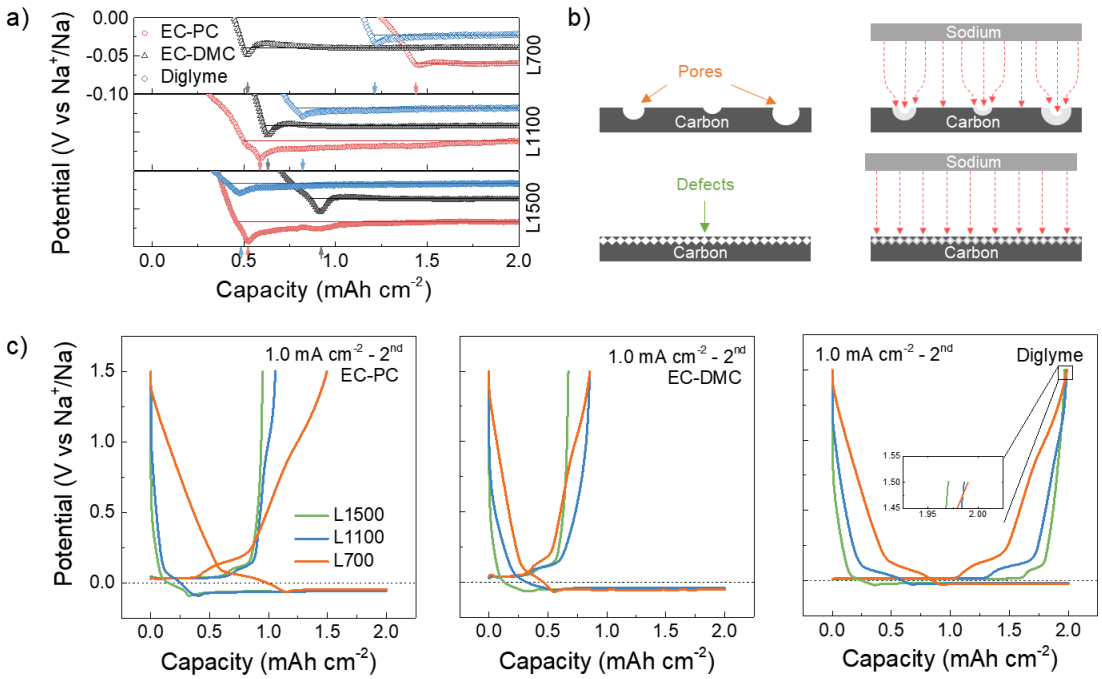


Figure A3.5. a) The potential-capacity profiles (the 1st cycle) at 1 mA cm^{-2} showing initial nucleation overpotentials of sodium deposition on L700, L1100 and L1500 using 1 M $NaCF_3SO_3$ in EC-PC, 1 M $NaCF_3SO_3$ in EC-DMC or 1 M $NaCF_3SO_3$ in diglyme, respectively; b) Schematic illustration of ion flux distribution and metallic deposition on the carbon with pore structures or defect structures; c) GCD curves (the 2nd cycle) of metallic sodium plating/stripping at 1mA cm^{-2} on L700, L1100 and L1500 using 1 M $NaCF_3SO_3$ in EC-PC, 1 M $NaCF_3SO_3$ in EC-DMC or 1 M $NaCF_3SO_3$ in diglyme, respectively.

The metallic deposition induced by pore structures on the surface of carbon materials is uneven because the pore structures cause the non-uniform ion flux distribution, which can also be proven by the finite element simulation results. In comparison, the metallic deposition induced by defect structures is more homogenous with a uniform ion flux distribution. In Figure S8a and b, the irreversible capacity can be observed in the ester-based electrolyte because of the repeated fragmentation and reconstruction of unstable solid electrolyte interphase (SEI) and the formation of "dead" sodium during cycling, but L700 still has the best reversibility compared with L1100 and L1500, which further proves the defect structures are more beneficial to the metallic deposition behaviours than pore structures.

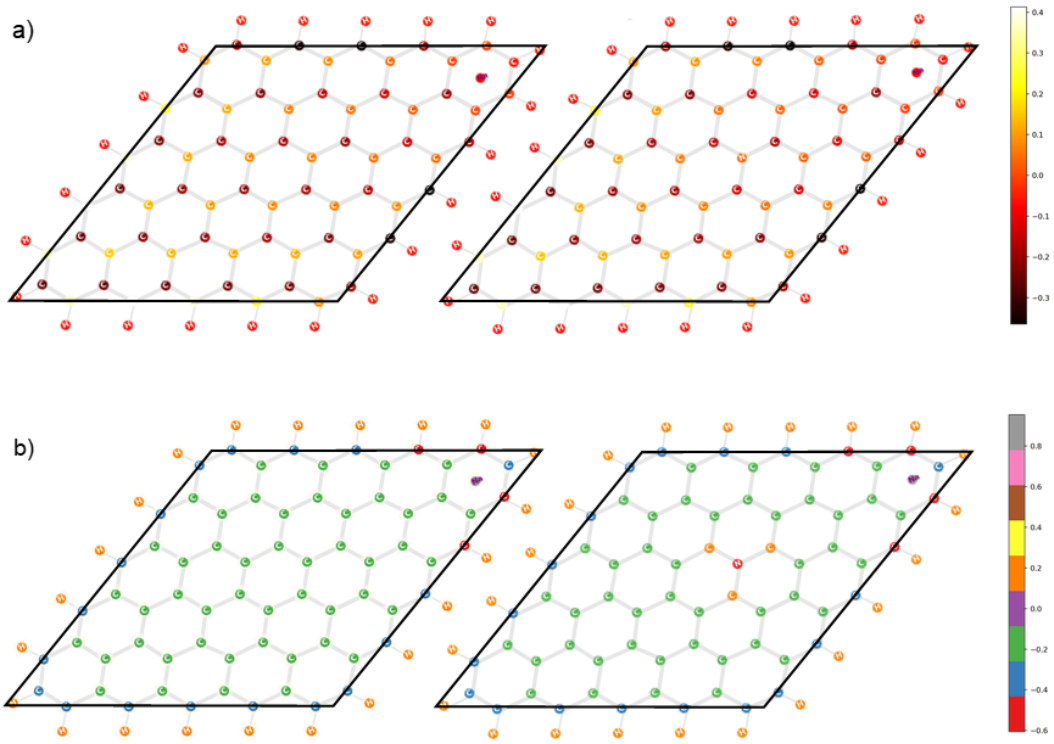


Figure A3.6. a) Left: Spin densities between sodium atoms and L1500 with intact graphene layers, Right: Spin densities between sodium atoms and L700 with quaternary nitrogen-doped graphene layers; b) Left: Local charge densities between sodium atoms and L1500 with intact graphene layers, Right: the local charge densities between sodium atoms and L700 with quaternary nitrogen-doped graphene layers.

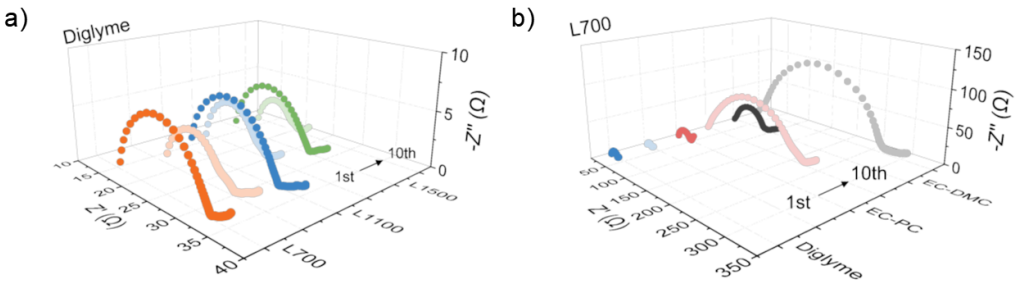


Figure A3.7. a) EIS plots of L700, L1100 and L1500 using 1 M $NaCF_3SO_3$ in diglyme before and after cycling; b) EIS plots of L700 using 1 M $NaCF_3SO_3$ in diglyme, 1 M $NaCF_3SO_3$ in EC-PC or 1 M $NaCF_3SO_3$ in EC-DMC before and after cycling.

The comparison of EIS with different carbon skeletons and electrolytes at plated states before and after cycling is also conducted. When the same substrate (L700) is employed, the charge transfer resistance in ester-based electrolytes is smaller than that in the ether-based electrolyte at the beginning, which means the initial ionic conductivity of the ether-based electrolyte is

lower. This result can be consistent with the finite element simulation exhibited before. However, after cycling, the charge transfer resistance in ester-based electrolytes significantly increases, while in the ether-based electrolyte, the charge transfer resistance decreases. This phenomenon further indicates the difference between ester- and ether-based electrolytes in the stability and ionic conductivity of intermediate phases formed during cycling.

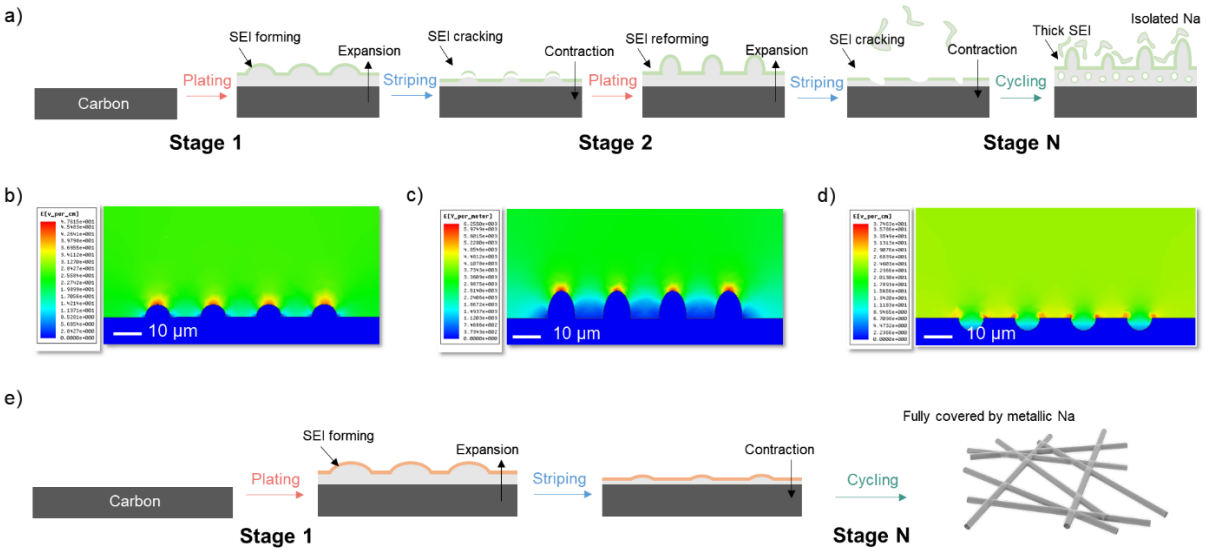


Figure A3.8. a) Schematic illustration of the sodium stripping and plating process in EC-PC or EC-DMC. Stage 1: The SEI forms and Na^+ ions insert into the carbon skeleton above 0 V vs Na^+/Na, while the metallic sodium keeps plating onto the carbon skeleton below 0 V vs Na^+/Na; Stage 2: The volume change caused by sodium plating and striping makes the SEI crack, followed by the reformation of the SEI. Afterwards, the uneven plating results in Na dendrites; Step N: sodium stripping isolates sodium dendrites into electrolytes. b-c) Finite element modelling of the electric fields in different stages of sodium plating and striping, which proves the rough surface can induce uneven current flows. e) Schematic illustration of the sodium stripping and plating process in diglyme, which is more uniform.

The reasons for cell fading in ester- and ether-based electrolytes differ. In EC-DMC and EC-PC, the SEI is unstable because a large number of inorganic components exists in SEI as described in the main text. During plating/stripping of metallic sodium, the large volume change of metallic sodium on carbon skeletons makes the SEI keep cracking and reforming. The rough surface caused by the reformation of the SEI would induce the uneven sodium plating and then form sodium dendrites. Importantly, the sodium dendrites would further induce the uneven sodium plating. Finally, the isolated sodium layers rapidly form above the

thick SEI of active metallic sodium, thus totally changing the plating and striping behaviours on the substrate (Figure A3.12 a and b). The SEI in diglyme, however, is more flexible and stable than that in carbonate-based electrolytes because of the continuous organic phase of the SEI in diglyme. In comparison to the plating and striping behaviours in EC-DMC and EC-PC, the metallic sodium can be plated and stripped uniformly during cycling without the endless reconstruction of the SEI. Only a few irreversible metallic sodium remains on the defect sites and surface of carbon skeletons because of the average Coulombic efficiency of 99.6%. After ultra-long cycling, the active sites are fully occupied by irreversible metallic sodium, followed by the plating of metallic sodium on the irreversible metallic sodium instead of active sites on carbon skeletons, thus changing the GCD curves in the end.

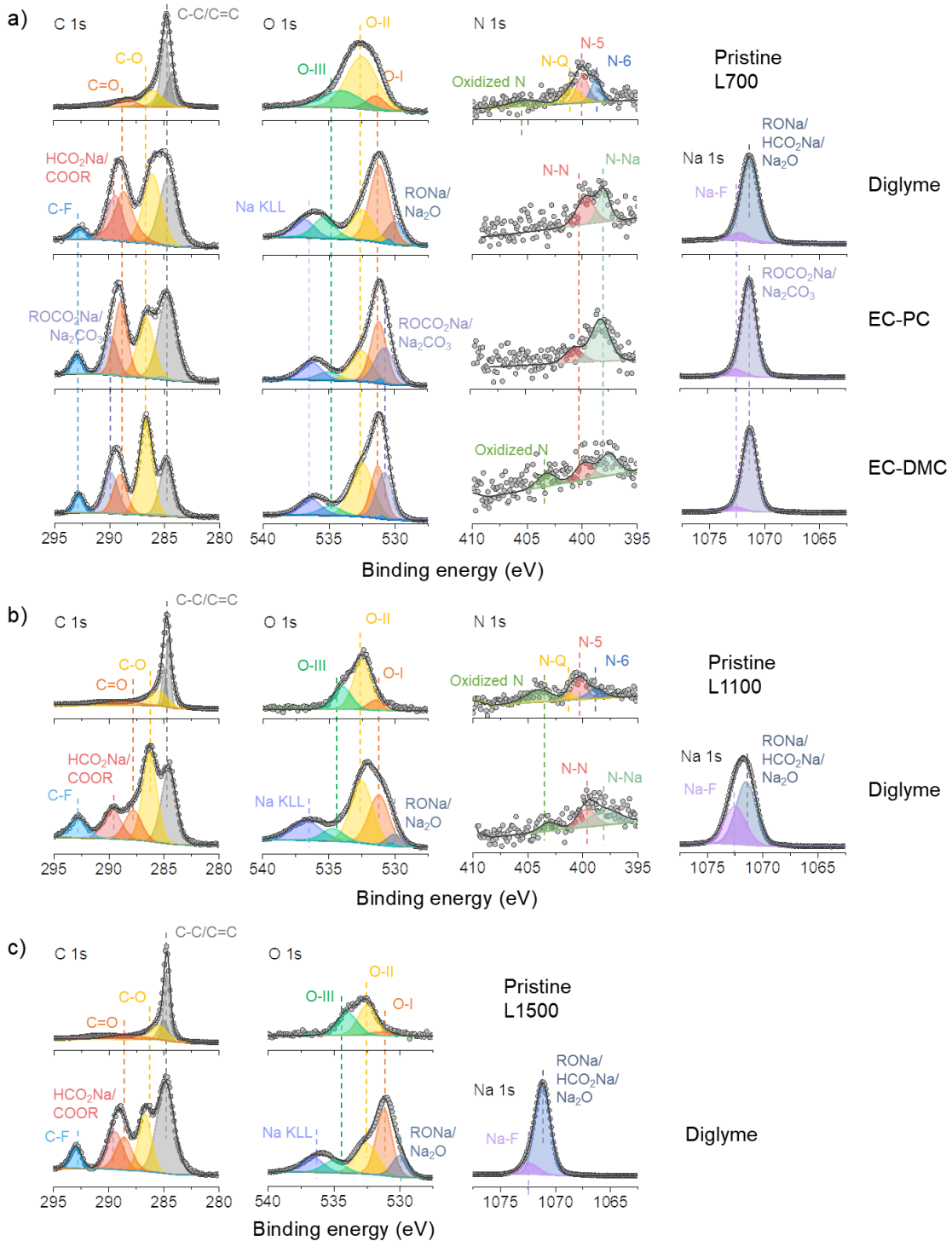


Figure A3.9. a) Fitted C 1s, O 1s, N 1s and Na 1s core-level XPS spectra of pristine L700, plated L700 using 1 M $NaCF_3SO_3$ in diglyme, plated L700 using 1 M $NaCF_3SO_3$ in EC-PC, and plated L700 using 1 M $NaCF_3SO_3$ in EC-DMC after the first cycle of metallic deposition at 1.0 mA cm^{-2} with a specific discharge capacity of 2.0 mAh cm^{-2}; b) Fitted C 1s, O 1s, N 1s and Na 1s core-level XPS spectra of pristine L1100, plated L1100 using 1 M $NaCF_3SO_3$ in diglyme after the same deposition process; c) Fitted C 1s, O 1s and Na 1s core-level XPS spectra of pristine L1500, plated L1500 using 1 M $NaCF_3SO_3$ in diglyme after the same deposition process.

In the study, all the SEI layers from the decomposition of the three electrolytes showed fluorinated interfaces. The fluorinated composition in SEI layers can improve the interface stability due to their strong electron-withdrawing property for tuning the electron density and frontier molecular orbitals of the SEI layers.[282, 283]

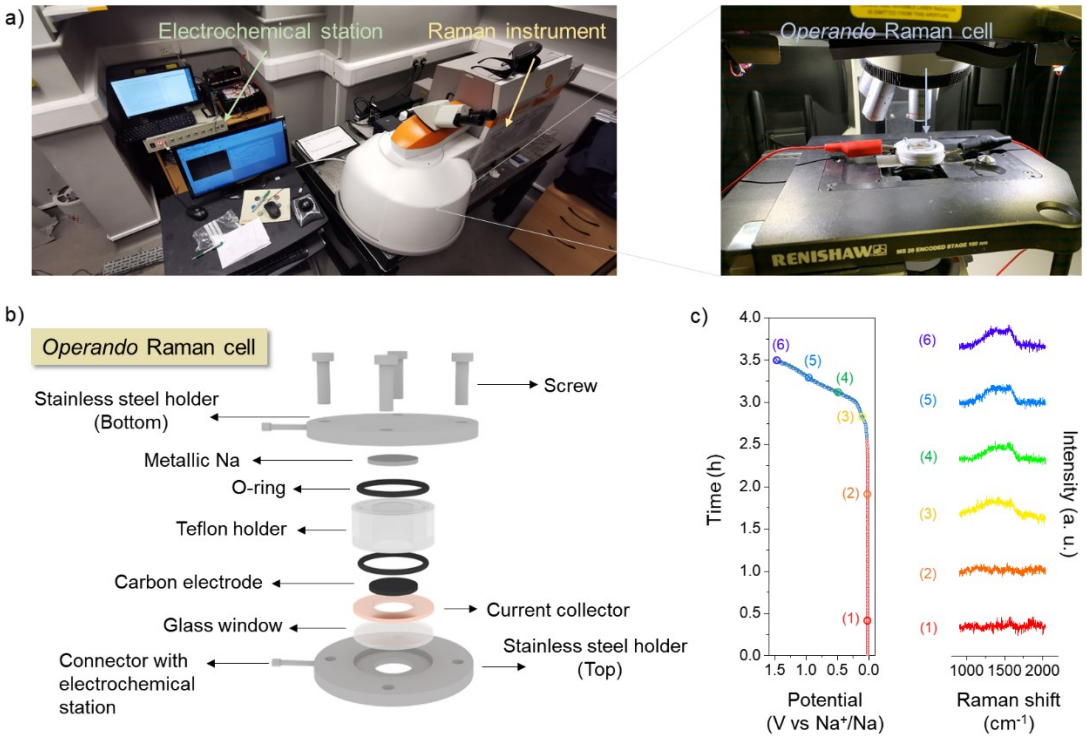


Figure A3.10. a) The photograph of *operando* Raman measurement; b) The configuration of the *operando* Raman cell; c) Raman spectra of L700 during the first stripping process in 1 M $NaCF_3SO_3$ in diglyme (right), with the corresponding plating electrochemical curve (left) at 0.5 mA cm^{-2}.

L700 has exhibited the largest sloping capacity (*i.e.,* insertion capacity) because of its abundant defects. In the half cell, the capacity can be categorised as the insertion capacity when the working potential is above 0 vs Na^+/Na. When the working potential is below 0 vs Na^+/Na, the deposition of metallic sodium onto the carbon mat happens, leading to the plating capacity in the charge-discharge curves of half cells. The insertion of sodium ions into carbon materials can be facilitated by defective structures. After that, the sodiophilic properties of carbon materials can be further enhanced because Na^+ ions exist in their structures. Therefore, the larger insertion capacity can contribute to the better durability of L700 for sodium plating and

stripping in the half cells. In addition, the insertion reactions are highly reversible since the sloping capacity can be observed from each charge-discharge curve of half cells.

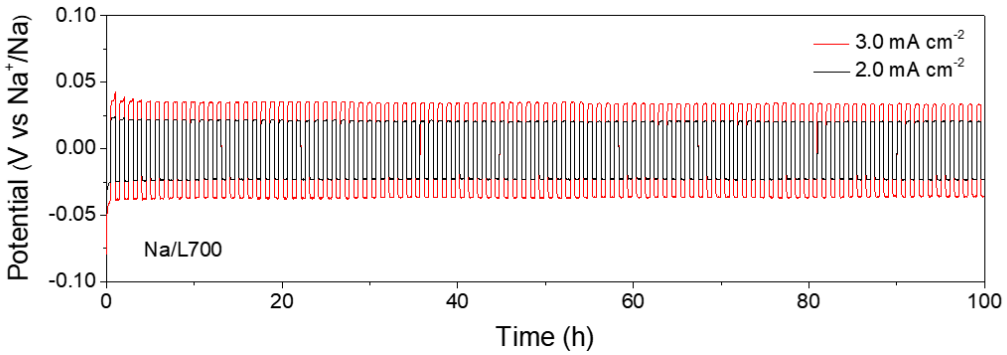


Figure A3.11. Cycling stability of Na/L700 composite anodes in the symmetrical cell at current densities of 2.0 and 3.0 mA cm^{-2} with a specific capacity of 1.0 and 1.5 mAh cm^{-2}, respectively, using 1 M $NaCF_3SO_3$ in diglyme.

Table A3.1. Fitted terms including A, a_1, a_2, B_1 and B_2 from SAXS.

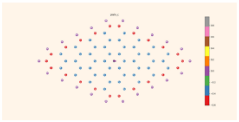
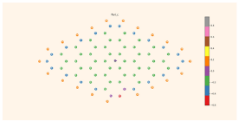
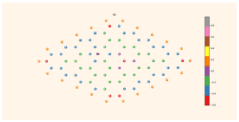
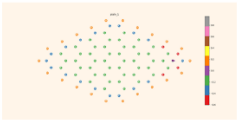
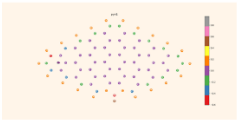
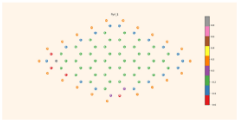
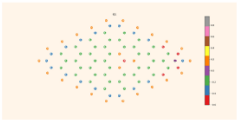
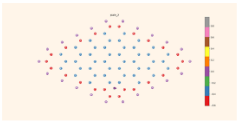
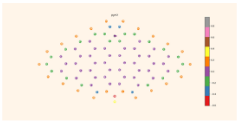
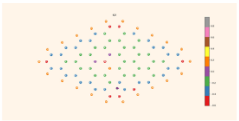
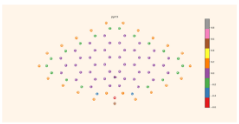
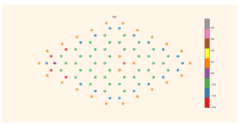
	A	a_1	a_2	B_1	B_2	C
L700	0.077	N/A	3.8	N/A	N/A	0.00499
L1100	0.46	3.3	N/A	7.8	0.72	N/A
L1500	0.28	2.8	N/A	11.9	1.48	N/A

Table A3.2. a) The calculated binding energy between sodium atoms (at different positions including centre and edges) and the graphene layers with(out) nitrogen doping;

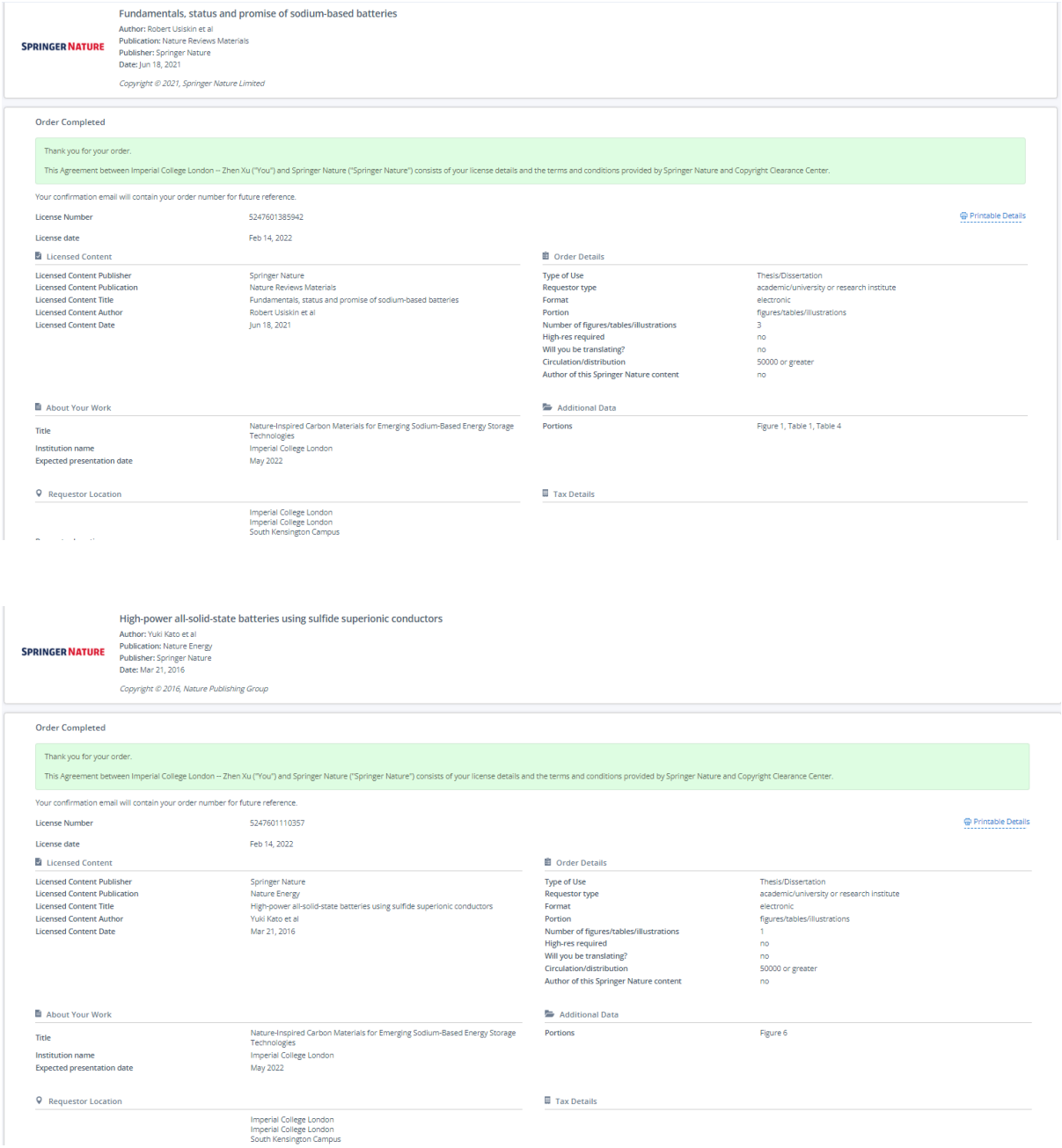
Position	Plain	Pyridinic	Pyrrolic	Quaternary
Center	-0.77	-0.73	N/A	-1.90
Edge 1	-1.83	-1.81	-1.67	-2.08
Edge 2	-1.07	N/A	-0.99	-1.83
Edge 3	N/A	N/A	-0.74	-2.06

Unit: eV

Table A3.2. b) the illustration of local charge densities between sodium atoms and graphene layers with(out) nitrogen doping.

Position	Plain	Pyridinic	Pyrrolic	Quaternary
Centre			N/A	
Edge 1				
Edge 2		N/A		
Edge 3	N/A	N/A		

A4. Premissions



Fundamentals, status and promise of sodium-based batteries

Author: Robert Usiskin et al
Publication: Nature Reviews Materials
Publisher: Springer Nature
Date: Jun 18, 2021

Copyright © 2021, Springer Nature Limited

Order Completed

Thank you for your order.

This Agreement between Imperial College London -- Zhen Xu ("You") and Springer Nature ("Springer Nature") consists of your license details and the terms and conditions provided by Springer Nature and Copyright Clearance Center.

Your confirmation email will contain your order number for future reference.

Printable Details

License Number	5247601385942
License date	Feb 14, 2022

Licensed Content

Licensed Content Publisher	Springer Nature
Licensed Content Publication	Nature Reviews Materials
Licensed Content Title	Fundamentals, status and promise of sodium-based batteries
Licensed Content Author	Robert Usiskin et al
Licensed Content Date	Jun 18, 2021

Order Details

Type of Use	Thesis/Dissertation
Requestor type	academic/university or research institute
Format	electronic
Portion	figures/tables/illustrations
Number of figures/tables/illustrations	3
High-res required	no
Will you be translating?	no
Circulation/distribution	50000 or greater
Author of this Springer Nature content	no

About Your Work

Title	Nature-Inspired Carbon Materials for Emerging Sodium-Based Energy Storage Technologies
Institution name	Imperial College London
Expected presentation date	May 2022

Additional Data

Portions	Figure 1, Table 1, Table 4

Requestor Location

Imperial College London
Imperial College London
South Kensington Campus

Tax Details

High-power all-solid-state batteries using sulfide superionic conductors

Author: Yuki Kato et al
Publication: Nature Energy
Publisher: Springer Nature
Date: Mar 21, 2016

Copyright © 2016, Nature Publishing Group

Order Completed

Thank you for your order.

This Agreement between Imperial College London -- Zhen Xu ("You") and Springer Nature ("Springer Nature") consists of your license details and the terms and conditions provided by Springer Nature and Copyright Clearance Center.

Your confirmation email will contain your order number for future reference.

Printable Details

License Number	5247601110357
License date	Feb 14, 2022

Licensed Content

Licensed Content Publisher	Springer Nature
Licensed Content Publication	Nature Energy
Licensed Content Title	High-power all-solid-state batteries using sulfide superionic conductors
Licensed Content Author	Yuki Kato et al
Licensed Content Date	Mar 21, 2016

Order Details

Type of Use	Thesis/Dissertation
Requestor type	academic/university or research institute
Format	electronic
Portion	figures/tables/illustrations
Number of figures/tables/illustrations	1
High-res required	no
Will you be translating?	no
Circulation/distribution	50000 or greater
Author of this Springer Nature content	no

About Your Work

Title	Nature-Inspired Carbon Materials for Emerging Sodium-Based Energy Storage Technologies
Institution name	Imperial College London
Expected presentation date	May 2022

Additional Data

Portions	Figure 6

Requestor Location

Imperial College London
Imperial College London
South Kensington Campus

Tax Details

1. Soft matter

0.00 GBP

Article: Cellulose nanowhiskers: promising materials for advanced applications

ISSN	1744-6848	**Publisher**	ROYAL SOCIETY OF CHEMISTRY
Type of Use	Republish in a thesis/dissertation	**Portion**	Image/photo/illustration

Hide Details

LICENSED CONTENT

Publication Title	Soft matter	**Publication Type**	e-Journal
Article Title	Cellulose nanowhiskers: promising materials for advanced applications	**Start Page**	303
Author/Editor	Royal Society of Chemistry (Great Britain)	**End Page**	315
Date	06/01/2005	**Issue**	2
Language	English	**Volume**	7
Country	United Kingdom of Great Britain and Northern Ireland	**URL**	http://www.rsc.org/Publishing/Jour...
Rightsholder	Royal Society of Chemistry		

REQUEST DETAILS

Portion Type	Image/photo/illustration	**Distribution**	Worldwide
Number of images / photos / illustrations	1	**Translation**	Original language of publication
Format (select all that apply)	Electronic	**Copies for the disabled?**	No
Who will republish the content?	Academic institution	**Minor editing privileges?**	Yes
Duration of Use	Life of current edition	**Incidental promotional use?**	No
Lifetime Unit Quantity	More than 2,000,000	**Currency**	GBP
Rights Requested	Main product		

NEW WORK DETAILS

Title	Nature-Inspired Carbon Materials for Emerging Sodium-Based Energy Storage Technologies	**Institution name**	Imperial College London
		Expected presentation date	2022-05-01
Instructor name	Prof. Magda Titirici		

SPRINGER NATURE

A cost and resource analysis of sodium-ion batteries

Author: Christoph Vaalma et al
Publication: Nature Reviews Materials
Publisher: Springer Nature
Date: Mar 13, 2018

Copyright © 2018, Macmillan Publishers Limited

Order Completed

Thank you for your order.

This Agreement between Imperial College London -- Zhen Xu ("You") and Springer Nature ("Springer Nature") consists of your license details and the terms and conditions provided by Springer Nature and Copyright Clearance Center.

Your confirmation email will contain your order number for future reference.

Printable Details

License Number	5247610436092
License date	Feb 14, 2022

Licensed Content

Licensed Content Publisher	Springer Nature
Licensed Content Publication	Nature Reviews Materials
Licensed Content Title	A cost and resource analysis of sodium-ion batteries
Licensed Content Author	Christoph Vaalma et al
Licensed Content Date	Mar 13, 2018

Order Details

Type of Use	Thesis/Dissertation
Requestor type	academic/university or research institute
Format	electronic
Portion	figures/tables/illustrations
Number of figures/tables/illustrations	2
High-res required	no
Will you be translating?	no
Circulation/distribution	50000 or greater
Author of this Springer Nature content	no

About Your Work

Title	Nature-Inspired Carbon Materials for Emerging Sodium-Based Energy Storage Technologies
Institution name	Imperial College London
Expected presentation date	May 2022

Additional Data

Portions	Figure 1, Figure 5

Requestor Location

Imperial College London
Imperial College London
South Kensington Campus

Tax Details



Towards K-Ion and Na-Ion Batteries as "Beyond Li-Ion"

Author: Shinichi Komaba, Shinichi Kumakura, Tomooki Hosaka, et al
Publication: The Chemical Record
Publisher: John Wiley and Sons
Date: Feb 14, 2018

© 2018 The Chemical Society of Japan & Wiley-VCH Verlag GmbH & Co. KGaA, Weinheim

Order Completed

Thank you for your order.

This Agreement between Imperial College London -- Zhen Xu ("You") and John Wiley and Sons ("John Wiley and Sons") consists of your license details and the terms and conditions provided by John Wiley and Sons and Copyright Clearance Center.

Your confirmation email will contain your order number for future reference.

Printable Details

License Number	5247610592347
License date	Feb 14, 2022

Licensed Content

Licensed Content Publisher	John Wiley and Sons
Licensed Content Publication	The Chemical Record
Licensed Content Title	Towards K-Ion and Na-Ion Batteries as "Beyond Li-Ion"
Licensed Content Author	Shinichi Komaba, Shinichi Kumakura, Tomooki Hosaka, et al
Licensed Content Date	Feb 14, 2018
Licensed Content Volume	18
Licensed Content Issue	4
Licensed Content Pages	21

Order Details

Type of use	Dissertation/Thesis
Requestor type	University/Academic
Format	Electronic
Portion	Figure/table
Number of figures/tables	1
Will you be translating?	No

About Your Work

Title	Nature-Inspired Carbon Materials for Emerging Sodium-Based Energy Storage Technologies
Institution name	Imperial College London
Expected presentation date	May 2022

Additional Data

Portions	Figure 6

Requestor Location

Imperial College London
Imperial College London
South Kensington Campus

Tax Details

Publisher Tax ID	EU826007151

ACS Publications

Electrode Materials of Sodium-Ion Batteries toward Practical Application

Author: Yangyang Huang, Yuheng Zheng, Xiang Li, et al
Publication: ACS Energy Letters
Publisher: American Chemical Society
Date: Jul 1, 2018

Copyright © 2018, American Chemical Society

PERMISSION/LICENSE IS GRANTED FOR YOUR ORDER AT NO CHARGE

This type of permission/license, instead of the standard Terms and Conditions, is sent to you because no fee is being charged for your order. Please note the following:

- Permission is granted for your request in both print and electronic formats, and translations.
- If figures and/or tables were requested, they may be adapted or used in part.
- Please print this page for your records and send a copy of it to your publisher/graduate school.
- Appropriate credit for the requested material should be given as follows: "Reprinted (adapted) with permission from (COMPLETE REFERENCE CITATION). Copyright (YEAR) American Chemical Society." Insert appropriate information in place of the capitalized words.
- One-time permission is granted only for the use specified in your RightsLink request. No additional uses are granted (such as derivative works or other editions). For any uses, please submit a new request.

If credit is given to another source for the material you requested from RightsLink, permission must be obtained from that source.

BACK CLOSE WINDOW



Hard Carbon Microtubes Made from Renewable Cotton as High-Performance Anode Material for Sodium-Ion Batteries

Author: Xuejie Huang, Liquan Chen, Maria-Magdalena Titirici, et al
Publication: Advanced Energy Materials
Publisher: John Wiley and Sons
Date: Jun 17, 2016

© 2016 WILEY-VCH Verlag GmbH & Co. KGaA, Weinheim

Order Completed

Thank you for your order.

This Agreement between Imperial College London -- Zhen Xu ("You") and John Wiley and Sons ("John Wiley and Sons") consists of your license details and the terms and conditions provided by John Wiley and Sons and Copyright Clearance Center.

Your confirmation email will contain your order number for future reference.

Printable Details

License Number	5247610948652
License date	Feb 14, 2022

Licensed Content

Licensed Content Publisher	John Wiley and Sons
Licensed Content Publication	Advanced Energy Materials
Licensed Content Title	Hard Carbon Microtubes Made from Renewable Cotton as High-Performance Anode Material for Sodium-Ion Batteries
Licensed Content Author	Xuejie Huang, Liquan Chen, Maria-Magdalena Titirici, et al
Licensed Content Date	Jun 17, 2016
Licensed Content Volume	6
Licensed Content Issue	18
Licensed Content Pages	9

Order Details

Type of use	Dissertation/Thesis
Requestor type	University/Academic
Format	Electronic
Portion	Figure/table
Number of figures/tables	2
Will you be translating?	No

About Your Work

Title	Nature-Inspired Carbon Materials for Emerging Sodium-Based Energy Storage Technologies
Institution name	Imperial College London
Expected presentation date	May 2022

Additional Data

Portions	Figure 1, Figure 2

Requestor Location

Imperial College London
Imperial College London
South Kensington Campus

Tax Details

Publisher Tax ID	EU826007151

A phosphorene–graphene hybrid material as a high-capacity anode for sodium-ion batteries

Author: Jie Sun et al
Publication: Nature Nanotechnology
Publisher: Springer Nature
Date: Sep 7, 2015

Copyright © 2015, Nature Publishing Group

Order Completed

Thank you for your order.

This Agreement between Imperial College London -- Zhen Xu ("You") and Springer Nature ("Springer Nature") consists of your license details and the terms and conditions provided by Springer Nature and Copyright Clearance Center.

Your confirmation email will contain your order number for future reference.

Printable Details

License Number	5247611145138
License date	Feb 14, 2022

Licensed Content

Licensed Content Publisher	Springer Nature
Licensed Content Publication	Nature Nanotechnology
Licensed Content Title	A phosphorene–graphene hybrid material as a high-capacity anode for sodium-ion batteries
Licensed Content Author	Jie Sun et al
Licensed Content Date	Sep 7, 2015

Order Details

Type of Use	Thesis/Dissertation
Requestor type	academic/university or research institute
Format	electronic
Portion	figures/tables/illustrations
Number of figures/tables/illustrations	1
High-res required	no
Will you be translating?	no
Circulation/distribution	50000 or greater
Author of this Springer Nature content	no

About Your Work

Title	Nature-Inspired Carbon Materials for Emerging Sodium-Based Energy Storage Technologies
Institution name	Imperial College London
Expected presentation date	May 2022

Additional Data

Portions	Figure 1

Requestor Location

Imperial College London
Imperial College London
South Kensington Campus

Tax Details

Highly Stable Sodium Batteries Enabled by Functional Ionic Polymer Membranes

Author: Lynden A. Archer, Zhengyuan Tu, Pooja Nath, et al
Publication: Advanced Materials
Publisher: John Wiley and Sons
Date: Jan 23, 2017

© 2017 WILEY-VCH Verlag GmbH & Co. KGaA, Weinheim

Order Completed

Thank you for your order.

This Agreement between Imperial College London -- Zhen Xu ("You") and John Wiley and Sons ("John Wiley and Sons") consists of your license details and the terms and conditions provided by John Wiley and Sons and Copyright Clearance Center.

Your confirmation email will contain your order number for future reference.

Printable Details

License Number	5247611270374
License date	Feb 14, 2022

Licensed Content

Licensed Content Publisher	John Wiley and Sons
Licensed Content Publication	Advanced Materials
Licensed Content Title	Highly Stable Sodium Batteries Enabled by Functional Ionic Polymer Membranes
Licensed Content Author	Lynden A. Archer, Zhengyuan Tu, Pooja Nath, et al
Licensed Content Date	Jan 23, 2017
Licensed Content Volume	29
Licensed Content Issue	12
Licensed Content Pages	8

Order Details

Type of use	Dissertation/Thesis
Requestor type	University/Academic
Format	Electronic
Portion	Figure/table
Number of figures/tables	1
Will you be translating?	No

About Your Work

Title	Nature-Inspired Carbon Materials for Emerging Sodium-Based Energy Storage Technologies
Institution name	Imperial College London
Expected presentation date	May 2022

Additional Data

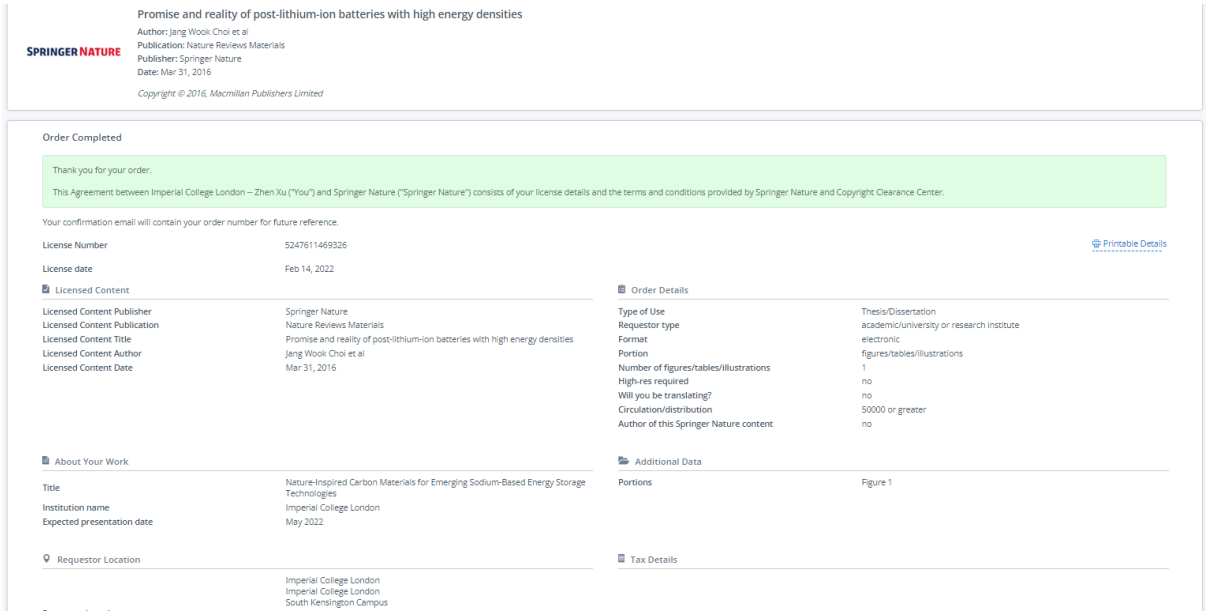
Portions	Figure 3

Requestor Location

Imperial College London
Imperial College London
South Kensington Campus

Tax Details

Publisher Tax ID	EU826007151



Promise and reality of post-lithium-ion batteries with high energy densities

Author: Jang Wook Choi et al
Publication: Nature Reviews Materials
Publisher: Springer Nature
Date: Mar 31, 2016

Copyright © 2016, Macmillan Publishers Limited

Order Completed

Thank you for your order.

This Agreement between Imperial College London -- Zhen Xu ("You") and Springer Nature ("Springer Nature") consists of your license details and the terms and conditions provided by Springer Nature and Copyright Clearance Center.

Your confirmation email will contain your order number for future reference.

Printable Details

License Number	5247611469326
License date	Feb 14, 2022

Licensed Content

Licensed Content Publisher	Springer Nature
Licensed Content Publication	Nature Reviews Materials
Licensed Content Title	Promise and reality of post-lithium-ion batteries with high energy densities
Licensed Content Author	Jang Wook Choi et al
Licensed Content Date	Mar 31, 2016

Order Details

Type of Use	Thesis/Dissertation
Requestor type	academic/university or research institute
Format	electronic
Portion	figures/tables/illustrations
Number of figures/tables/illustrations	1
High-res required	no
Will you be translating?	no
Circulation/distribution	50000 or greater
Author of this Springer Nature content	no

About Your Work

Title	Nature-Inspired Carbon Materials for Emerging Sodium-Based Energy Storage Technologies
Institution name	Imperial College London
Expected presentation date	May 2022

Additional Data

Portions	Figure 1

Requestor Location

Imperial College London
Imperial College London
South Kensington Campus

Tax Details

2. Energy & environmental science

0.00 GBP

Article: Peanut shell hybrid sodium ion capacitor with extreme energy–power rivals lithium ion capacitors

ISSN	17545692	Publisher	Royal Society of Chemistry
Type of Use	Republish in a thesis/dissertation	Portion	Image/photo/illustration

Hide Details

LICENSED CONTENT

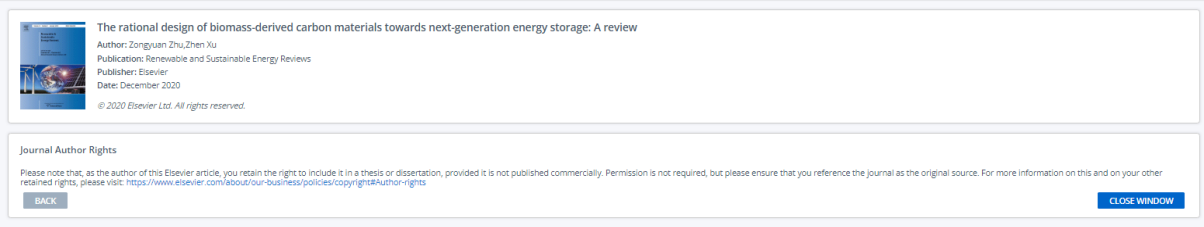
Publication Title	Energy & environmental science	Rightsholder	Royal Society of Chemistry
Article Title	Peanut shell hybrid sodium ion capacitor with extreme energy–power rivals lithium ion capacitors	Publication Type	Journal
		Start Page	941
Author/Editor	Royal Society of Chemistry (Great Britain)	End Page	955
		Issue	3
Date	01/01/2008	Volume	8
Language	English		
Country	United Kingdom of Great Britain and Northern Ireland		

REQUEST DETAILS

Portion Type	Image/photo/illustration	Distribution	Worldwide
Number of images / photos / illustrations	1	Translation	Original language of publication
		Copies for the disabled?	No
Format (select all that apply)	Electronic	Minor editing privileges?	Yes
Who will republish the content?	Academic institution	Incidental promotional use?	No
Duration of Use	Life of current edition	Currency	GBP
Lifetime Unit Quantity	More than 2,000,000		
Rights Requested	Main product		

NEW WORK DETAILS

Title	Nature-Inspired Carbon Materials for Emerging Sodium-Based Energy Storage Technologies	Institution name	Imperial College London
		Expected presentation date	2022-05-01
Instructor name	Prof. Magda Titirici		



The rational design of biomass-derived carbon materials towards next-generation energy storage: A review

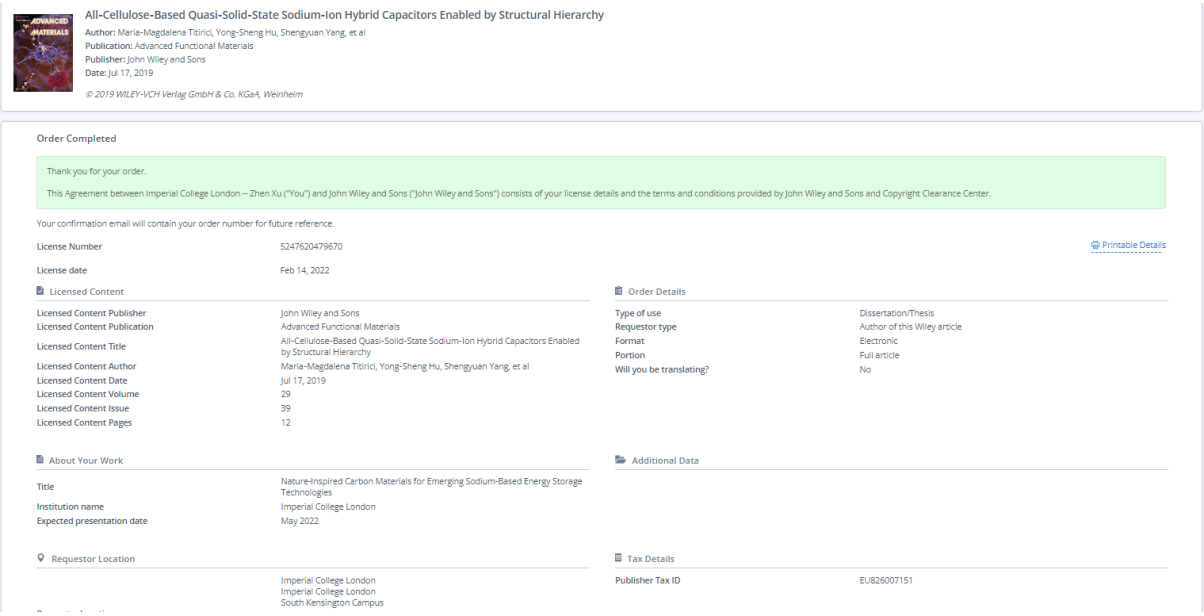
Author: Zongyuan Zhu,Zhen Xu
Publication: Renewable and Sustainable Energy Reviews
Publisher: Elsevier
Date: December 2020

© 2020 Elsevier Ltd. All rights reserved.

Journal Author Rights

Please note that, as the author of this Elsevier article, you retain the right to include it in a thesis or dissertation, provided it is not published commercially. Permission is not required, but please ensure that you reference the journal as the original source. For more information on this and on your other retained rights, please visit: https://www.elsevier.com/about/our-business/policies/copyright#Author-rights

BACK CLOSE WINDOW



All-Cellulose-Based Quasi-Solid-State Sodium-Ion Hybrid Capacitors Enabled by Structural Hierarchy

Author: Maria-Magdalena Titirici, Yong-Sheng Hu, Shengyuan Yang, et al
Publication: Advanced Functional Materials
Publisher: John Wiley and Sons
Date: Jul 17, 2019

© 2019 WILEY-VCH Verlag GmbH & Co. KGaA, Weinheim

Order Completed

Thank you for your order.

This Agreement between Imperial College London -- Zhen Xu ("You") and John Wiley and Sons ("John Wiley and Sons") consists of your license details and the terms and conditions provided by John Wiley and Sons and Copyright Clearance Center.

Your confirmation email will contain your order number for future reference.

License Number	5247620479670
License date	Feb 14, 2022

Printable Details

Licensed Content

Licensed Content Publisher	John Wiley and Sons
Licensed Content Publication	Advanced Functional Materials
Licensed Content Title	All-Cellulose-Based Quasi-Solid-State Sodium-Ion Hybrid Capacitors Enabled by Structural Hierarchy
Licensed Content Author	Maria-Magdalena Titirici, Yong-Sheng Hu, Shengyuan Yang, et al
Licensed Content Date	Jul 17, 2019
Licensed Content Volume	29
Licensed Content Issue	39
Licensed Content Pages	12

Order Details

Type of use	Dissertation/Thesis
Requestor type	Author of this Wiley article
Format	Electronic
Portion	Full article
Will you be translating?	No

About Your Work

Title	Nature-Inspired Carbon Materials for Emerging Sodium-Based Energy Storage Technologies
Institution name	Imperial College London
Expected presentation date	May 2022

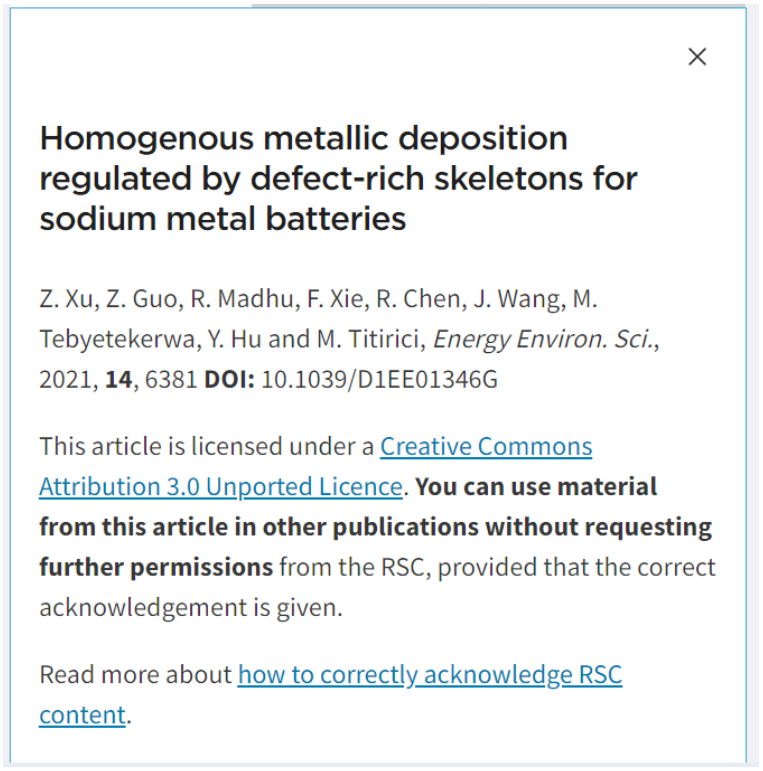
Additional Data

Requestor Location

Imperial College London
Imperial College London
South Kensington Campus

Tax Details

Publisher Tax ID	EU826007151



Homogenous metallic deposition regulated by defect-rich skeletons for sodium metal batteries

Z. Xu, Z. Guo, R. Madhu, F. Xie, R. Chen, J. Wang, M. Tebyetekerwa, Y. Hu and M. Titirici, *Energy Environ. Sci.*, 2021, **14**, 6381 **DOI:** 10.1039/D1EE01346G

This article is licensed under a Creative Commons Attribution 3.0 Unported Licence. **You can use material from this article in other publications without requesting further permissions** from the RSC, provided that the correct acknowledgement is given.

Read more about how to correctly acknowledge RSC content.



The Role of Hydrothermal Carbonization in Sustainable Sodium-Ion Battery Anodes

Author: Zhen Xu, Jing Wang, Zhenyu Guo, et al
Publication: Advanced Energy Materials
Publisher: John Wiley and Sons
Date: Mar 19, 2022

© 2022 The Authors. Advanced Energy Materials published by Wiley-VCH GmbH

Open Access Article

This is an open access article distributed under the terms of the Creative Commons CC BY license, which permits unrestricted use, distribution, and reproduction in any medium, provided the original work is properly cited.

You are not required to obtain permission to reuse this article.

For an understanding of what is meant by the terms of the Creative Commons License, please refer to Wiley's Open Access Terms and Conditions.

Permission is not required for this type of reuse.

Wiley offers a professional reprint service for high quality reproduction of articles from over 1400 scientific and medical journals. Wiley's reprint service offers:

- Peer reviewed research or reviews
- Tailored collections of articles
- A professional high quality finish
- Glossy journal style color covers
- Company or brand customisation
- Language translations
- Prompt turnaround times and delivery directly to your office, warehouse or congress.

Please contact our Reprints department for a quotation. Email corporatesaleseurope@wiley.com or corporatesalesusa@wiley.com or corporatesalesDE@wiley.com.



Toward Emerging Sodium-Based Energy Storage Technologies: From Performance to Sustainability

Author: Zhen Xu, Jing Wang
Publication: Advanced Energy Materials
Publisher: John Wiley and Sons
Date: Jun 13, 2022

© 2022 The Authors. Advanced Energy Materials published by Wiley-VCH GmbH

Open Access Article

This is an open access article distributed under the terms of the Creative Commons CC BY license, which permits unrestricted use, distribution, and reproduction in any medium, provided the original work is properly cited.

You are not required to obtain permission to reuse this article.

For an understanding of what is meant by the terms of the Creative Commons License, please refer to Wiley's Open Access Terms and Conditions.

Permission is not required for this type of reuse.

Wiley offers a professional reprint service for high quality reproduction of articles from over 1400 scientific and medical journals. Wiley's reprint service offers:

- Peer reviewed research or reviews
- Tailored collections of articles
- A professional high quality finish
- Glossy journal style color covers
- Company or brand customisation
- Language translations
- Prompt turnaround times and delivery directly to your office, warehouse or congress.

Please contact our Reprints department for a quotation. Email corporatesaleseurope@wiley.com or corporatesalesusa@wiley.com or corporatesalesDE@wiley.com.

Bibliography

1. Global Temperature. https://climate.nasa.gov/vital-signs/global-temperature/.
2. Fossil Fuels. https://ourworldindata.org/fossil-fuels.
3. P. V. Kamat, *Acs Energy Lett*, 2019, **4**, 2757-2759.
4. M. D. Slater, D. Kim, E. Lee and C. S. Johnson, *Adv. Funct. Mater.*, 2013, **23**, 947-958.
5. Y.-G. Lee, S. Fujiki, C. Jung, N. Suzuki, N. Yashiro, R. Omoda, D.-S. Ko, T. Shiratsuchi, T. Sugimoto, S. Ryu, J. H. Ku, T. Watanabe, Y. Park, Y. Aihara, D. Im and I. T. Han, *Nat. Energy*, 2020, **5**, 299-308.
6. G. Harper, R. Sommerville, E. Kendrick, L. Driscoll, P. Slater, R. Stolkin, A. Walton, P. Christensen, O. Heidrich, S. Lambert, A. Abbott, K. Ryder, L. Gaines and P. Anderson, *Nature*, 2019, **575**, 75-86.
7. B. Dunn, H. Kamath and J. M. Tarascon, *Science*, 2011, **334**, 928-935.
8. R. Usiskin, Y. X. Lu, J. Popovic, M. Law, P. Balaya, Y. S. Hu and J. Maier, *Nat. Rev. Mater.*, 2021, **6**, 1020-1035.
9. N. Yabuuchi, K. Kubota, M. Dahbi and S. Komaba, *Chem. Rev.*, 2014, **114**, 11636-11682.
10. J. Y. Hwang, S. T. Myung and Y. K. Sun, *Chem. Soc. Rev.*, 2017, **46**, 3529-3614.
11. J. Ding, W. Hu, E. Paek and D. Mitlin, *Chem. Rev.*, 2018, **118**, 6457-6498.
12. H. Wang, C. Zhu, D. Chao, Q. Yan and H. J. Fan, *Adv. Mater.*, 2017, **29**.
13. B. Lee, E. Paek, D. Mitlin and S. W. Lee, *Chem. Rev.*, 2019, **119**, 5416-5460.
14. L. L. Fan and X. F. Li, *Nano Energy*, 2018, **53**, 630-642.
15. C. Zhao, Y. Lu, J. Yue, D. Pan, Y. Qi, Y.-S. Hu and L. Chen, *J. Energy Chem.*, 2018, **27**, 1584-1596.
16. Y. S. Hu, S. Komaba, M. Forsyth, C. Johnson and T. Rojo, *Small Methods*, 2019, **3**, 1900184.
17. Y. Kato, S. Hori, T. Saito, K. Suzuki, M. Hirayama, A. Mitsui, M. Yonemura, H. Iba and R. Kanno, *Nat. Energy*, 2016, **1**, 16030.
18. Z. Y. Zhu and Z. Xu, *Renew. Sustain. Energy Rev.*, 2020, **134**, 110308.
19. M. M. Titirici, R. J. White, N. Brun, V. L. Budarin, D. S. Su, F. del Monte, J. H. Clark and M. J. MacLachlan, *Chem. Soc. Rev.*, 2015, **44**, 250-290.
20. H. Zhu, W. Luo, P. N. Ciesielski, Z. Fang, J. Y. Zhu, G. Henriksson, M. E. Himmel and L. Hu, *Chem Rev*, 2016, **116**, 9305-9374.
21. C. F. Shih, T. Zhang, J. H. Li and C. L. Bai, *Joule*, 2018, **2**, 1925-1949.
22. S. J. Eichhorn, *Soft Matter*, 2011, **7**, 303-315.
23. E. Goikolea, V. Palomares, S. Wang, I. R. Larramendi, X. Guo, G. Wang and T. Rojo, *Adv Energy Mater*, 2020, **10**, 2002055.
24. H. Liu, X. B. Cheng, J. Q. Huang, S. Kaskel, S. L. Chou, H. S. Park and Q. Zhang, *Acs Mater Lett*, 2019, **1**, 217-229.
25. D. Castelvecchi and E. Stoye, *Nature*, 2019, **574**, 308-308.
26. C. Vaalma, D. Buchholz, M. Weil and S. Passerini, *Nat. Rev. Mater.*, 2018, **3**, 18013.
27. F. Yu, Z. C. Liu, R. W. Zhou, D. M. Tan, H. X. Wang and F. X. Wang, *Mater Horiz*, 2018, **5**, 529-535.
28. J. N. Harb, T. F. Fuller, *Electrochemical Engineering*, Wiley, Hoboken, 2018.

29. J. O'M. Bockris, A. K. N. Reddy, M. Gamboa-Aldeco, *Modern Electrochemistry 2A. Fundamentals of Electrodics*, Springer, New York, 2000.
30. H. Huang, R. Xu, Y. Feng, S. Zeng, Y. Jiang, H. Wang, W. Luo and Y. Yu, *Adv. Mater.*, 2020, **32**, e1904320.
31. U. Krewer, F. Röder, E. Harinath, R. D. Braatz, B. Bedürftig and R. Findeisen, *J. Electrochem. Soc.*, 2018, **165**, A3656-A3673.
32. Y. Shao, M. F. El-Kady, J. Sun, Y. Li, Q. Zhang, M. Zhu, H. Wang, B. Dunn and R. B. Kaner, *Chem. Rev.*, 2018, **118**, 9233-9280.
33. A. R. C. Bredar, A. L. Chown, A. R. Burton and B. H. Farnum, *ACS Appl. Energy Mater.*, 2020, **3**, 66-98.
34. F. Xie, Z. Xu, A. C. S. Jensen, F. X. Ding, H. Au, J. Y. Feng, H. Luo, M. Qiao, Z. Y. Guo, Y. X. Lu, A. J. Drew, Y. S. Hu and M. M. Titirici, *J. Mater. Chem. A*, 2019, **7**, 27567-27575.
35. C. Fang, J. Li, M. Zhang, Y. Zhang, F. Yang, J. Z. Lee, M. H. Lee, J. Alvarado, M. A. Schroeder, Y. Yang, B. Lu, N. Williams, M. Ceja, L. Yang, M. Cai, J. Gu, K. Xu, X. Wang and Y. S. Meng, *Nature*, 2019, **572**, 511-515.
36. J. B. Goodenough and Y. Kim, *Chem Mater*, 2009, **22**, 587-603.
37. S. Komaba, W. Murata, T. Ishikawa, N. Yabuuchi, T. Ozeki, T. Nakayama, A. Ogata, K. Gotoh and K. Fujiwara, *Adv. Funct. Mater.*, 2011, **21**, 3859-3867.
38. Z. W. Seh, J. Sun, Y. Sun and Y. Cui, *ACS Cent. Sci.*, 2015, **1**, 449-455.
39. F. Xie, Z. Xu, A. C. S. Jensen, H. Au, Y. Lu, V. Araullo-Peters, A. J. Drew, Y. S. Hu and M. M. Titirici, *Adv. Funct. Mater.*, 2019, **29**, 1901072.
40. D. Lin, Y. Liu and Y. Cui, *Nat. Nanotechnol.*, 2017, **12**, 194-206.
41. J. W. Xiang, L. Y. Yang, L. X. Yuan, K. Yuan, Y. Zhang, Y. Y. Huang, J. Lin, F. Pan and Y. H. Huang, *Joule*, 2019, **3**, 2334-2363.
42. Y. Q. Fu, Q. L. Wei, G. X. Zhang and S. H. Sun, *Adv Energy Mater*, 2018, **8**, 1703058.
43. F. Xie, Z. Xu, Z. Guo and M.-M. Titirici, *Prog. Energy*, 2020, **2**, 042002.
44. P. K. Nayak, L. Yang, W. Brehm and P. Adelhelm, *Angew. Chem. Int. Ed.*, 2018, **57**, 102-120.
45. K. Kubota, M. Dahbi, T. Hosaka, S. Kumakura and S. Komaba, *Chem. Rec.*, 2018, **18**, 459-479.
46. J. B. Goodenough, *Energy Storage Mater*, 2015, **1**, 158-161.
47. Z. Jian, W. Luo and X. Ji, *J. Am. Chem. Soc.*, 2015, **137**, 11566-11569.
48. J. Zhao, X. X. Zou, Y. J. Zhu, Y. H. Xu and C. S. Wang, *Adv. Funct. Mater.*, 2016, **26**, 8103-8110.
49. Y. Li, Y. Lu, P. Adelhelm, M. M. Titirici and Y. S. Hu, *Chem. Soc. Rev.*, 2019, **48**, 4655-4687.
50. H. S. Hou, X. Q. Qiu, W. F. Wei, Y. Zhang and X. B. Ji, *Adv Energy Mater*, 2017, **7**.
51. J. Q. Deng, W. B. Luo, S. L. Chou, H. K. Liu and S. X. Dou, *Adv Energy Mater*, 2018, **8**, 1701428.
52. W. Luo, F. Shen, C. Bommier, H. Zhu, X. Ji and L. Hu, *Acc. Chem. Res.*, 2016, **49**, 231-240.
53. Y. X. Wang, Y. X. Wang, Y. X. Wang, X. M. Feng, W. H. Chen, X. P. Ai, H. X. Yang and Y. L. Cao, *Chem*, 2019, **5**, 2547-2570.

54. X. W. Dou, I. Hasa, D. Saurel, C. Vaalma, L. M. Wu, D. Buchholz, D. Bresser, S. Komaba and S. Passerini, *Mater. Today*, 2019, **23**, 87-104.
55. Q. S. Meng, Y. X. Lu, F. X. Ding, Q. Q. Zhang, L. Q. Chen and Y. S. Hu, *Acs Energy Lett*, 2019, **4**, 2608-2612.
56. Y. Y. Huang, Y. H. Zheng, X. Li, F. Adams, W. Luo, Y. H. Huang and L. B. Hu, *Acs Energy Lett*, 2018, **3**, 1604-1612.
57. Y. M. Li, Y. S. Hu, M. M. Titirici, L. Q. Chen and X. J. Huang, *Adv Energy Mater*, 2016, **6**, 1600659.
58. K. Tang, L. J. Fu, R. J. White, L. H. Yu, M. M. Titirici, M. Antonietti and J. Maier, *Adv Energy Mater*, 2012, **2**, 873-877.
59. D. F. Xu, C. J. Chen, J. Xie, B. Zhang, L. Miao, J. Cai, Y. H. Huang and L. N. Zhang, *Adv Energy Mater*, 2016, **6**, 1501929.
60. H. Au, H. Alptekin, A. C. S. Jensen, E. Olsson, C. A. O'Keefe, T. Smith, M. Crespo-Ribadeneyra, T. F. Headen, C. P. Grey, Q. Cai, A. J. Drew and M. M. Titirici, *Energy Environ. Sci.*, 2020, **13**, 3469-3479.
61. J. M. Stratford, A. K. Kleppe, D. S. Keeble, P. A. Chater, S. S. Meysami, C. J. Wright, J. Barker, M. M. Titirici, P. K. Allan and C. P. Grey, *J. Am. Chem. Soc.*, 2021, **143**, 14274-14286.
62. Y. Qi, Y. Lu, F. Ding, Q. Zhang, H. Li, X. Huang, L. Chen and Y. S. Hu, *Angew. Chem. Int. Ed.*, 2019, **58**, 4361-4365.
63. C. L. Zhao, Q. D. Wang, Y. X. Lu, B. H. Li, L. Q. Chen and Y. S. Hu, *Sci. Bull.*, 2018, **63**, 1125-1129.
64. F. Xie, Z. Xu, Z. Guo, Y. Lu, L. Chen, M.-M. Titirici and Y.-S. Hu, *Sci. China Chem.*, 2021, **64**, 1679-1692.
65. H. Xiong, M. D. Slater, M. Balasubramanian, C. S. Johnson and T. Rajh, *J. Phys. Chem. Lett.*, 2011, **2**, 2560-2565.
66. Y. S. Wang, W. Zhu, A. G. Fi, C. Kim and K. Zaghib, *Front. Energy Res.*, 2019, **7**, 28.
67. J. Y. Hwang, H. L. Du, B. N. Yun, M. G. Jeong, J. S. Kim, H. Kim, H. G. Jung and Y. K. Sun, *Acs Energy Lett*, 2019, **4**, 494-501.
68. M. N. Tahir, B. Oschmann, D. Buchholz, X. Dou, I. Lieberwirth, M. Panthofer, W. Tremel, R. Zentel and S. Passerini, *Adv Energy Mater*, 2016, **6**, 1501489.
69. A. V. Desai, R. E. Morris and A. R. Armstrong, *Chemsuschem*, 2020, **13**, 4866-4884.
70. Y. Park, D. S. Shin, S. H. Woo, N. S. Choi, K. H. Shin, S. M. Oh, K. T. Lee and S. Y. Hong, *Adv. Mater.*, 2012, **24**, 3562-3567.
71. J. Liu, P. Lyu, Y. Zhang, P. Nachtigall and Y. Xu, *Adv. Mater.*, 2018, **30**, 1705401.
72. F. X. Wu, C. L. Zhao, S. Q. Chen, Y. X. Lu, Y. L. Hou, Y. S. Hu, J. Maier and Y. Yu, *Mater. Today*, 2018, **21**, 960-973.
73. J. Sun, H. W. Lee, M. Pasta, H. Yuan, G. Zheng, Y. Sun, Y. Li and Y. Cui, *Nat. Nanotechnol.*, 2015, **10**, 980-985.
74. Z. Li, J. Ding and D. Mitlin, *Acc. Chem. Res.*, 2015, **48**, 1657-1665.
75. L. Baggetto, P. Ganesh, R. P. Meisner, R. R. Unocic, J. C. Jumas, C. A. Bridges and G. M. Veith, *J Power Sources*, 2013, **234**, 48-59.
76. S. Liu, J. K. Feng, X. F. Bian, J. Liu and H. Xu, *Energy Environ. Sci.*, 2016, **9**, 1229-

1236.
77. W. S. Ma, K. B. Yin, H. Gao, J. Z. Niu, Z. Q. Peng and Z. H. Zhang, *Nano Energy*, 2018, **54**, 349-359.
78. B. Farbod, K. Cui, W. P. Kalisvaart, M. Kupsta, B. Zahiri, A. Kohandehghan, E. M. Lotfabad, Z. Li, E. J. Luber and D. Mitlin, *Acs Nano*, 2014, **8**, 4415-4429.
79. L. Y. Hu, X. S. Zhu, Y. C. Du, Y. F. Li, X. S. Zhou and J. C. Bao, *Chem Mater*, 2015, **27**, 8138-8145.
80. H. Y. Lu, L. Wu, L. F. Xiao, X. P. Ai, H. X. Yang and Y. L. Cao, *Electrochim Acta*, 2016, **190**, 402-408.
81. G. L. Chang, Y. F. Zhao, L. Dong, D. P. Wilkinson, L. Zhang, Q. S. Shao, W. Yan, X. L. Sun and J. J. Zhang, *J. Mater. Chem. A*, 2020, **8**, 4996-5048.
82. J. F. Ni, L. Li and J. Lu, *Acs Energy Lett*, 2018, **3**, 1137-1144.
83. Y. Zhu, Y. Wen, X. Fan, T. Gao, F. Han, C. Luo, S. C. Liou and C. Wang, *Acs Nano*, 2015, **9**, 3254-3264.
84. H. Jin, H. Wang, Z. Qi, D. S. Bin, T. Zhang, Y. Wan, J. Chen, C. Chuang, Y. R. Lu, T. S. Chan, H. Ju, A. M. Cao, W. Yan, X. Wu, H. Ji and L. J. Wan, *Angew. Chem. Int. Ed.*, 2020, **59**, 2318-2322.
85. T. Hou, X. Sun, D. Xie, M. Wang, A. Fan, Y. Chen, S. Cai, C. Zheng and W. Hu, *Chemistry*, 2018, **24**, 14786-14793.
86. Z.-J. Zhang, Y.-X. Wang, S.-L. Chou, H.-J. Li, H.-K. Liu and J.-Z. Wang, *J Power Sources*, 2015, **280**, 107-113.
87. L. Wang, J. Światowska, S. Dai, M. Cao, Z. Zhong, Y. Shen and M. Wang, *Mater. Today Energy*, 2019, **11**, 46-60.
88. J. P. Yang, T. F. Zhou, R. Zhu, X. Q. Chen, Z. P. Guo, J. W. Fan, H. K. Liu and W. X. Zhang, *Adv Mater Interfaces*, 2016, **3**, 1500464.
89. Z. Ali, T. Zhang, M. Asif, L. N. Zhao, Y. Yu and Y. L. Hou, *Mater. Today*, 2020, **35**, 131-167.
90. R. A. W. Dryfe, *Curr Opin Electroche*, 2019, **13**, 119-124.
91. D. W. Su, S. X. Dou and G. X. Wang, *Adv Energy Mater*, 2015, **5**, 1401205.
92. C. Zhu, X. Mu, P. A. van Aken, Y. Yu and J. Maier, *Angew. Chem. Int. Ed.*, 2014, **53**, 2152-2156.
93. J. Wang, C. Luo, T. Gao, A. Langrock, A. C. Mignerey and C. Wang, *Small*, 2015, **11**, 473-481.
94. H. Zhang, I. Hasa and S. Passerini, *Adv Energy Mater*, 2018, **8**, 1702582.
95. M. Hu, Y. Jiang, W. Sun, H. Wang, C. Jin and M. Yan, *ACS Appl. Mater. Interfaces*, 2014, **6**, 19449-19455.
96. F. Xie, L. Zhang, C. Ye, M. Jaroniec and S. Z. Qiao, *Adv. Mater.*, 2019, **31**, e1800492.
97. T. Li, A. Qin, L. Yang, J. Chen, Q. Wang, D. Zhang and H. Yang, *ACS Appl. Mater. Interfaces*, 2017, **9**, 19900-19907.
98. S. Wei, S. Choudhury, J. Xu, P. Nath, Z. Tu and L. A. Archer, *Adv. Mater.*, 2017, **29**, 1605512.
99. Y. Lee, J. Lee, J. Lee, K. Kim, A. Cha, S. Kang, T. Wi, S. J. Kang, H. W. Lee and N. S. Choi, *ACS Appl. Mater. Interfaces*, 2018, **10**, 15270-15280.
100. L. M. Suo, O. Borodin, Y. S. Wang, X. H. Rong, W. Sun, X. L. Fan, S. Y. Xu, M. A.

Schroeder, A. V. Cresce, F. Wang, C. Y. Yang, Y. S. Hu, K. Xu and C. S. Wang, *Adv Energy Mater*, 2017, **7**, 1701189.
101. L. Jiang, L. Liu, J. Yue, Q. Zhang, A. Zhou, O. Borodin, L. Suo, H. Li, L. Chen, K. Xu and Y. S. Hu, *Adv. Mater.*, 2020, **32**, e1904427.
102. L. Suo, O. Borodin, T. Gao, M. Olguin, J. Ho, X. Fan, C. Luo, C. Wang and K. Xu, *Science*, 2015, **350**, 938-943.
103. Y. Zhao, L. V. Goncharova, A. Lushington, Q. Sun, H. Yadegari, B. Wang, W. Xiao, R. Li and X. Sun, *Adv. Mater.*, 2017, **29**, 1606663.
104. C. Zhao, L. Liu, X. Qi, Y. Lu, F. Wu, J. Zhao, Y. Yu, Y.-S. Hu and L. Chen, *Adv Energy Mater*, 2018, **8**, 1703012.
105. H. C. Gao, S. Xin, L. G. Xue and J. B. Goodenough, *Chem*, 2018, **4**, 833-844.
106. X. L. Cheng, J. Pan, Y. Zhao, M. Liao and H. S. Peng, *Adv Energy Mater*, 2018, **8**, 1702184.
107. Z. Z. Zhang, Q. Q. Zhang, C. Ren, F. Luo, Q. Ma, Y. S. Hu, Z. B. Zhou, H. Li, X. J. Huang and L. Q. Chen, *J. Mater. Chem. A*, 2016, **4**, 15823-15828.
108. S. S. Chi, X. G. Qi, Y. S. Hu and L. Z. Fan, *Adv Energy Mater*, 2018, **8**, 1702764.
109. B. Sun, P. Li, J. Zhang, D. Wang, P. Munroe, C. Wang, P. H. L. Notten and G. Wang, *Adv. Mater.*, 2018, **30**, e1801334.
110. B. Sun, P. Xiong, U. Maitra, D. Langsdorf, K. Yan, C. Wang, J. Janek, D. Schroder and G. Wang, *Adv. Mater.*, 2020, **32**, e1903891.
111. C. W. Wang, H. Xie, L. Zhang, Y. H. Gong, G. Pastel, J. Q. Dai, B. Y. Liu, E. D. Wachsman and L. B. Hu, *Adv Energy Mater*, 2018, **8**, 1701963.
112. W. Yang, W. Yang, L. B. Dong, G. J. Shao, G. X. Wang and X. W. Peng, *Nano Energy*, 2021, **80**, 105563.
113. L. Ye, M. Liao, T. Zhao, H. Sun, Y. Zhao, X. Sun, B. Wang and H. Peng, *Angew. Chem. Int. Ed.*, 2019, **58**, 17054-17060.
114. F. Wu, J. H. Zhou, R. Luo, Y. X. Huang, Y. Mei, M. Xie and R. J. Chen, *Energy Storage Mater*, 2019, **22**, 376-383.
115. D. Cao, Q. Zhang, A. M. Hafez, Y. Jiao, Y. Ma, H. Li, Z. Cheng, C. Niu and H. Zhu, *Small Methods*, 2019, DOI: 10.1002/smtd.201800539, 1800539.
116. X. Xiang, K. Zhang and J. Chen, *Adv. Mater.*, 2015, **27**, 5343-5364.
117. J. X. Wu, J. P. Liu, Z. H. Lu, K. Lin, Y. Q. Lyu, B. H. Li, F. Ciucci and J. K. Kim, *Energy Storage Mater*, 2019, **23**, 8-16.
118. P. Hartmann, C. L. Bender, M. Vracar, A. K. Durr, A. Garsuch, J. Janek and P. Adelhelm, *Nat. Mater.*, 2013, **12**, 228-232.
119. W. J. Li, C. Han, W. L. Wang, F. Gebert, S. L. Chou, H. K. Liu, X. H. Zhang and S. X. Dou, *Adv Energy Mater*, 2017, **7**, 1700274.
120. Z. Dai, U. Mani, H. T. Tan and Q. Yan, *Small Methods*, 2017, **1**, 1700098.
121. A. Tripathi, A. Rudola, S. R. Gajjela, S. B. Xi and P. Balaya, *J. Mater. Chem. A*, 2019, **7**, 25944-25960.
122. N. Yabuuchi, M. Kajiyama, J. Iwatate, H. Nishikawa, S. Hitomi, R. Okuyama, R. Usui, Y. Yamada and S. Komaba, *Nat. Mater.*, 2012, **11**, 512-517.
123. X. Rong, E. Hu, Y. Lu, F. Meng, C. Zhao, X. Wang, Q. Zhang, X. Yu, L. Gu, Y.-S. Hu, H. Li, X. Huang, X.-Q. Yang, C. Delmas and L. Chen, *Joule*, 2019, **3**, 503-517.

124. X. H. Rong, J. Liu, E. Y. Hu, Y. J. Liu, Y. Wang, J. P. Wu, X. Q. Yu, K. Page, Y. S. Hu, W. L. Yang, H. Li, X. Q. Yang, L. Q. Chen and X. J. Huang, *Joule*, 2018, **2**, 125-140.
125. R. A. House, J.-J. Marie, M. A. Pérez-Osorio, G. J. Rees, E. Boivin and P. G. Bruce, *Nat. Energy*, 2021, **6**, 781-789.
126. R. A. House, U. Maitra, M. A. Perez-Osorio, J. G. Lozano, L. Jin, J. W. Somerville, L. C. Duda, A. Nag, A. Walters, K. J. Zhou, M. R. Roberts and P. G. Bruce, *Nature*, 2020, **577**, 502-508.
127. T. Jin, H. Li, K. Zhu, P. F. Wang, P. Liu and L. Jiao, *Chem. Soc. Rev.*, 2020, **49**, 2342-2377.
128. Y. Qi, Z. Tong, J. Zhao, L. Ma, T. Wu, H. Liu, C. Yang, J. Lu and Y.-S. Hu, *Joule*, 2018, **2**, 2348-2363.
129. Y. Jiang, Z. Z. Yang, W. H. Li, L. C. Zeng, F. S. Pan, M. Wang, X. Wei, G. T. Hu, L. Gu and Y. Yu, *Adv Energy Mater*, 2015, **5**, 1402104.
130. X. Zhang, X. Rui, D. Chen, H. Tan, D. Yang, S. Huang and Y. Yu, *Nanoscale*, 2019, **11**, 2556-2576.
131. M. Law, V. Ramar and P. Balaya, *J Power Sources*, 2017, **359**, 277-284.
132. J. F. Qian, C. Wu, Y. L. Cao, Z. F. Ma, Y. H. Huang, X. P. Ai and H. X. Yang, *Adv Energy Mater*, 2018, **8**, 1702619.
133. K. Hurlbutt, S. Wheeler, I. Capone and M. Pasta, *Joule*, 2018, **2**, 1950-1960.
134. Y. You, X. L. Wu, Y. X. Yin and Y. G. Guo, *Energy Environ. Sci.*, 2014, **7**, 1643-1647.
135. J. Song, L. Wang, Y. Lu, J. Liu, B. Guo, P. Xiao, J. J. Lee, X. Q. Yang, G. Henkelman and J. B. Goodenough, *J. Am. Chem. Soc.*, 2015, **137**, 2658-2664.
136. L. W. Jiang, Y. X. Lu, C. L. Zhao, L. L. Liu, J. N. Zhang, Q. Q. Zhang, X. Shen, J. M. Zhao, X. Q. Yu, H. Li, X. J. Huang, L. Q. Chen and Y. S. Hu, *Nat. Energy*, 2019, **4**, 495-503.
137. P. Adelhelm, P. Hartmann, C. L. Bender, M. Busche, C. Eufinger and J. Janek, *Beilstein J. Nanotechnol.*, 2015, **6**, 1016-1055.
138. X. Xu, D. Zhou, X. Qin, K. Lin, F. Kang, B. Li, D. Shanmukaraj, T. Rojo, M. Armand and G. Wang, *Nat. Commun.*, 2018, **9**, 3870.
139. M. Salama, Rosy, R. Attias, R. Yemini, Y. Gofer, D. Aurbach and M. Noked, *Acs Energy Lett*, 2019, **4**, 436-446.
140. N. Ortiz-Vitoriano, T. P. Batcho, D. G. Kwabi, B. Han, N. Pour, K. P. Yao, C. V. Thompson and Y. Shao-Horn, *J. Phys. Chem. Lett.*, 2015, **6**, 2636-2643.
141. H. Yuan, T. Liu, Y. Liu, J. Nai, Y. Wang, W. Zhang and X. Tao, *Chem. Sci.*, 2019, **10**, 7484-7495.
142. M. M. Ottakam Thotiyl, S. A. Freunberger, Z. Peng and P. G. Bruce, *J. Am. Chem. Soc.*, 2013, **135**, 494-500.
143. A. Ponrouch, E. Marchante, M. Courty, J. M. Tarascon and M. R. Palacin, *Energy Environ. Sci.*, 2012, **5**, 8572-8583.
144. Y. Q. Li, Y. Yang, Y. X. Lu, Q. Zhou, X. G. Qi, Q. S. Meng, X. H. Rong, L. Q. Chen and Y. S. Hu, *Acs Energy Lett*, 2020, **5**, 1156-1158.
145. Y. Yamada, J. Wang, S. Ko, E. Watanabe and A. Yamada, *Nat. Energy*, 2019, **4**, 269-280.
146. Y. Li, Y. Li, A. Pei, K. Yan, Y. Sun, C. L. Wu, L. M. Joubert, R. Chin, A. L. Koh, Y. Yu,

J. Perrino, B. Butz, S. Chu and Y. Cui, *Science*, 2017, **358**, 506-510.
147. K. Westman, R. Dugas, P. Jankowski, W. Wieczorek, G. Gachot, M. Morcrette, E. Irisarri, A. Ponrouch, M. R. Palacin, J. M. Tarascon and P. Johansson, *ACS Appl. Energy Mater.*, 2018, **1**, 2671-2680.
148. L. Fan, S. Y. Wei, S. Y. Li, Q. Li and Y. Y. Lu, *Adv Energy Mater*, 2018, **8**, 1702657.
149. Z. Z. Zhang, Z. Y. Zou, K. Kaup, R. J. Xiao, S. Q. Shi, M. Avdeev, Y. S. Hu, D. Wang, B. He, H. Li, X. J. Huang, L. F. Nazar and L. Q. Chen, *Adv Energy Mater*, 2019, **9**, 1902373.
150. T. Famprikis, O. U. Kudu, J. A. Dawson, P. Canepa, F. Fauth, E. Suard, M. Zbiri, D. Dambournet, O. J. Borkiewicz, H. Bouyanfif, S. P. Emge, S. Cretu, J. N. Chotard, C. P. Grey, W. G. Zeier, M. S. Islam and C. Masquelier, *J. Am. Chem. Soc.*, 2020, **142**, 18422-18436.
151. M. C. Bay, M. Wang, R. Grissa, M. V. F. Heinz, J. Sakamoto and C. Battaglia, *Adv Energy Mater*, 2019, **10**, 1902899.
152. Y. W. Zheng, Q. W. Pan, M. Clites, B. W. Byles, E. Pomerantseva and C. Y. Li, *Adv Energy Mater*, 2018, **8**, 1801885.
153. A. Boschin and P. Johansson, *Electrochim Acta*, 2015, **175**, 124-133.
154. M. Y. Zhang, M. X. Li, Z. Chang, Y. F. Wang, J. Gao, Y. S. Zhu, Y. P. Wu and W. Huang, *Electrochim Acta*, 2017, **245**, 752-759.
155. K. K. Kumar, M. Ravi, Y. Pavani, S. Bhavani, A. K. Sharma and V. V. R. N. Rao, *J. Membr. Sci.*, 2014, **454**, 200-211.
156. Y. L. Ni'mah, M.-Y. Cheng, J. H. Cheng, J. Rick and B.-J. Hwang, *J Power Sources*, 2015, **278**, 375-381.
157. X. W. Yu and A. Manthiram, *Matter*, 2019, **1**, 439-451.
158. Y. Gao, Z. Yan, J. L. Gray, X. He, D. Wang, T. Chen, Q. Huang, Y. C. Li, H. Wang, S. H. Kim, T. E. Mallouk and D. Wang, *Nat. Mater.*, 2019, **18**, 384-389.
159. J. W. Choi and D. Aurbach, *Nat. Rev. Mater.*, 2016, **1**, 16013.
160. P. Lu, Y. Sun, H. F. Xiang, X. Liang and Y. Yu, *Adv Energy Mater*, 2018, **8**, 1702434.
161. H. Hou, C. E. Banks, M. Jing, Y. Zhang and X. Ji, *Adv. Mater.*, 2015, **27**, 7861-7866.
162. A. B. Jorge, R. Jervis, A. P. Periasamy, M. Qiao, J. Y. Feng, L. N. Tran and M. M. Titirici, *Adv Energy Mater*, 2020, **10**, 1902494.
163. V. Aravindan, M. Ulaganathan and S. Madhavi, *J. Mater. Chem. A*, 2016, **4**, 7538-7548.
164. F. Wang, X. Wang, Z. Chang, X. Wu, X. Liu, L. Fu, Y. Zhu, Y. Wu and W. Huang, *Adv. Mater.*, 2015, **27**, 6962-6968.
165. Y. E. Zhu, L. P. Yang, J. Sheng, Y. N. Chen, H. C. Gu, J. P. Wei and Z. Zhou, *Adv Energy Mater*, 2017, **7**.
166. J. Ding, H. L. Wang, Z. Li, K. Cui, D. Karpuzov, X. H. Tan, A. Kohandehghan and D. Mitlin, *Energy Environ. Sci.*, 2015, **8**, 941-955.
167. N. Kurra, M. Alhabeb, K. Maleski, C. H. Wang, H. N. Alshareef and Y. Gogotsi, *Acs Energy Lett*, 2018, **3**, 2094-2100.
168. W. Zuo, R. Li, C. Zhou, Y. Li, J. Xia and J. Liu, *Adv. Sci.*, 2017, **4**, 1600539.
169. X. Wang, S. Kajiyama, H. Iinuma, E. Hosono, S. Oro, I. Moriguchi, M. Okubo and A. Yamada, *Nat. Commun.*, 2015, **6**, 6544.
170. K. Kuratani, M. Yao, H. Senoh, N. Takeichi, T. Sakai and T. Kiyobayashi, *Electrochim*

Acta, 2012, **76**, 320-325.
171. L. Zhao, L. Z. Fan, M. Q. Zhou, H. Guan, S. Qiao, M. Antonietti and M. M. Titirici, *Adv. Mater.*, 2010, **22**, 5202-5206.
172. L. Fan, K. Lin, J. Wang, R. Ma and B. Lu, *Adv. Mater.*, 2018, **30**, e1800804.
173. M. Sevilla and A. B. Fuertes, *Chemsuschem*, 2016, **9**, 1880-1888.
174. M. Sevilla, G. A. Ferrero and A. B. Fuertes, *Chem Mater*, 2017, **29**, 6900-6907.
175. M. M. Titirici, *Adv Energy Mater*, 2021, **11**, 2003700.
176. J. Wang, P. Nie, B. Ding, S. Dong, X. Hao, H. Dou and X. Zhang, *Journal of Materials Chemistry A*, 2017, **5**, 2411-2428.
177. Y. Habibi, L. A. Lucia and O. J. Rojas, *Chem. Rev.*, 2010, **110**, 3479-3500.
178. P. Schlee, S. Herou, R. Jervis, P. R. Shearing, D. J. L. Brett, D. Baker, O. Hosseinaei, P. Tomani, M. M. Murshed, Y. Li, M. J. Mostazo-López, D. Cazorla-Amorós, A. B. Jorge Sobrido and M.-M. Titirici, *Chem. Sci.*, 2019, DOI: 10.1039/c8sc04936j.
179. B. Hu, K. Wang, L. Wu, S. H. Yu, M. Antonietti and M. M. Titirici, *Adv. Mater.*, 2010, **22**, 813-828.
180. K. E. Shopsowitz, H. Qi, W. Y. Hamad and M. J. Maclachlan, *Nature*, 2010, **468**, 422-425.
181. S. Hérou, M. Crespo Ribadeneyra, P. Schlee, H. Luo, L. Cristian Tanase, C. Roβberg and M. Titirici, *J. Energy Chem.*, 2021, **53**, 36-48.
182. S. Hérou, M. Crespo and M. Titirici, *CrystEngComm*, 2020, **22**, 1560-1567.
183. S. Herou, M. C. Ribadeneyra, R. Madhu, V. Araullo-Peters, A. Jensen, P. Schlee and M. Titirici, *Green Chem*, 2019, **21**, 550-559.
184. X. Wang, G. Pawar, Y. Li, X. Ren, M. Zhang, B. Lu, A. Banerjee, P. Liu, E. J. Dufek, J.-G. Zhang, J. Xiao, J. Liu, Y. S. Meng and B. Liaw, *Nat. Mater.*, 2020, **19**, 1339-1345.
185. C. Zhou, J. Wang, X. Zhu, K. Chen, Y. Ouyang, Y. Wu, Y.-E. Miao and T. Liu, *Nano Res*, 2021, **14**, 1541-1550.
186. B. J. Inkson, in *Materials Characterization Using Nondestructive Evaluation (NDE) Methods*, eds. G. Hübschen, I. Altpeter, R. Tschuncky and H.-G. Herrmann, Woodhead Publishing, 2016, DOI: https://doi.org/10.1016/B978-0-08-100040-3.00002-X, pp. 17-43.
187. Z. Fan, L. Zhang, D. Baumann, L. Mei, Y. Yao, X. Duan, Y. Shi, J. Huang, Y. Huang and X. Duan, *Adv Mater*, 2019, **31**, e1900608.
188. X. Zheng, B. Zhang, H. Sanei, H. Bao, Z. Meng, C. Wang and K. Li, *Marine and Petroleum Geology*, 2019, **100**, 165-178.
189. D. A. Stevens and J. R. Dahn, *J. Electrochem. Soc.*, 2000, **147**, 4428.
190. A. C. Ferrari and D. M. Basko, *Nat. Nanotechnol.*, 2013, **8**, 235-246.
191. E. Korin, N. Froumin and S. Cohen, *ACS Biomaterials Science & Engineering*, 2017, **3**, 882-889.
192. X. Ma, C. Yuan and X. Liu, *Materials (Basel)*, 2013, **7**, 75-84.
193. C. Bommier, T. W. Surta, M. Dolgos and X. Ji, *Nano Lett.*, 2015, **15**, 5888-5892.
194. H. Liu, Z. Xu, Z. Guo, J. Feng, H. Li, T. Qiu and M. Titirici, *Philos. Trans. A Math. Phys. Eng. Sci.*, 2021, **379**, 20200340.
195. L. C. Dreyer, A. L. Niemann and M. Z. Hauschild, *Int. J. Life Cycle Assess.*, 2003, **8**, 191-200.

196. G. W. T. M. J. Frisch, H. B. Schlegel, G. E. Scuseria, M. A. Robb, J. R. Cheeseman, G. Scalmani, V. Barone, G. A. Petersson, H. Nakatsuji, X. Li, M. Caricato, A. Marenich, J. Bloino, B. G. Janesko, R. Gomperts, B. Mennucci, H. P. Hratchian, J. V. Ortiz, A. F. Izmaylov, J. L. Sonnenberg, D. Williams-Young, F. Ding, F. Lipparini, F. Egidi, J. Goings, B. Peng, A. Petrone, T. Henderson, D. Ranasinghe, V. G. Zakrzewski, J. Gao, N. Rega, G. Zheng, W. Liang, M. Hada, M. Ehara, K. Toyota, R. Fukuda, J. Hasegawa, M. Ishida, T. Nakajima, Y. Honda, O. Kitao, H. Nakai, T. Vreven, K. Throssell, J. A. Montgomery, Jr., J. E. Peralta, F. Ogliaro, M. Bearpark, J. J. Heyd, E. Brothers, K. N. Kudin, V. N. Staroverov, T. Keith, R. Kobayashi, J. Normand, K. Raghavachari, A. Rendell, J. C. Burant, S. S. Iyengar, J. Tomasi, M. Cossi, J. M. Millam, M. Klene, C. Adamo, R. Cammi, J. W. Ochterski, R. L. Martin, K. Morokuma, O. Farkas, J. B. Foresman, and D. J. Fox, *Gaussian 09 (Revision A.02), Gaussian, Inc., Wallingford CT*, 2016.
197. J. P. Perdew, K. Burke and M. Ernzerhof, *Phys. Rev. Lett.*, 1996, **77**, 3865-3868.
198. A. D. Becke, *J. Chem. Phys.*, 1993, **98**, 5648-5652.
199. E. D. Glendening, C. R. Landis and F. Weinhold, *J. Comput. Chem.*, 2013, **34**, 1429-1437.
200. H. Yadegari, M. A. Koronfel, K. Wang, D. B. Thornton, I. E. L. Stephens, C. Molteni, P. D. Haynes and M. P. Ryan, *Acs Energy Lett*, 2021, **6**, 1633-1638.
201. J. Peters, D. Buchholz, S. Passerini and M. Weil, *Energy Environ. Sci.*, 2016, **9**, 1744-1751.
202. S. A. Nicolae, H. Au, P. Modugno, H. Luo, A. E. Szego, M. Qiao, L. Li, W. Yin, H. J. Heeres, N. Berge and M.-M. Titirici, *Green Chem*, 2020, **22**, 4747-4800.
203. P. Modugno and M. M. Titirici, *Chemsuschem*, 2021, **14**, 5271-5282.
204. Z. Xu, F. Xie, J. Wang, H. Au, M. Tebyetekerwa, Z. Guo, S. Yang, Y. S. Hu and M. M. Titirici, *Adv. Funct. Mater.*, 2019, **29**, 1903895.
205. S. A. Nicolae, J. Louis-Therese, S. Gaspard, P. Á. Szilágyi and M. M. Titirici, *Nano Select*, 2021, DOI: 10.1002/nano.202100099.
206. C. Casiraghi, A. C. Ferrari and J. Robertson, *Phys Rev B*, 2005, **72**, 085401.
207. A. C. Ferrari and J. Robertson, *Phys Rev B*, 2000, **61**, 14095-14107.
208. A. C. Ferrari, J. C. Meyer, V. Scardaci, C. Casiraghi, M. Lazzeri, F. Mauri, S. Piscanec, D. Jiang, K. S. Novoselov, S. Roth and A. K. Geim, *Phys. Rev. Lett.*, 2006, **97**, 187401.
209. E. Olsson, J. Cottom and Q. Cai, *Small*, 2021, **17**, e2007652.
210. H. He, D. Sun, Y. Tang, H. Wang and M. Shao, *Energy Storage Mater*, 2019, **23**, 233-251.
211. D. S. Bin, Y. M. Li, Y. G. Sun, S. Y. Duan, Y. X. Lu, J. M. Ma, A. M. Cao, Y. S. Hu and L. J. Wan, *Adv Energy Mater*, 2018, **8**, 1800855.
212. H. Zhang, H. Ming, W. Zhang, G. Cao and Y. Yang, *ACS Appl. Mater. Interfaces*, 2017, **9**, 23766-23774.
213. Y. Zheng, Y. Wang, Y. Lu, Y.-S. Hu and J. Li, *Nano Energy*, 2017, **39**, 489-498.
214. Y. Wen, K. He, Y. Zhu, F. Han, Y. Xu, I. Matsuda, Y. Ishii, J. Cumings and C. Wang, *Nat. Commun.*, 2014, **5**, 4033.
215. X. Li, J. Sun, W. Zhao, Y. Lai, X. Yu and Y. Liu, *Adv. Funct. Mater.*, 2021, 2106980.
216. Z. Xu, Z. Y. Guo, R. Madhu, F. Xie, R. X. Chen, J. Wang, M. Tebyetekerwa, Y. S. Hu

and M. M. Titirici, *Energy Environ. Sci.*, 2021, **14**, 6381-6393.
217. J. S. Weaving, A. Lim, J. Millichamp, T. P. Neville, D. Ledwoch, E. Kendrick, P. F. McMillan, P. R. Shearing, C. A. Howard and D. J. L. Brett, *ACS Appl. Energy Mater.*, 2020, **3**, 7474-7484.
218. P. Ge, S. Li, L. Xu, K. Zou, X. Gao, X. Cao, G. Zou, H. Hou and X. Ji, *Adv Energy Mater*, 2019, **9**, 1803035.
219. J. Wang, Z. Xu, J. C. Eloi, M. M. Titirici and S. J. Eichhorn, *Adv. Funct. Mater.*, 2022, DOI: 10.1002/adfm.202110862, 2110862.
220. X. Zheng, H. Fu, C. Hu, H. Xu, Y. Huang, J. Wen, H. Sun, W. Luo and Y. Huang, *J. Phys. Chem. Lett.*, 2019, **10**, 707-714.
221. J. Bae, Y. Qian, Y. Li, X. Zhou, J. B. Goodenough and G. Yu, *Energy Environ. Sci.*, 2019, **12**, 3319-3327.
222. L. Ye, M. Liao, H. Sun, Y. Yang, C. Tang, Y. Zhao, L. Wang, Y. Xu, L. Zhang, B. Wang, F. Xu, X. Sun, Y. Zhang, H. Dai, P. G. Bruce and H. Peng, *Angew. Chem. Int. Ed.*, 2019, **58**, 2437-2442.
223. D. Iribarren, J. F. Peters and J. Dufour, *Fuel*, 2012, **97**, 812-821.
224. A. Mohammadi, G. Venkatesh, M. Sandberg, S. Eskandari, S. Joseph and K. Granström, *Sustainability*, 2020, **12**, 9026.
225. H. Li, L. Peng, Y. Zhu, D. Chen, X. Zhang and G. Yu, *Energy Environ. Sci.*, 2016, **9**, 3399-3405.
226. P. Trogadas, V. Ramani, P. Strasser, T. F. Fuller and M. O. Coppens, *Angew. Chem. Int. Ed.*, 2016, **55**, 122-148.
227. K. E. Shopsowitz, W. Y. Hamad and M. J. MacLachlan, *Angew. Chem. Int. Ed.*, 2011, **50**, 10991-10995.
228. H. L. Zhu, F. Shen, W. Luo, S. Z. Zhu, M. H. Zhao, B. Natarajan, J. Q. Dai, L. H. Zhou, X. L. Ji, R. S. Yassar, T. Li and L. B. Hu, *Nano Energy*, 2017, **33**, 37-44.
229. Y. Cao, L. Xiao, M. L. Sushko, W. Wang, B. Schwenzer, J. Xiao, Z. Nie, L. V. Saraf, Z. Yang and J. Liu, *Nano Lett.*, 2012, **12**, 3783-3787.
230. Y. M. Li, L. Q. Mu, Y. S. Hu, H. Li, L. Q. Chen and X. J. Huang, *Energy Storage Mater*, 2016, **2**, 139-145.
231. V. Augustyn, P. Simon and B. Dunn, *Energy Environ. Sci.*, 2014, **7**, 1597-1614.
232. Y. Gogotsi and R. M. Penner, *Acs Nano*, 2018, **12**, 2081-2083.
233. J. Niu, J. J. Liang, R. Shao, M. Y. Liu, M. L. Dou, Z. L. Li, Y. Q. Huang and F. Wang, *Nano Energy*, 2017, **41**, 285-292.
234. Y. Ma, Q. Guo, M. Yang, Y. Wang, T. Chen, Q. Chen, X. Zhu, Q. Xia, S. Li and H. Xia, *Energy Storage Mater*, 2018, **13**, 134-141.
235. J. Deng, T. Y. Xiong, F. Xu, M. M. Li, C. L. Han, Y. T. Gong, H. Y. Wang and Y. Wang, *Green Chem*, 2015, **17**, 4053-4060.
236. P. Iamprasertkun, A. Krittayavathananon and M. Sawangphruk, *Carbon*, 2016, **102**, 455-461.
237. C. Zhijiang, S. Xingjuan and F. Yanan, *J Power Sources*, 2013, **227**, 53-59.
238. J. Z. Chen, X. Y. Zhou, C. T. Mei, J. L. Xu, S. Zhou and C. P. Wong, *J Power Sources*, 2017, **342**, 48-55.
239. H. Li, L. Peng, Y. Zhu, X. Zhang and G. Yu, *Nano Lett.*, 2016, **16**, 5938-5943.

240. C. Wang, F. X. Wang, Z. C. Liu, Y. J. Zhao, Y. Liu, Q. Yue, H. W. Zhu, Y. H. Deng, Y. P. Wu and D. Y. Zhao, *Nano Energy*, 2017, **41**, 674-680.
241. Y. Dall'Agnese, P. L. Taberna, Y. Gogotsi and P. Simon, *J. Phys. Chem. Lett.*, 2015, **6**, 2305-2309.
242. J. Ding, Z. Li, K. Cui, S. Boyer, D. Karpuzov and D. Mitlin, *Nano Energy*, 2016, **23**, 129-137.
243. H. C. Gao, W. D. Zhou, K. Park and J. B. Goodenough, *Adv Energy Mater*, 2016, **6**, 1600467.
244. Y. Y. Wang, B. H. Hou, Y. N. Wang, H. Y. Lu, J. Z. Guo, Q. L. Ning, J. P. Zhang, C. L. Lu and X. L. Wu, *J. Mater. Chem. A*, 2018, **6**, 6578-6586.
245. J.-Y. Hwang, S.-T. Myung, J.-H. Lee, A. Abouimrane, I. Belharouak and Y.-K. Sun, *Nano Energy*, 2015, **16**, 218-226.
246. B. W. Xiao, F. A. Soto, M. Gu, K. S. Han, J. H. Song, H. Wang, M. H. Engelhard, V. Murugesan, K. T. Mueller, D. Reed, V. L. Sprenkle, P. B. Balbuena and X. L. Li, *Adv Energy Mater*, 2018, **8**, 1801441.
247. S. Y. Dong, Y. L. Xu, L. Y. Wu, H. Dou and X. G. Zhang, *Energy Storage Mater*, 2018, **11**, 8-15.
248. Z. Chen, V. Augustyn, X. Jia, Q. Xiao, B. Dunn and Y. Lu, *Acs Nano*, 2012, **6**, 4319-4327.
249. J. Yin, L. Qi and H. Wang, *ACS Appl. Mater. Interfaces*, 2012, **4**, 2762-2768.
250. M. Yang and Z. Zhou, *Adv. Sci.*, 2017, **4**, 1600408.
251. M. X. Li, X. W. Wang, Y. Q. Yang, Z. Chang, Y. P. Wu and R. Holze, *J Membrane Sci*, 2015, **476**, 112-118.
252. W. Zhou, Z. Wang, Y. Pu, Y. Li, S. Xin, X. Li, J. Chen and J. B. Goodenough, *Adv. Mater.*, 2019, **31**, 1805574.
253. G. H. Chen, F. Zhang, Z. M. Zhou, J. R. Li and Y. B. Tang, *Adv Energy Mater*, 2018, **8**, 1801219.
254. X. Hu, Z. Li, Y. Zhao, J. Sun, Q. Zhao, J. Wang, Z. Tao and J. Chen, *Sci. Adv.*, 2017, **3**.
255. M. Tebyetekerwa, I. Marriam, Z. Xu, S. Yang, H. Zhang, F. Zabihi, R. Jose, S. Peng, M. Zhu and S. Ramakrishna, *Energy Environ. Sci.*, 2019, DOI: 10.1039/c8ee02607f.
256. O. Schmidt, S. Melchior, A. Hawkes and I. Staffell, *Joule*, 2019, **3**, 81-100.
257. M. Tebyetekerwa, Z. Xu, W. Li, X. Wang, I. Marriam, S. Peng, S. Ramkrishna, S. Yang and M. Zhu, *ACS Appl. Energy Mater.*, 2018, **1**, 377-386.
258. M. Tebyetekerwa and S. Ramakrishna, *Matter*, 2020, **2**, 279-283.
259. Z. F. Li, Y. C. Chen, Z. L. Jian, H. Jiang, J. J. Razink, W. F. Stickle, J. C. Neuefeind and X. L. Ji, *Chem Mater*, 2018, **30**, 4536-4542.
260. R. Guo, C. Lv, W. Xu, J. Sun, Y. Zhu, X. Yang, J. Li, J. Sun, L. Zhang and D. Yang, *Adv Energy Mater*, 2020, **10**, 1903652.
261. M. Titirici, *Nat. Catal.*, 2019, **2**, 642-643.
262. M. H. Lee, S. J. Kim, D. Chang, J. Kim, S. Moon, K. Oh, K.-Y. Park, W. M. Seong, H. Park, G. Kwon, B. Lee and K. Kang, *Mater. Today*, 2019, **29**, 26-36.
263. J. L. Ma, F. L. Meng, Y. Yu, D. P. Liu, J. M. Yan, Y. Zhang, X. B. Zhang and Q. Jiang, *Nat. Chem.*, 2019, **11**, 64-70.
264. M. Q. Zhu, S. M. Li, B. Li, Y. J. Gong, Z. G. Du and S. B. Yang, *Sci. Adv.*, 2019, **5**,

eaau6264.
265. J. Cui, S. Yao, M. Ihsan-Ul-Haq, J. Wu and J.-K. Kim, *Adv Energy Mater*, 2019, **9**, 1802777.
266. Y. Jie, X. Liu, Z. Lei, S. Wang, Y. Chen, F. Huang, R. Cao, G. Zhang and S. Jiao, *Angew. Chem. Int. Ed.*, 2020, **59**, 3505-3510.
267. G. Huang, J. Han, F. Zhang, Z. Wang, H. Kashani, K. Watanabe and M. Chen, *Adv. Mater.*, 2019, **31**, e1805334.
268. H. Li, D. Chao, B. Chen, X. Chen, C. Chuah, Y. Tang, Y. Jiao, M. Jaroniec and S.-Z. Qiao, *Journal of the American Chemical Society*, 2020, **142**, 2012-2022.
269. E. Olsson, J. Cottom, H. Au, M.-M. Titirici and Q. Cai, *Carbon*, 2021, **177**, 226-243.
270. X. Hu, P. H. Joo, H. Wang, E. Matios, C. Wang, J. Luo, X. Lu, K. Yang and W. Li, *Adv. Funct. Mater.*, 2019, **29**, 1807974.
271. J. Liu, Y. Zhang, L. Zhang, F. Xie, A. Vasileff and S. Z. Qiao, *Adv. Mater.*, 2019, **31**, e1901261.
272. R. Zhang, X. Shen, X.-B. Cheng and Q. Zhang, *Energy Storage Mater*, 2019, **23**, 556-565.
273. W. Chen, Y. Hu, W. Lv, T. Lei, X. Wang, Z. Li, M. Zhang, J. Huang, X. Du, Y. Yan, W. He, C. Liu, M. Liao, W. Zhang, J. Xiong and C. Yan, *Nat. Commun.*, 2019, **10**, 4973.
274. Z. Ye, S. Xie, Z. Cao, L. Wang, D. Xu, H. Zhang, J. Matz, P. Dong, H. Fang, J. Shen and M. Ye, *Energy Storage Mater*, 2021, **37**, 378-386.
275. F. Xie, H. Li, X. Wang, X. Zhi, D. Chao, K. Davey and S.-Z. Qiao, *Adv Energy Mater*, 2021, **11**, 2003419.
276. W. Liu, Y. Xia, W. Wang, Y. Wang, J. Jin, Y. Chen, E. Paek and D. Mitlin, *Adv Energy Mater*, 2019, **9**, 1802918.
277. B. A. Zhang, C. M. Ghimbeu, C. Laberty, C. Vix-Guterl and J. M. Tarascon, *Adv Energy Mater*, 2016, **6**, 1501588.
278. Y. Yao, H. Wang, H. Yang, S. Zeng, R. Xu, F. Liu, P. Shi, Y. Feng, K. Wang, W. Yang, X. Wu, W. Luo and Y. Yu, *Adv. Mater.*, 2020, **32**, e1905658.
279. B. Chen, D. Chao, E. Liu, M. Jaroniec, N. Zhao and S.-Z. Qiao, *Energy Environ. Sci.*, 2020, **13**, 1096-1131.
280. Y. Qiao, H. Yang, Z. Chang, H. Deng, X. Li and H. Zhou, *Nat. Energy*, 2021, **6**, 653-662.
281. H. Alptekin, H. Au, A. C. S. Jensen, E. Olsson, M. Goktas, T. F. Headen, P. Adelhelm, Q. Cai, A. J. Drew and M.-M. Titirici, *ACS Appl. Energy Mater.*, 2020, **3**, 9918-9927.
282. W. Zhang, S. Zhang, L. Fan, L. Gao, X. Kong, S. Li, J. Li, X. Hong and Y. Lu, *Acs Energy Lett*, 2019, **4**, 644-650.
283. Y. Yang, D. M. Davies, Y. Yin, O. Borodin, J. Z. Lee, C. Fang, M. Olguin, Y. Zhang, E. S. Sablina, X. Wang, C. S. Rustomji and Y. S. Meng, *Joule*, 2019, **3**, 1986-2000.